79-06

National Space Science Data Center/
World Data Center A For Rockets and Satellites

A Study of Inner Zone Electron Data and Their Comparison With Trapped Radiation Models

August 1979

NSSDC/WDC-A-R&S 79-06

A Study of Inner Zone Electron Data and their Comparison with Trapped Radiation Models

by

Michael J. Teague

Norman J. Schofield

King W. Chan

James I. Vette

August 1979

National Space Science Data Center (NSSDC)/
World Data Center A for Rockets and Satellites (WDC-A-R&S)
National Aeronautics and Space Administration
Goddard Space Flight Center
Greenbelt, Maryland 20771

This document makes use of the international metric units according to the Système International d'Unites (SI) with the exception of gauss units, which were not converted. In certain cases, conventional units that are the bases of measurements and calculations reported are stated in parentheses following the computed SI equivalents.

CONTENTS

TABLES

ILLUSTRATIONS

ILLUSTRATIONS (Concluded)

I. INTRODUCTION

The purpose of this document is twofold. First, the document presents a summary of the recent inner radiation zone electron data available from the National Space Science Data Center. Second, the document presents an intercomparison of these data, describing the morphology of the inner radiation zone, and compares the data with the current generation of inner zone trapped electron models.

An analytic representation of the inner zone equatorial pitch angle distribution is presented. This model is based upon data from eight satellites and is used to reduce all data to the form of equatorial flux. In general, in previous data comparisons, different pitch angle distributions were used for data reduction; an important feature of the present analysis is the use of a common distribution. The data are compared with the inner zone models AE-6 (*Teague et al.*, 1976) and AE-5 1967 (*Teague and Vette*, 1972). For those L values for which storm-time variations are large, the data are event integrated using a simple storm model.

The conclusion from this analysis is that, with few exceptions, the data are observed to be in good agreement. Although it is evident that no Starfish-free high-energy electron measurements are available from the inner portion of the inner radiation zone, the general conclusion is that the AE-6 model provides a good description of the present solar maximum environment.

II. MORPHOLOGY OF THE INNER RADIATION ZONE

Data from the following satellites were used in the present analysis: OV3-3, OV1-13, OV1-19, OGO 5, OGO 1, OGO 3, 1963-083C, and OSO 4. The data

are summarized in Table 1 and the time and energy coverage are shown in Figure 1. In this figure the energy interval of a channel is marked by a vertical bar and the nominal energy of a threshold channel is indicated by a single upward arrow. The time span of a data channel is represented by the length of the horizontal bar together with the spacecraft designation. In many cases the time coverage varies with the L value and the horizontal bars indicate that data were obtained at some L values. For the OV3-3 and OV1-19 satellites, the energy interval of some channels overlaps. The overlap regions are indicated by cross hatching. In general, data were sorted into 0.1 L bins for $L \geq 1.4$ and 0.05 L bins for $1 < 1.4$. Processing of the individual data sets is discussed in Appendix A.

A. The Equatorial Pitch Angle Distribution Model

In order to reduce the data in an efficient and consistent manner, an analytic equatorial pitch angle distribution was developed. The following form was adopted for fluxes within approximately two orders of magnitude of the equatorial flux:

$$\log_{10} J = C \text{ for } 90^\circ \geq \alpha_0 \geq \alpha_h \qquad (1)$$

and

$$= a_0 + a_1 x + a_2 x^2 + a_3 x^3 + a_4 x^4 \text{ for } \alpha_h > \alpha_0 \geq \alpha_m$$

where

$$x = (90 - \alpha_0)^2$$

These equations define a pitch angle α_h above which the flux is independent of equatorial pitch angle, α_0. For equatorial pitch angles in the range α_h to α_m, a polynominal is used. In the region of the atmospheric cutoff for $L \geq 1.4$, $\alpha_0 < \alpha_m$, a high order polynomial of the form

$$\log_{10} J = a + b\, \alpha_0^{-18} \qquad (2)$$

is used for which an atmospheric cutoff pitch angle, α_c, is defined as the angle at which the flux is three orders of magnitude below $J(\alpha_m)$, and then

$$a = \log_{10} J(\alpha_m) - 3Y/(Y-1)$$

and

$$b = 3\ \alpha_c^{1.8}/(Y-1)$$

where

$$Y = (\alpha_c/\alpha_m)^{1.8}$$

For $L < 1.4$, the $\alpha_0^{-1.8}$ expression is not used and equation (1) is extended to the range $\alpha_h > \alpha_0 \geq \alpha_c$ for which α_c is defined as the pitch angle at which the flux is four orders of magnitude below the equatorial value or 1 electron/(cm^2·s·sr·keV), whichever angle is greater.

The coefficients of the equatorial pitch angle distribution model are given in Table 2, and the family of curves given by equation (1) is compared for various L values in Figures 2 and 3 by normalizing at 90° equatorial pitch angle to a flux of 1 electron/(cm^2·s·sr·keV). In addition, to facilitate comparison, the curves in the upper panel in Figure 2 are normalized to $\alpha_m(L = 2.4)$ using the expression

$$\alpha_{0_{\text{Norm}}}(L) = \alpha_0(L) + \alpha_m(2.4) - \alpha_m(L)$$

and the curves in Figure are normalized to $\alpha_m(L = 2.2)$ using a similar expression. Note that neither a_0 nor C are given in Table 2, because these parameters represent the absolute flux at any L value and energy and do not relate to the shape of the equatorial pitch angle distribution.

Over the range $1.4 \leq L \leq 2.2$, two sets of coefficients for equation (1) were required to adequately describe the energy dependence of the equatorial pitch angle distribution. For higher and lower L values, insufficient data were available to observe any energy dependence. Similarly, for equation (2), energy dependence was not included in the coefficients.

The coefficients of equation (1) were determined by weighted least

squares fit to data from the following satellites: 1963-038C, OV3-3, OV1-13, OV1-19, OGO 5, OGO 1, and OGO 3. The most useful data sets in this respect were OV1-13, OGO 5, and, at low L values, 1963-038C. Where possible, the coefficients were determined from data obtained during magnetically quiet periods. The analytic fits are compared with representative data in Figures 4 through 40 for various L values and energies. With the exception of the normalized curves shown for 1963-038C and OSO 4, the equatorial differential flux shown in these figures has units of electrons/($cm^2 \cdot s \cdot sr \cdot keV$). For the curves shown in Figures 5, 6, and 9, the OSO 4 data have been normalized to the 1963-038C data at the lowest B value of the OSO 4 observations. In Figure 11 the 1963-038C data are normalized to Day 258, 1967.

Most of the data shown in Figures 4 through 40 were used only in determining the fit given by equation (1). The low pitch angle data, obtained near the atmospheric cutoff and used for determining the coefficients of equation (2), are shown in Figures 41 through 48 for L = 1.4 through 2.4. Normalized data are shown from the following satellites: OGO 5, OGO 3, OSO 4, 1963-038C, OV3-3, and OV1-13. Because of the general shortage of data in the region of the atmospheric cutoff, the data were normalized with respect to time and energy at $\alpha_0 = \alpha_m$. Because the OV1-13 satellite provided the most significant data set for $\alpha_0 > \alpha_m$, the data were normalized to 500 keV and day 140 1968. The 1963-038C data are not shown explicitly, but separate fits were made to these data and the resulting curves are shown in Figures 41 through 46.

Weighted least squares fits were performed to the data and the fitted curves are shown in Figures 41 through 48. The smallest pitch angle for which these curves are shown corresponds to the model atmospheric cutoff

pitch angle, α_c. Estimates of α_c based upon the data are shown as horizontal bars. These cutoff angles are summarized in Figure 49, where the L dependence is shown for $1.2 \leq L \leq 2.4$. Because the mirror point B value is a more sensitive parameter in this region, this parameter is also shown and may be compared with the H_{min} curves for 50 km and 100 km, calculated using the Goddard Space Flight Center 12/66 magnetic field model updated to an epoch of January 1968.

The data presented in Figures 4 through 48 indicated that, in general, the shape of the quiet time equatorial pitch angle distribution in the inner zone is described to better than a factor of two accuracy for all pitch angles by the model given in equations (1) and (2) and Table 2. The exceptions are at low L values ($L < 1.35$), high L values ($L > 2.2$), and at pitch angles within approximately 3° of α_c for which data coverage is poor and considerable scatter is evident. In these regions the fit is accurate to no better than a factor of three.

As noted previously, the fit is largely based upon quiet time data. Using OGO 5 data, *West et al.* (1973) observed considerable variation in the shape of the outer zone pitch angle distribution correlated with magnetic activity. In the inner zone, magnetic activity has a significant effect on flux levels for $L \geq 1.7$. Unfortunately, with the present data base, the satellites providing good pitch angle coverage at these L values (viz. OV1-13 and OGO 5) did not have good coverage during magnetic storms. However, a limited amount of data is available, and quiet time and storm time pitch angle distributions are compared in Figures 50 and 51 at $L = 2.0$ and 2.4, respectively. These data indicate that within

the limited pitch angle coverage, no time dependence of the pitch angle distribution is observed, therefore the fit described in this section is applied to storm time and quiet time data.

B. Data Intercomparison and Morphology

The fit presented in Section II.A. was used to reduce the data to equatorial flux for the purposes of intercomparing data and examining temporal variations. Flux vs time plots are presented in Figures 52 through 118 for the following satellites: OV3-3, OV1-13, OV1-19, OGO 5, OGO 1, and OGO 3. OSO 4 equatorial flux radial profiles are given in Figure 119. The problems involved with processing the individual data sets using the model are discussed in Appendix A.

The data are compared and discussed under the two general headings of long and short term temporal variations. The former category includes such effects as the decay of particles injected by the Starfish detonation in 1962 and long term flux changes correlated with solar cycle variations. The latter category refers exclusively to magnetic storm effects. These effects are rarely greater than a factor of two in the flux for $L < 1.7$. For instance, the largest magnetic storm observed in the data used in the present analysis occurred in May 1967 (peak daily mean Dst = -243) and, in Figure 112 at $L = 1.6$, it can be seen that the OGO 3 data show flux variations of less than a factor of two at any energy.

Quiet time inner zone spectra are presented in Figures 120 through 134 for L values 1.2 through 2.4. Data are shown from time intervals for which data are relatively abundant and for which several data sets are available. The data shown are grouped into four general epochs (see Figure 1):

Oct. - Nov. 1964	OGO 1
Pre-Sept. 1966 storm	OV3-3, OGO 3
Pre-June 1968 storm	OV1-13, OSO 4, OGO 5
Jan. 1970	OV1-19

The general agreement between the OGO 3 and the OV3-3 quiet time data is good, particularly for the data taken near 0.5 MeV. The only discrepancy is evident over the L range 1.4 to 1.8 for which the high energy (1.33 MeV) OGO 3 data are between a factor of two and five higher than the comparable OV3-3 data. A possible explanation may be that the proton correction given by *Vampola* (1975) for the high energy OV3-3 channels may be excessive.

The general agreement among the quiet time data from OGO 5, OV1-13, and OSO 4 is good. The exceptions are the two lower energy channels of the OV1-13 detector, which appear to be significantly lower than the comparable data for L > 1.3. In addition, at a few L values, the OSO 4 data are significantly lower (e.g., L = 1.5) or higher (e.g., L = 1.9, E = 397 keV) than the OGO 5 data. However, the general good agreement of the OSO 4 data with other data may be taken as a measure of the accuracy of the pitch angle distribution over a wide range of equatorial pitch angles because the actual OSO 4 fluxes are in excess of two orders of magnitude below the equatorial perpendicular fluxes shown in Figures 121 through 129.

The general quiet time morphology of the inner zone over the interval from near solar minimum in 1964 to near solar maximum in 1969 is characterized in Figures 135 through 137. Three L values are shown cor-

responding to the inner edge of the zone (L = 1.4), the peak of the zone (L = 1.8), and the slot region (L = 2.4). Data were interpolated and normalized to three energies using the quiet time spectra and averaged where appropriate at any given time: 80 keV (OGO 1 and 3 at ~84 keV and OGO 5 at 79 keV), 500 keV (OGO 1 and 3 at 491 keV, OGO 5 at 479 keV, OV3-3 at 475 keV, OV1-13 at 500 keV, and OV1-19 at 444 keV and 537 keV), and 800 keV (OGO 5 at 822 keV, OV3-3 at 712 keV and 957 keV, and OV1-13 at 670 keV).

A salient feature of the data shown in Figures 135 and 136 is the significant flux decrease observed at the higher energies over the time period 1964 to 1966. This is attributable to the decay of the artificial particles injected by the Starfish explosion in July 1962. The extent of the influence of these particles on the inner radiation zone electron flux was discussed by *Teague and Stassinopoulos* (1972). They suggest that the longer lived artificial particles are at approximately 1.6 MeV at L = 1.3 and that the fluxes of these particles reach the natural background levels approximately 8 years after Starfish (i.e., beyond the time coverage of the present data). With the exception of OGO 1 data none of the data presented in this report are influenced by artificial particles for $L \geq 1.7$ or at any L value for $E \lesssim 300$ keV. To a significant extent, however, OV3-3 and OGO 3 data are influenced outside this range. The OGO 5, OV1-13, and OSO 4 data appear to be almost completely free of the effects of artificial particle with the exception of the high energy channels (E > 822 keV) from OGO 5 at low L values (L = 1.5). The separation of the data into three distinct groups indicating various

phases of the decay of the Starfish particles can be clearly seen in Figure 122. The relatively abundant artificial particles are at the higher energies such as those shown in Figure 138 for L = 1.5. The data in this figure were normalized to 1.5 MeV, and the OV3-3 and OGO 3 data were averaged. The AE-2 model is taken from *Vette et al.* (1966). The STARAD data from late 1962 were taken from *West* (1976). The Starfish model of *Teague and Stassinopoulos* (1972) shows excellent agreement with the data at all epochs between 1962 and 1968.

An additional feature of Figures 135 through 137 is the flux variations at energies, L values, and times away from those that are Starfish-influenced. The variations are dramatized by the guidelines and appear to show a quiet time flux increase from solar minimum to solar maximum. The largest variation is a factor of four, although in some cases the flux increase is only slightly larger than the error bars. The effect is more pronounced at the peak of the inner zone than in the slot region. Observations over a wider Starfish-free time period are required before this effect can be convincingly associated with solar cycle variations. In fact, in the region of the inner zone peak where the effect is largest, the distinction between quiet time and storm time variations becomes difficult to make and is perhaps arbitrary. For instance, in Figure 57 at L = 1.8, it is probably not appropriate to identify the flux level at 712 keV before the May 1967 storm as quiet because the effects of the earlier September 1966 storm may still be decaying. On the other hand, at L = 2.0 in Figure 59, the decay process from the September 1966 storm is clearly complete before the May 1967 storm occurs and the prestorm

flux for the later storm is significantly higher than the earlier storm. An additional effect is apparent in Figure 92, in which the OGO 5 data show at all energies a significant flux decrease leading up to the October 1968 storm. Although there is no significant enhancement of the flux around the time of the June 1968 storm, a reduction of the flux occurs following this storm. The conclusion is that it is not possible to separate completely the inner zone flux into two independent components of storm time and quiet time flux.

Seven magnetic storms were observed during the time period for which data are presented in this report. The timing of these storms in relation to the data is shown in Figures 1, 136, and 137, and the relative magnitudes of the storms as indicated by the Dst index are shown in Table 3. Figure 1 shows that the two large events of September 1966 and May 1967 and the small event of June 1968 were observed by two satellites. However, it should be noted that little data are available from the OV3-3 satellite for the May 1967 storm (e.g., Figure 59) and from the OV1-13 satellite for the June 1968 storm. The peak storm spectra for those three storms are compared in Figure 139 for L = 2.4. An approximate quiet time spectra is shown for comparison. With the exception of the 300-keV and 475-keV OV3-3 data, plotted as different symbols, the various comparable data sets agree very well. A similar situation is evident at L = 2.0 shown in Figure 140. It is clear from Figures 139 and 140 that, relative to the quiet time spectra, storm flux enhancements are more pronounced at higher energies. Also, at the lower L value, the enhancement of the high energy spectra is significantly reduced compared to the higher L value, whereas at lower energies the enhancement remains relatively unchanged.

The general characteristic of magnetic storm effects in the inner zone is that they become larger at any given L value as the Dst index associated with the magnetic field changes becomes larger. The storm effects decrease rapidly for the lower inner zone L values. Significant storm time flux variations are not observed below L = 1.7, except for large events such as the May 1967 storm. These characteristics are summarized in Figure 141, which compares the quiet time and peak storm time radial profiles at 500 keV for the seven storms observed during the time period studied in this report. Comparing this figure with Table 3, it can be seen that the peak fluxes at any L value order with the peak hourly mean Dst index. That is, if an inner zone magnetic storm enhancement occurs, its magnitude correlates with the Dst index. However, it is not always true that if a Dst event occurs, an associated inner zone enhancement will occur. A further observation may be made concerning the rise time of the storm flux to the peak value. At high L values in the inner zone, the rise is rapid and occurs shortly following the peak Dst change. For instance, in Figure 63 the peak flux occurs on day 249, which is 2 days after the peak Dst change. At lower L values the rise becomes more gradual. In Figures 59 and 57 at L = 2.0 and 1.8, respectively, the peak fluxes occur on Days 265 and 280. At all of these L values a rapid flux change does occur on Day 249, but the magnitude of this change becomes a smaller percentage of the peak flux toward the lower L values.

III. COMPARISON OF THE CURRENT ELECTRON MODELS WITH DATA

The inner zone electron models presently distributed by NSSDC are

AE-6 (*Teague et al.*, 1976) for solar maximum and AE-5 1975 (*Teague and Vette*, 1974) for solar minimum. Both models are intended to reflect the natural electron environment and do not include the effects of the artificial particles injected by the Starfish event as the earlier model AE-5 1967 (*Teague and Vette*, 1972) did. Most of the data presented in this document were obtained around the epoch of 1967 and, at low L values, include the effects of the artificial particles. These data will be compared with the AE-5 1967 model, although this model is not presently distributed.

The dependence of the model flux on B value is identical for the three models AE-6, AE-5 1967, and AE-5 1975. The model pitch angle distribution is compared with the present polynomial pitch angle distribution in Figure 142 for L = 1.5- 1.8, and 2.4. In each case the curves correspond to 100-keV electrons, and the region near cutoff is not shown. The curves for L = 1.5 are typical of the L range 1.4 to 1.7. The model curve was based largely upon the OGO 3 data (*Teague and Vette*, 1972) with the result that this curve is flatter away from the cutoff region than the polynomial pitch angle distribution. This is discussed at length in Appendix A.5. At these L values the model and the polynomial pitch angle distributions agree within a factor of two for near equatorial pitch angles ($\alpha_0 \leq 45°$ at L = 1.5, for instance) but larger differences are apparent at lower pitch angles. The curves shown for L = 1.8 are typical of the L range 1.7 to 2.0 and show agreement to better than a factor of two for all pitch angles away from the cutoff region. The curves shown for L = 2.4 are typical of the high inner zone L values.

The model curve was based largely upon the OGO 3 data that provided poor pitch angle coverage near the equator at these L values. The curves shown in Figure 142 for L = 2.4 are normalized at 45°, and it is evident that the agreement is good for pitch angles below 70°, but that factor of three differences can be seen at the equator. For L values in the range 1.25 to 1.35, the AE-6/AE-5 model pitch angle distribution was determined largely from the 1963-038C data. The polynomial distributions are compared with these data in Figures 6, 8, and 11 where it can be seen that the agreement is good. As a result, the polynomial and the model pitch angle distributions for these L values also show good agreement (better than a factor of two). The model and data cutoff pitch angles and B values are compared in Figure 49. The model cutoff B value or pitch angle corresponds to the value for which the 40-keV omnidirectional flux equals 1 electron/(cm^2•keV•s). Although the data points given in Figure 49 correspond to a cutoff that is defined a little differently (see Section II.A), the change of flux with B in this region is so rapid that these differences are insignificant, and the data and model may be compared. The cutoff given by the present polynomial occurs at a consistently higher B value than that given by the present electron models, although the data and model agree within the error bars for L > 2 and L < 1.4. It should be noted that these differences do not represent a major restriction of the model because they occur in regions where the flux levels are extremely low.

In comparing the data and the present inner zone models it should be noted that the models are not intended to reflect the flux at a given

point in space at a given time, but rather are intended to give the user an estimate of the time-averaged environment at that point in space. The potential difference between these situations can be seen from Figure 141, in which AE-6 can be compared with peak storm flux data. At high inner zone L values, storm effects with characteristic times on the order of days result in flux variations of several orders of magnitude. The model AE-6 endeavors to represent an approximate average storm situation and may differ from the maximum and minimum observed flux at any given time by factors in excess of 10. As a result, the model is compared directly with data only for those energies and L values for which short term temporal variations are small. The models AE-5 1967 and AE-6 can be compared with these data in Figures 120 through 126. In addition, the models are compared with 1963-038C data for $L \leq 1.3$ in Figure 143. The data in this figure were either measured at the equator or near enough to the equator for the observed flux to be pitch angle independent. The general agreement between the data and the model is good. As noted in Section II.B, the higher energy data for $L \leq 1.7$ are influenced by artificial Starfish electrons. The AE-5 1967 model was primarily a fit to OGO 3 and OV3-3 data taken over the time period 1966-67. In Figures 120 through 126, therefore, the AE-5 1967 model should be compared with data from this epoch. In general, for those energies for which AE-5 1967 is significantly different from the AE-6 model, the former model is significantly higher than the comparable data. At the time of the generation of the AE-5 1967 model, a provisional OV3-3 data set was used. Subsequently, the calibration of the OV3-3 spectrometer was changed, result-

ing in a significant reduction in the apparent observed fluxes (*Teague and Vette*, 1974). The high energy OGO 5 and OV1-13 data obtained in 1968 are more appropriately compared with the AE-6 model because this model is intended to be free of artificial Starfish particles. However, the Starfish model of *Teague and Stassinopoulos* (1972) predicts that the 1.53-MeV and 2.82-MeV OGO 5 data contain a significant artificial component for $L \leq 1.5$, and it is reasonable to expect that the natural flux levels are below those measured by OGO 5 in early 1968. The AE-6 model reflects this qualitatively, although quantitative confirmation of AE-6 for $E > 1.5$ MeV and $L \leq 1.5$ must await data taken at later epochs.

At energies for which AE-5 1967 and AE-6 are not significantly different, the general agreement between the models and the data is good. However, at some L values (e.g., L = 1.4, Figure 124), the model is lower than the data by a factor of two for energies $E \lesssim 150$ keV. This results from the differences between the pitch angle distributions used for AE-6 and the present polynomial expressions. In Figure 142, at L = 1.5, it can be seen that the polynomial expression differs from the AE-6 model by close to a factor of two at 45°, and that normalization of data from this pitch angle would result in equatorial fluxes based upon the polynomial curve approximately a factor of two higher than those resulting from the AE-6 model distribution.

As noted earlier, for those L values and energies for which the temporal variations because of storm activity are significant, direct comparison of the model and data is not appropriate. Comparison of the model with data integrated over a given storm, however, would show how accu-

rately the model would predict short term average fluxes in the inner zone. The following simple storm model is assumed for the storm time flux j(t):

$$j(t) = [\Delta j_s + (j_{q_0} - j_{q_1})] \exp(-t/\tau) + j_{q_1} \quad (3)$$

As shown in Figure 144, this model postulates a sharp rise from a prestorm flux j_{q_0} to a peak flux $j_p = j_{q_0} + \Delta j_s$ followed by an exponential decay with characteristic depletion time τ to a post storm flux j_{q_1}. This model is quite appropriate for the higher L values, such as L = 2.4 (shown in Figure 63), but for the lower L values, such as L = 1.9 (shown in Figure 58), the sharp rise has become rounded and the simple model is only an approximation. Equation (3) may be integrated over time T_E (the event integration time) to give the event integrated flux as:

$$J_E(T_E) = \frac{\tau}{T_E}[\Delta j_s + (j_{q_0} - j_{q_1})][1 - \exp(-T_E/\tau)] + j_{q_1} \quad (4)$$

Estimates of the parameters in this equation were determined for all storms and all data sets for $L \geq 1.7$, and the event integrated flux was obtained for T_E = 30, 90, and 180 days. Estimates of the error in J_E were obtained from the error equation:

$$\sigma_E^2 = \sigma_q^2 + (J_E - j_{q_1})^2 \left\{ \frac{\sigma_\tau^2}{\tau^2} \left[1 - \frac{(T_E/\tau)e^{-T_E/\tau}}{(1 - e^{-T_E/\tau})} \right]^2 + \frac{\sigma_q^2 + \sigma_p^2}{(\Delta j_s + j_{q_0} - j_{q_1})^2} \right\} \quad (5)$$

where σ_q, σ_p, and σ_τ are the errors in the post-storm flux j_{q_1}, the peak flux j_p, and the depletion time τ, respectively.

Event-integrated radial profiles for T_E = 90 days are shown in Figures 145 and 146 for 500-keV and 800-keV electrons, respectively. In some cases interpolation was performed to reduce the data to the desired

energy. Data from the April 1965 storm are not shown at 800 keV because little OGO 1 data were available at 1330 keV. Comparing Figures 145 and 146, it is interesting to note that the event integrated data have quite different shapes from the peak flux data as a result of the pronounced decrease of depletion time τ with increasing L value ($t \approx 90$ d at $L = 1.8$ and $\tau = 9$ d at $L = 2.4$ and 500 keV). As may be expected, the AE-6 model is a considerably better estimator of the event integrated flux than of the peak flux. At 500 keV, AE-6 is between a factor of two and three lower than the event integrated flux for the largest observed storm (May 1967). At 800 keV, in Figure 146, the corresponding factor is three to four. Note that the September 1966 storm may perhaps be regarded as a typical inner zone storm and that the model AE-6 gives the event integrated flux for this storm to within the minimum model error (factor of two) at both 500 keV and 800 keV. For $L < 2.2$, this is the case for all energies as may be seen from the spectrum shown in Figure 147. For $L \geq 2.2$, the AE-6 model is less successful at high energies, as may be seen in Figure 148 for $L = 2.4$. For $E > 800$ keV, the model is typically a factor of three lower than the September 1966 event-integrated flux and an order of magnitude lower than the large May 1967 event. AE-6 must, therefore, be regarded as low by more than the minimum model error for $L \geq 2.2$ and $E \geq 800$ keV. The observed differences, however, are consistent with the confidence codes for AE-6 given by *Teague et al.* (1976). The event integrated flux (equation 4) is a function of the event integration time T_E. Arbitrarily, data are presented for a 90-day event integration time, and while this may be a reasonable minimum mission duration, the event

integrated flux and thus the model's ability to estimate it may vary considerably with T_E. At low L values and/or low energies for which either the peak flux is within a factor of two or three of the prestorm flux or τ is long with respect to T_E, the event integration time has relatively little effect upon J_E. On the other hand, for small τ, the effect may be substantial. This is shown in Figure 149 where J_E is shown as a function of T_E for 712 keV at L = 1.7 and 2.4. Within the error bars given by equation (5), the event integrated flux for other values of T_E and E $\geq$ 400 keV (30 $\leq T_E \leq$ 180 days) may be estimated from the expression $J_E \propto 1/T_E^N$ where N varies linearly with L values from 1.0 at L = 2.4 and 0.5 at L = 1.9.

IV. CONCLUSIONS

In comparing the inner zone electron flux measurements made by the OGO 1, OGO 3, OGO 5, OV1-13, OV1-19, OV3-3, OSO 4, and 1963-038C satellites, the general agreement was found to be excellent. A number of systematic differences were observed resulting from the decay of the artificial Starfish particles and the long term variation of the flux at quiet times that are possibly correlated with solar cycle variations. A number of differences were observed between comparable data sets that are considered to be indicative of possible problems with certain measurements. These are summarized as follows: (1) an apparent saturation effect in the OV3-3 data gave spurious pitch angle distributions for 300-keV and 475-keV electrons for L $\leq$ 2.1 and for higher energy electrons for L $\leq$ 1.7 (Appendix A.1). An effort to correct this by omitting pitch

angles over which this effect occurred resulted in low equatorial fluxes at 300 keV and 475 keV (Section II.B); (2) the OGO 1 and 3 data pitch angle distributions for all energies and $1.4 \leq L \leq 1.7$ are flatter than those given by other data sets. Despite this, the data showed self-consistency, and special OGO 1 and 3 pitch angle distributions were obtained to determine equatorial fluxes (Appendix A.5). These fluxes showed good agreement with other data sets. However, the 1.33 MeV OGO 3 data appeared to be a factor of two to five higher than the comparable OV3-3 data. It was suggested that this discrepancy may result from the proton correction to the latter data set (Section II and Appendix A.1); and (3) the two lower energy channels of the OV1-13 spectrometer gave measurements significantly lower than comparable data (Section II.B).

The trapped electron models were compared directly with the data for $L \leq 1.6$. In general, the agreement is good and better than the model confidence codes would suggest. However, little Starfish-free high energy ($E > 1.5$-MeV) data are available for comparison with the AE-6 model for $L \leq 1.5$. In this region confirmation of the model must await more such data. At higher L values the data were event integrated for the various storms and compared with the AE-6 model and, in general, the agreement was good. Three problem areas were identified on the basis of comparison with the data: (1) the model atmospheric cutoff B value is too low by approximately 0.005 gauss at all L values (Section III); (2) for $E < 150$ keV and low L values, AE-6 is low by a factor of 2 to 2-1/2 (Section IV); and (3) for $E \geq 800$ keV and $L \geq 2.2$ the model is low in relation to the integrated data (Section III).

APPENDIX A. DATA PROCESSING AND REDUCTION

The data used in this report are summarized in Figure 1 and Table 1. In this appendix the processing and reduction of the individual data are discussed and archival flux vs time data sets are presented. As noted in the Introduction, all the data are reduced using the same equatorial pitch angle distribution at a given L value and energy. As a consequence, meaningful intercomparisons of the data may be made.

A1. OV3-3 Data

The OV3-3 data were obtained using the Aerospace Corporation electron spectrometer. The principal investigator was Dr. A. L. Vampola. The experiment was described by *Vampola* (1969). These data provided good time coverage throughout the last half of 1966 but provided only a few points in 1967. Good pitch angle coverage was given for $L < 2.0$. In the present analysis, these are the only data that provide significant measurements for $E > 822$ keV.

The OV3-3 data were processed using the method documented by *Vampola* (1975). In the inner radiation zone the data were contaminated by protons. Correction for the proton contamination was achieved using the expression $0.8\ P/(1 - \cos\alpha)$, where P is the proton monitor count rate and α is the local pitch angle. Following *Vampola* (1975), all data for $\alpha < 25°$ were edited out.

Examples of the OV3-3 equatorial pitch angle distributions are presented in Figures 10, 15, 20, 27, 30, 33, and 36, and some normalized small pitch angle data are shown in Figures 47 and 48. In the course of

processing the data, a saturation-like effect was observed for the low energy channels. An example is shown in Figure 150. In general, the level of the saturation-like effect was time and L value independent. In the subsequent processing of the OV3-3 data, equatorial pitch angles above the value α_s, at which this effect became apparent, were excluded. Values of α_s are given in Table 4.

The OV3-3 data were reduced using the model equatorial pitch angle distribution given in Section II.A, and the resulting equatorial flux vs time plots are shown in Figures 52 through 63 for the L range 1.3 to 2.4. For $L \geq 1.8$, three plots are given per L value, each showing three channels of data. At lower L values the highest three energy channels are fully contaminated by protons, therefore only two plots are shown.

A2. OV1-13 Data

The OV1-13 data were obtained by the Air Force Geophysical Laboratory (AFGL) electron spectrometer. The principal investigator was Dr. L. Katz. The experiment was described by *Paolini et al.* (1968); recalibration of the experiment was described by *Rothwell and Moomey* (1972). Data were available for, at most, 14 separate days over a short period in 1968 (60 days), but the pitch angle coverage was excellent for all L values $1.25 \leq L \leq 2.4$. In this L range the electron data were contaminated by omnidirectional protons with $E > 75$ MeV (*Rothwell and Moomey*, 1972). In an effort to correct for this contamination it was assumed that the count rate registered by the 900-keV electron channel on quiet days (Days 137-159 1968) resulted entirely from protons. An example of the resulting proton B distribution is shown in Figure 151, and the radial profile of

the proton correction at the minimum B observed at each L value is shown in Figure 152. The proton B distribution was approximated by two linear equations giving the proton count rate, P, as:

$$\log_{10} P = a_1 B + b_1 \quad \text{for } B < B_{Cr}$$

and

$$a_2 B + b_1 + B_{Cr} (a_1 - a_2) \quad \text{for } B > B_{Cr}$$

For values of B for which these expressions gave count rates less than 6.5/s a proton count rate of 6.5/s was assumed. Values of the constants are given in Table 5 and an example is shown in Figure 151. *Rothwell and Moomey* (1972) give the proton count rate for the spectrometer as $P = A J_p$ (> 50 MeV) where J_p is the omnidirectional proton flux and A = 0.25 cm^2. The AP-8 trapped proton environment (*Sawyer and Vette*, 1976) may be used to estimate J_p; the results are shown in Figures 151 and 152. As a result of the favorable comparison it may be assumed that the present proton correction is adequate. Examples of the proton-corrected equatorial pitch angle distributions are shown in Figures 4, 7, 17, 19, 22, 23, 25, 29, 34, and 40. Normalized low pitch angle data are shown in Figures 41 through 48.

The OV1-13 data were reduced using the model equatorial pitch angle distribution and the resulting equatorial flux vs time plots are shown in Figures 64 through 78 for the L range 1.2 to 2.4.

A3. OV1-19 Data

The OV1-19 data were obtained using the Aerospace Corporation magnetic electron spectrometers. The principal investigator was Dr. A. L. Vampola. The instrument and the geometric efficiency factors used in processing the data were described by *Vampola* (1971). The data coverage

spans the period from early 1969 to the beginning of 1970.

In this report only some preliminary results of the data analysis are presented. Measurements of the fluxes within ±3° of the locally mirroring direction were selected so that the scatter of the data, caused by the finite apertures of the detectors, can be reduced. Because the correction of the pronounced proton contamination in the inner zone has not yet been determined, only data with energies below 537 keV and $L \geq 1.8$ are presented. In this case the effect of contamination is expected to be minimal. Examples of this provisional pitch angle data are shown in Figures 26, 32, 38, and 39. When more information about the proton contamination and the angular response of the detectors becomes available, more OV1-19 data can be used.

The OV1-19 data were reduced using the model equatorial pitch angle distribution, and the resulting equatorial flux vs time plots are shown in Figures 74 through 85 for the L range 1.8 to 2.4.

A4. OGO 5 Data

The OGO 5 data were obtained using the Lawrence Livermore Laboratory electron spectrometer. The principal investigator was Dr. H. I. West, Jr. and the experiment was described by *West et al.* (1969). These data provided good pitch angle coverage for $E \leq 822$ keV and for $L \geq 1.30$. The time coverage was good at high inner zone L values but was successively reduced for $L < 1.8$. Examples of the equatorial pitch angle distributions for OGO 5 are shown in Figures 8, 12, 13, 14, 16, 18, 21, 24, 31, and 37, and some normalized low pitch angle data are given in Figures 41 through 48.

The OGO 5 data were reduced using the model equatorial pitch angle distribution and the resulting flux vs time plots are shown in Figures 86 through 98 for the L range 1.3 to 2.4.

A5. OGO 1 and OGO 3 Data

The OGO 1 and 3 data were obtained using the University of Minnesota electron spectrometers. The principal investigator was Prof. J. R. Winckler. A reevaluation of the calibration of these spectrometers was performed by *Teague* (1970) and the resulting calibration constants appear in Table 2. The data from these satellites provide good time, L value, and pitch angle coverage, except for the data from late 1967, which have poor pitch angle coverage at high L values and little coverage at low L values. Because the intensity thresholds of the two higher energy channels were set at a high level, there is a small amount of high energy OGO 3 data, and the data provided by OGO 1 largely reflect artificial Starfish particles.

Examples of the OGO 3 equatorial pitch angle distribution are shown in Figures 28 and 35. In comparing the shape of OGO 1 and 3 equatorial pitch angle distributions with those from other satellites it became apparent that the OGO 1 and 3 distributions for $1.4 \leq L \leq 1.7$ showed a significantly slower cutoff toward the lower pitch angles. This effect is shown in Figure 153 in which a fit to the OGO 3 data is compared with the polynomial model given in Section II.A. The origin of the effect is unknown but it is observed to be systematic, however. As a result, specific OGO 1 and 3 equatorial pitch angle distributions were derived for the L range 1.4 to 1.7 for the purposes of reducing the data to equatorial flux. The form of the distribution is identical to the polynomial given

in Section II.A, and the coefficients are given in Table 6. Note that the specific OGO 1 and 3 distributions agree with the model distribution for fluxes within an order of magnitude of the equatorial flux. Normalized small pitch angle OGO 3 data at high inner zone L values are shown in Figures 47 and 48. Reduced OGO 1 and 3 equatorial flux vs time plots are shown in Figures 99 to 108 and Figures 109 to 118, respectively, for the L range 1.3 to 2.4.

A6. 1963-038C Data

The 1963-038C data were obtained by the Applied Physics Laboratory (APL) integral flux experiment. The principal investigator was Dr. C. O. Bostrom, and the data were presented by *Beall* (1969). These data were used to a limited extent in the present study primarily for determining the equatorial pitch angle distribution for $L < 1.4$ because data from other satellites in this region were generally scattered. Normalized mirror-point distributions for these L values are shown in Figures 5, 6, 9, and 11. At higher L values the 1963-038C data were used in the region of the atmospheric cutoff. Fits were made to the mirror-point distributions given by *Beall* (1969) and are shown in the equatorial pitch angle distribution plots given in Figures 41 through 46. Flux vs time curves are not presented for 1963-038C because these were given previously by *Beall* (1969) for specified B intervals. If desired, these curves may be reduced to the equator using the model given in Section II.A.

A7. OSO 4 Data

The OSO 4 data were obtained by the Lawrence Livermore Laboratory

experiment. The principal investigator was Dr. J. A. Waggoner. The experiment was described by *Knox* (1972). The data were of limited value because the pitch angle coverage was poor and a large proton correction was required at low L value (*Knox*, 1972). However, the data were useful in defining the atmospheric cutoff region of the equatorial pitch angle distribution. Normalized OSO 4 data are shown in Figures 41 through 46. Flux vs time curves are not presented because only a few days of data were available. However, the equatorial pitch angle distribution model given in Section II was used to generate the OSO 4 radial profiles in Figure 119. It should be noted that large factors, $0(10^2)$, were used to reduce these data to the equator. The error bars in these figures result from the time and pitch angle averaging and the proton correction.

REFERENCES

Beall, D.S., *Graphs of Selected Data from Satellite 1963-038C for 1963-1967*, Applied Physics Laboratory/Johns Hopkins University TG1050-1 - TG1050-5.

Knox, R.J., *OSO-4 Electron Observations in the Edge of the Inner Radiation Zone*, UCRL-51185, Livermore, CA, February 1972.

Paolini, F.R., G.C. Theodoridis and W.F. Welsh, "Satellite Instrumentation for Charged Particle Measurements - Magnetic Analyzers for 0.1- to 1.0-MeV Electrons," *IEEE Trans. on Nucl. Sci.*, NS-15, 194-99, February 1968.

Rothwell, P.L and W.R. Moomey, *Calibration of a Magnetic Spectrometer Designed to Measure 0.1- to 1.0-MeV Electrons in Space*, AFCRL-72-0710, December 1972.

Sawyer, D.M. and J.I. Vette, *AP-8 Trapped Proton Environment for Solar Maximum and Solar Minimum*, NSSDC/WDC-A-R&S 76-06, NASA-GSFC TMX-72605, December 1976.

Teague, M.J., *The Calibration Constants for the OGO 1/3 Electron Spectrometer*, NSSDC/WDC-A-R&S 70-14, October 1970.

Teague, M.J. and E.G. Stassinopoulos, *A Model of the Starfish Flux in the Inner Radiation Zone*, NASA-GSFC TMX-66211, December 1972.

Teague, M.J. and J.I. Vette, *The Inner Zone Electron Model AE-5*, NSSDC/WDC-A-R&S 72-10, November 1972.

Teague, M.J. and J.I. Vette, *A Model of the Trapped Electron Population for Solar Minimum*, NSSDC/WDC-A-R&S 74-03, April 1974.

Teague, M.J., K.W. Chan and J.I. Vette, *AE-6: A Model Environment of Trapped Electrons for Solar Maximum*, NSSDC/WDC-A-R&S 76-04, May 1976.

Vampola, A.L., "Access of Solar Electrons to the Closed Field Lines," *J. Geophys. Res., 76*, January 1971.

Vampola, A.L., "Energetic Electrons at Latitudes Above the Outer Zone Cutoff, "*J. Geophys. Res., 74*, March 1969.

Vampola, A. L., The Energetic Electron Environment in Circular Polar Orbits, *Aerospace Corp. Report TR-0076 (6260-20)-2, July 1975.*

Vette, J.I., A. Lucero, J. Wright, Models of the Trapped Radiation Environment Vol. II: Inner and Outer Zone Electrons, *NASA SP-3024, 1966.*

West, H.I., Jr. and R. Buck, "A Study of Electron Spectra in the Inner Belt," *J. Geophys. Res.*, *81*, September 1976.

West, H.I., Jr., R.M. Buck, and J.R. Walton, "Electron Pitch Angle Distributions throughout the Magnetosphere as Observed on OGO 5," *J. Geophys. Res.*, *78*, March 1973.

West, H.I., Jr., et al., *The LRL Electron and Proton Spectrometer on NASA's Orbiting Geophysical Observatory V(E) (Instrumentation and Calibration)*, UCRL-50572, Livermore, CA, June 1969.

Table 1. Summary of Data Used in the Present Analysis

Satellite NSSDC ID Principal Investigator(s)	Time Coverage	Energy Range (keV)	Center Energy (keV)	Calibration		Comments
				Value C*	Reference	
OGO 1 64-054A-21A Winckler, J.R.	9/64-10/65	36- 133 133- 292 292- 690 690-1970 1970-4740	84 212 491 1330 3355	3.691 6.23 6.1 6.66 7.794	*Teague and Vette* (1972)	
OGO 3 66-049A-22A Winckler, J.R.	6/66-12/67	Same as OGO 1	Same as OGO 1	Same as OGO 1	Same as OGO 1	Poor L and pitch angle coverage at high L for late 1967
OGO 5 68-014A-06C West, H.I.	3/68-1/69	56- 102 122- 194 230- 302 427- 531 637-1007 1270-1790 2550-3090	79 158 266 479 822 1530 2820		*West et al.* (1969)	Less time coverage at low L values; little data for E ≥ 1530 keV
OV1-13 68-026A-02A Katz, L.	5/68-7/68	140- 180 185- 235 450- 550 620- 720 850- 950	160 210 500 670 900		*Paolini et al.* (1968)	Good pitch angle coverage at all L values
OV3-3 66-070A-05D Vampola, A.L.	7/66-8/67	225- 375 350- 600 574.5- 849.5 814.5-1099.5 1075-1375 1329-1651 1615-1926 1880-2200 2147-2472	300 475 712 957 1225 1490 1770 2010 2310		*Vampola* (1969)	Few data points in 1967; poor equatorial pitch angle coverage at high L values

*Flux = counts/s • C

electrons/(cm^2•s•sr•keV) for OGO 1 and 3.

electrons/(cm^2•s•sr) for 1963-038C.

Table 1. Summary of Data Used in the Present Analysis (concluded)

Satellite NSSDC ID Principal Investigator(s)	Time Coverage	Energy Range (keV)	Center Energy (keV)	Calibration		Comments
				Value C*	Reference	
OSO 4 67-100A-046A Wagonner, J.A.	3/68	80.5- 121 121- 171 171- 258 258- 537 537- 900	101 151 215 398 718		*Knox* (1972)	Coverage of pitch angles near cutoff only
OV1-19 69-025C-05 Vampola, A.L.	3/69-2/70	168- 216 285- 339 348- 404 415- 473 423- 656	198 312 377 444 537		*Vampola* (1971)	Proton contamination not corrected
1963-038C-01 Bostrom, C.O. Williams, D.I.	9/63-12/67	> 255		487.7	*Teague and Vette* (1972)	Used mostly at lowest L values

*Flux = counts/s • C

electrons/(cm^2•s•sr•keV) for OGO 1 and 3.

electrons/(cm^2•s•sr) for 1963-038C.

Table 2. Coefficients for the Analytic Equatorial Pitch-Angle Distribution

L Value	E (keV)	$a_1 \times 10^4$	$a_2 \times 10^7$	$a_3 \times 10^{10}$	$a_4 \times 10^{14}$	α_h (deg)	α_m (deg)	α_c (deg)
1.2	All	110.0	-402.5	475.2	-2456.0	75.0	-	61.6
1.25	All	26.9	-122.6	134.5	-620.9	77.8	-	55.7
1.3	All	48.86	-105.4	9.56	-265.1	68.0	-	50.7
1.35	All	-6.312	-0.9535	6.142	-56.05	69.0	-	46.9
1.4	<500	9.104	-27.36	20.51	-58.64	70.0	48.0	43.3
	≥500	13.06	-32.96	22.83	-61.52			
1.5	<500	12.75	-24.56	14.41	-30.86	70.0	41.0	37.2
	≥500	7.416	-20.53	12.85	-28.83			
1.6	<500	6.883	-12.08	6.055	-12.06	70.0	36.0	32.4
	≥500	9.811	-17.15	8.415	-15.27			
1.7	<350	2.104	-6.711	3.548	-6.686	72.5	32.0	29.0
	≥350	-1.665	-5.106	3.33	-6.5			
1.8	<822	-0.2274	-4.143	2.152	-3.632	75.0	30.0	26.1
	≥822	-0.94	-5.627	2.618	-4.172			
1.9	<822	-1.762	-2.632	1.397	-2.238	75.0	27.5	23.7
	≥822	-2.056	-3.301	1.722	-2.702			
2.0	<900	-2.098	-1.777	0.8971	-1.372	77.5	24.0	21.5
	≥900	-2.179	-2.287	1.088	-1.573			
2.1	<900	-2.242	-1.52	0.7384	-1.054	77.5	23.0	19.85
	≥900	-2.599	-1.687	0.858	-1.235			
2.2	<822	-2.68	-0.919	0.498	-0.6898	80.0	22.0	18.3
	≥822	-3.42	-0.3856	0.3346	-0.5526			
2.3	All	-2.519	-1.448	0.6945	-0.8938	85.0	20.0	16.9
2.4	All	-3.298	-0.9659	0.5169	-0.6551	90.0	18.5	15.5

Table 3. Inner Zone Geomagnetic Storm Data

Date of Storm	Peak Hourly Mean Dst Index	Peak Flux at L = 2.4 and 500 keV*
April 1965	-185	2.9×10^4
September 1966	-229	5.0×10^4
May 1967	-418	1.9×10^5
June 1968	-94	9.8×10^3
October 1968	-231	1.5×10^5
May 1969	-133	1.6×10^4
September 1969	-128	7.5×10^3

*electrons/cm^2•s•sr•keV.

Table 4. OV3-3 Saturation Equatorial Pitch Angles*

L Value	Energy (keV)			
	300	475	712	957
1.3	58	62	68	N
1.4	52	52	62	68
1.5	47	47	58	N
1.6	40	50	58	N
1.7	46	46	70	N
1.8	47	47	N	N
1.9	48	50	N	N
2.0	50	50	N	N
2.1	52	55	N	N

*In units of degrees.

N: No saturation-like effect observed.

Table 5. OV1-13 Proton Correction Coefficients

L Value	a_1	a_2	b_1	B_{Cr}
1.2	-30.03	-61.6	8.117	-193
1.25	-18.35	-43.85	6.179	-1885
1.3	-13.34	-53.84	5.339	-202
1.35	-12.98	-123.42	5.339	-2194
1.4	-8.18	-26.46	4.549	-1763
1.5	-8.9	-45.48	4.458	-2
1.6	-10.97	-32.33	4.549	-202
1.7	-11.31	-28.97	4.161	-2205
1.8	-16.33	-3.4	3.978	-169
1.9	-13.98	-5.65	3.456	-1275
2.0	-27.34	-7.05	3.814	-061
2.1	-40.71	-2.49	3.887	-0625
2.2	-25.84	-	2.883	-
2.3	-30.57	-5.39	2.436	-045
2.4	-18.87	-	1.87	-

$\log_{10} P = a_1 B + b_1$ for $B < B_{Cr}$

$= a_2 B + b_1 + B_{Cr} (a_1 - a_2)$ for $B \geq B_{Cr}$

Units: P counts/s

Table 6. Coefficients for OGO 3 Pitch-Angle Distribution

L Value	$a_1 \times 10^4$	$a_2 \times 10^7$	$a_3 \times 10^{11}$	$a_4 \times 10^{15}$	α_h (deg)
1.4	-4.713	0.3259	-3.535	0.5987	70.0
1.5	-2.701	-0.4408	-2.652	2.685	70.0
1.6	2.842	-8.73	39.65	-61.92	70.0
1.7	-4.258	1.639	-6.806	6.327	72.5

Page intentionally left blank

Page intentionally left blank

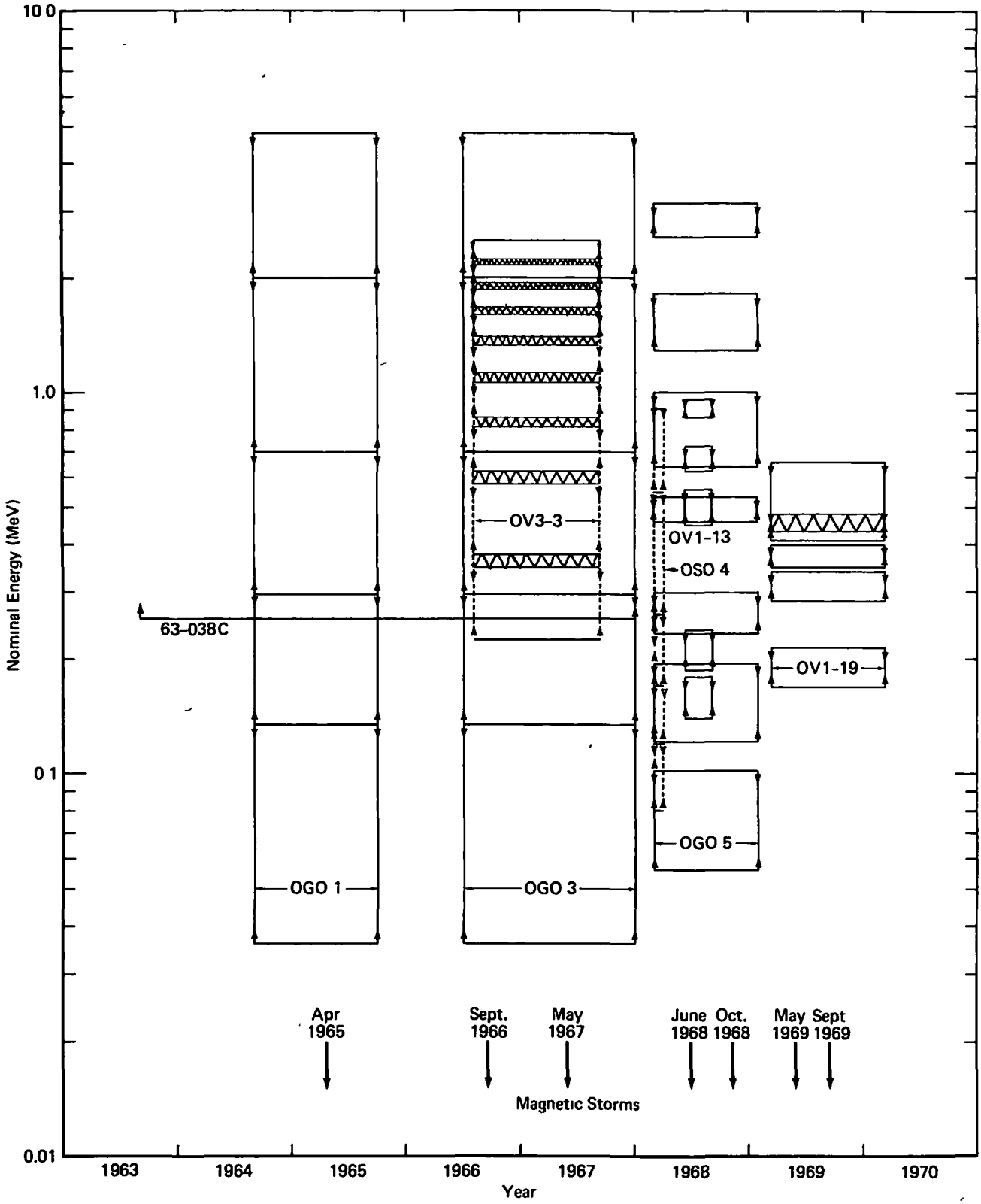

Figure 1. Energy-Time Coverage of the Data Used in the Present Analysis

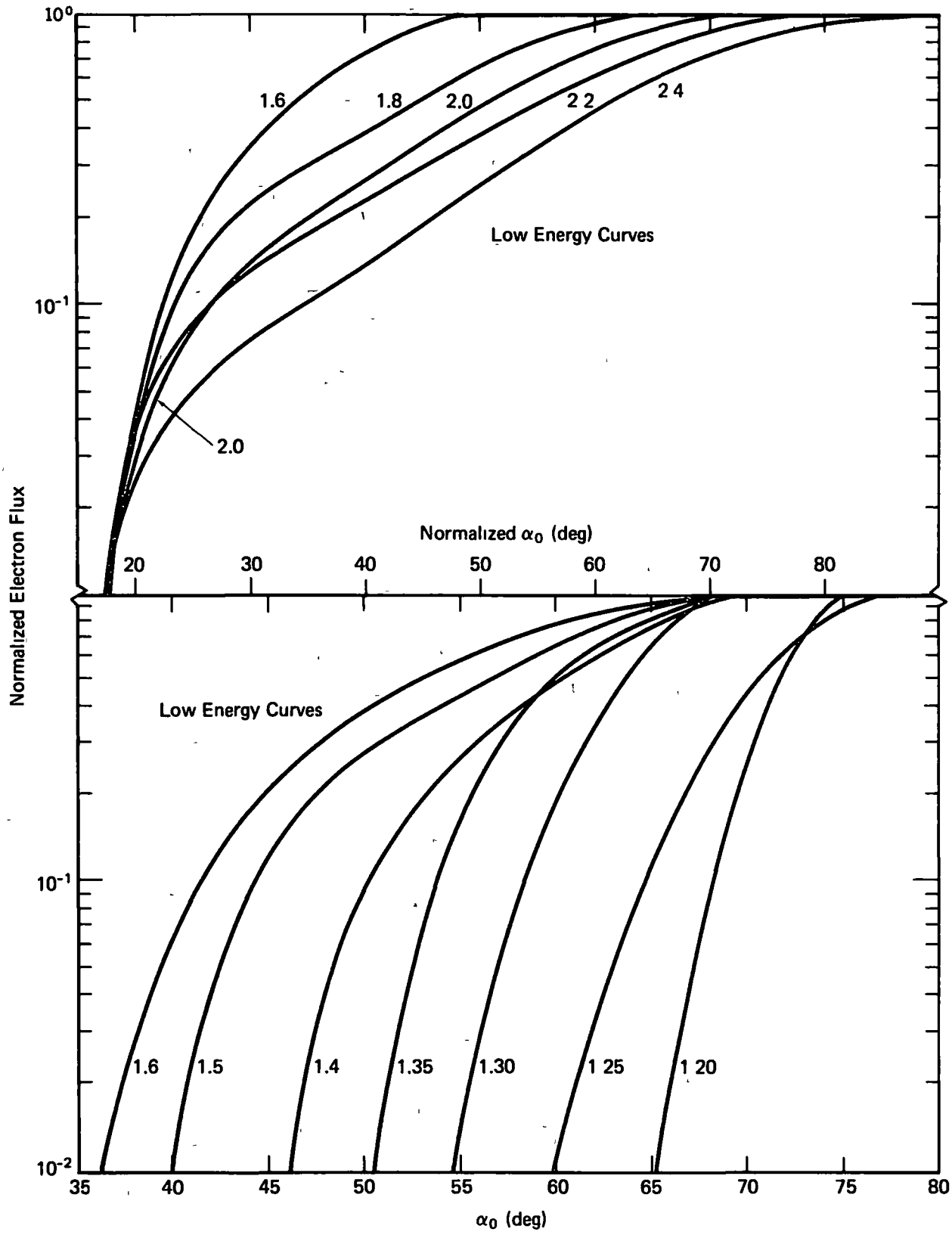

Figure 2. The Analytical Equatorial Pitch Angle Distribution. Low-Energy Curves

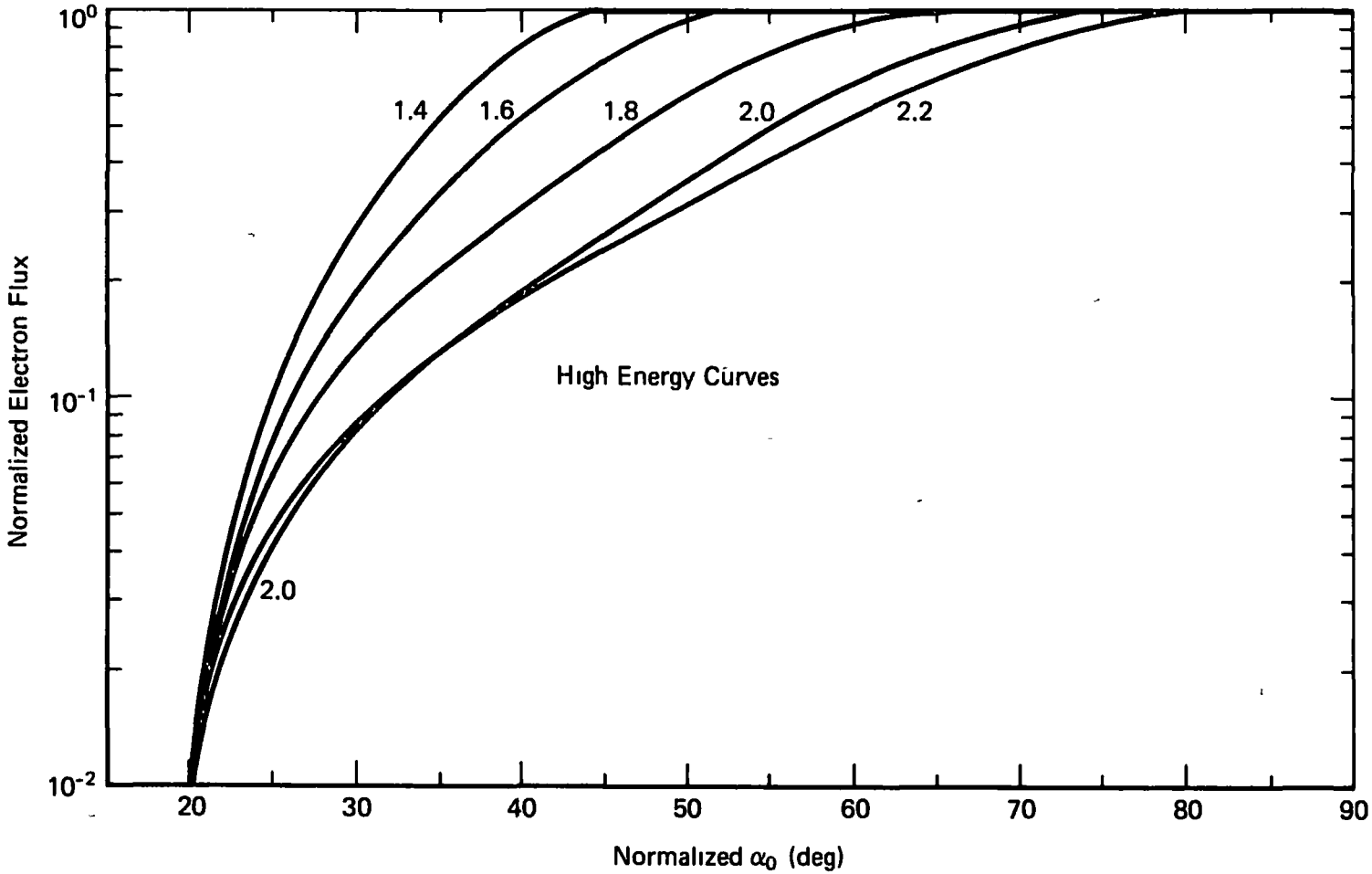

Figure 3. The Analytical Equatorial Pitch Angle Distribution. High-Energy Curves

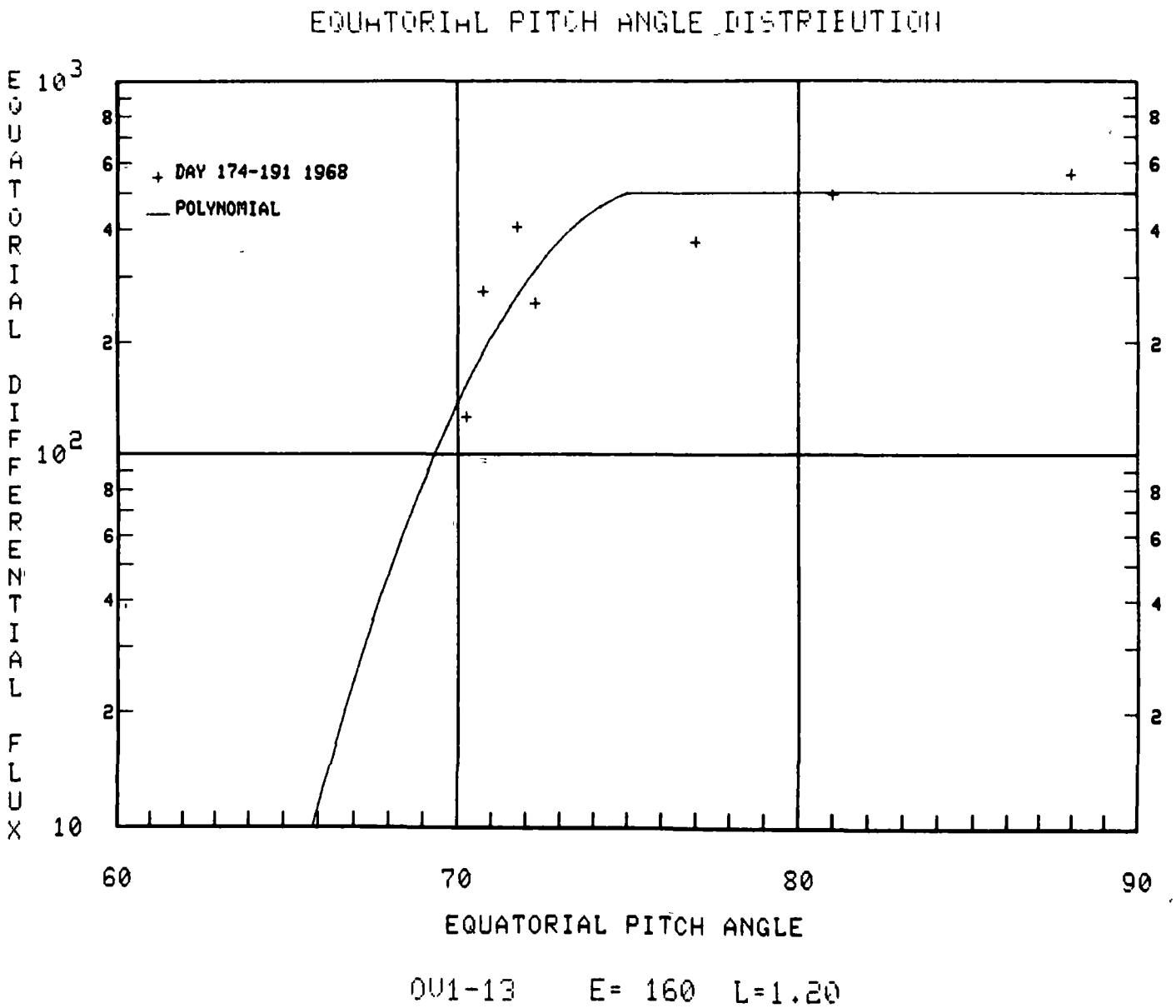
EQUATORIAL PITCH ANGLE DISTRIBUTION
EQUATORIAL DIFFERENTIAL FLUX
10^3
10^2
10
8
6
4
2
+ DAY 174-191 1968
POLYNOMIAL
60
70
80
90
EQUATORIAL PITCH ANGLE
OV1-13 E= 160 L=1.20

Figure 4

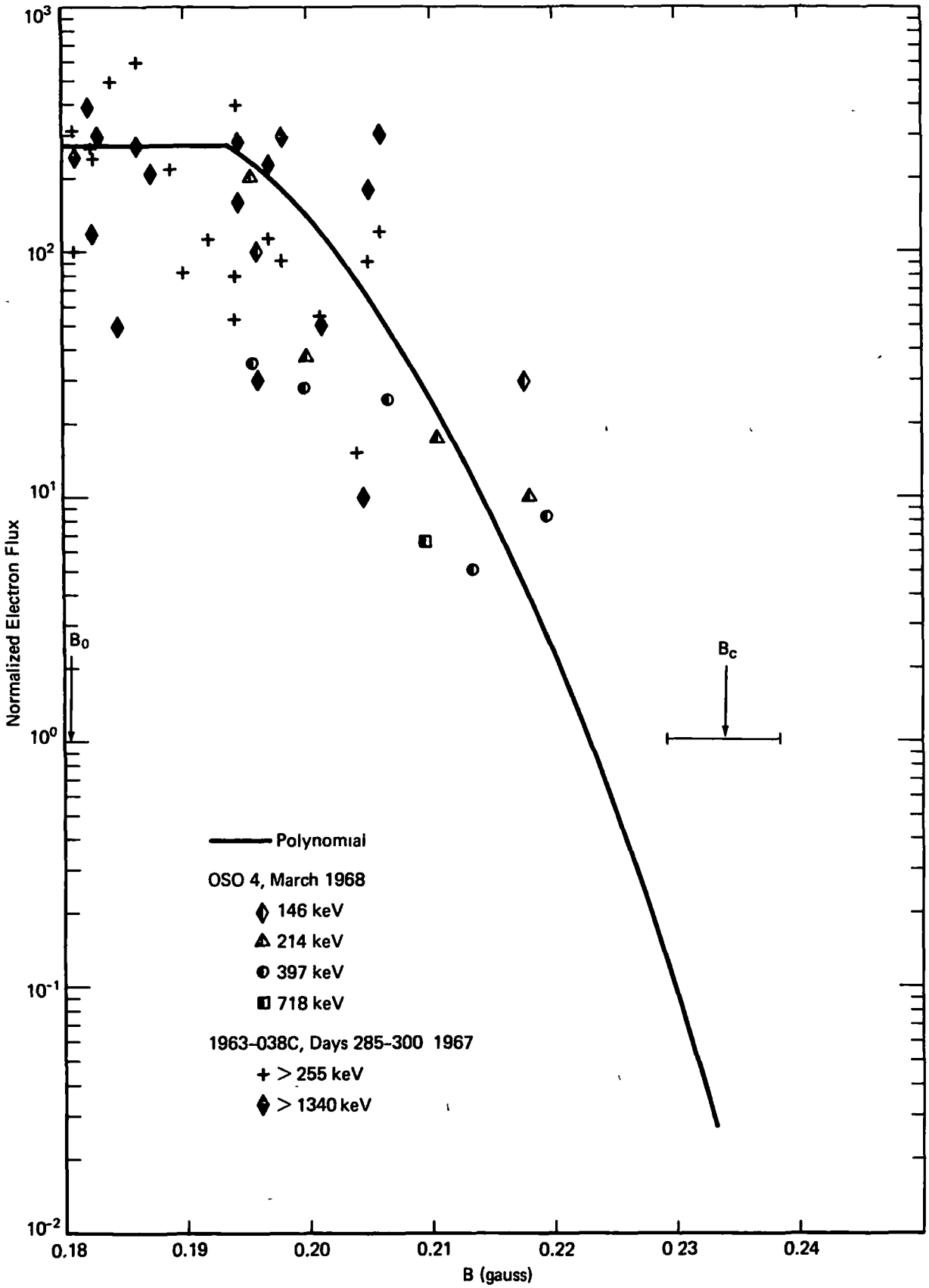

Figure 5. Normalized Mirror-Point Distributions at L = 1.2

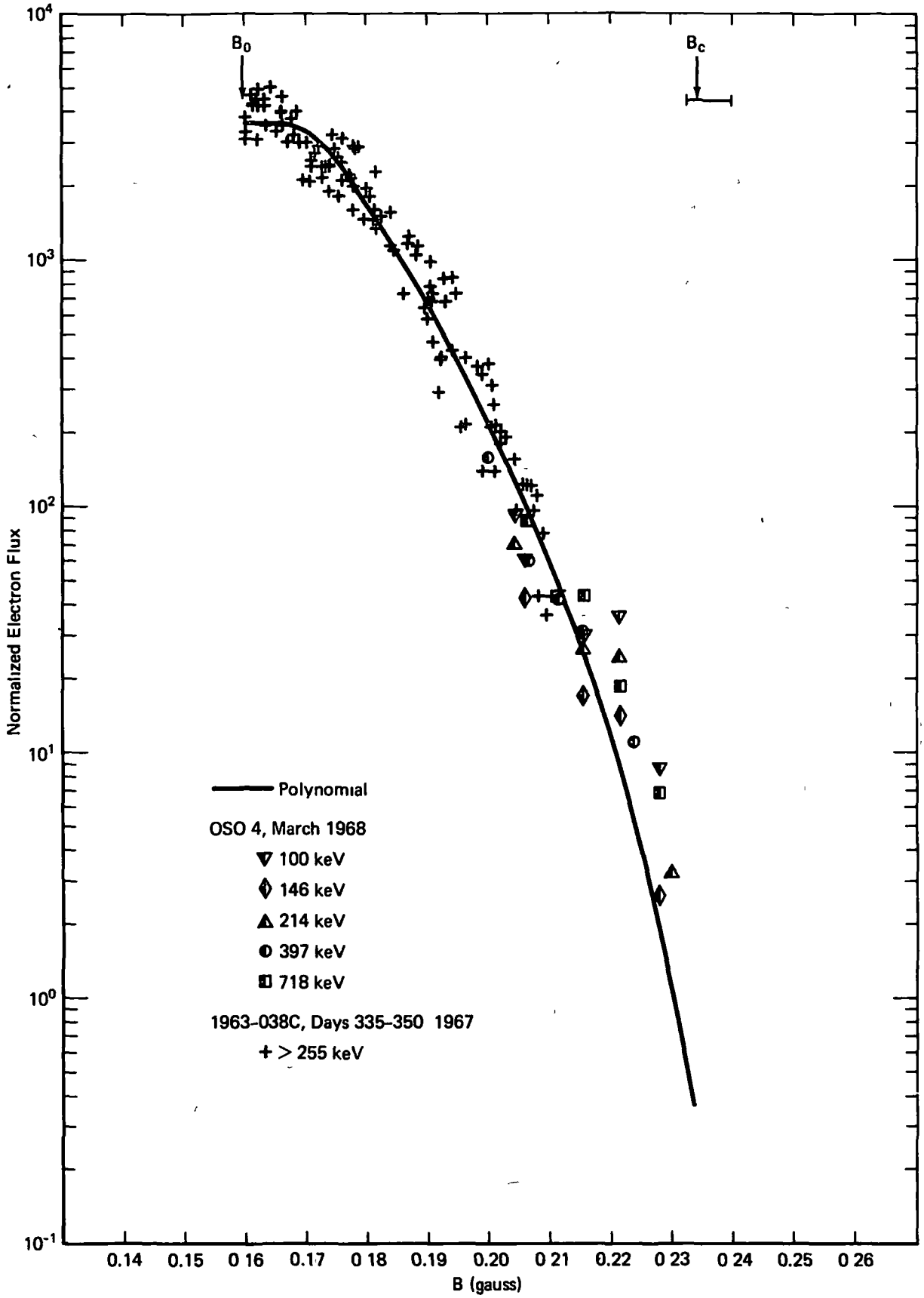

Figure 6. Normalized Mirror-Point Distributions at L = 1.25

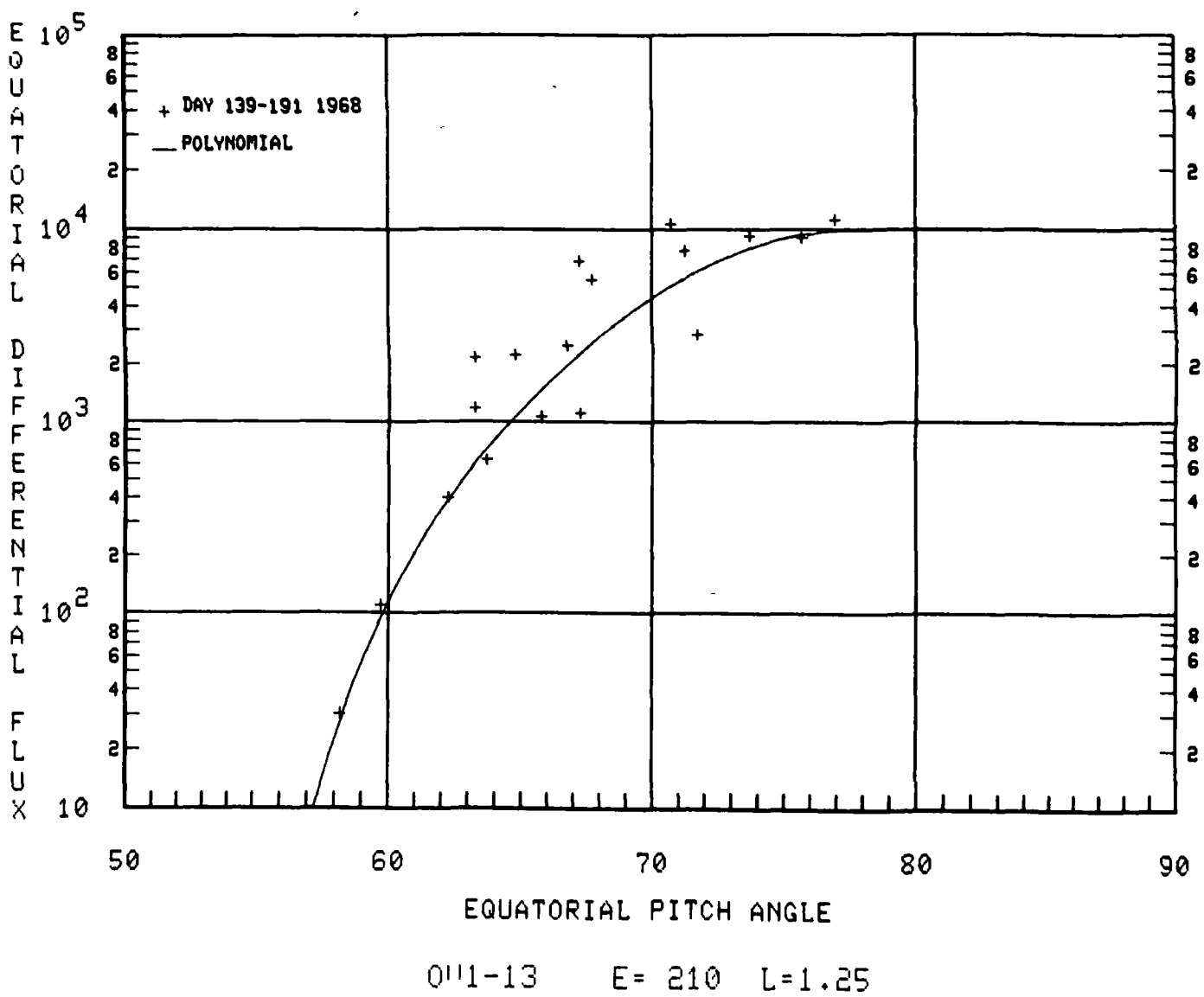
EQUATORIAL PITCH ANGLE DISTRIBUTION
EQUATORIAL DIFFERENTIAL FLUX
DAY 139-191 1968
POLYNOMIAL
EQUATORIAL PITCH ANGLE
0°1-13 E= 210 L=1.25

Figure 7

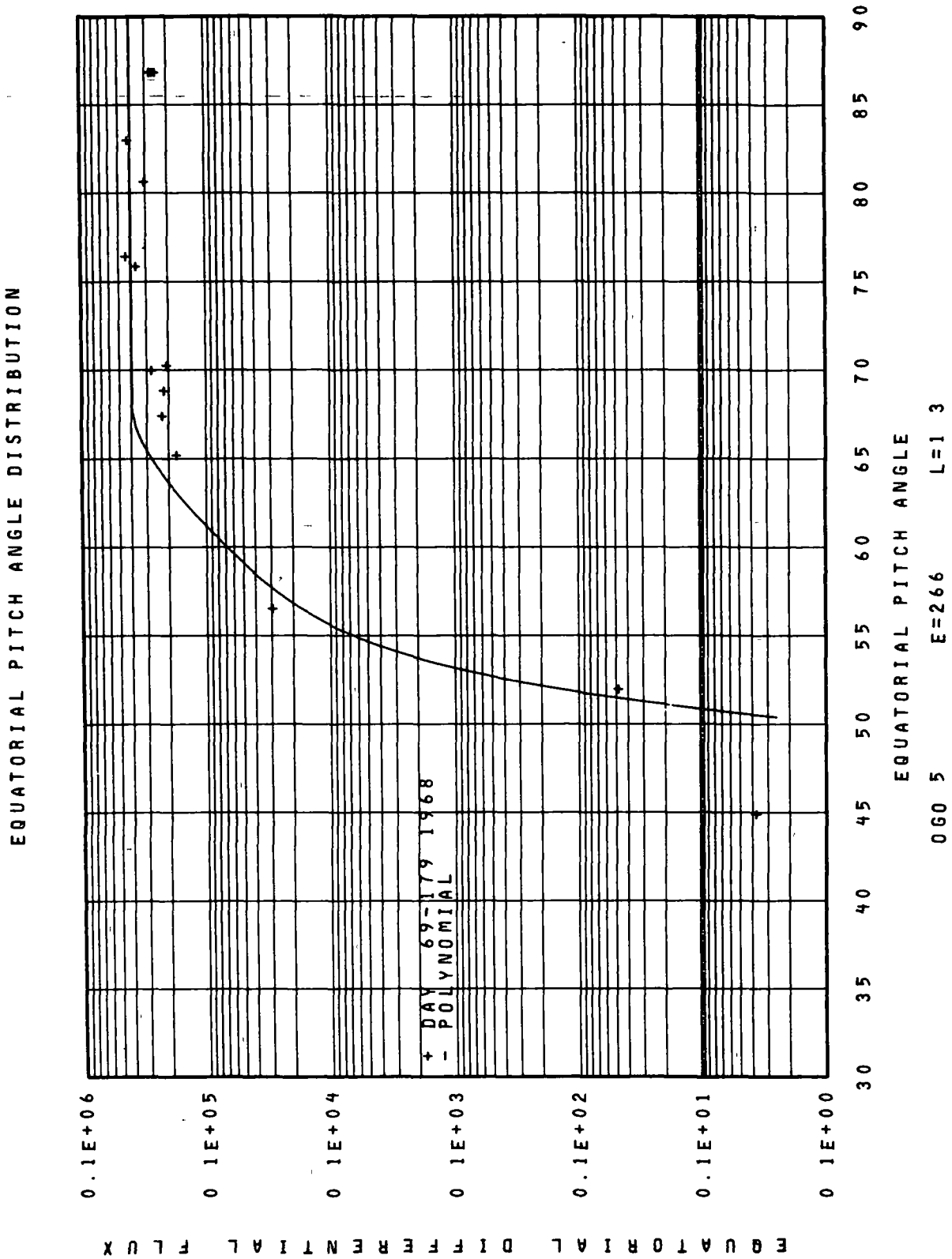
EQUATORIAL PITCH ANGLE DISTRIBUTION
+ DAY 69-179 1968
- POLYNOMIAL
EQUATORIAL DIFFERENTIAL FLUX
0.1E+06
0 1E+05
0 1E+04
0 1E+03
0.1E+02
0.1E+01
0 1E+00
30 35 40 45 50 55 60 65 70 75 80 85 90
EQUATORIAL PITCH ANGLE
OGO 5 E=266 L=1 3

Figure 8

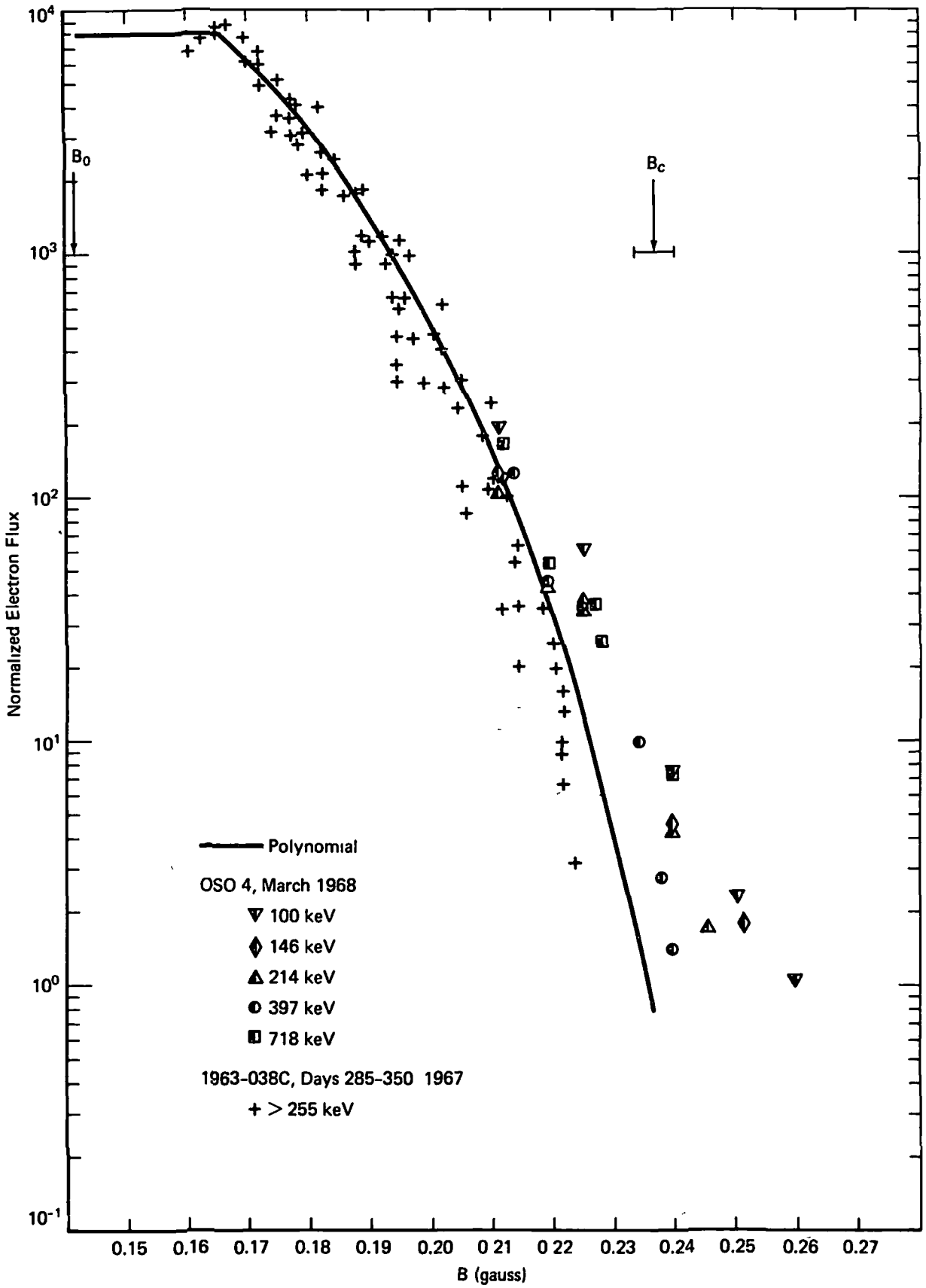

Figure 9. Normalized Mirror-Point Distribution at L = 1.3

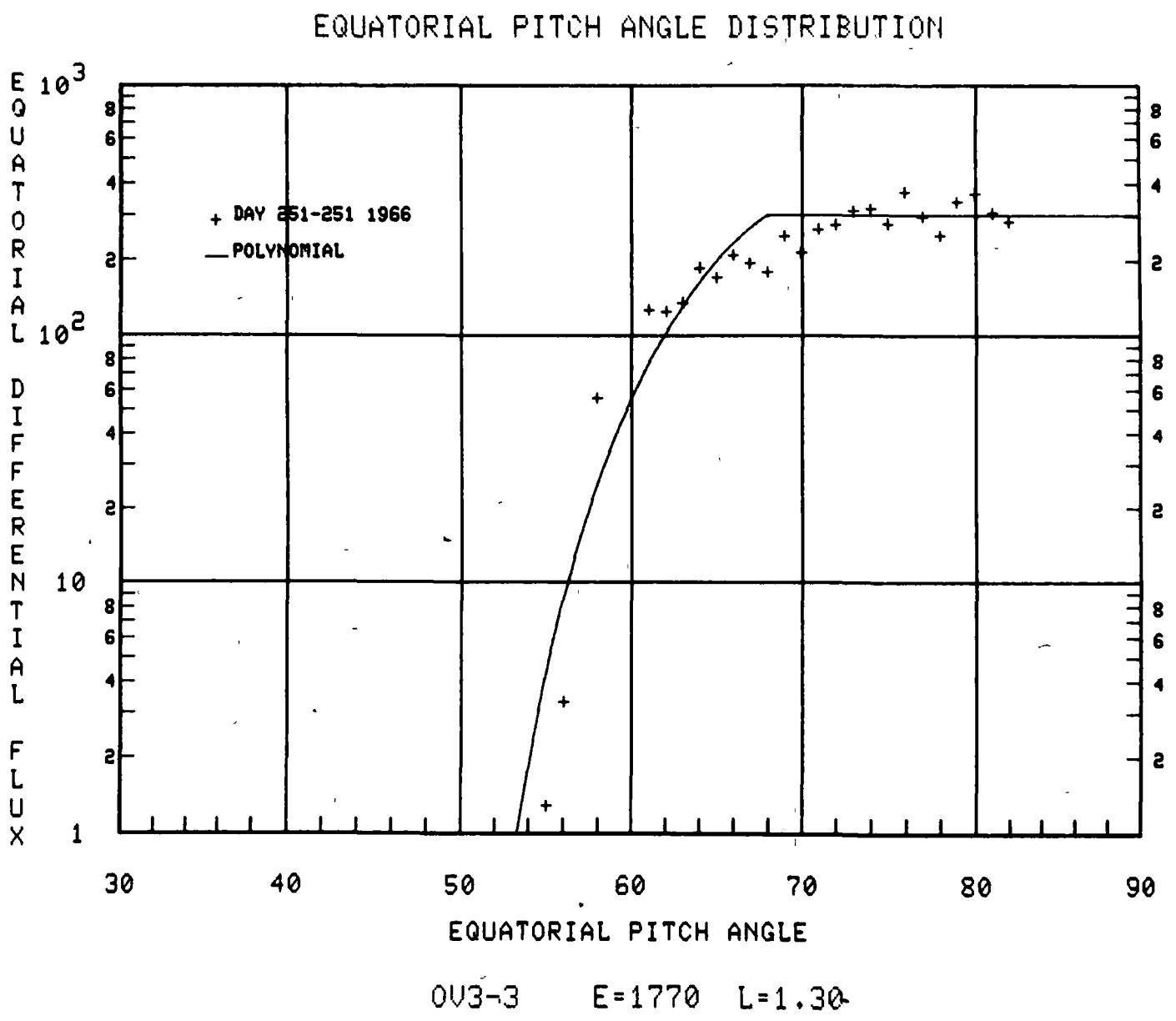
EQUATORIAL PITCH ANGLE DISTRIBUTION
EQUATORIAL DIFFERENTIAL FLUX
+ DAY 251-251 1966
POLYNOMIAL
EQUATORIAL PITCH ANGLE
OV3-3 E=1770 L=1.30

Figure 10

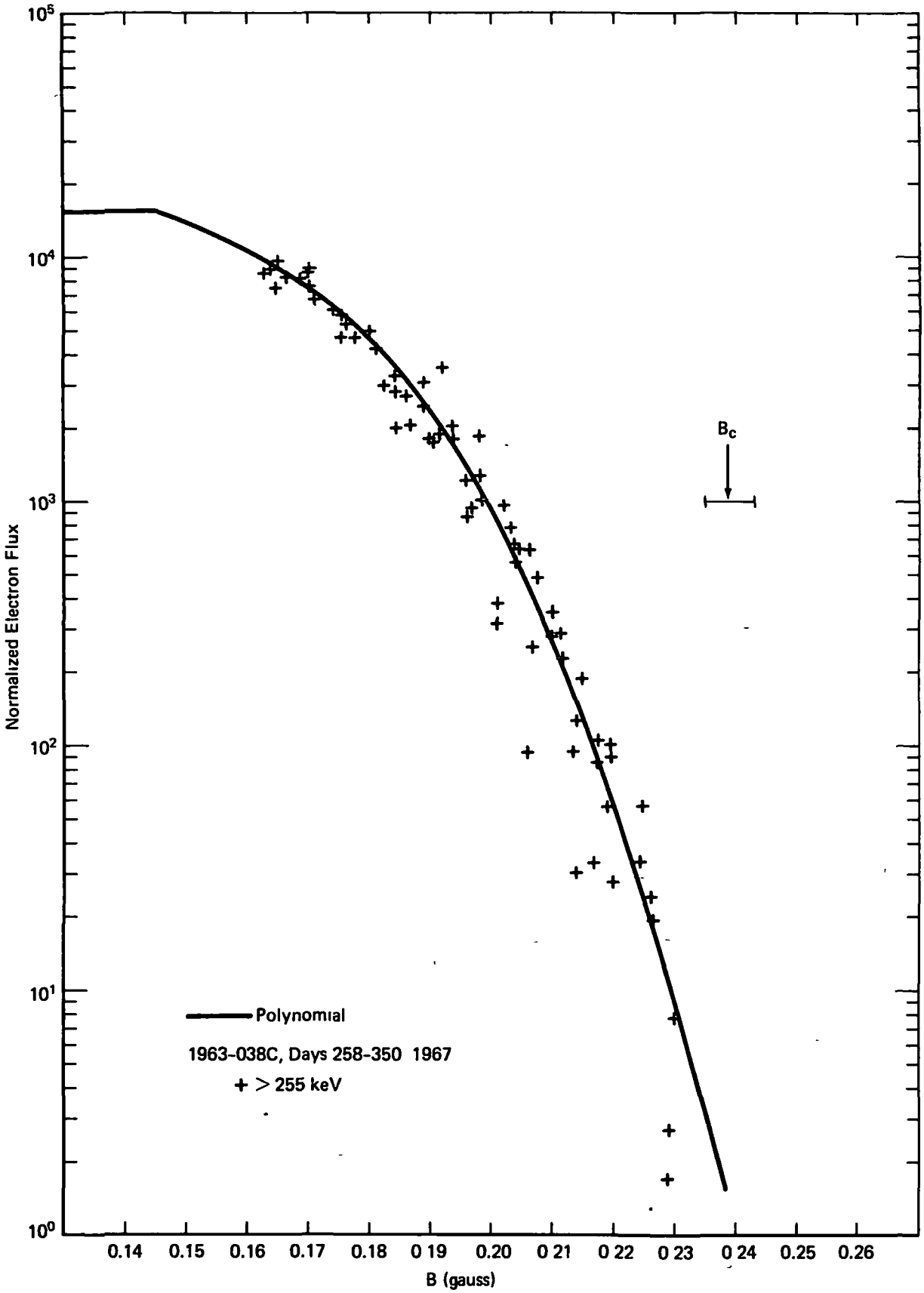

Figure 11. Normalized Mirror-Point Distribution at L = 1.35

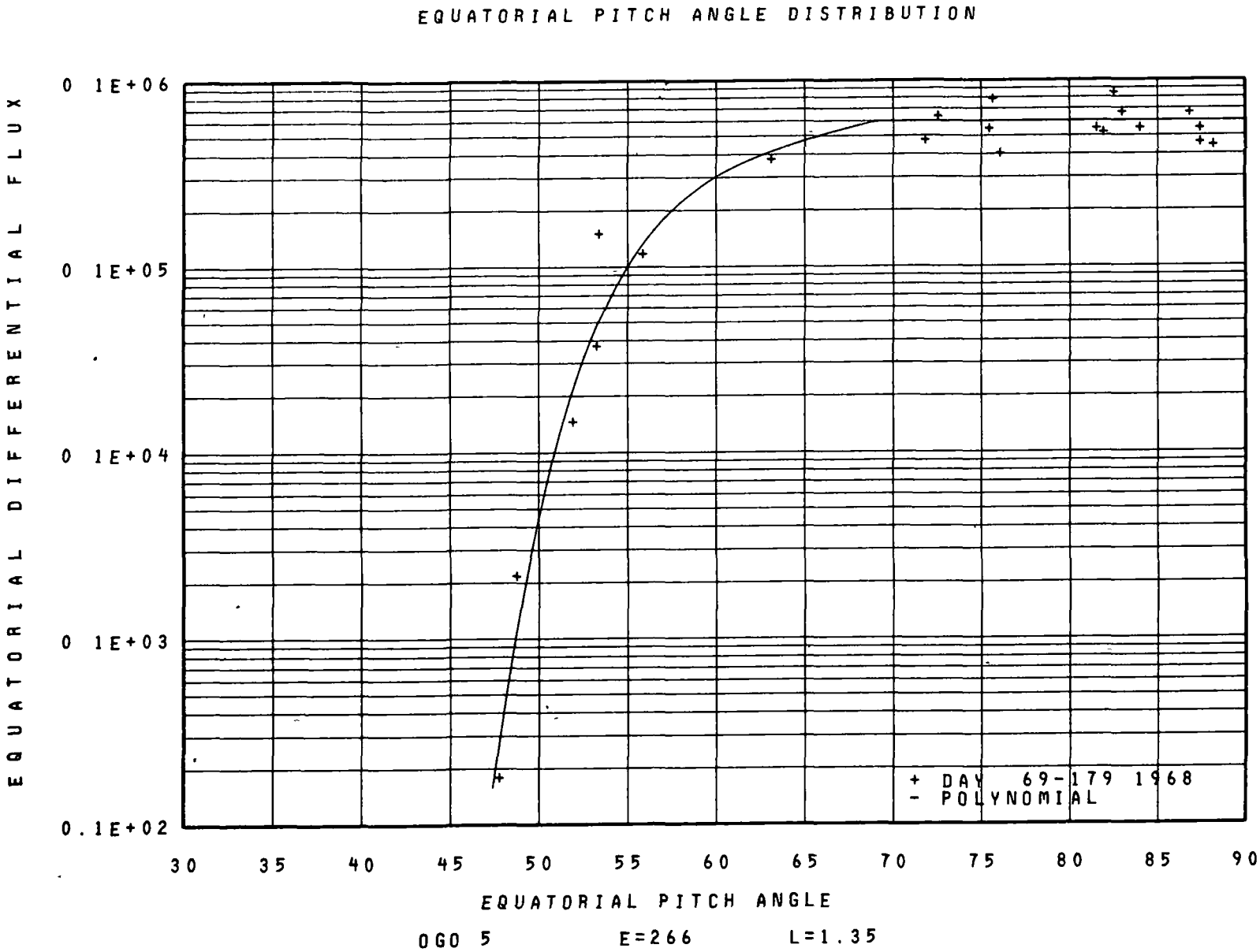
EQUATORIAL PITCH ANGLE DISTRIBUTION
EQUATORIAL DIFFERENTIAL FLUX
0 1E+06
0 1E+05
0 1E+04
0 1E+03
0.1E+02
30
35
40
45
50
55
60
65
70
75
80
85
90
EQUATORIAL PITCH ANGLE
+ DAY 69-179 1968
- POLYNOMIAL
OGO 5 E=266 L=1.35

Figure 12

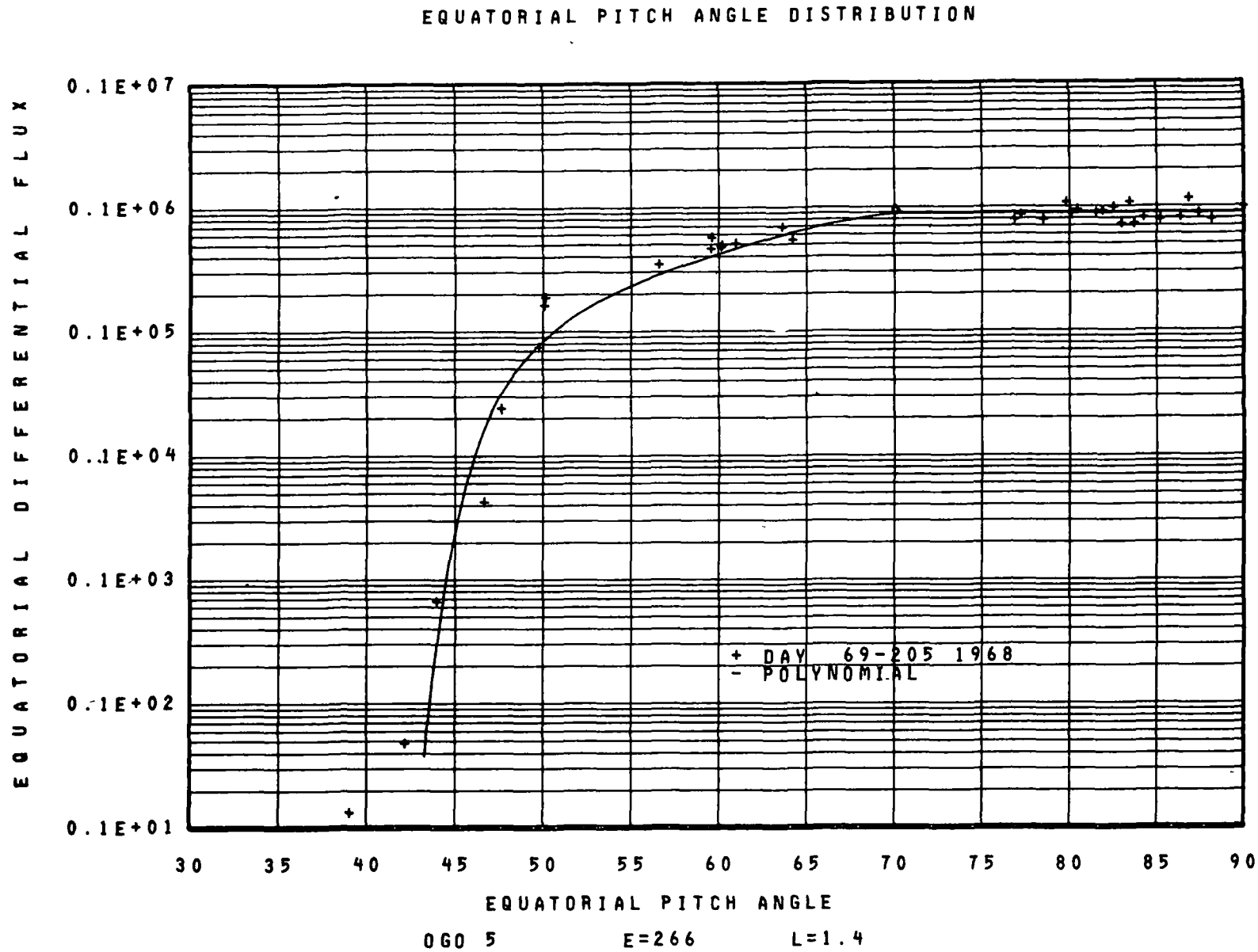
EQUATORIAL PITCH ANGLE DISTRIBUTION
EQUATORIAL DIFFERENTIAL FLUX
0.1E+07
0.1E+06
0.1E+05
0.1E+04
0.1E+03
0.1E+02
0.1E+01
30
35
40
45
50
55
60
65
70
75
80
85
90
EQUATORIAL PITCH ANGLE
+ DAY 69-205 1968
- POLYNOMIAL
OGO 5 E=266 L=1.4

Figure 13

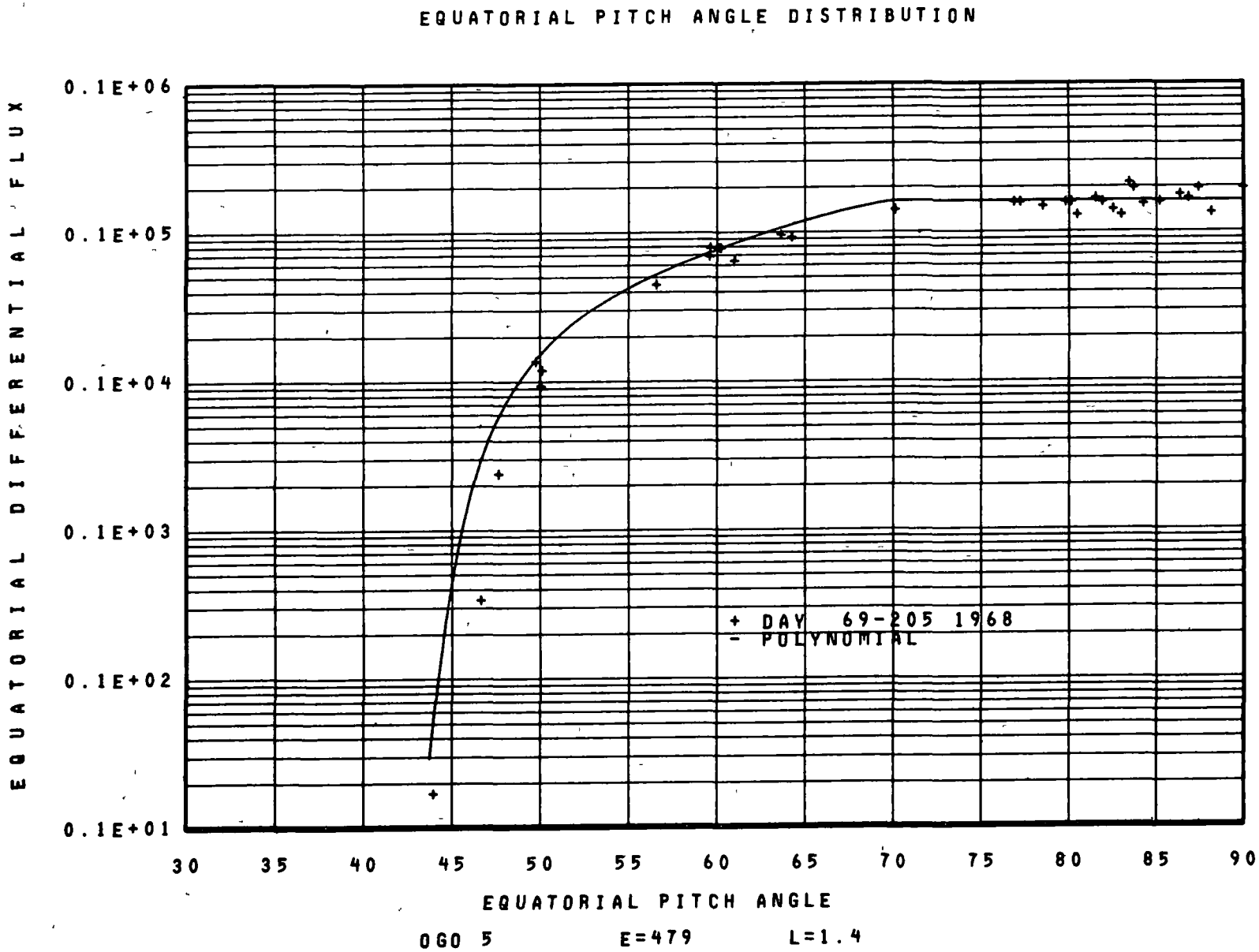
EQUATORIAL PITCH ANGLE DISTRIBUTION
EQUATORIAL DIFFERENTIAL FLUX
0.1E+06
0.1E+05
0.1E+04
0.1E+03
0.1E+02
0.1E+01
30
35
40
45
50
55
60
65
70
75
80
85
90
+ DAY 69-205 1968
- POLYNOMIAL
EQUATORIAL PITCH ANGLE
OGO 5
E=479
L=1.4

Figure 14

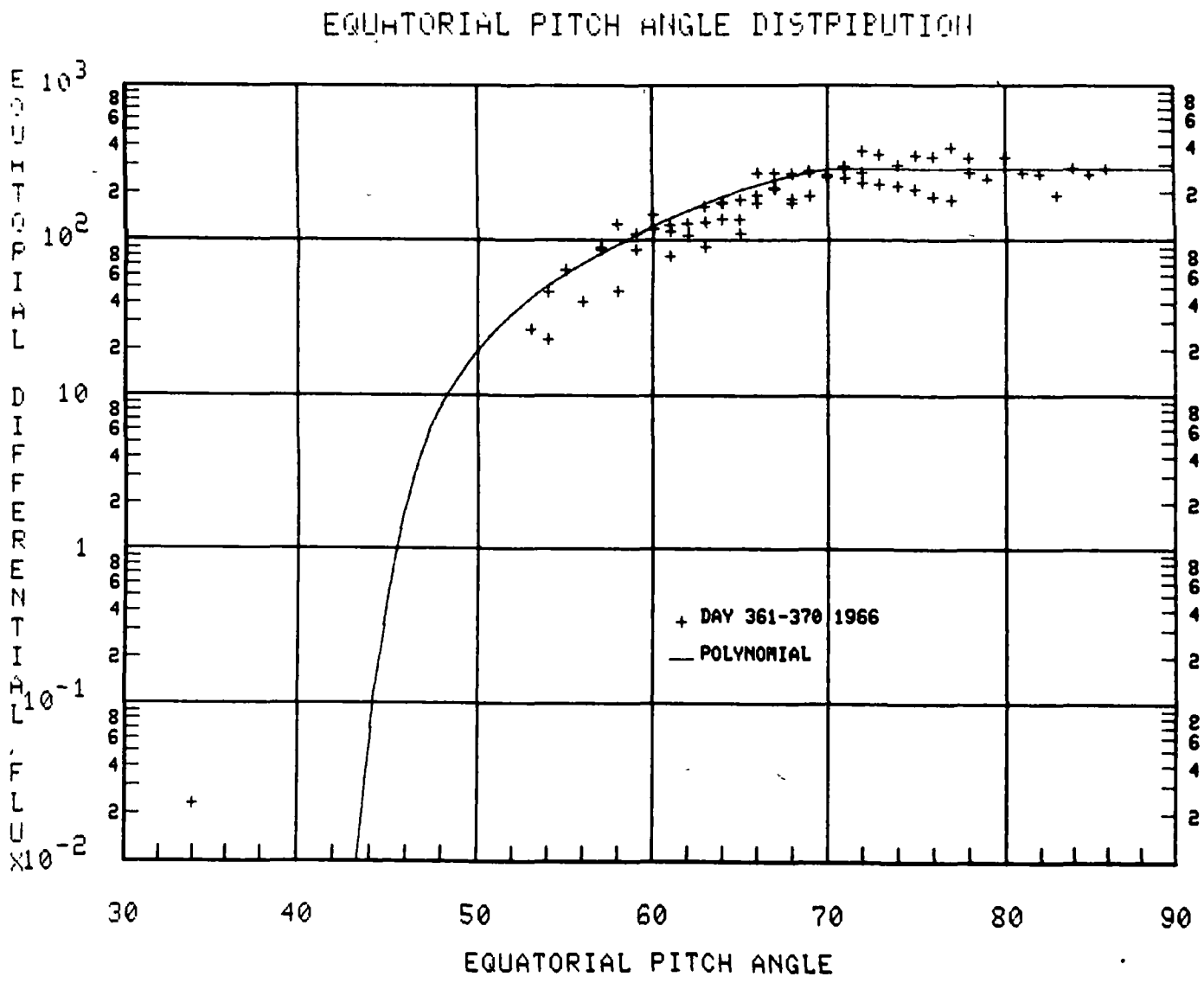
EQUATORIAL PITCH ANGLE DISTRIBUTION
DIFFERENTIAL FLUX
10^3
10^2
10
1
10^{-1}
$X10^{-2}$
+ DAY 361-370 1966
— POLYNOMIAL
30
40
50
60
70
80
90
EQUATORIAL PITCH ANGLE
OV3-3. E=1225 L=1.40

Figure 15

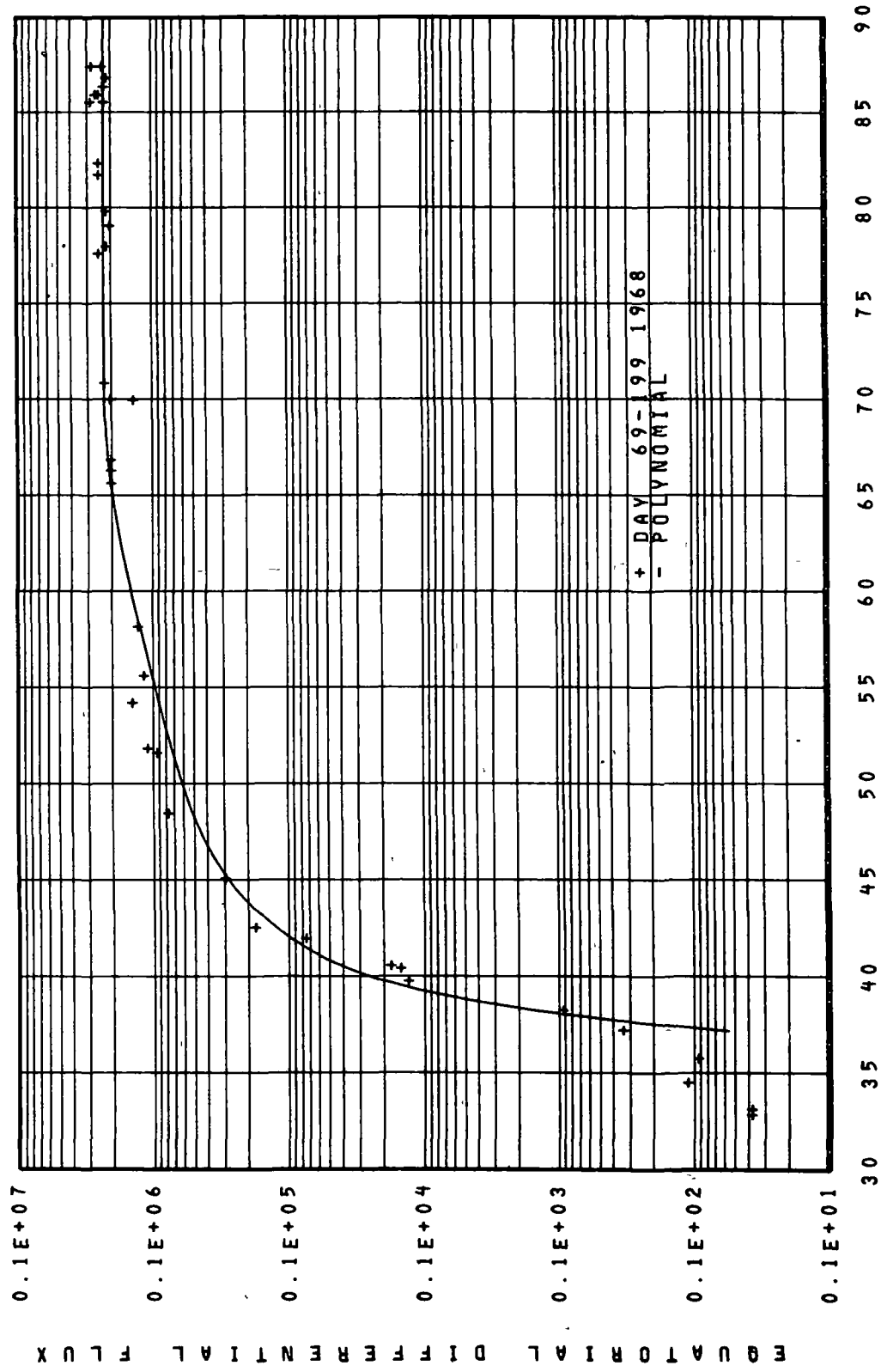
EQUATORIAL PITCH ANGLE DISTRIBUTION
+ DAY 69-199 1968
- POLYNOMIAL
EQUATORIAL DIFFERENTIAL FLUX
0.1E+07
0.1E+06
0.1E+05
0.1E+04
0.1E+03
0.1E+02
0.1E+01
30 35 40 45 50 55 60 65 70 75 80 85 90
EQUATORIAL PITCH ANGLE
OGO 5 E=158 L=1 5

Figure 16

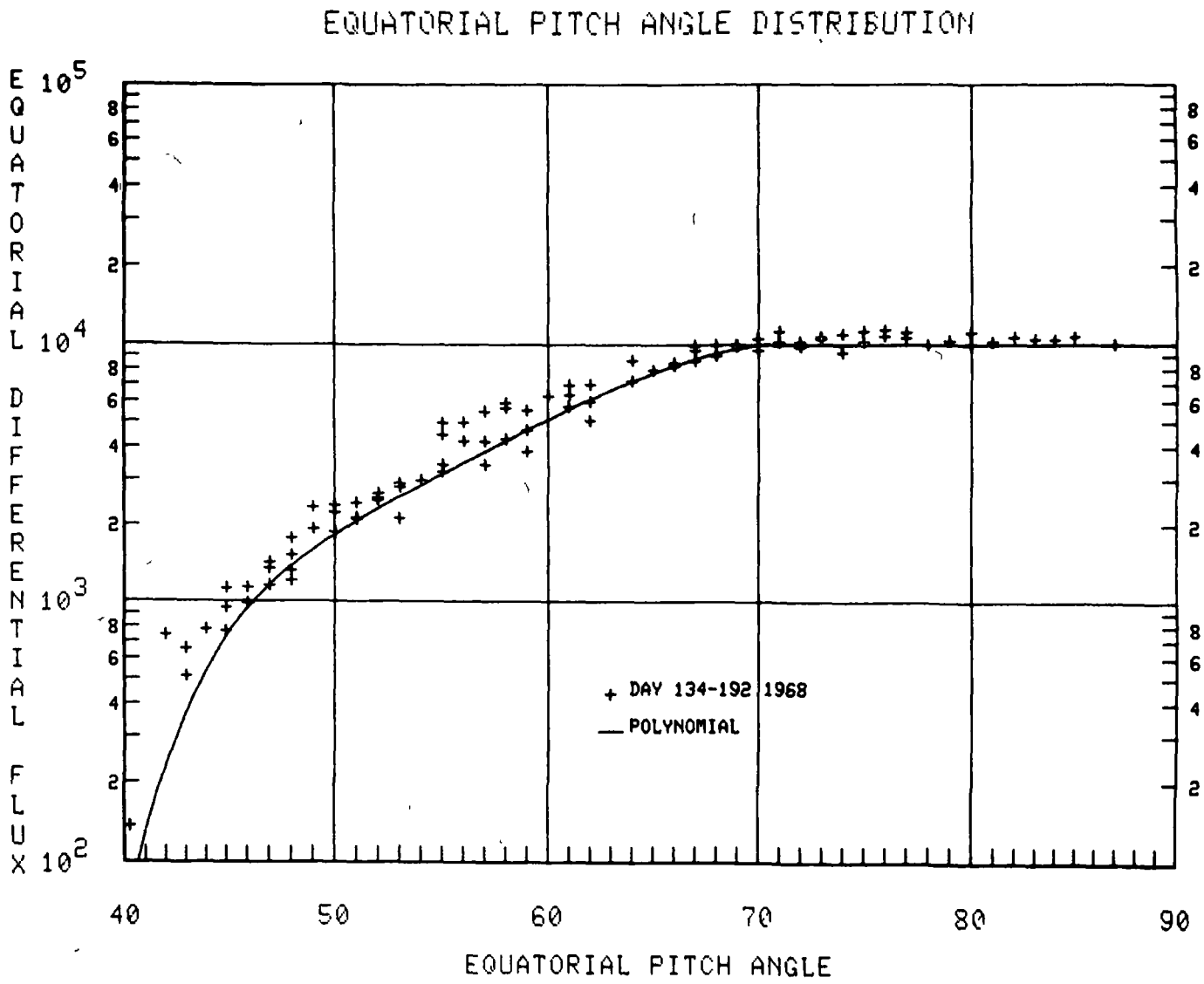
EQUATORIAL PITCH ANGLE DISTRIBUTION
EQUATORIAL DIFFERENTIAL FLUX
10^5
10^4
10^3
10^2
8
6
4
2
+ DAY 134-192 1968
POLYNOMIAL
40
50
60
70
80
90
EQUATORIAL PITCH ANGLE
001-13 E= 500 L=1.50

Figure 17

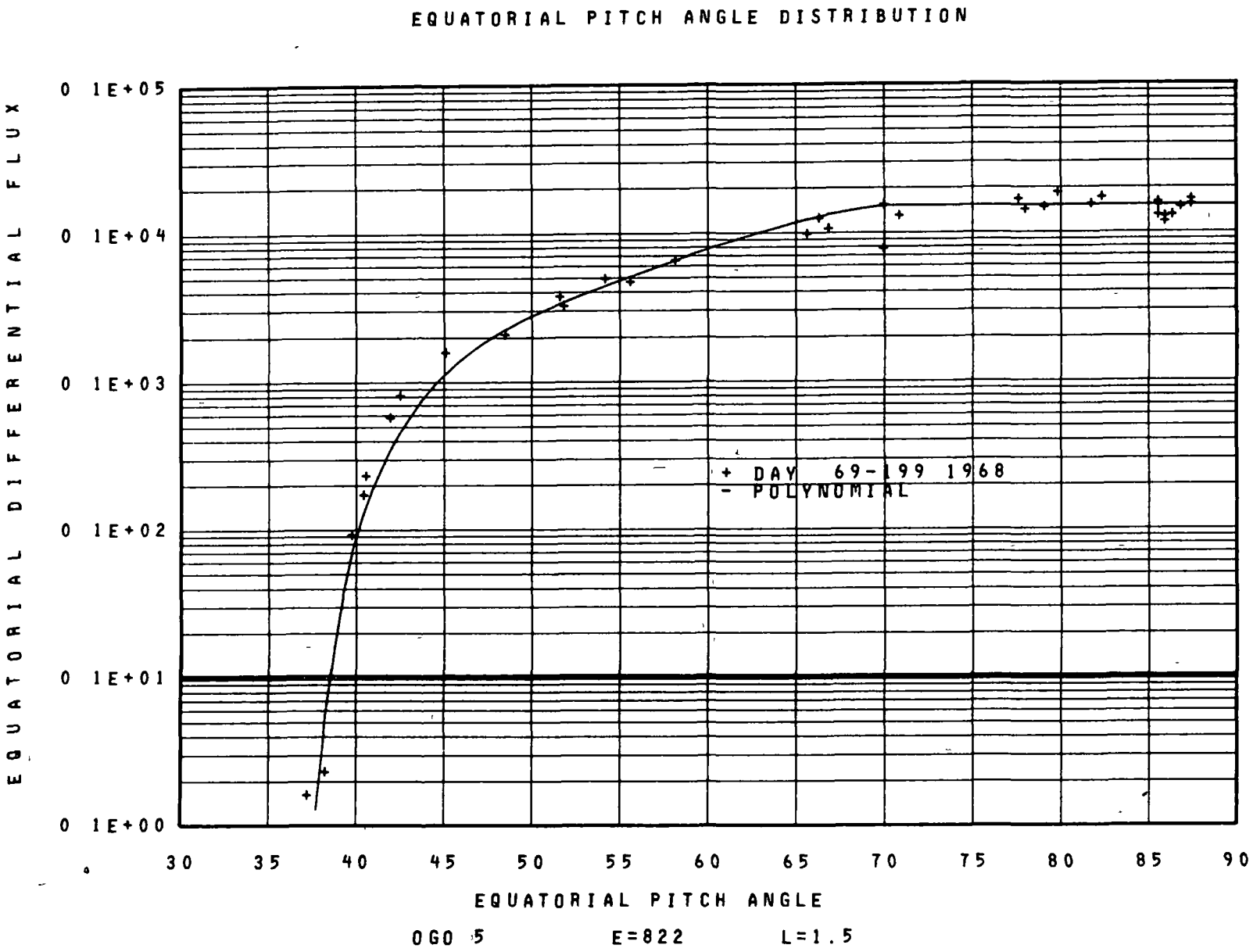
EQUATORIAL PITCH ANGLE DISTRIBUTION
EQUATORIAL DIFFERENTIAL FLUX
0 1E+05
0 1E+04
0 1E+03
0 1E+02
0 1E+01
0 1E+00
30
35
40
45
50
55
60
65
70
75
80
85
90
+ DAY 69-199 1968
- POLYNOMIAL
EQUATORIAL PITCH ANGLE
OGO 5
E=822
L=1.5

Figure 18

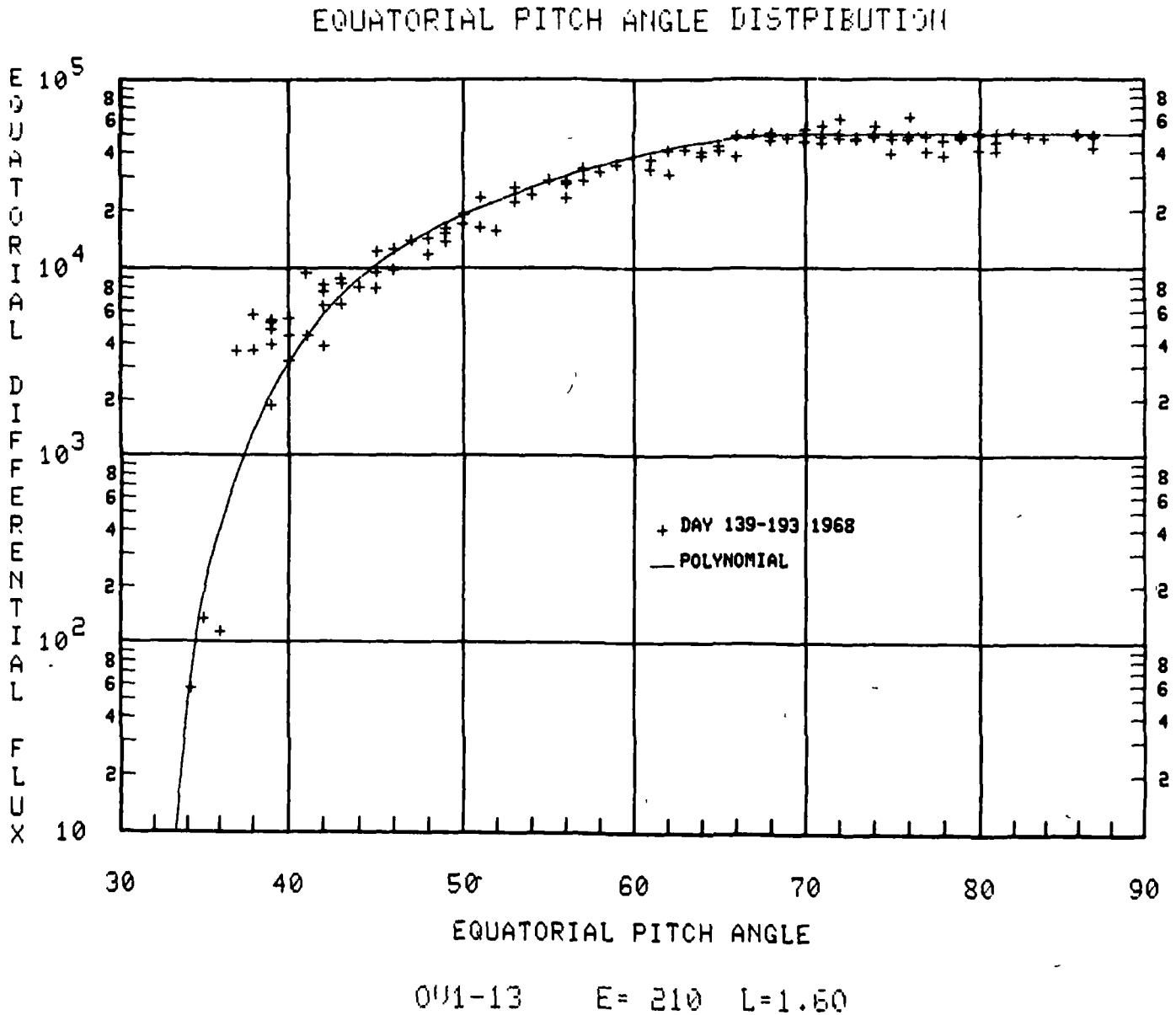
EQUATORIAL PITCH ANGLE DISTRIBUTION
EQUATORIAL DIFFERENTIAL FLUX
10^5
10^4
10^3
10^2
10
30
40
50
60
70
80
90
EQUATORIAL PITCH ANGLE
+ DAY 139-193 1968
— POLYNOMIAL
001-13 E= 210 L=1.60

Figure 19

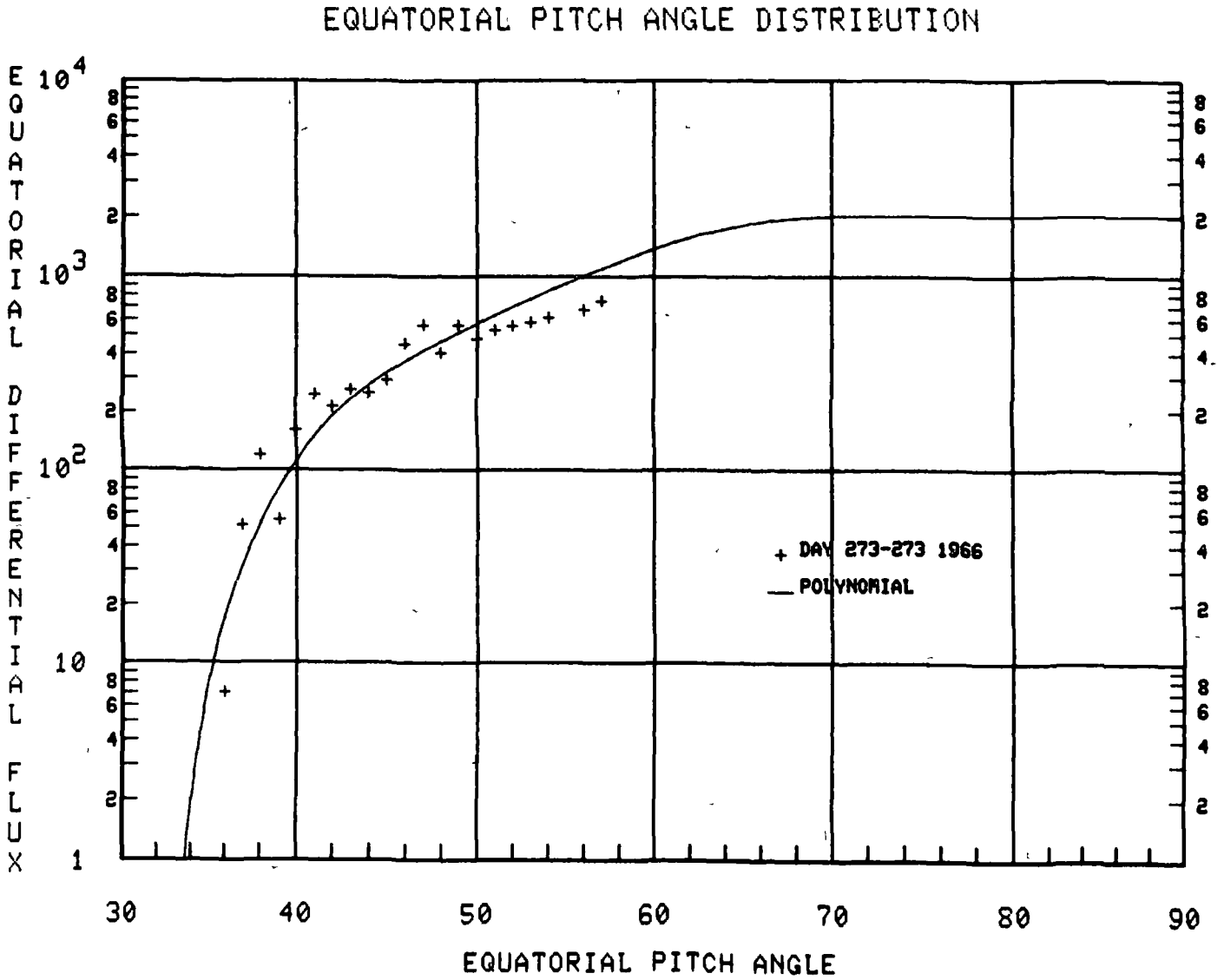
EQUATORIAL PITCH ANGLE DISTRIBUTION
EQUATORIAL DIFFERENTIAL FLUX
10^4
10^3
10^2
10
1
8
6
4
2
30
40
50
60
70
80
90
+ DAY 273-273 1966
POLYNOMIAL
EQUATORIAL PITCH ANGLE
OV3-3 E= 712 L=1.60

Figure 20

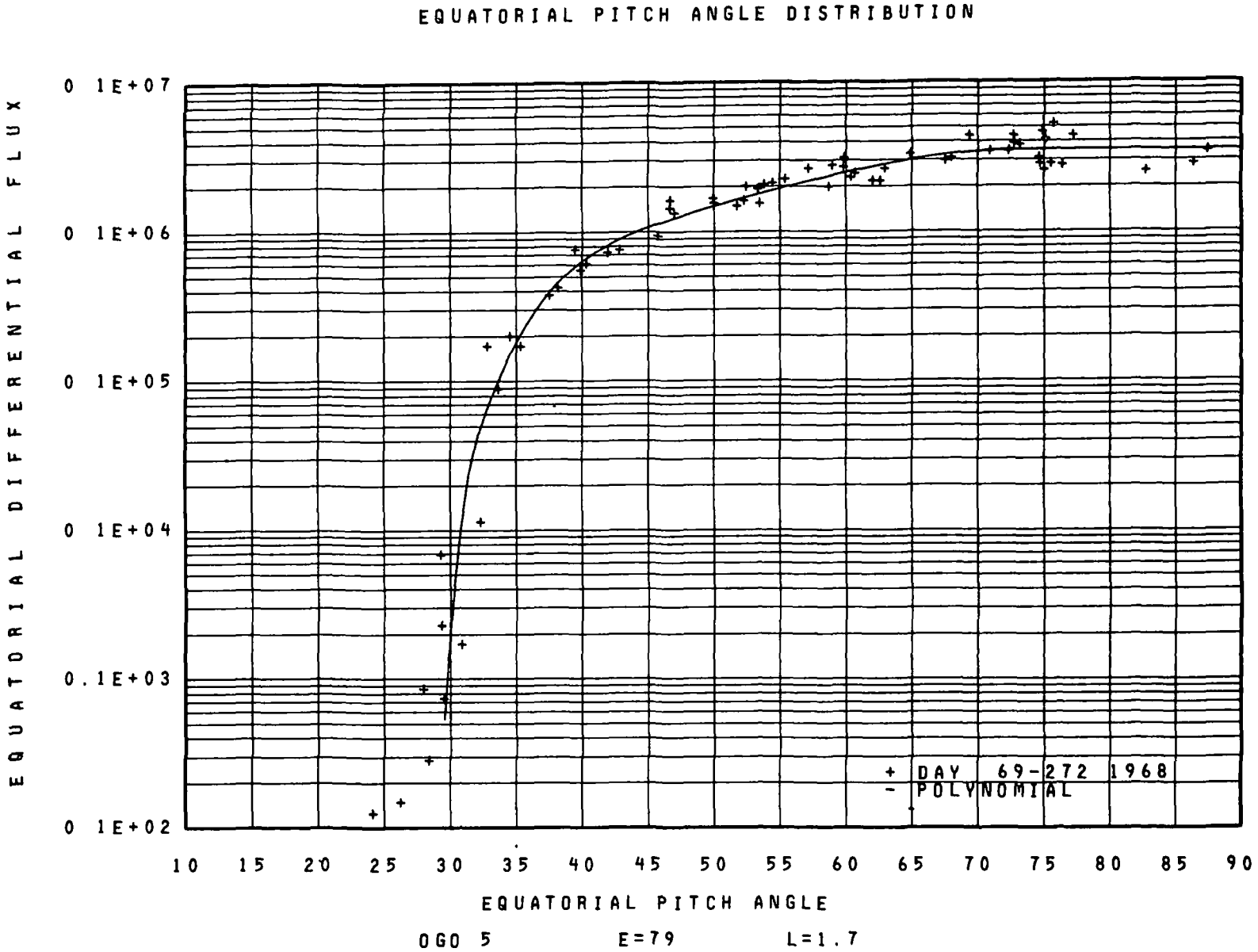
EQUATORIAL PITCH ANGLE DISTRIBUTION
EQUATORIAL DIFFERENTIAL FLUX
0 1E+07
0 1E+06
0 1E+05
0 1E+04
0.1E+03
0 1E+02
10 15 20 25 30 35 40 45 50 55 60 65 70 75 80 85 90
EQUATORIAL PITCH ANGLE
+ DAY 69-272 1968
- POLYNOMIAL
OGO 5 E=79 L=1.7

Figure 21

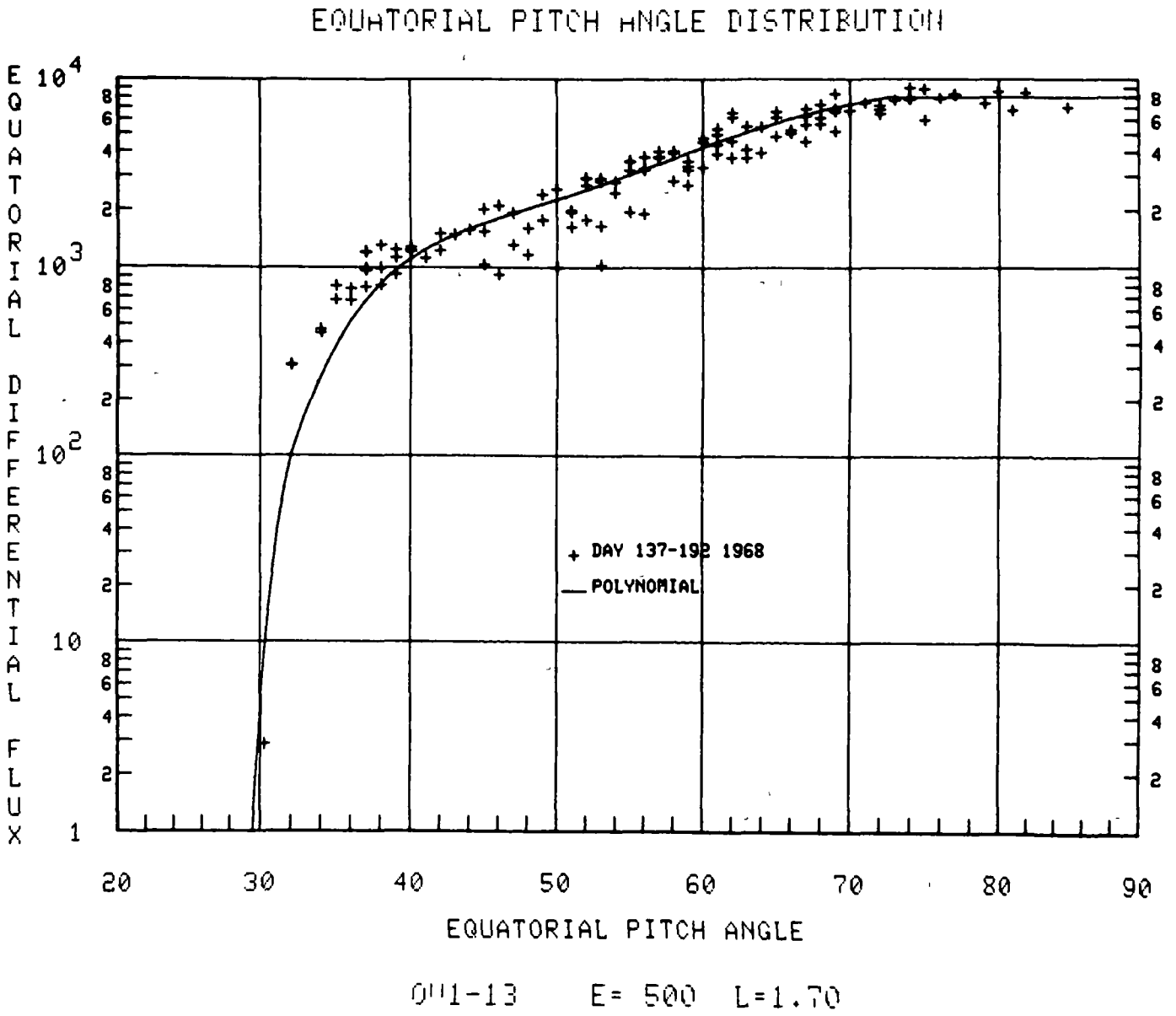
EQUATORIAL PITCH ANGLE DISTRIBUTION
EQUATORIAL DIFFERENTIAL FLUX
10^4
10^3
10^2
10
1
+ DAY 137-192 1968
POLYNOMIAL
20
30
40
50
60
70
80
90
EQUATORIAL PITCH ANGLE
001-13 E= 500 L=1.70

Figure 22

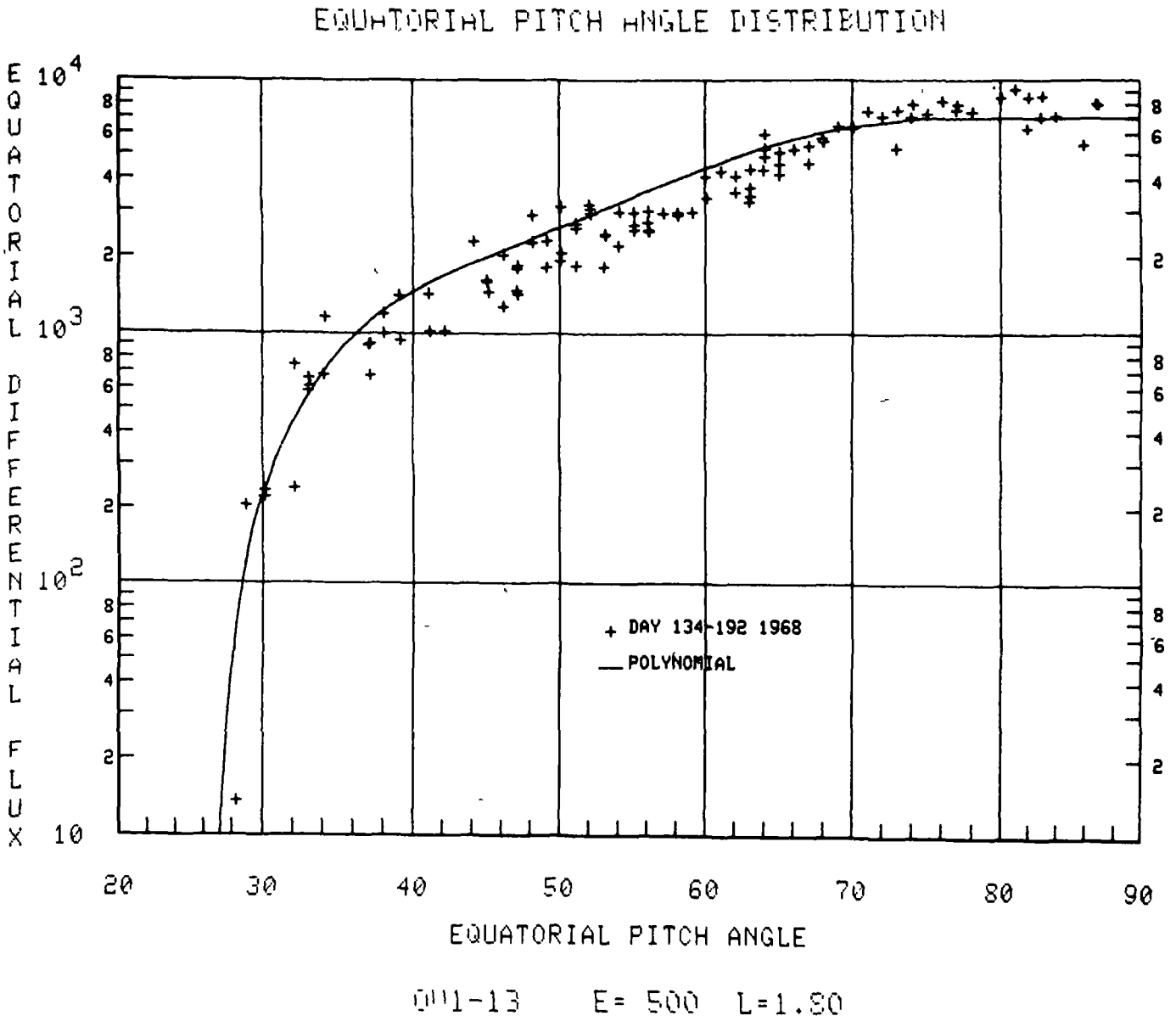
EQUATORIAL PITCH ANGLE DISTRIBUTION
EQUATORIAL DIFFERENTIAL FLUX
10^4
10^3
10^2
10
8
6
4
2
20
30
40
50
60
70
80
90
+ DAY 134-192 1968
POLYNOMIAL
EQUATORIAL PITCH ANGLE
001-13 E= 500 L=1.80

Figure 23

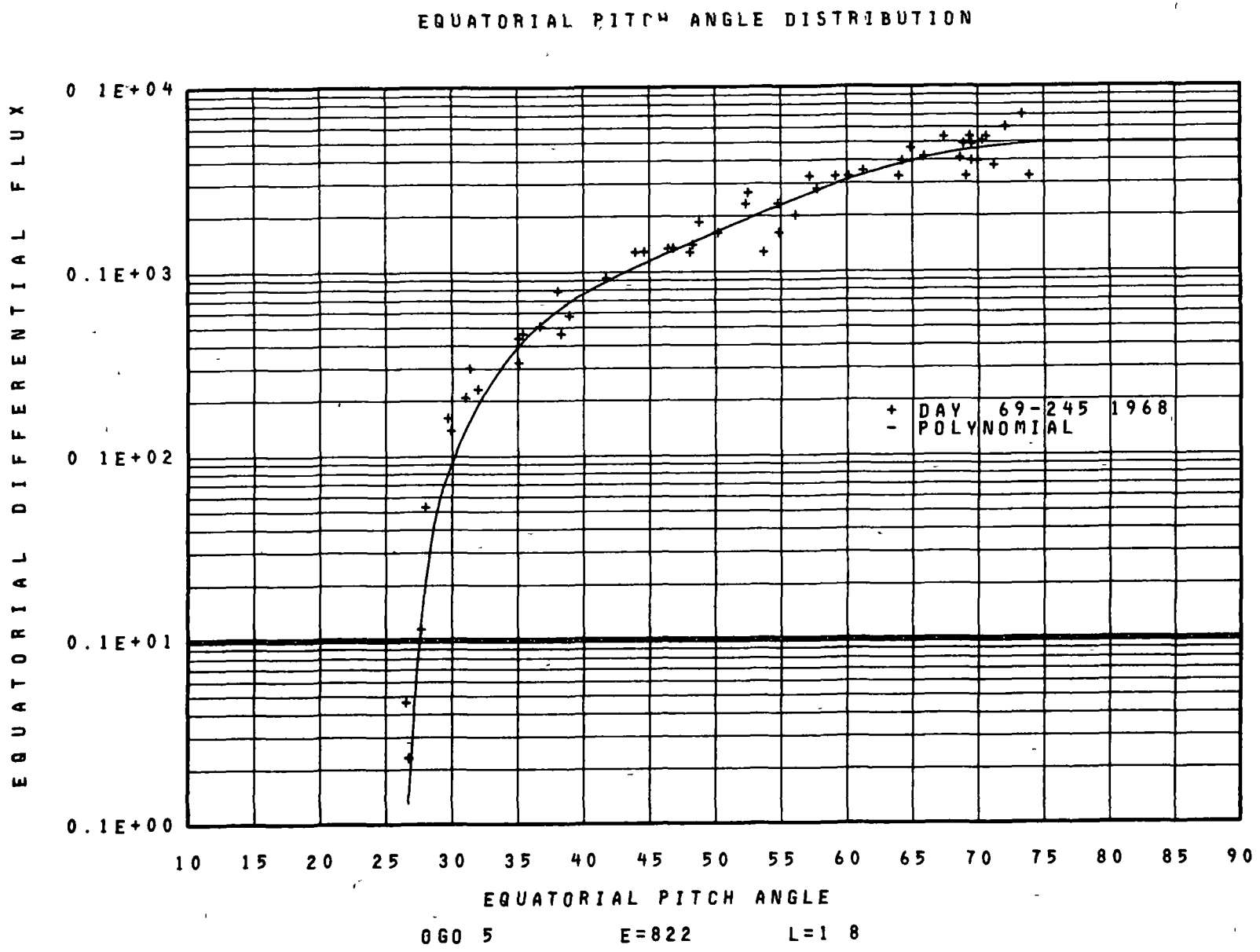
EQUATORIAL PITCH ANGLE DISTRIBUTION
EQUATORIAL DIFFERENTIAL FLUX
0 1E+04
0.1E+03
0 1E+02
0.1E+01
0.1E+00
10 15 20 25 30 35 40 45 50 55 60 65 70 75 80 85 90
EQUATORIAL PITCH ANGLE
+ DAY 69-245 1968
- POLYNOMIAL
OGO 5 E=822 L=1 8

Figure 24

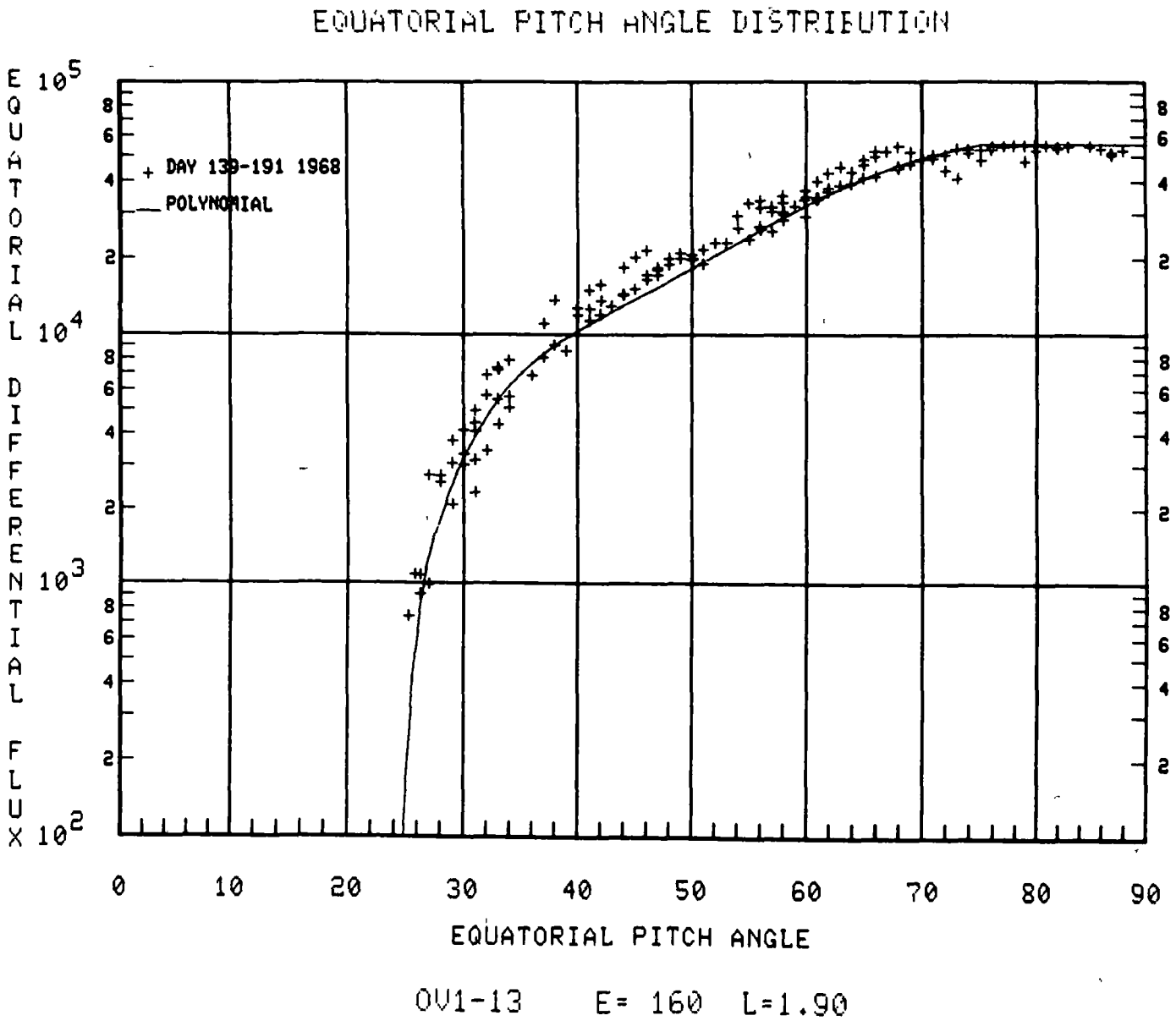
EQUATORIAL PITCH ANGLE DISTRIBUTION
EQUATORIAL DIFFERENTIAL FLUX
DAY 139-191 1968
POLYNOMIAL
EQUATORIAL PITCH ANGLE
OV1-13 E= 160 L=1.90

Figure 25

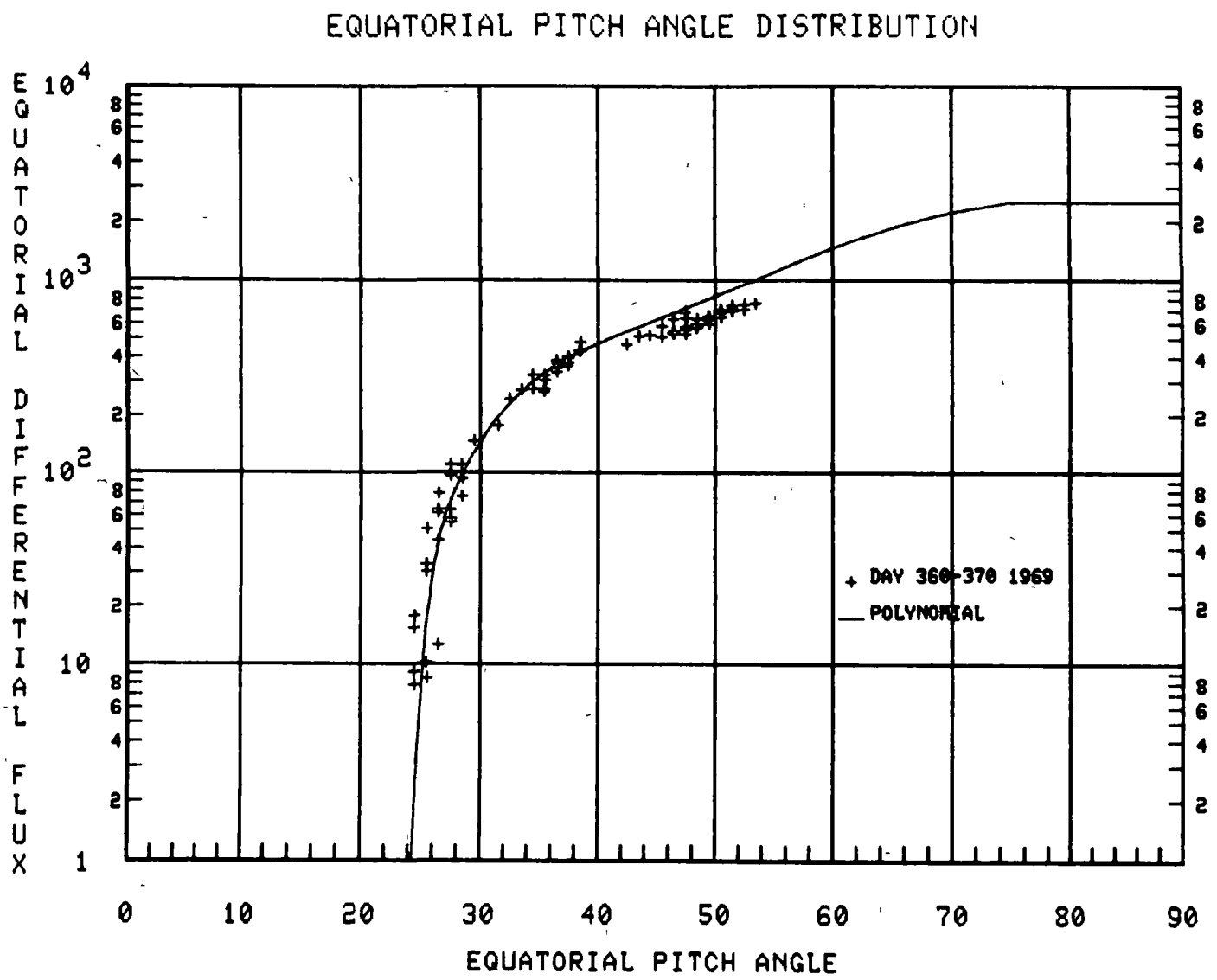
EQUATORIAL PITCH ANGLE DISTRIBUTION
EQUATORIAL DIFFERENTIAL FLUX
EQUATORIAL PITCH ANGLE
+ DAY 360-370 1969
POLYNOMIAL
OV1-19 E= 537 L=1.90

Figure 26

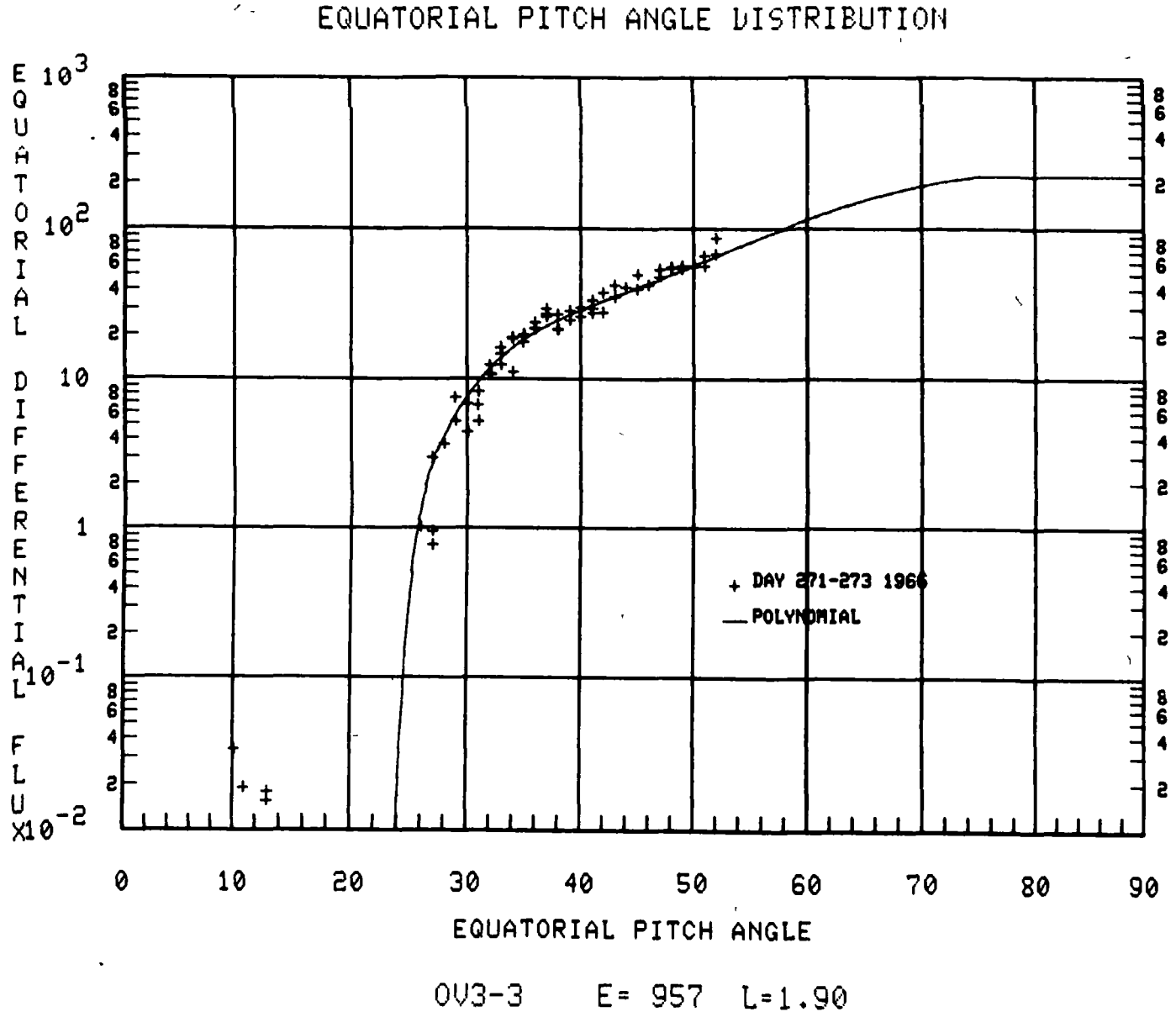
EQUATORIAL PITCH ANGLE DISTRIBUTION
EQUATORIAL DIFFERENTIAL FLUX
10^3
10^2
10
1
10^{-1}
10^{-2}
+ DAY 271-273 1966
POLYNOMIAL
0
10
20
30
40
50
60
70
80
90
EQUATORIAL PITCH ANGLE
OV3-3 E= 957 L=1.90

Figure 27

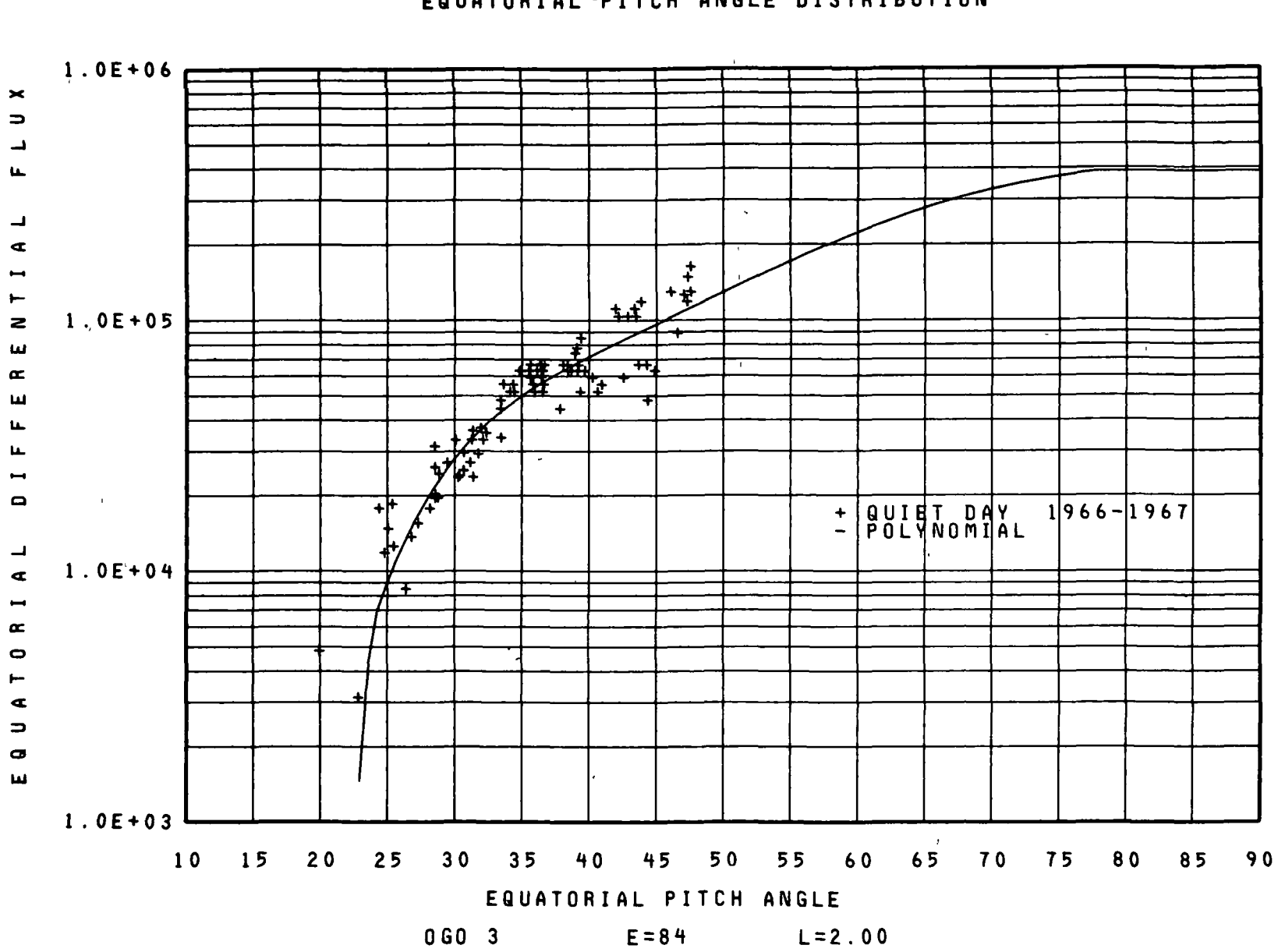
EQUATORIAL PITCH ANGLE DISTRIBUTION
EQUATORIAL DIFFERENTIAL FLUX
1.0E+06
1.0E+05
1.0E+04
1.0E+03
10 15 20 25 30 35 40 45 50 55 60 65 70 75 80 85 90
EQUATORIAL PITCH ANGLE
+ QUIET DAY 1966-1967
- POLYNOMIAL
OGO 3 E=84 L=2.00

Figure 28

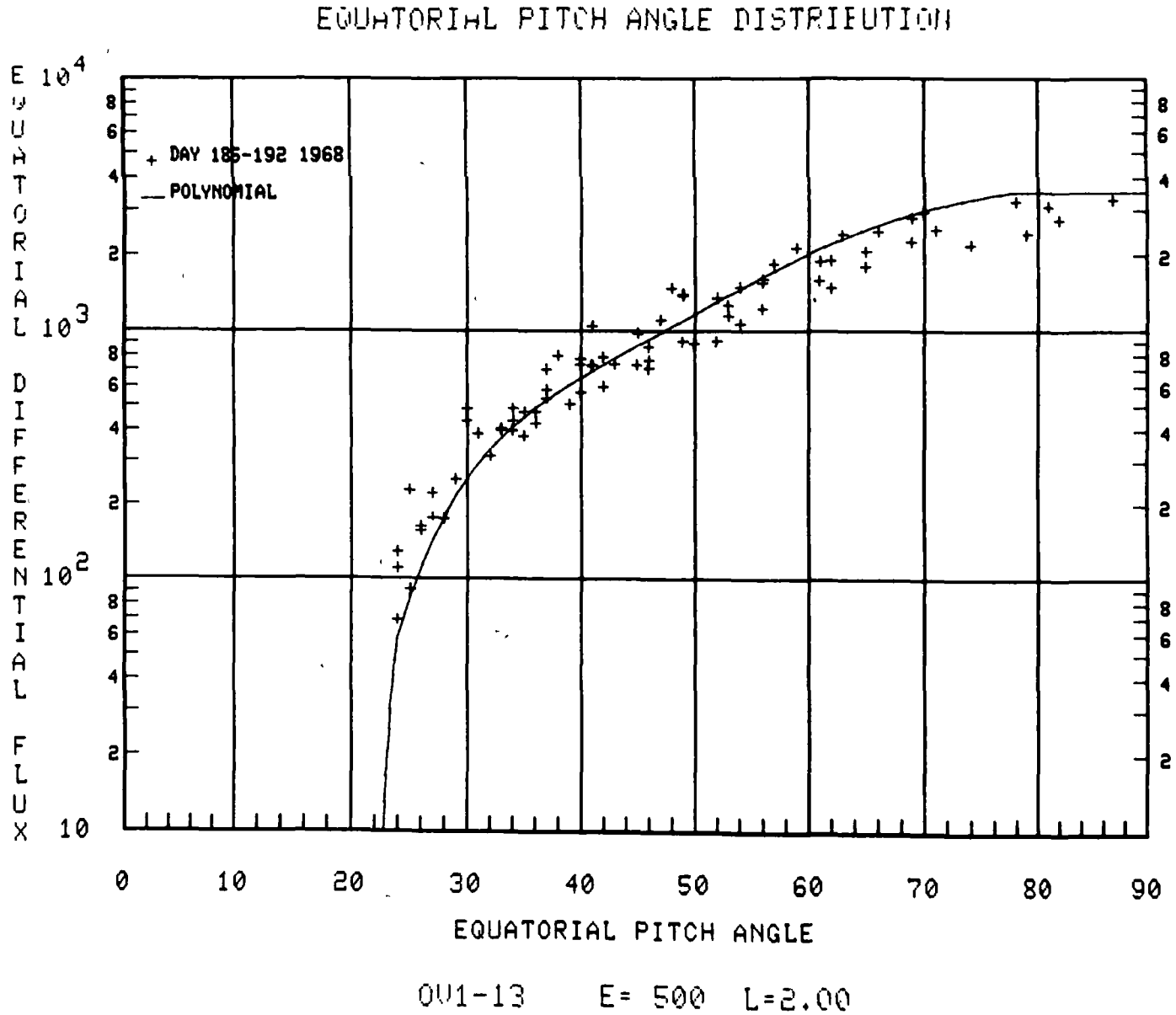
EQUATORIAL PITCH ANGLE DISTRIBUTION
EQUATORIAL DIFFERENTIAL FLUX
DAY 185-192 1968
POLYNOMIAL
EQUATORIAL PITCH ANGLE
OV1-13 E= 500 L=2.00

Figure 29

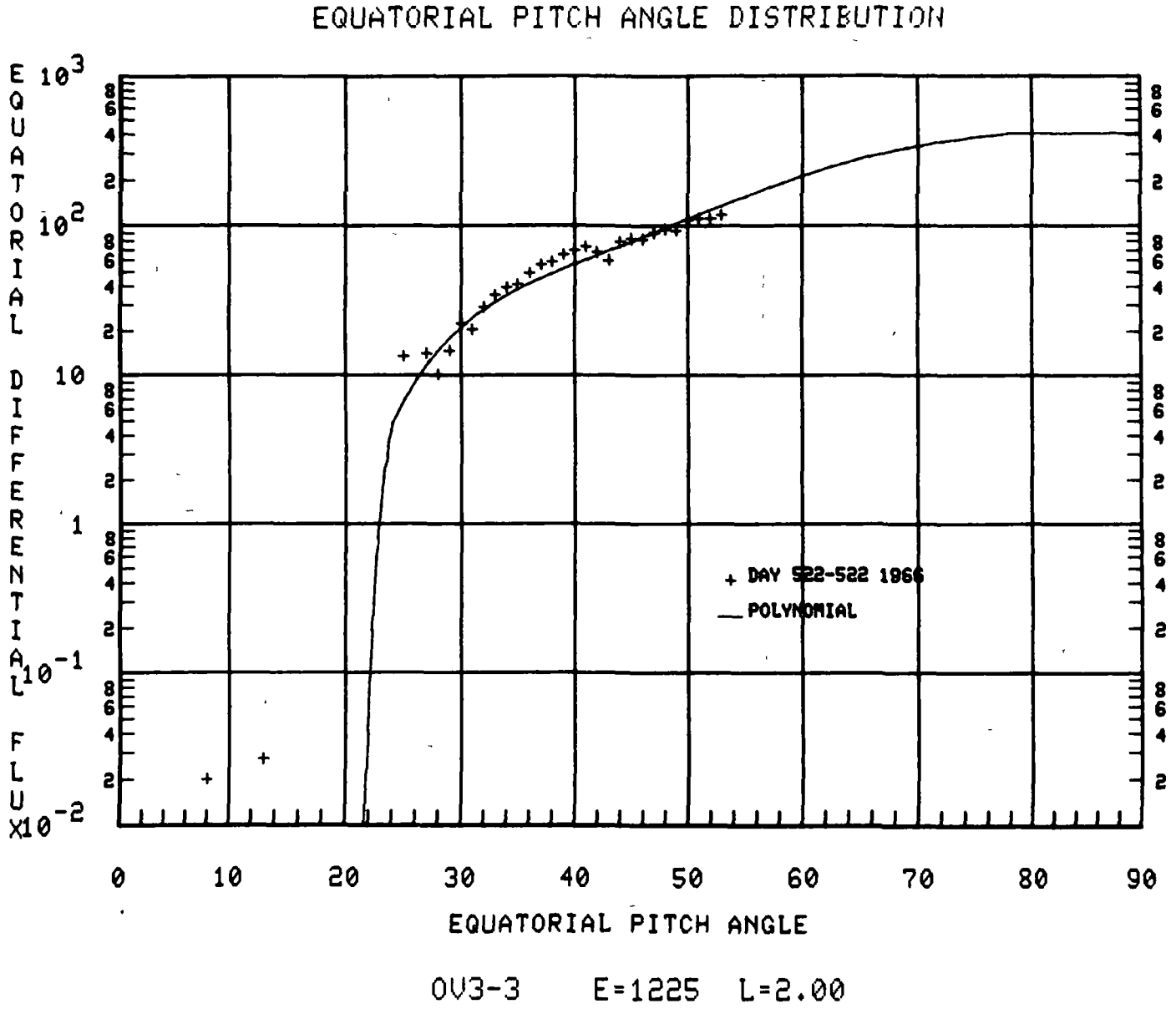
EQUATORIAL PITCH ANGLE DISTRIBUTION
EQUATORIAL DIFFERENTIAL FLUX
10^3
10^2
10
1
10^{-1}
10^{-2}
+ DAY 522-522 1966
POLYNOMIAL
0
10
20
30
40
50
60
70
80
90
EQUATORIAL PITCH ANGLE
OV3-3 E=1225 L=2.00

Figure 30

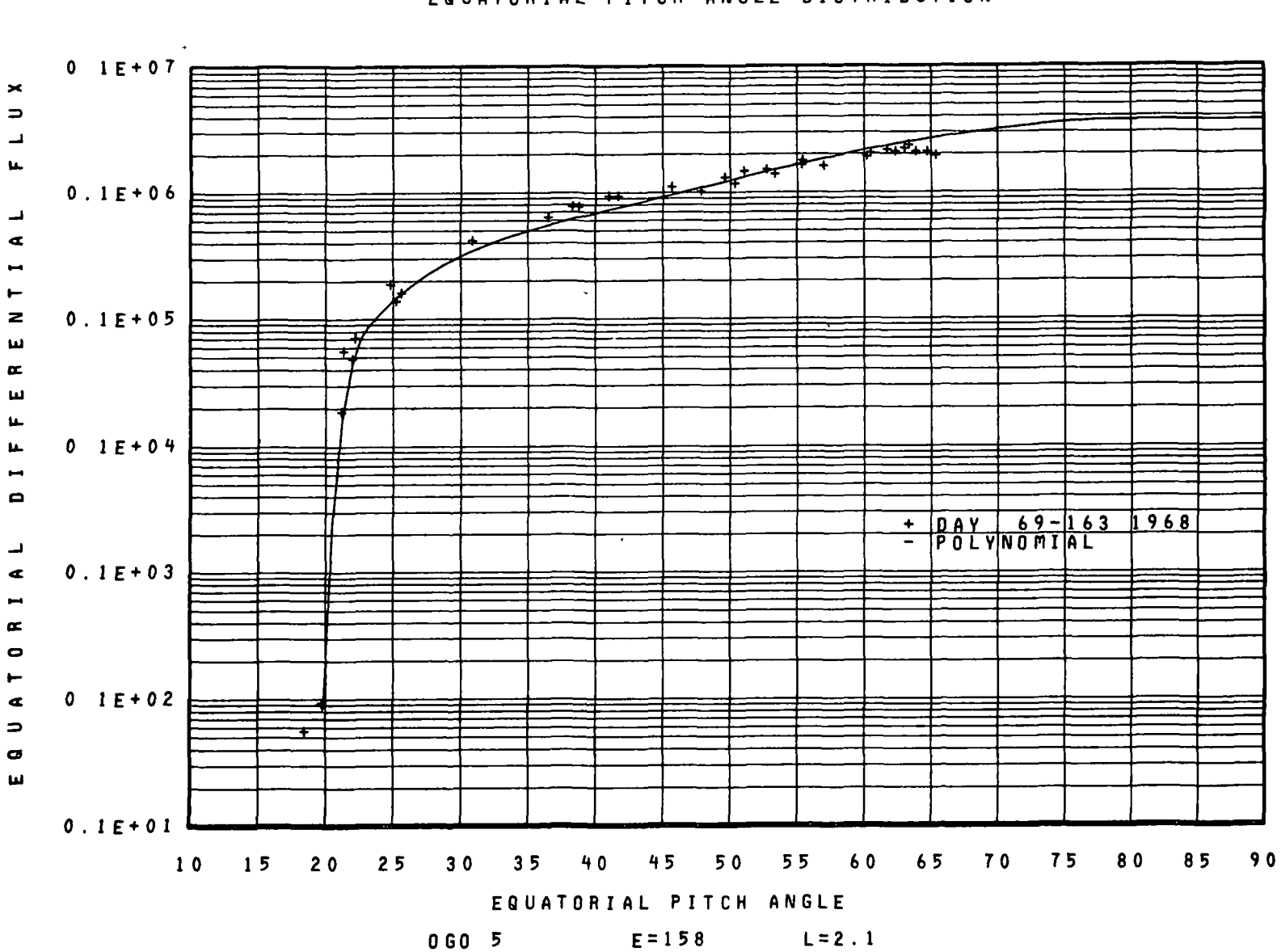
EQUATORIAL PITCH ANGLE DISTRIBUTION
EQUATORIAL DIFFERENTIAL FLUX
0 1E+07
0.1E+06
0.1E+05
0 1E+04
0.1E+03
0 1E+02
0.1E+01
+ DAY 69-163 1968
- POLYNOMIAL
10 15 20 25 30 35 40 45 50 55 60 65 70 75 80 85 90
EQUATORIAL PITCH ANGLE
OGO 5 E=158 L=2.1

Figure 31

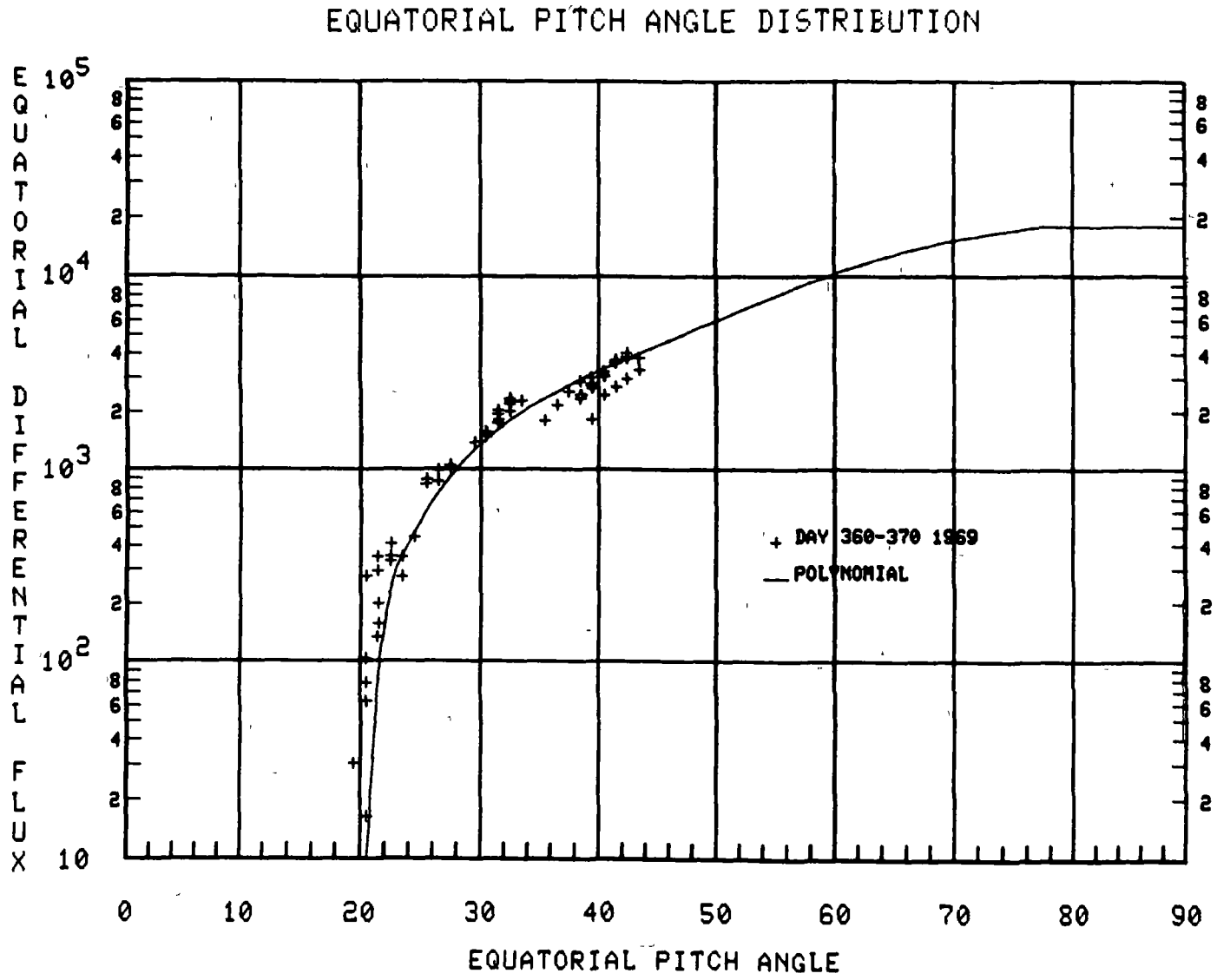
EQUATORIAL PITCH ANGLE DISTRIBUTION
EQUATORIAL DIFFERENTIAL FLUX
10^5
10^4
10^3
10^2
10
+ DAY 360-370 1969
POLYNOMIAL
0
10
20
30
40
50
60
70
80
90
EQUATORIAL PITCH ANGLE
OV1-19 E= 377 L=2.10

Figure 32

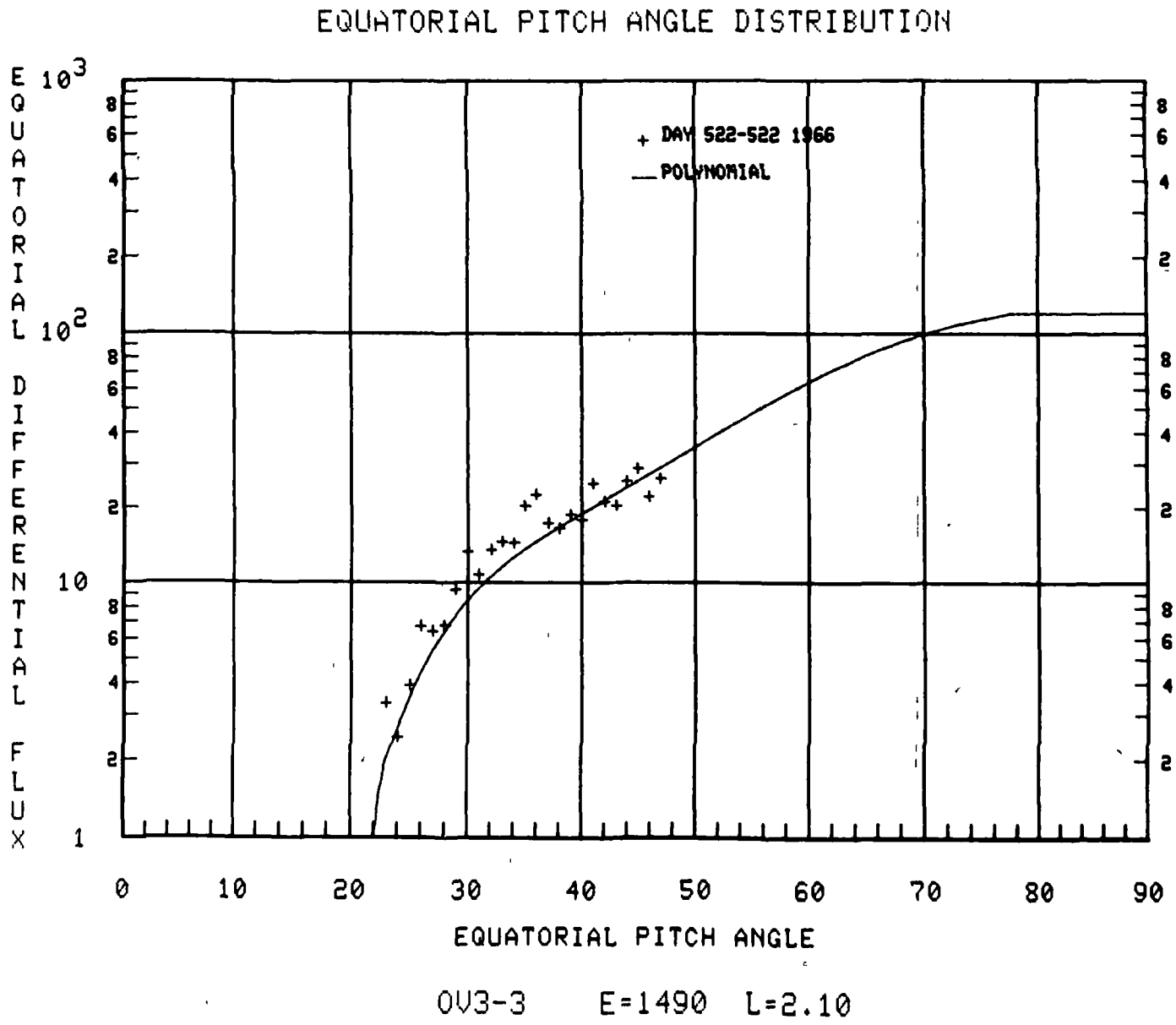
EQUATORIAL PITCH ANGLE DISTRIBUTION
EQUATORIAL DIFFERENTIAL FLUX
+ DAY 522-522 1966
POLYNOMIAL
EQUATORIAL PITCH ANGLE
OV3-3 E=1490 L=2.10

Figure 33

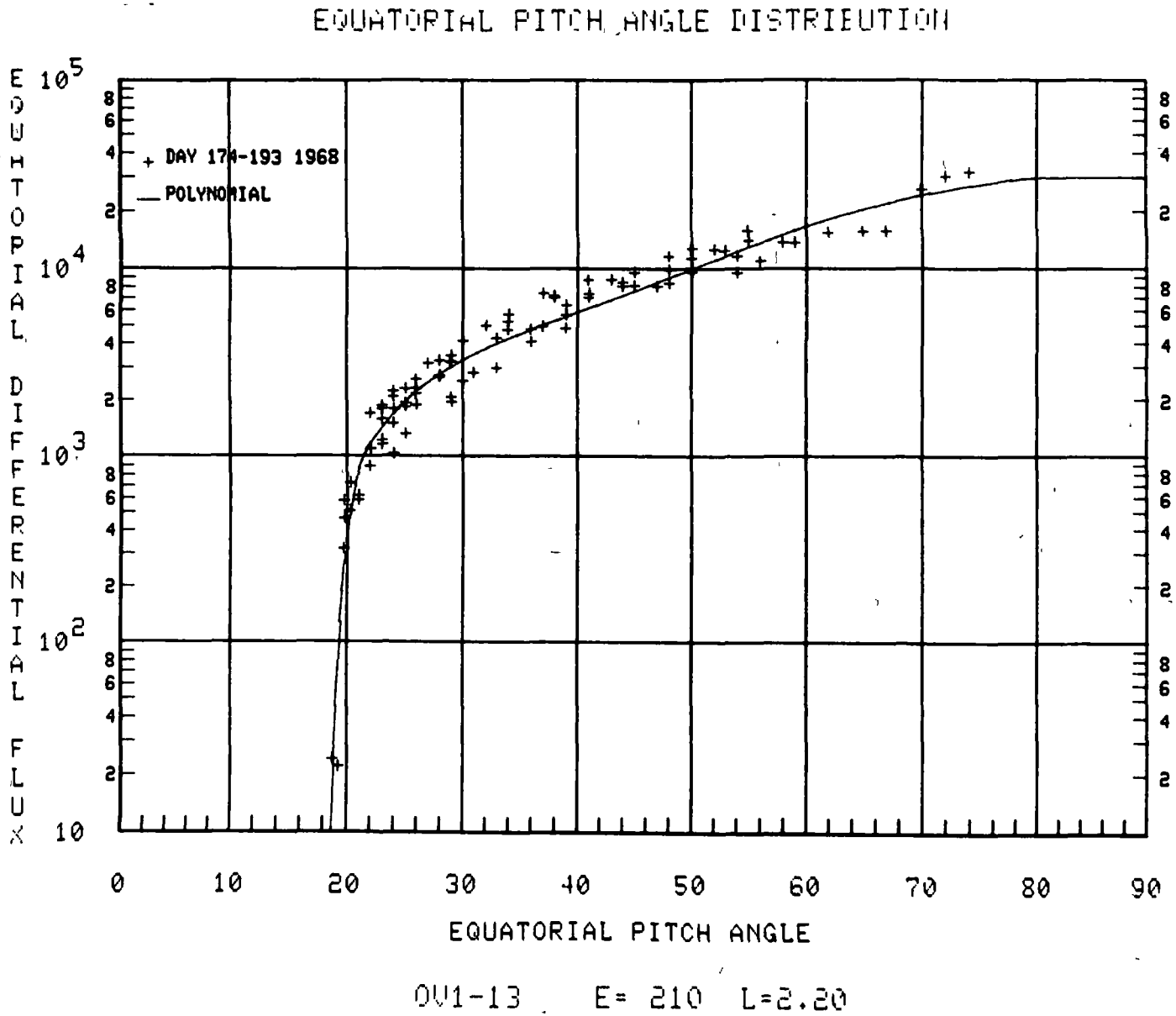
EQUATORIAL PITCH ANGLE DISTRIBUTION
EQUATORIAL DIFFERENTIAL FLUX
+ DAY 174-193 1968
— POLYNOMIAL
10^5
10^4
10^3
10^2
10
0
10
20
30
40
50
60
70
80
90
EQUATORIAL PITCH ANGLE
OV1-13 E= 210 L=2.20

Figure 34

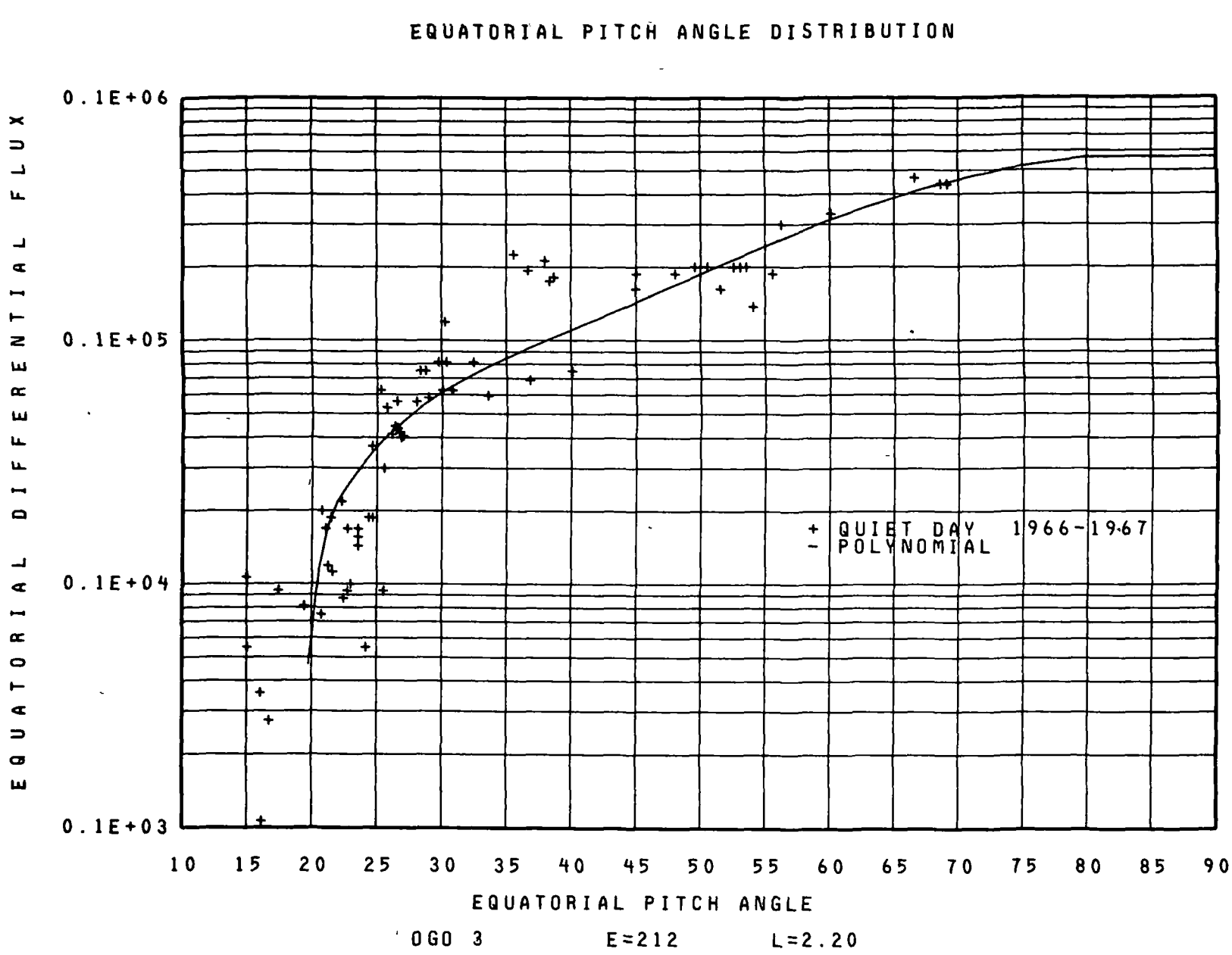
EQUATORIAL PITCH ANGLE DISTRIBUTION
EQUATORIAL DIFFERENTIAL FLUX
0.1E+06
0.1E+05
0.1E+04
0.1E+03
10 15 20 25 30 35 40 45 50 55 60 65 70 75 80 85 90
EQUATORIAL PITCH ANGLE
+ QUIET DAY 1966-1967
- POLYNOMIAL
OGO 3 E=212 L=2.20

Figure 35

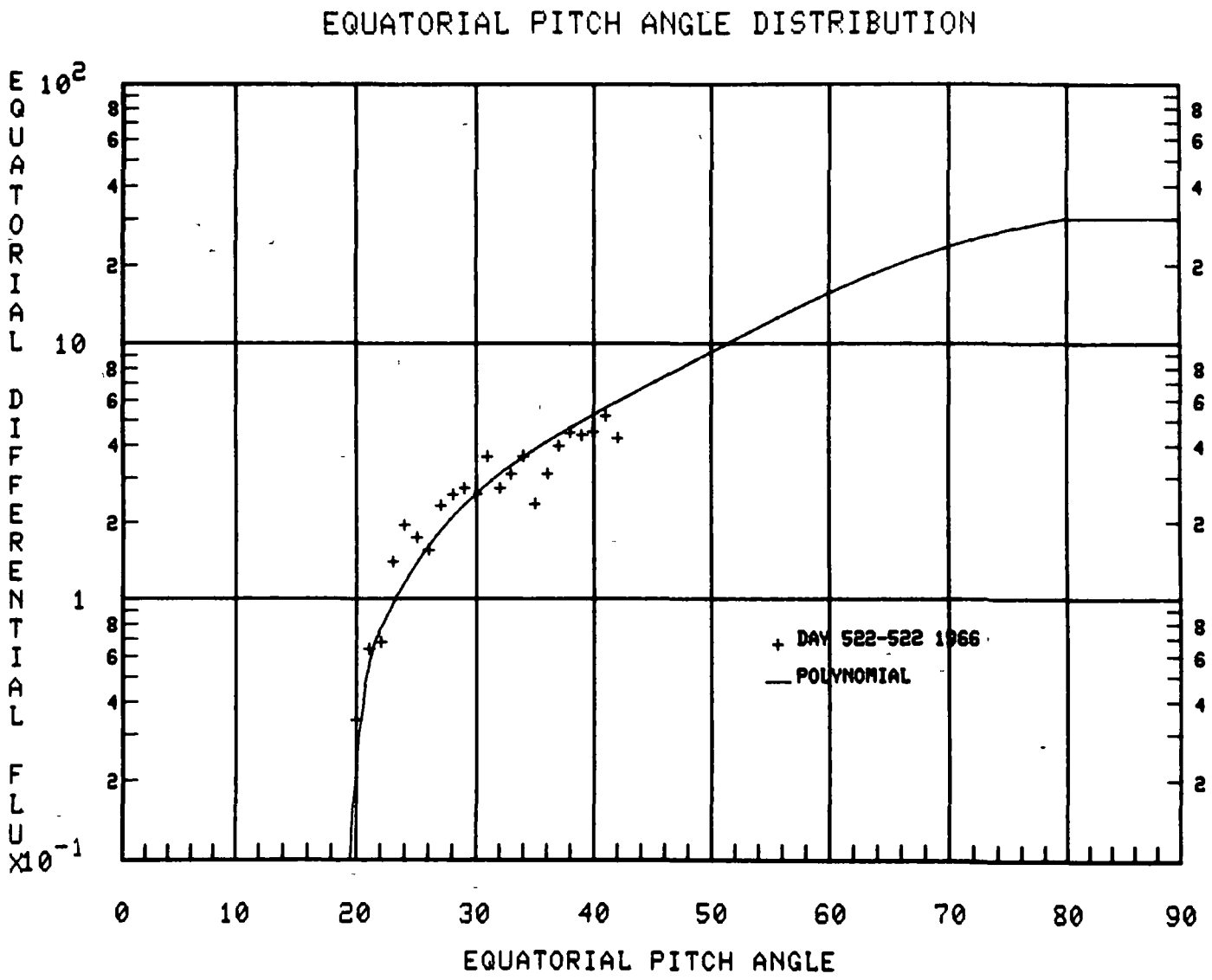
EQUATORIAL PITCH ANGLE DISTRIBUTION
EQUATORIAL DIFFERENTIAL FLUX
X10^2
10
1
X10^-1
8
6
4
2
0
10
20
30
40
50
60
70
80
90
EQUATORIAL PITCH ANGLE
+ DAY 522-522 1966
POLYNOMIAL
OV3-3 E=1770 L=2.20

Figure 36

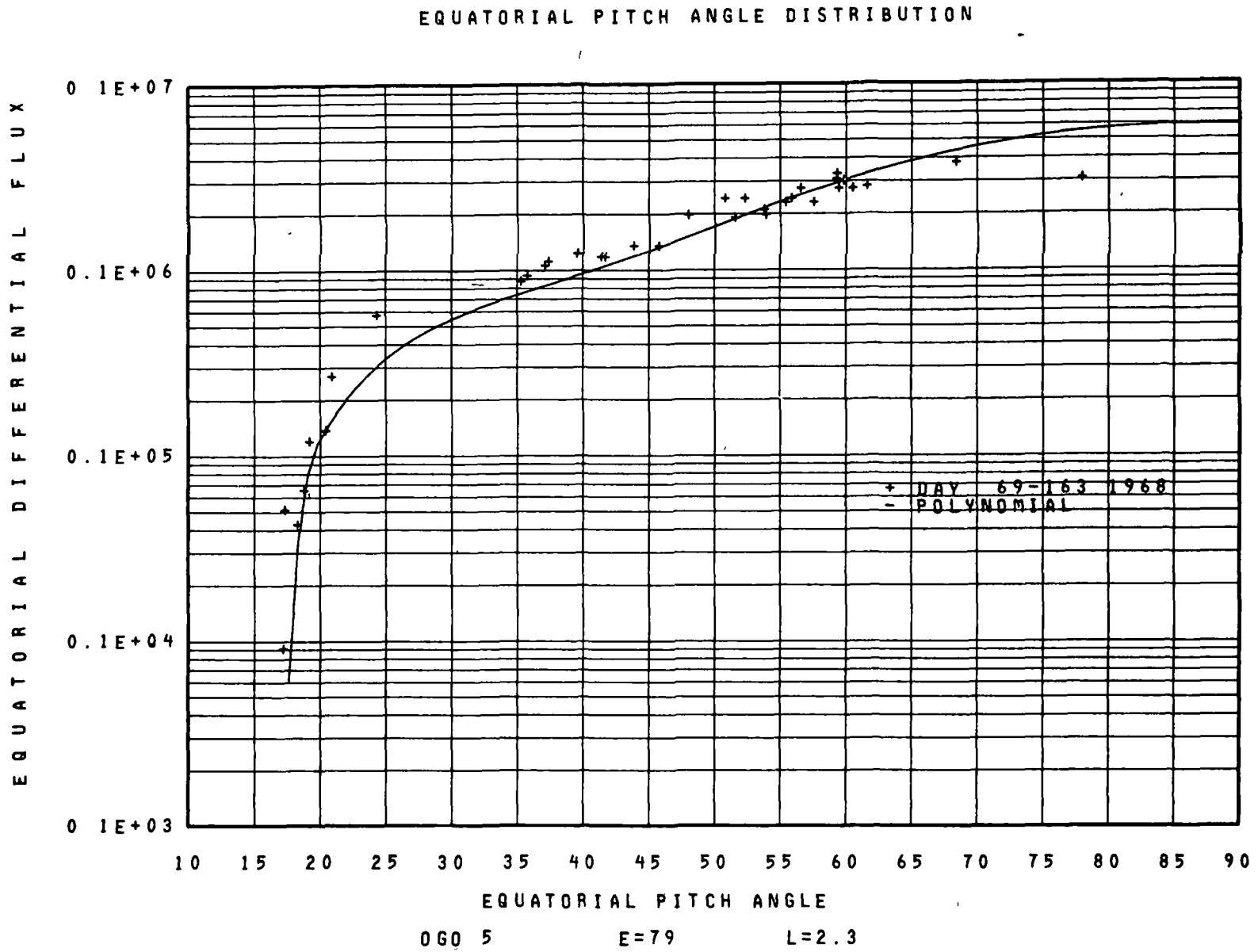
EQUATORIAL PITCH ANGLE DISTRIBUTION
EQUATORIAL DIFFERENTIAL FLUX
0 1E+07
0.1E+06
0.1E+05
0.1E+04
0 1E+03
10 15 20 25 30 35 40 45 50 55 60 65 70 75 80 85 90
EQUATORIAL PITCH ANGLE
+ DAY 69-163 1968
- POLYNOMIAL
OGO 5 E=79 L=2.3

Figure 37

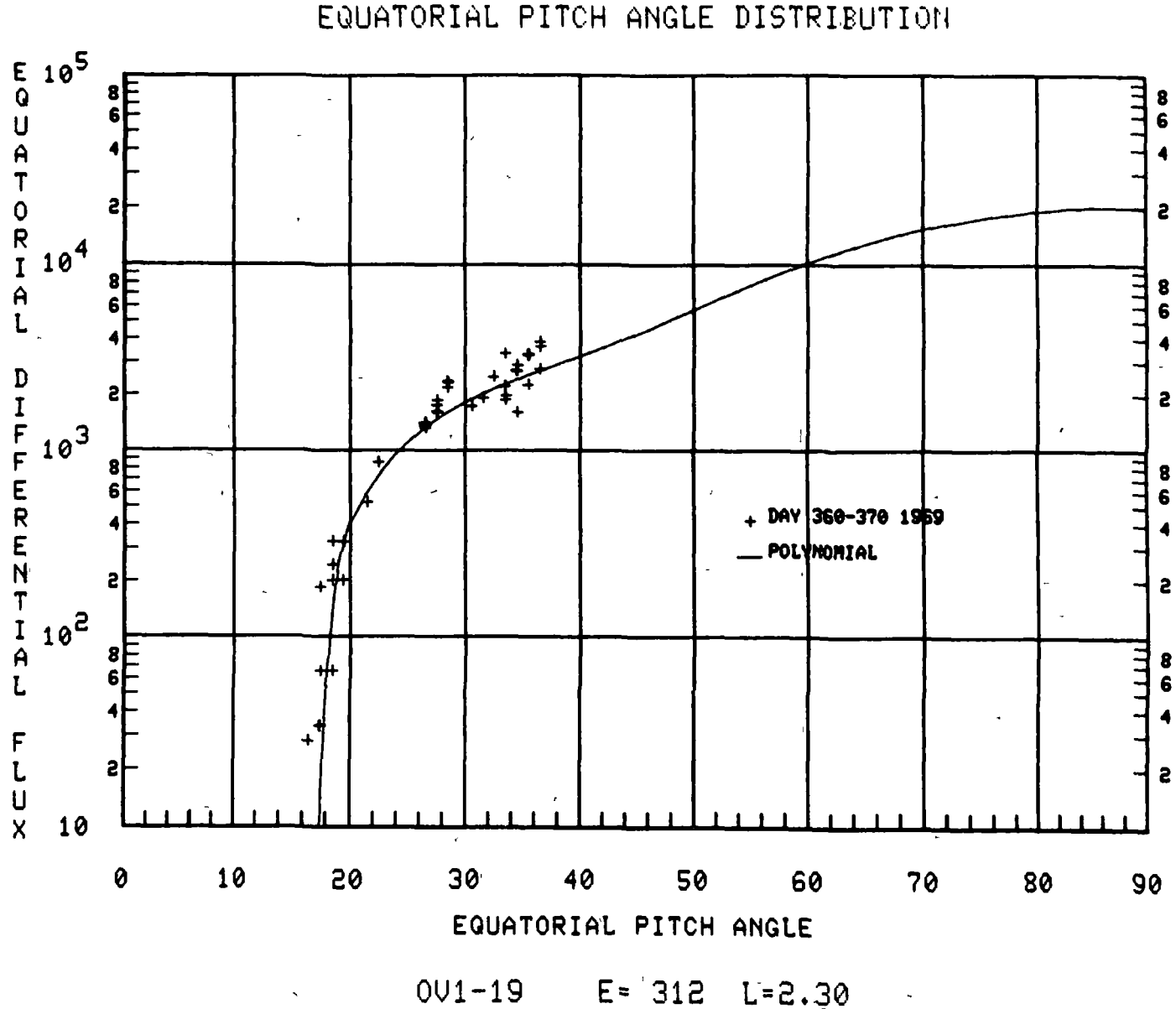
EQUATORIAL PITCH ANGLE DISTRIBUTION
EQUATORIAL DIFFERENTIAL FLUX
10^5
10^4
10^3
10^2
10
+ DAY 360-370 1969
POLYNOMIAL
0
10
20
30
40
50
60
70
80
90
EQUATORIAL PITCH ANGLE
OV1-19 E= 312 L=2.30

Figure 38

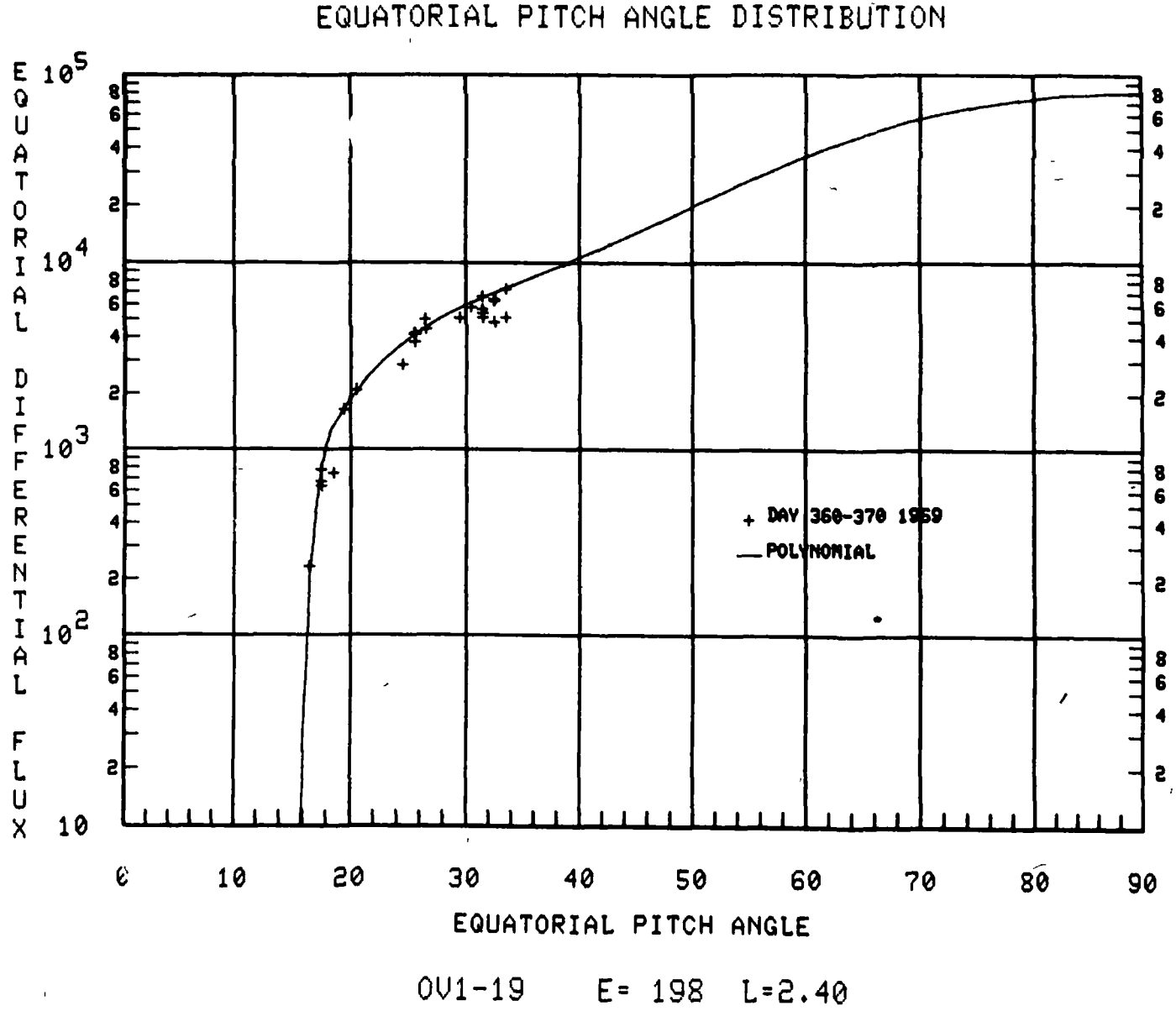
EQUATORIAL PITCH ANGLE DISTRIBUTION
EQUATORIAL DIFFERENTIAL FLUX
10^5
10^4
10^3
10^2
10
8
6
4
2
0
10
20
30
40
50
60
70
80
90
+ DAY 360-370 1969
POLYNOMIAL
EQUATORIAL PITCH ANGLE
OV1-19 E= 198 L=2.40

Figure 39

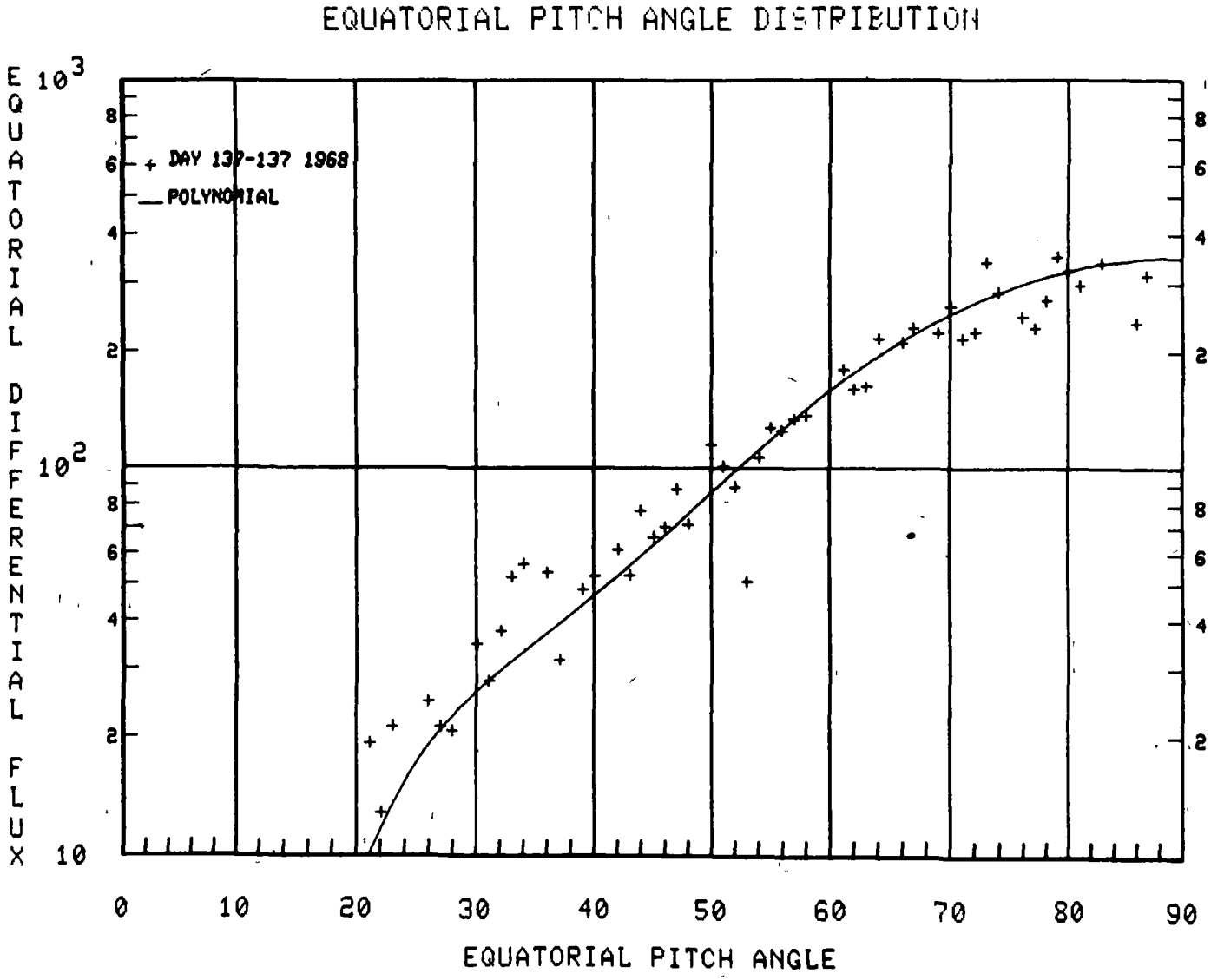
EQUATORIAL PITCH ANGLE DISTRIBUTION
EQUATORIAL DIFFERENTIAL FLUX
10^3
10^2
10
+ DAY 137-137 1968
POLYNOMIAL
0
10
20
30
40
50
60
70
80
90
EQUATORIAL PITCH ANGLE
OV1-13 E= 500 L=2.40

Figure 40

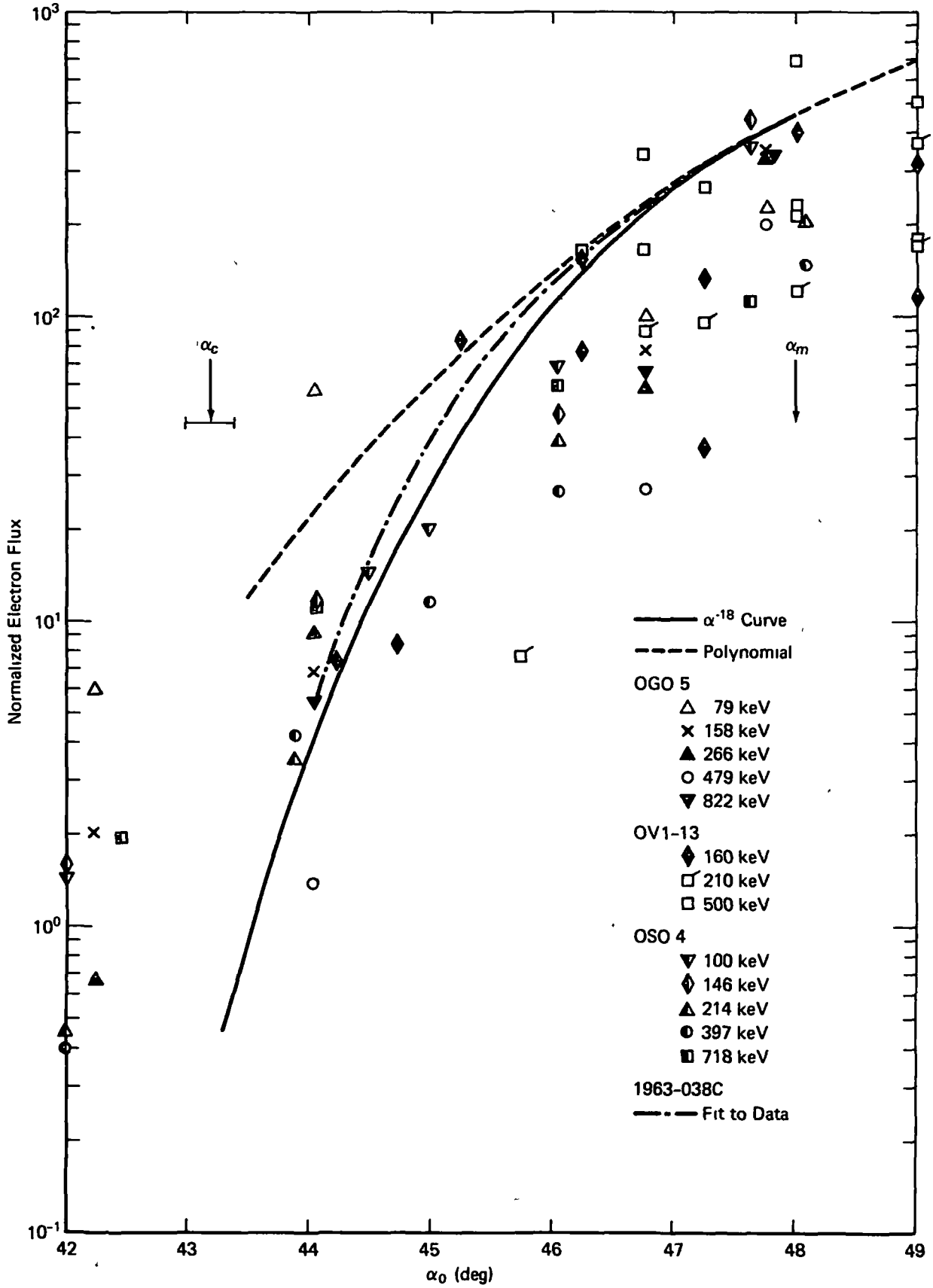

Figure 41. Normalized Low Pitch Angle Data at L = 1.4

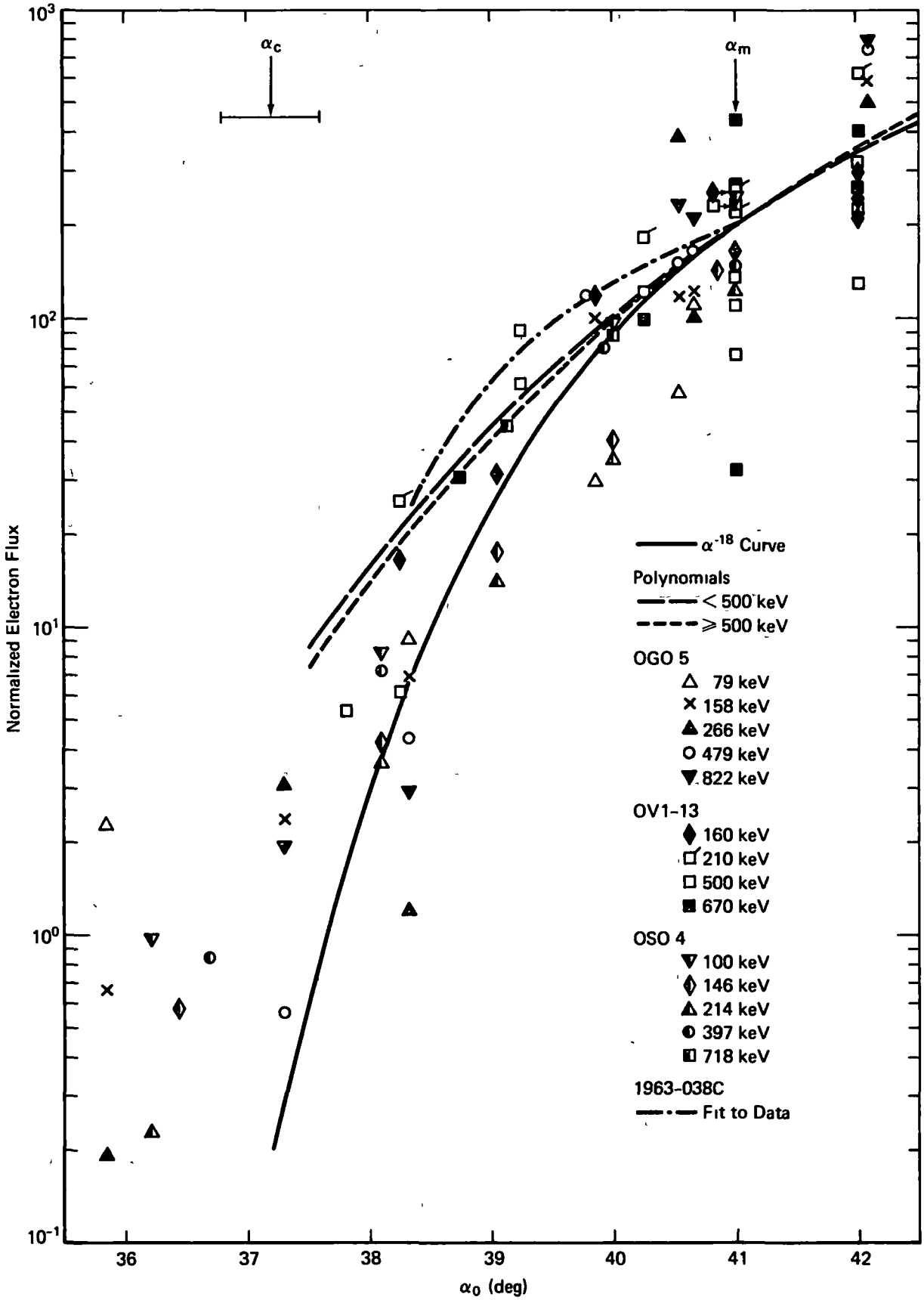

Figure 42. Normalized Low Pitch Angle Data at L = 1.5

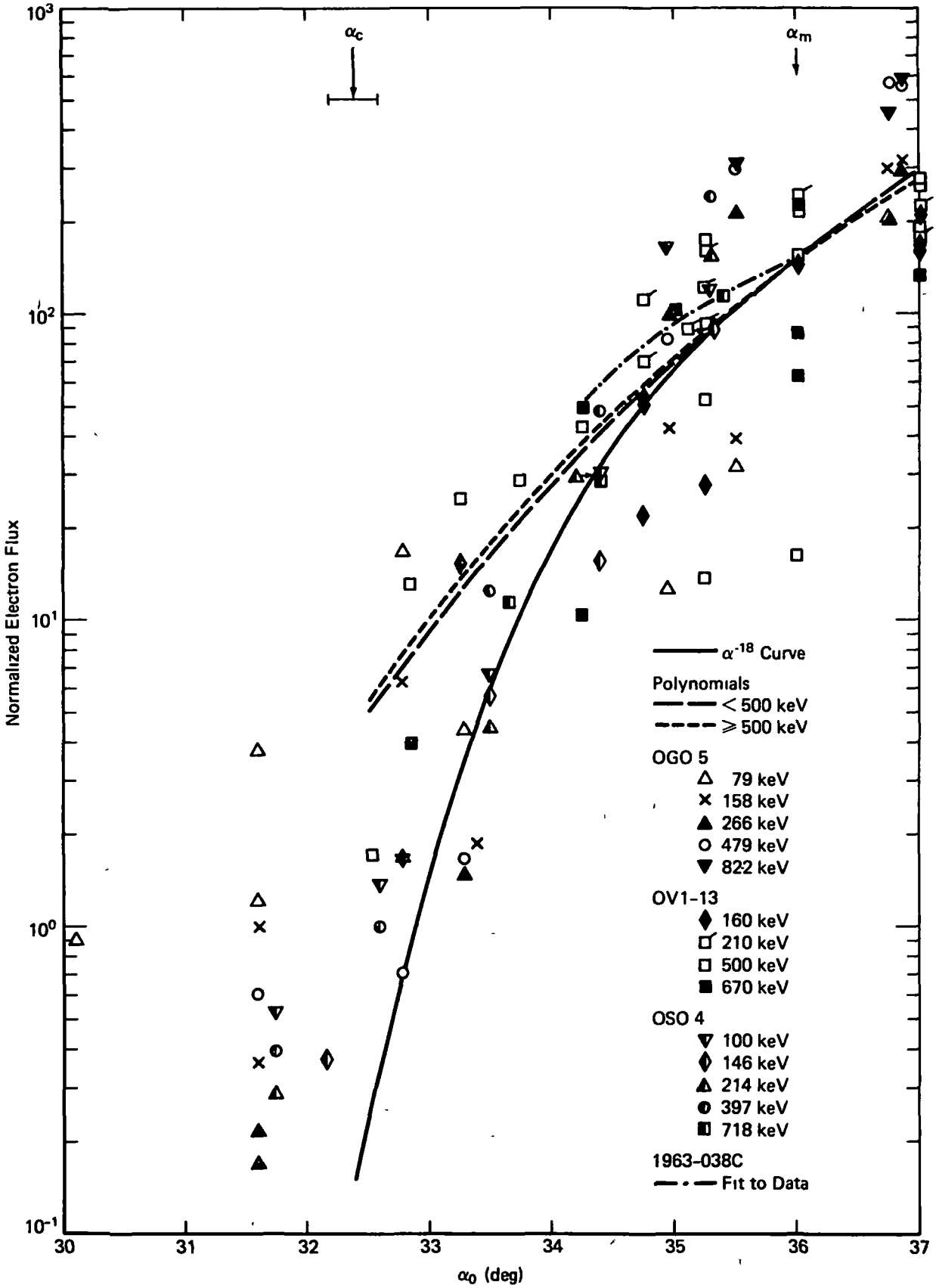

Figure 43. Normalized Low Pitch Angle Data at L = 1.6

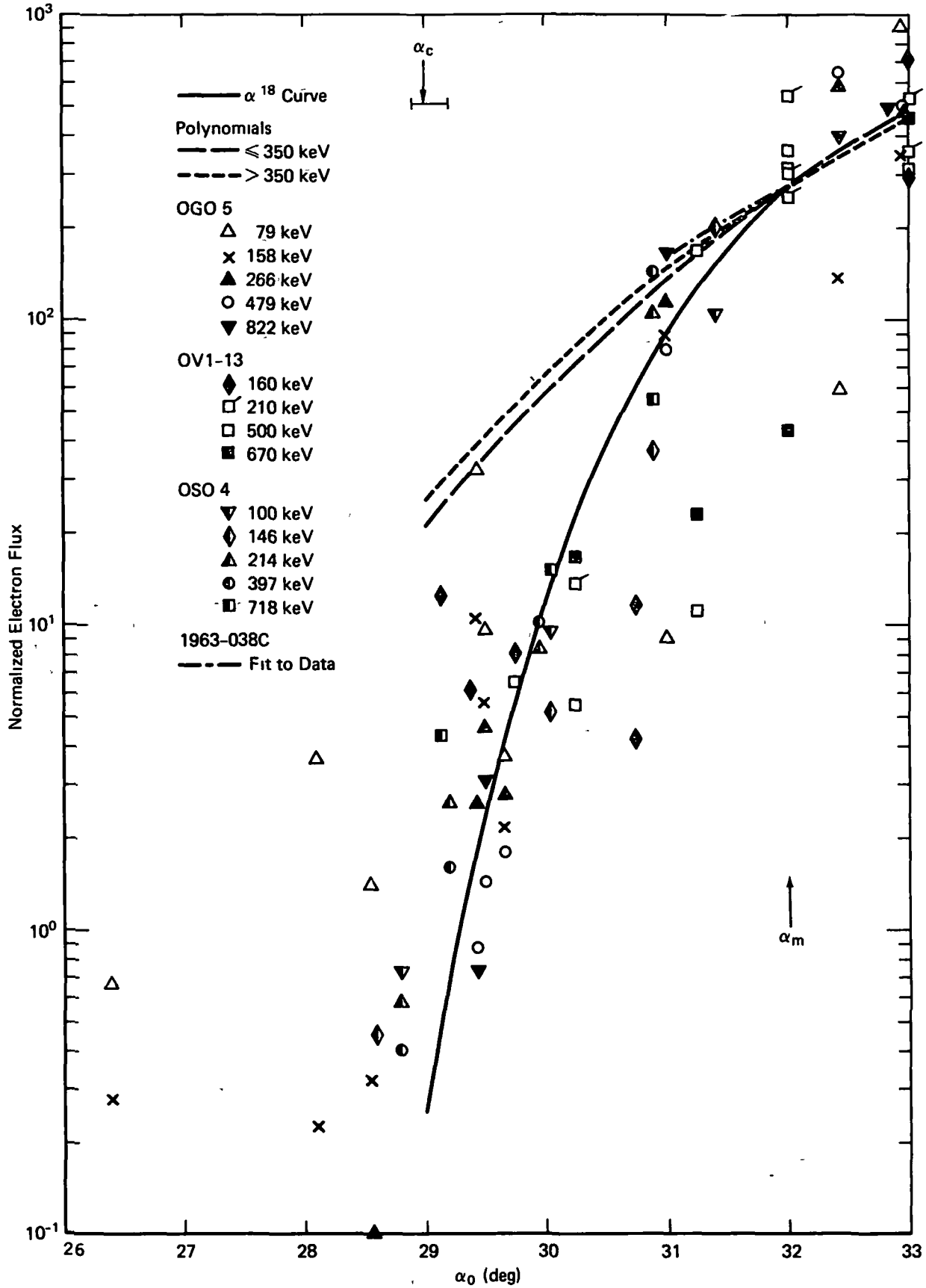

Figure 44. Normalized Low Pitch Angle Data at L = 1.7

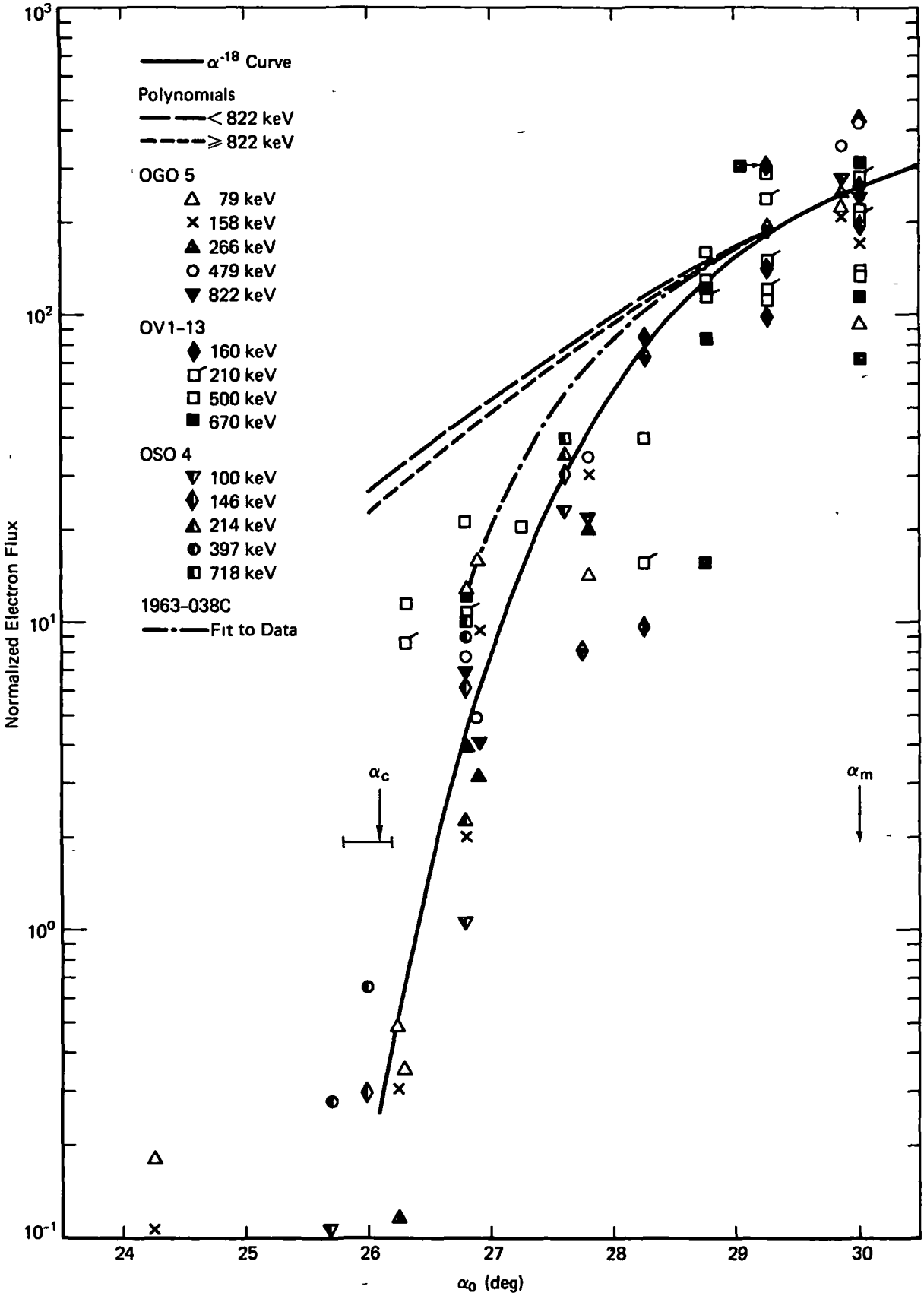

Figure 45. Normalized Low Pitch Angle Data at L = 1.8

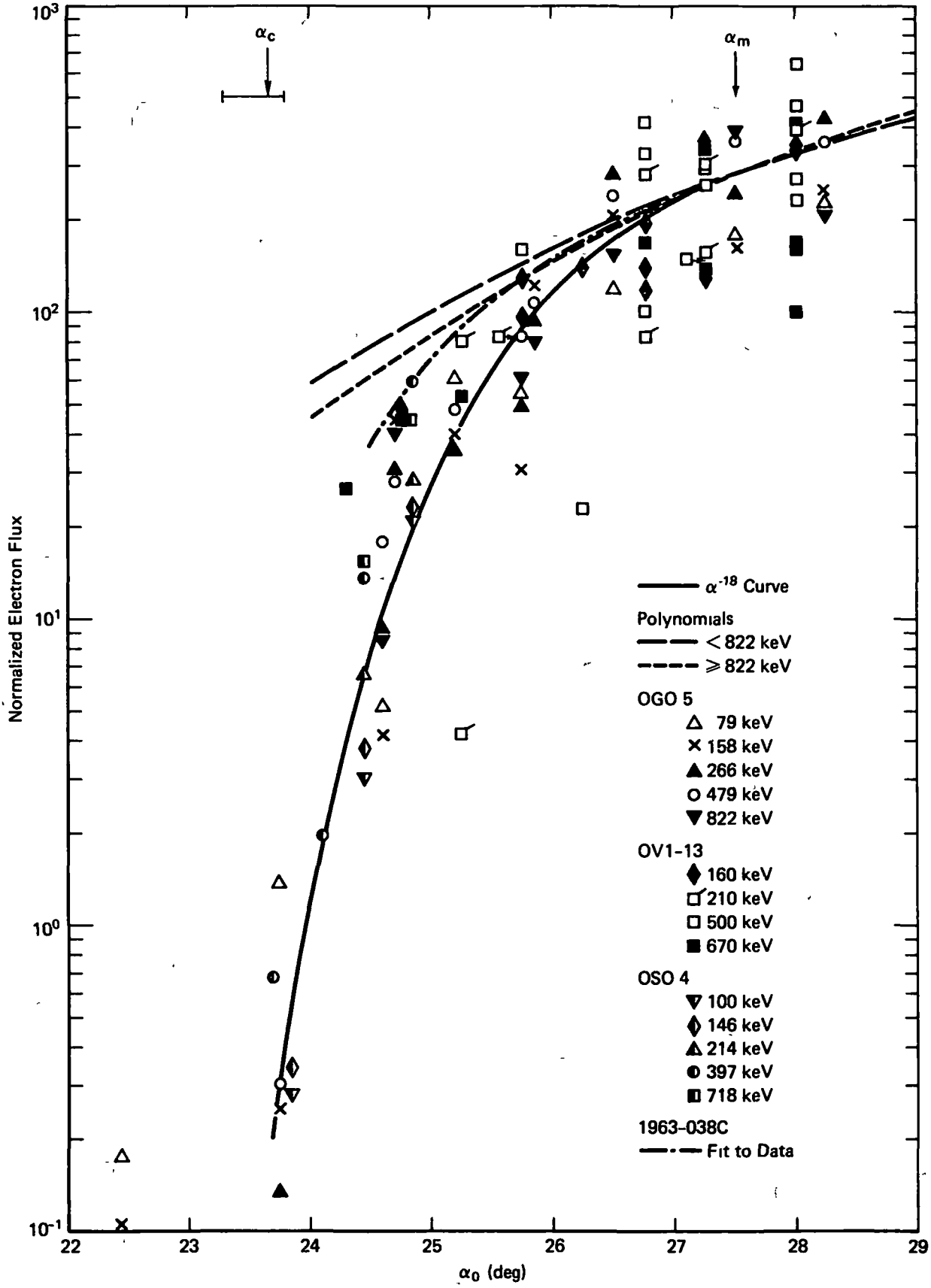

Figure 46. Normalized Low Pitch Angle Data at L = 1.9

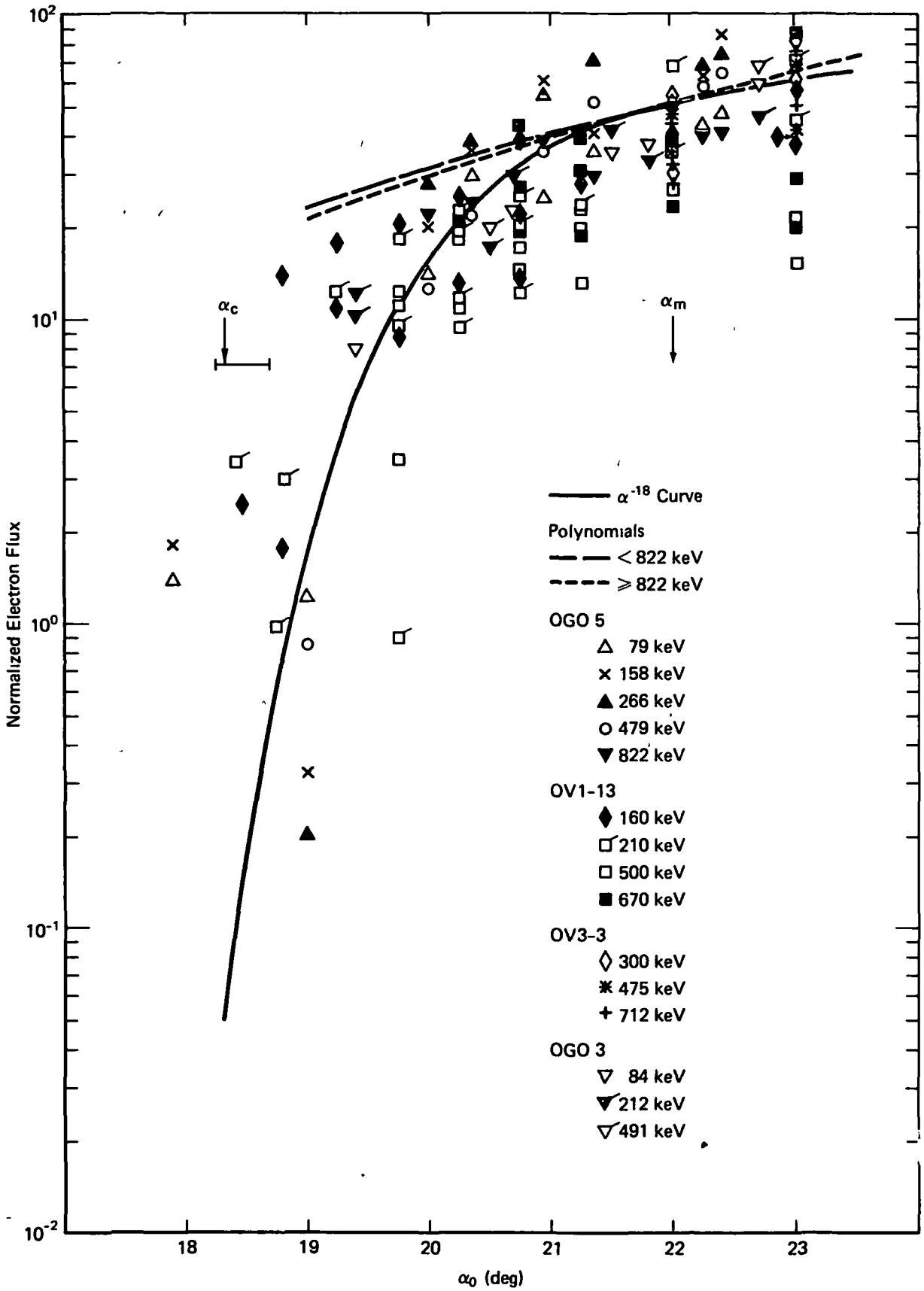

Figure 47. Normalized Low Pitch Angle Data at L = 2.2

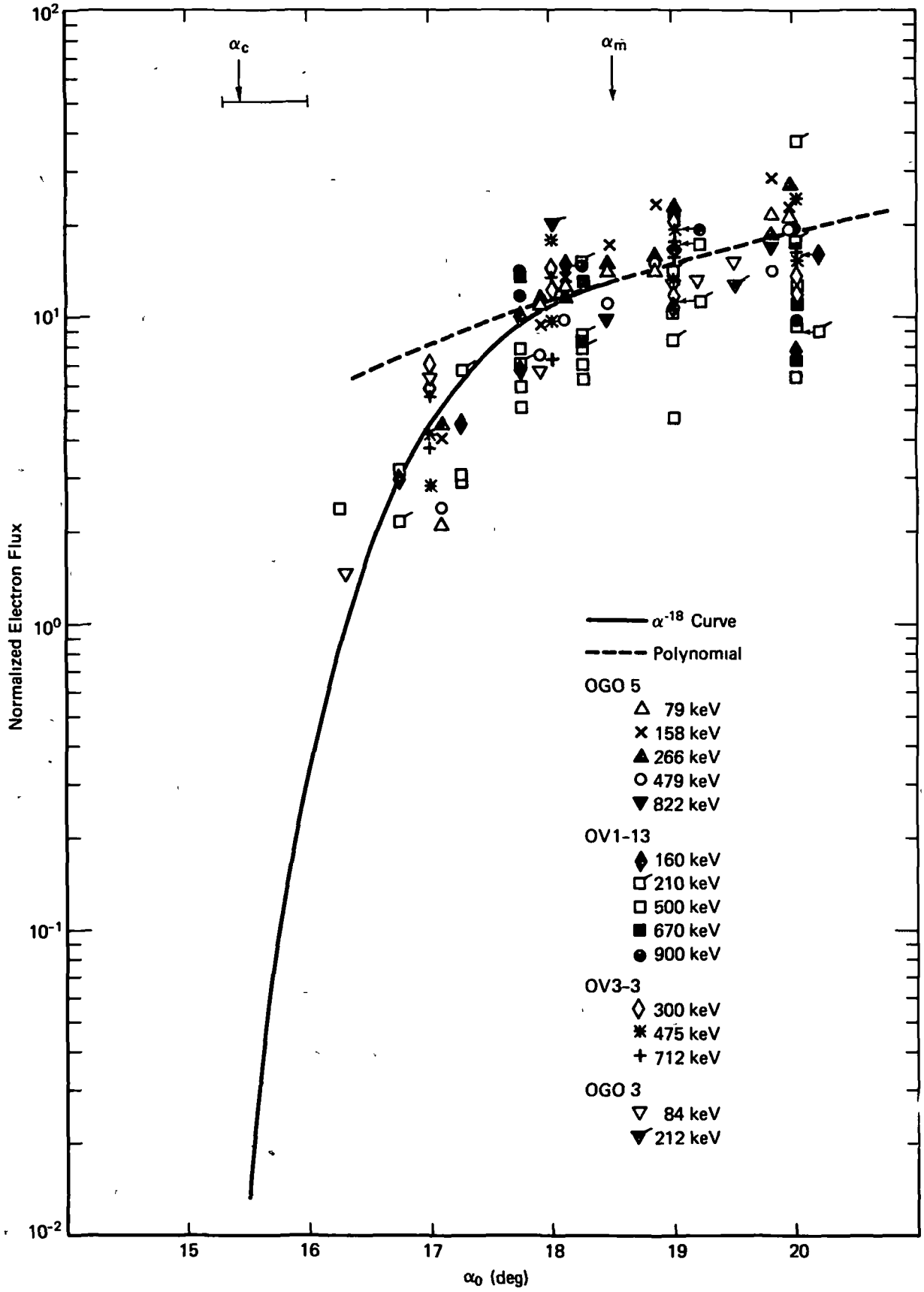

Figure 48. Normalized Low Pitch Angle Data at L = 2.4

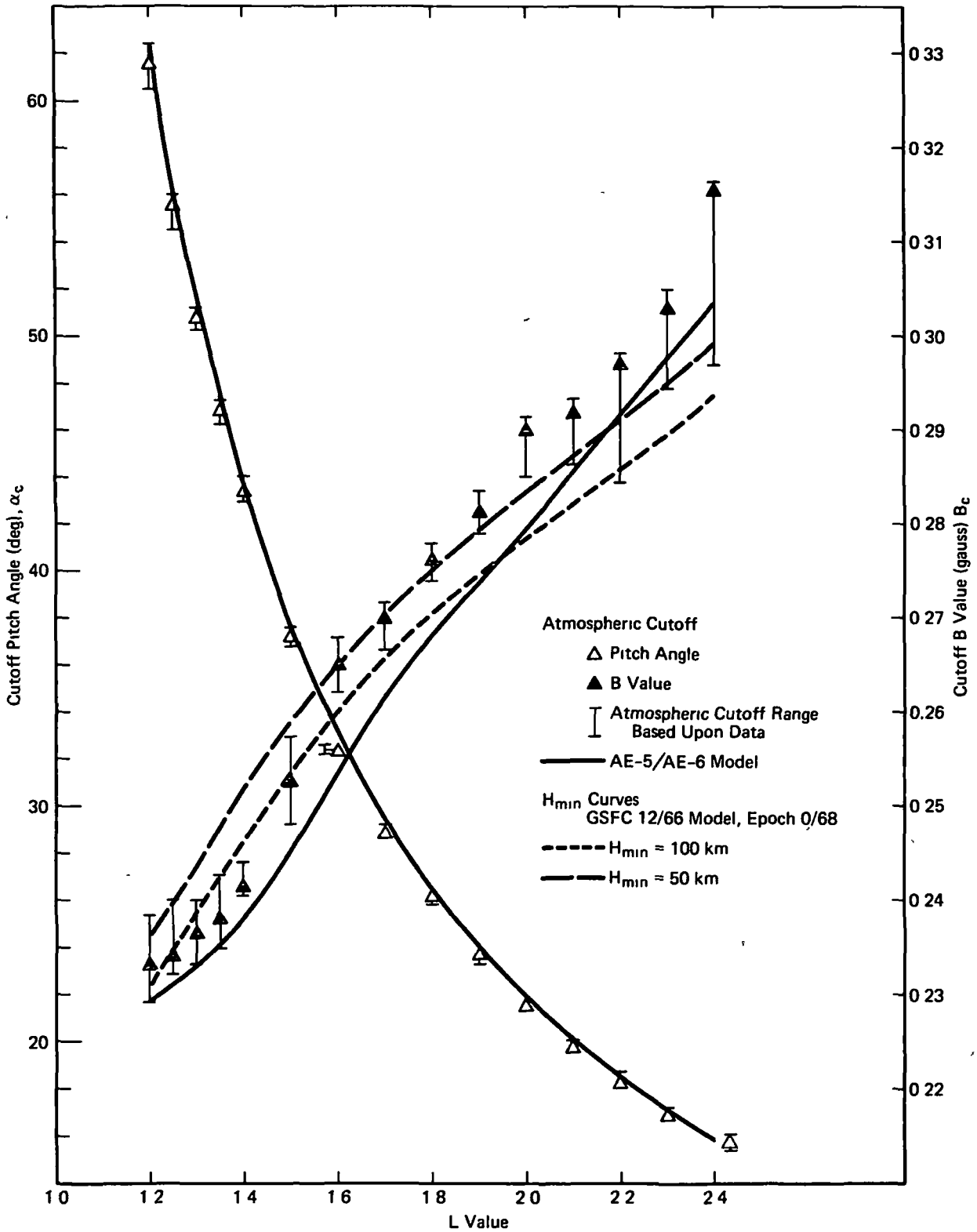

Figure 49. Atmospheric Cutoff Values

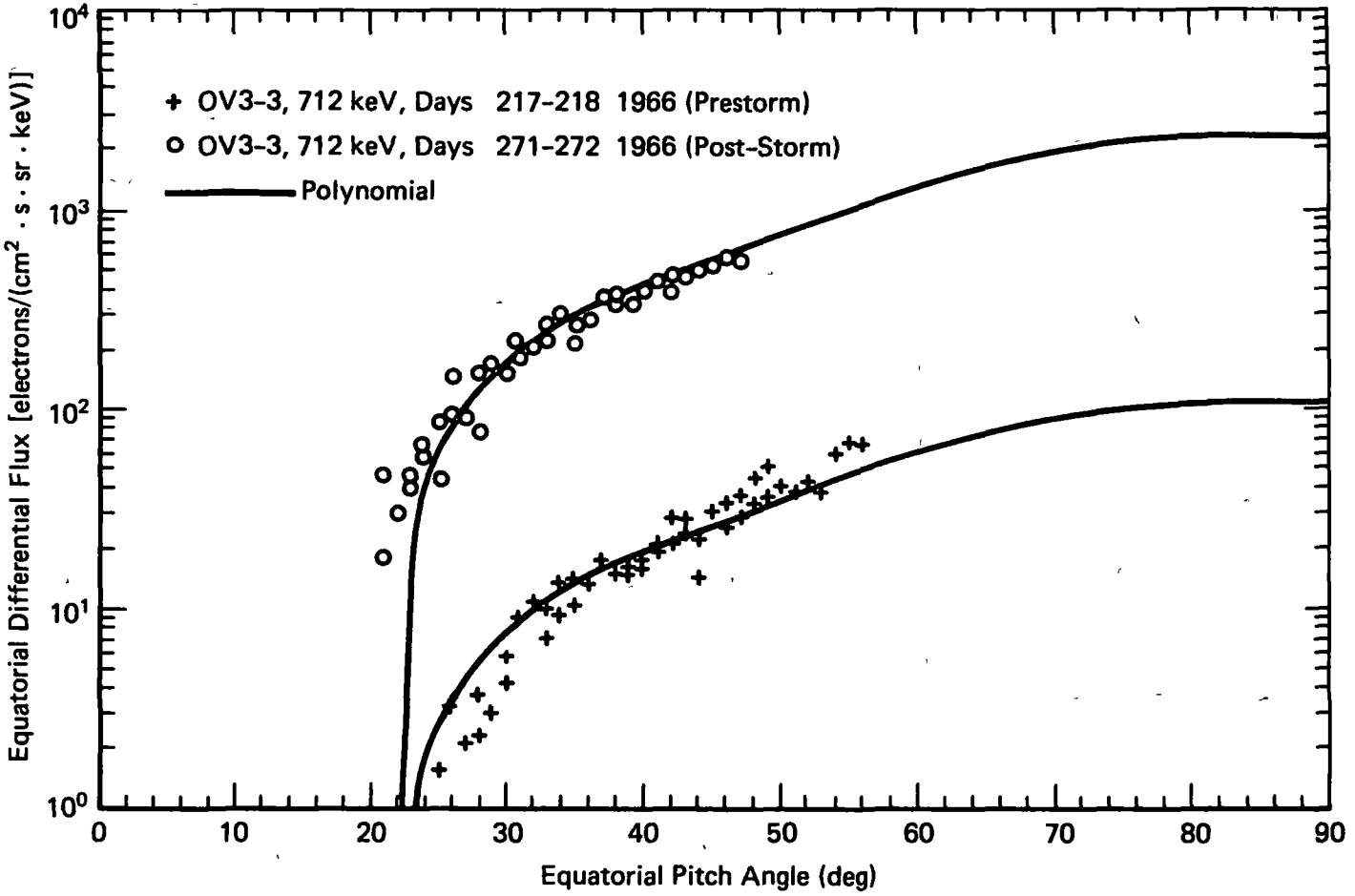

Figure 50. Comparison of Storm and Quiet Time Pitch Angle Distributions at L = 2.0

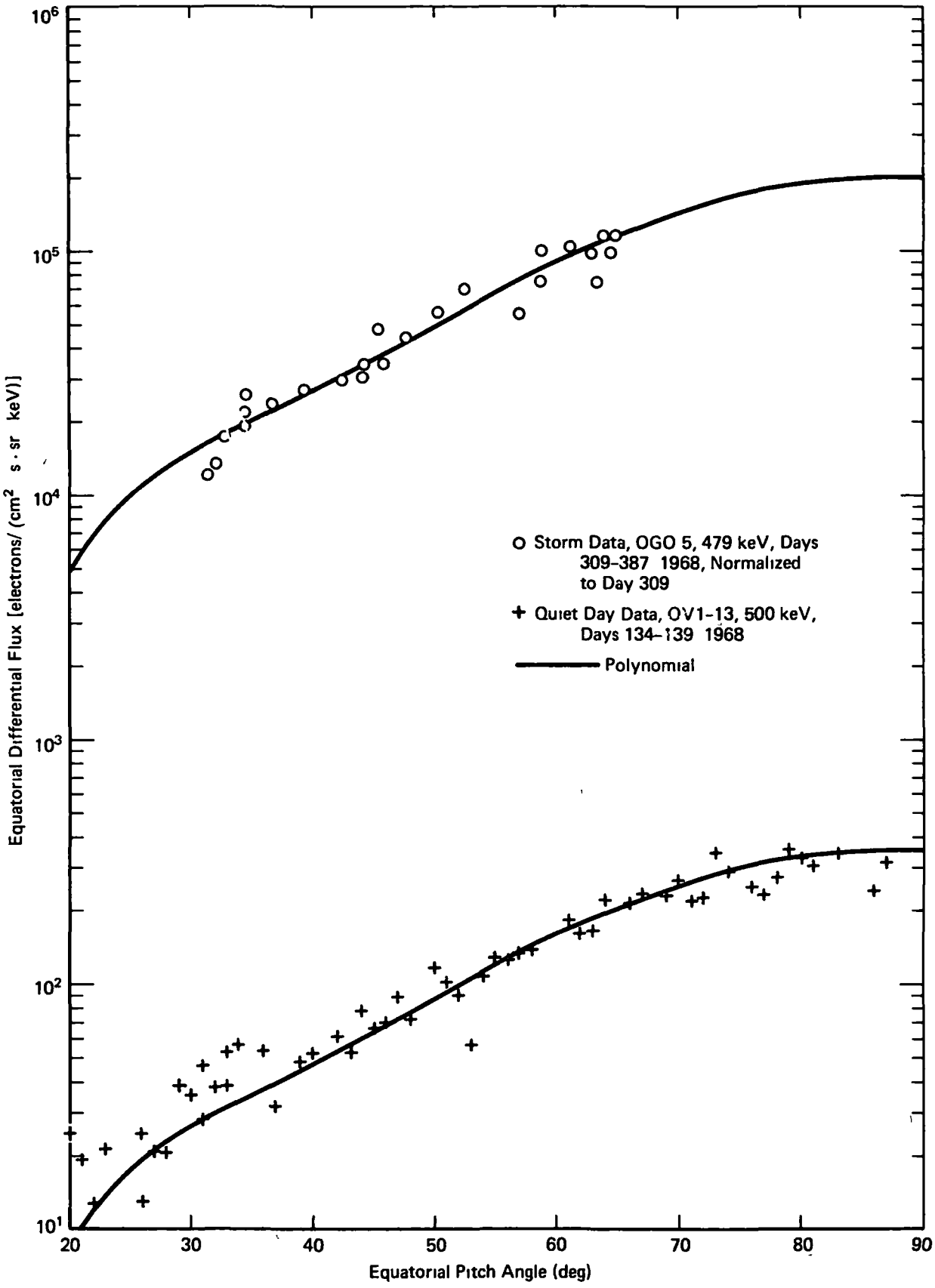

Figure 51. Comparison of Storm and Quiet Time Pitch Angle Distributions at L = 2.4

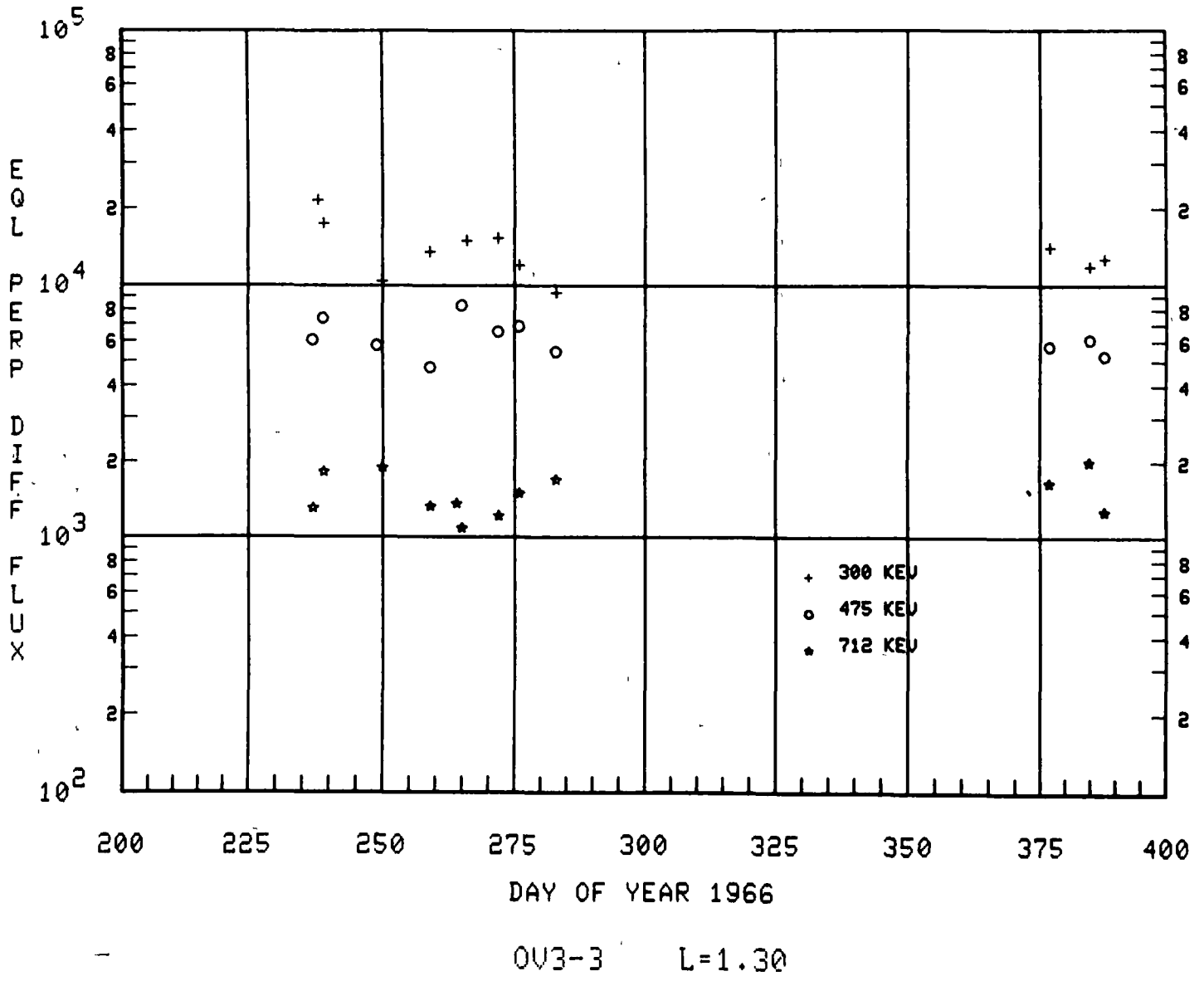
FLUX VERSUS TIME
EQL PERP DIFF FLUX
10^5
10^4
10^3
10^2
8
6
4
2
300 KEV
475 KEV
712 KEV
200
225
250
275
300
325
350
375
400
DAY OF YEAR 1966
OV3-3 L=1.30

Figure 52

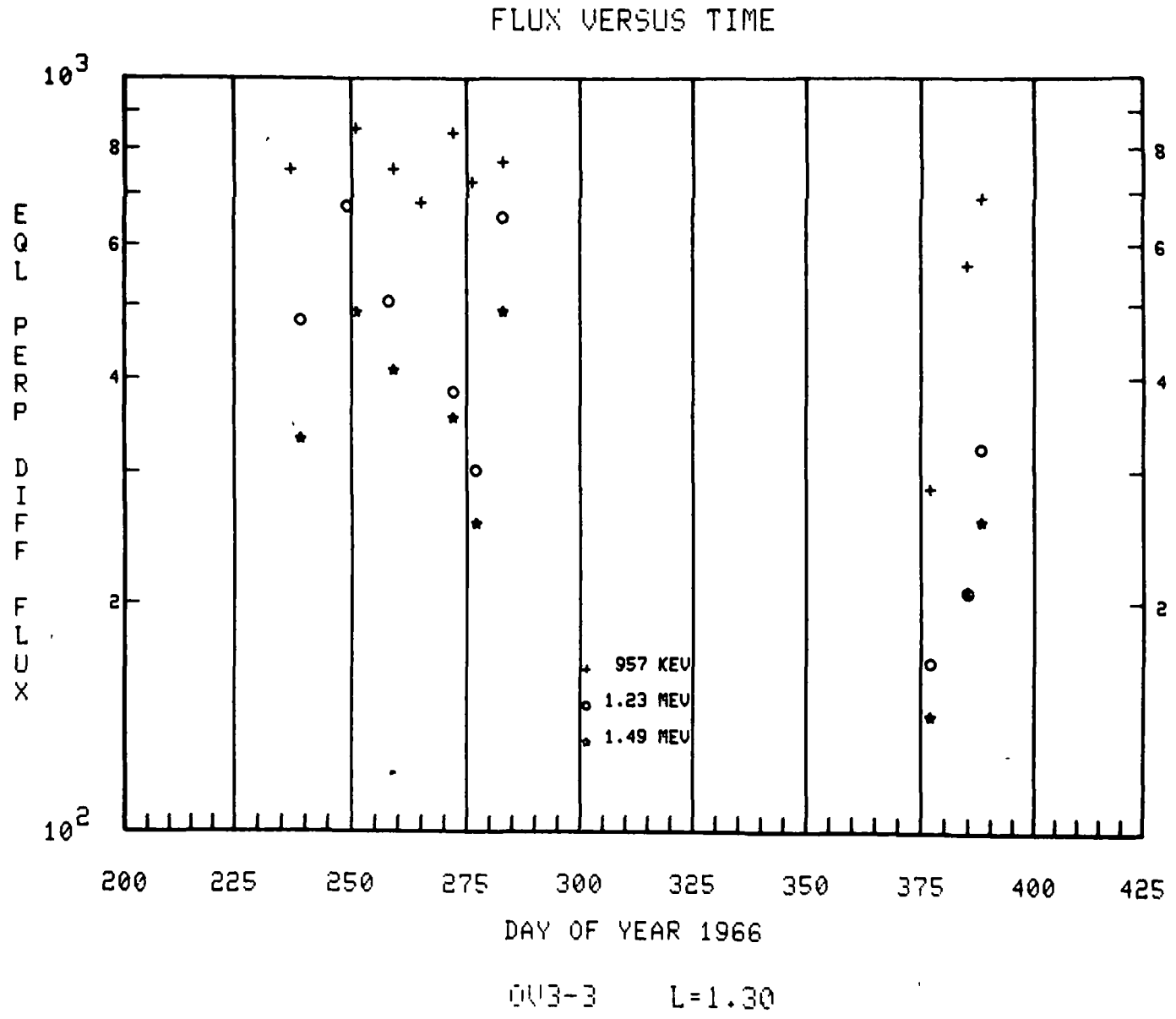

Figure 52 (concluded)

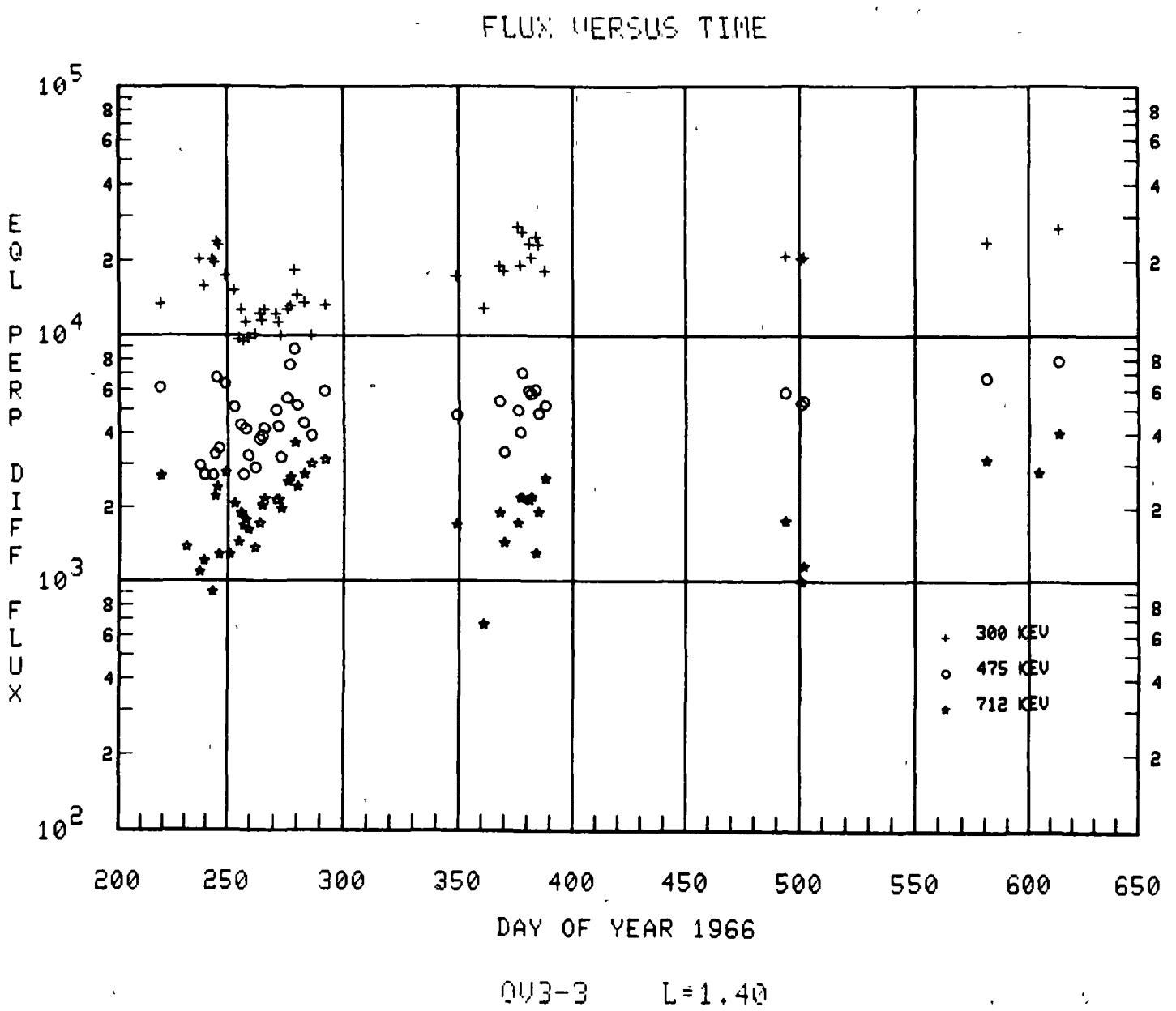
FLUX VERSUS TIME
EQ PERP DIF FLUX
10^5
10^4
10^3
10^2
8
6
4
2
200
250
300
350
400
450
500
550
600
650
DAY OF YEAR 1966
300 KEV
475 KEV
712 KEV
QV3-3 L=1.40

Figure 53

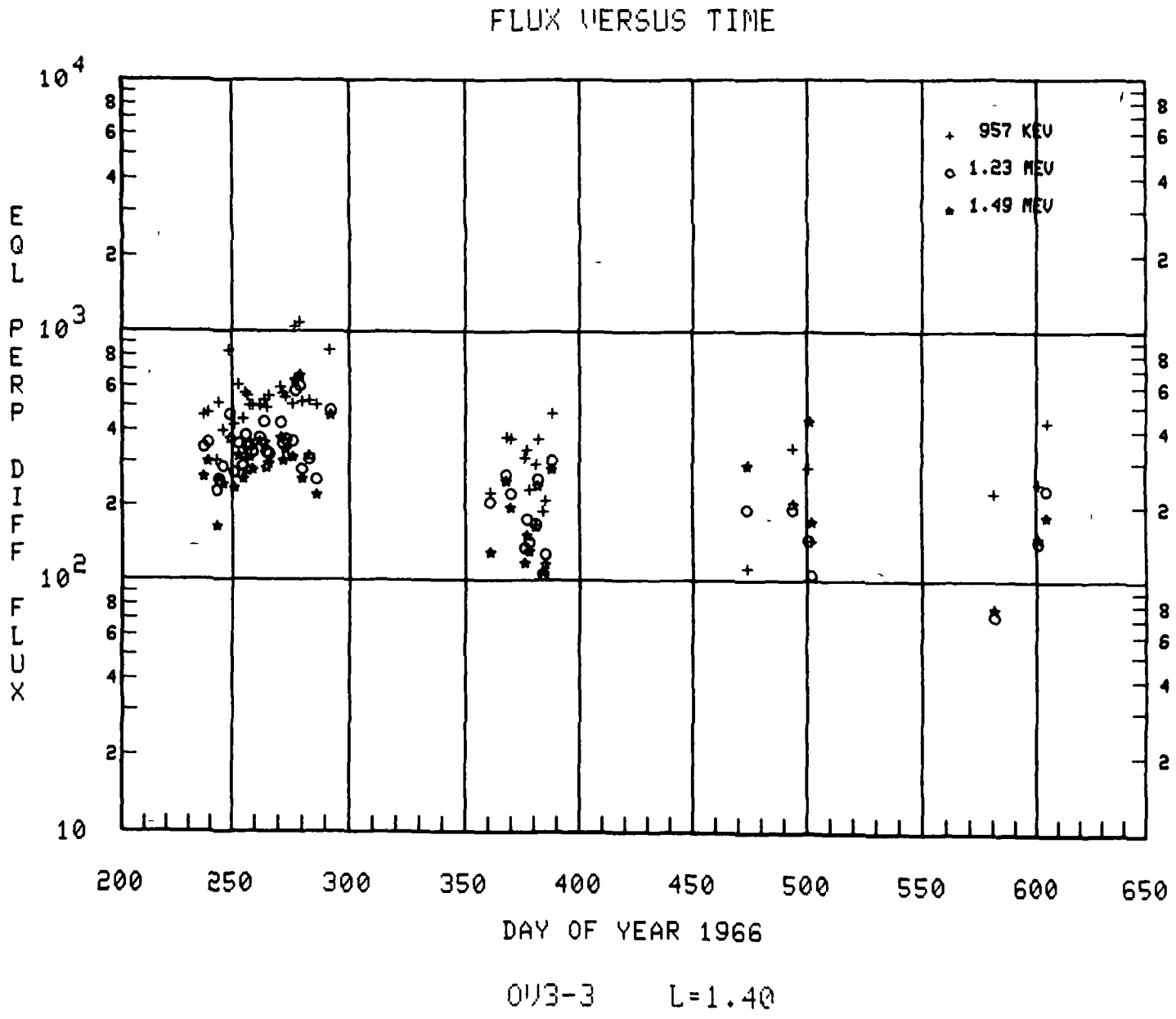

Figure 53 (concluded)

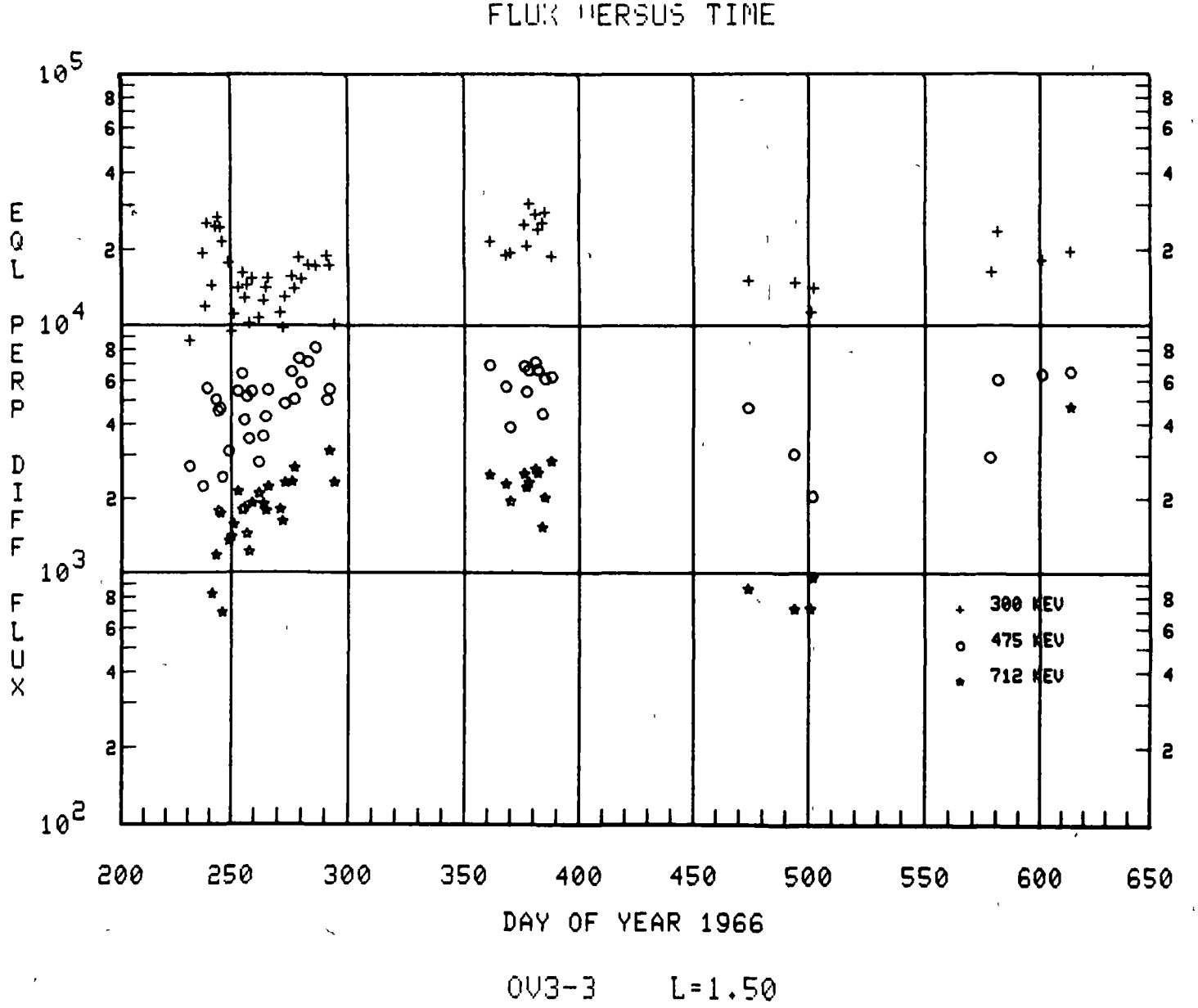
FLUX VERSUS TIME
EQL PERP DIF FLUX
DAY OF YEAR 1966
300 KEV
475 KEV
712 KEV
OV3-3 L=1.50

Figure 54

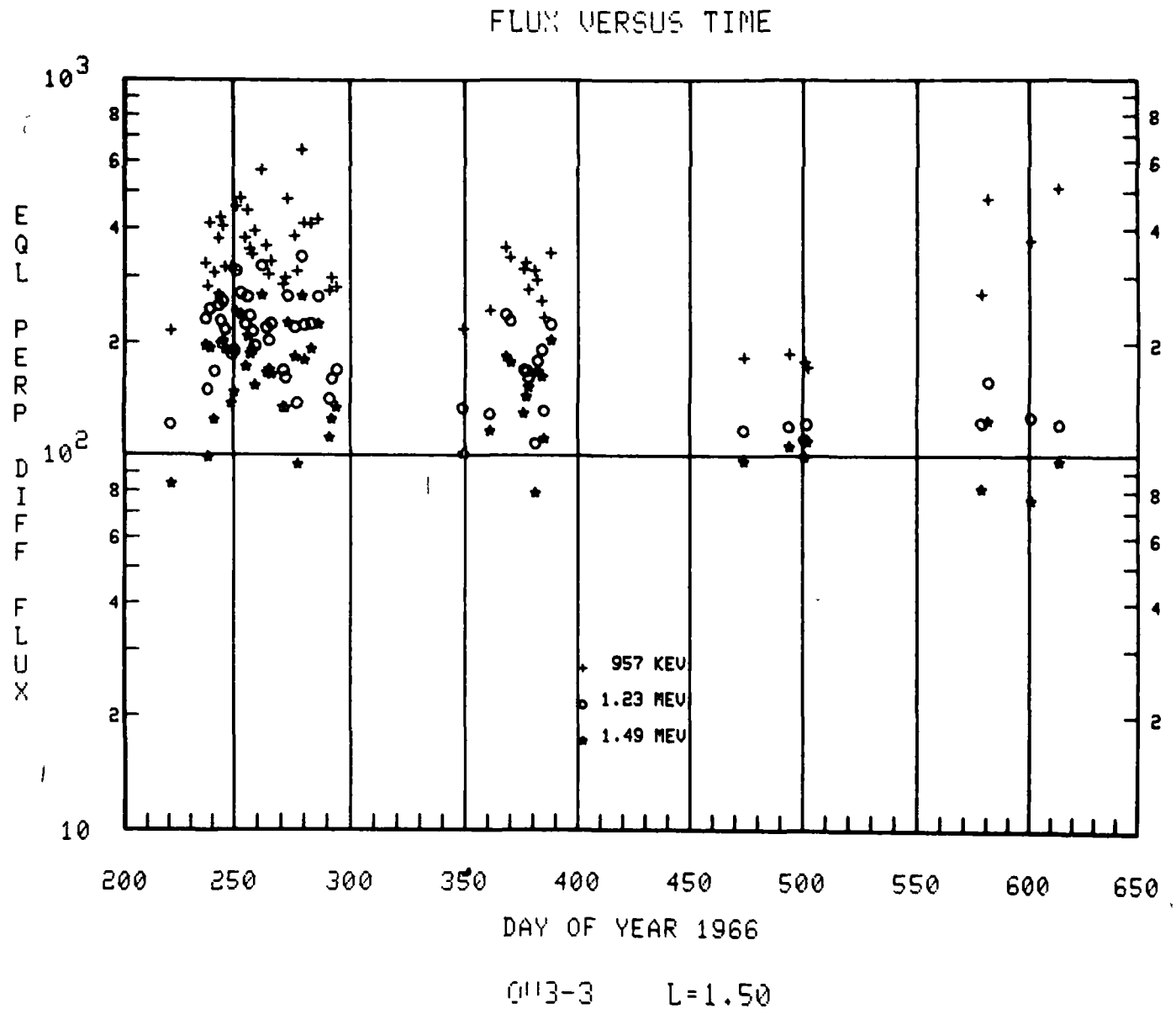

Figure 54 (concluded)

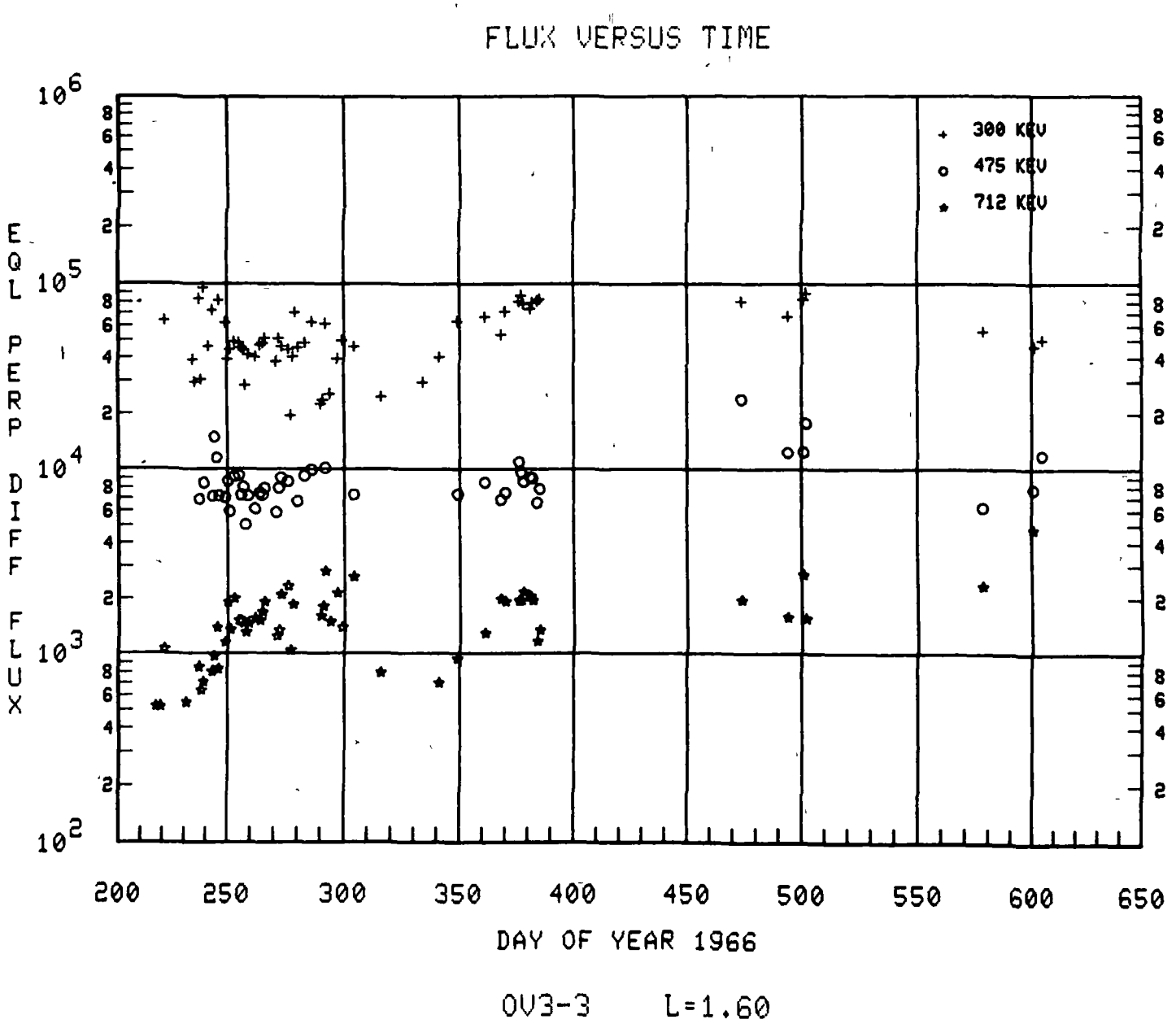
FLUX VERSUS TIME
300 KEV
475 KEV
712 KEV
EQL PERP DIFF FLUX
DAY OF YEAR 1966
OV3-3 L=1.60

Figure 55

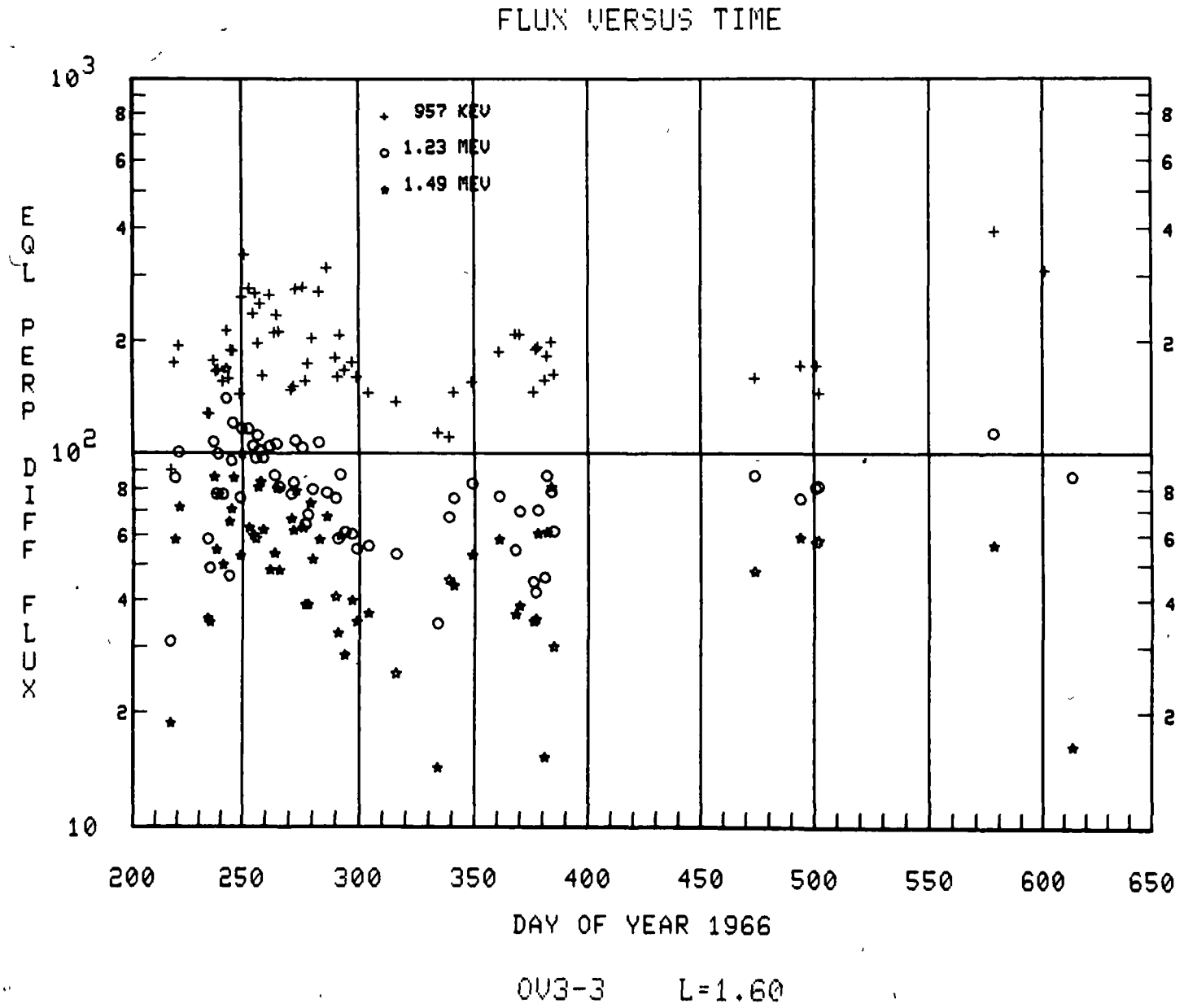
FLUX VERSUS TIME
957 KEV
1.23 MEV
1.49 MEV
EQL PERP DIFF FLUX
DAY OF YEAR 1966
OV3-3 L=1.60

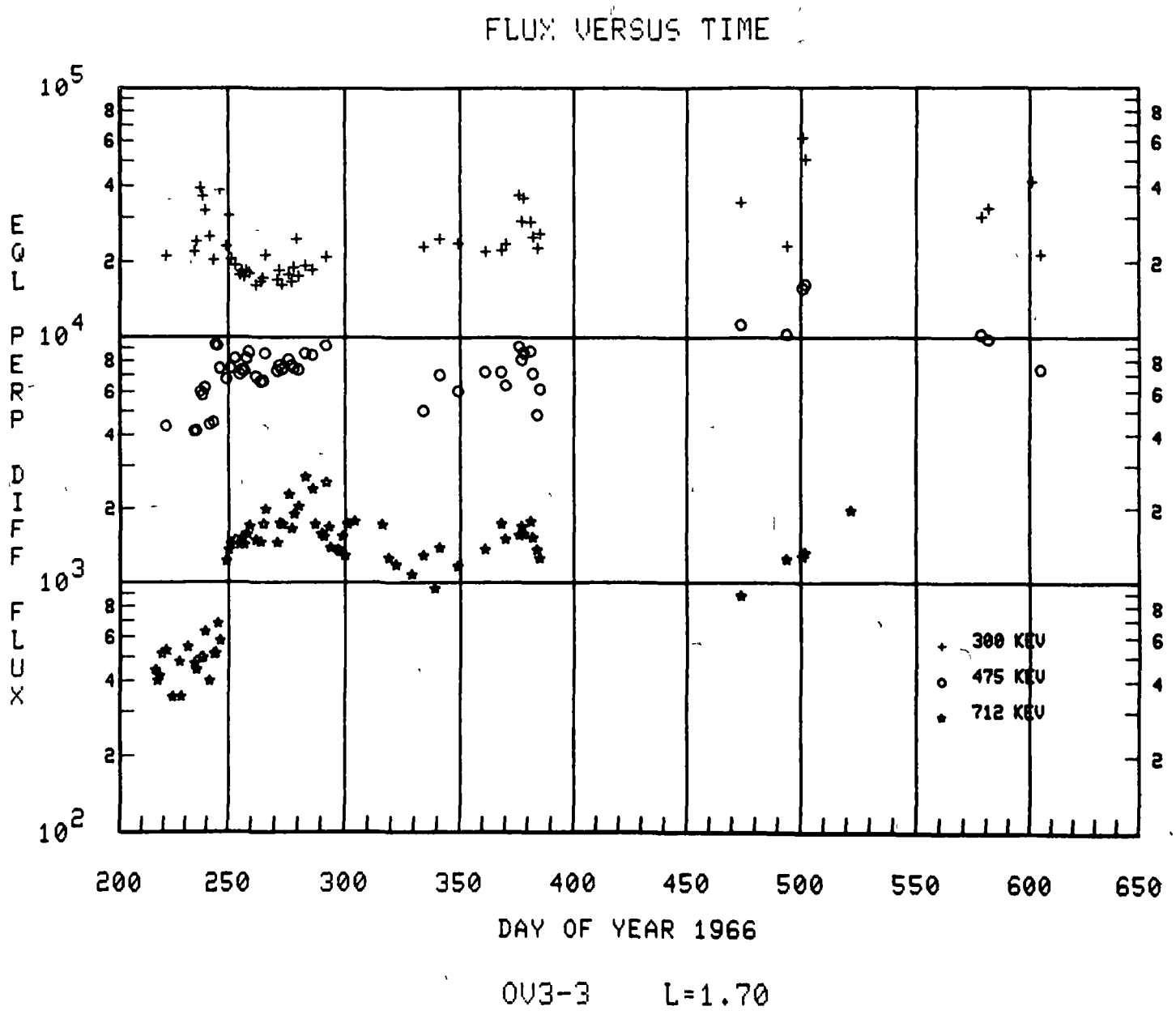
FLUX VERSUS TIME
EQL PERP DIF FLUX
10^5
10^4
10^3
10^2
8
6
4
2
200
250
300
350
400
450
500
550
600
650
300 KEV
475 KEV
712 KEV
DAY OF YEAR 1966
OV3-3 L=1.70

Figure 56

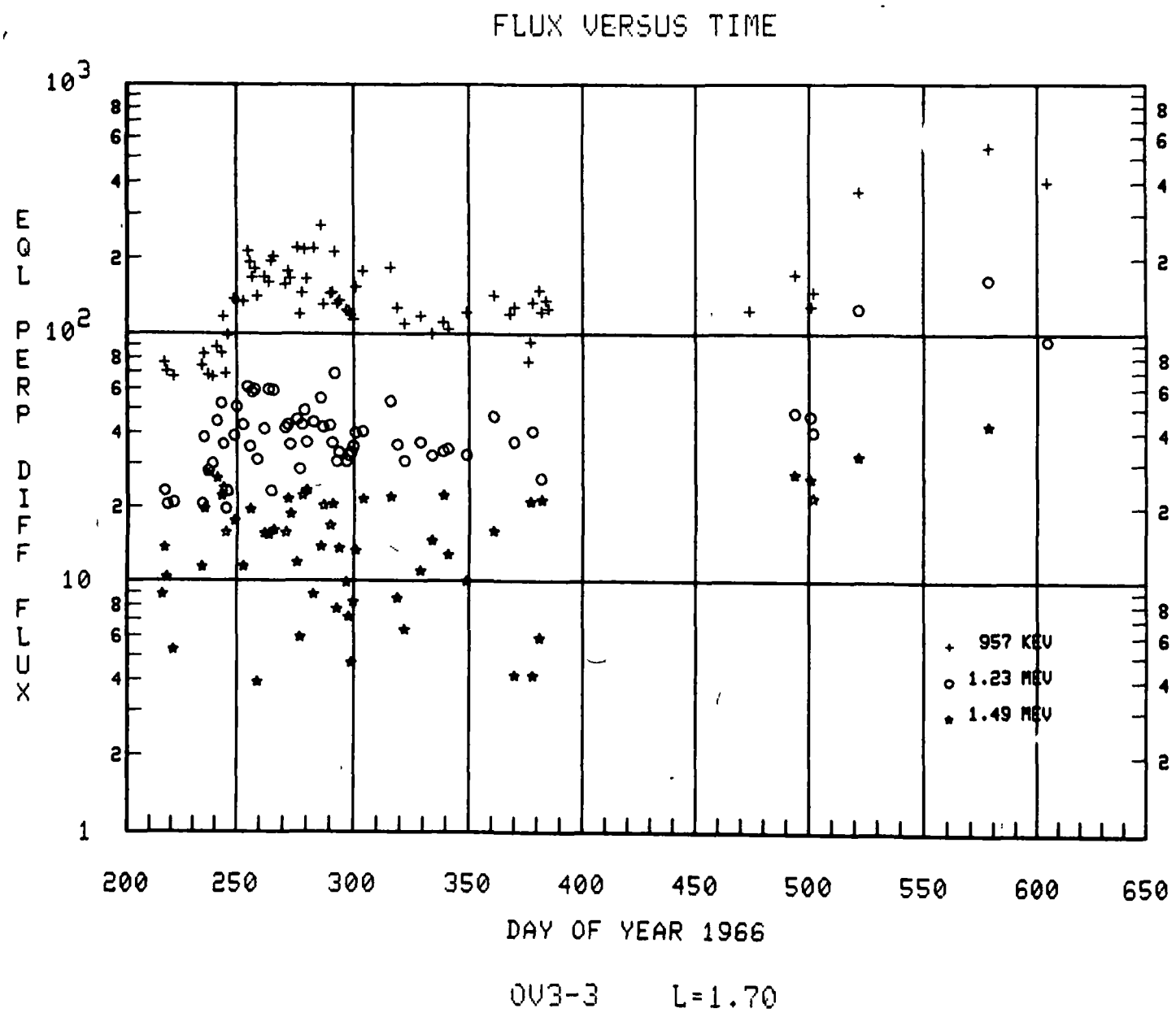

Figure 56 (concluded)

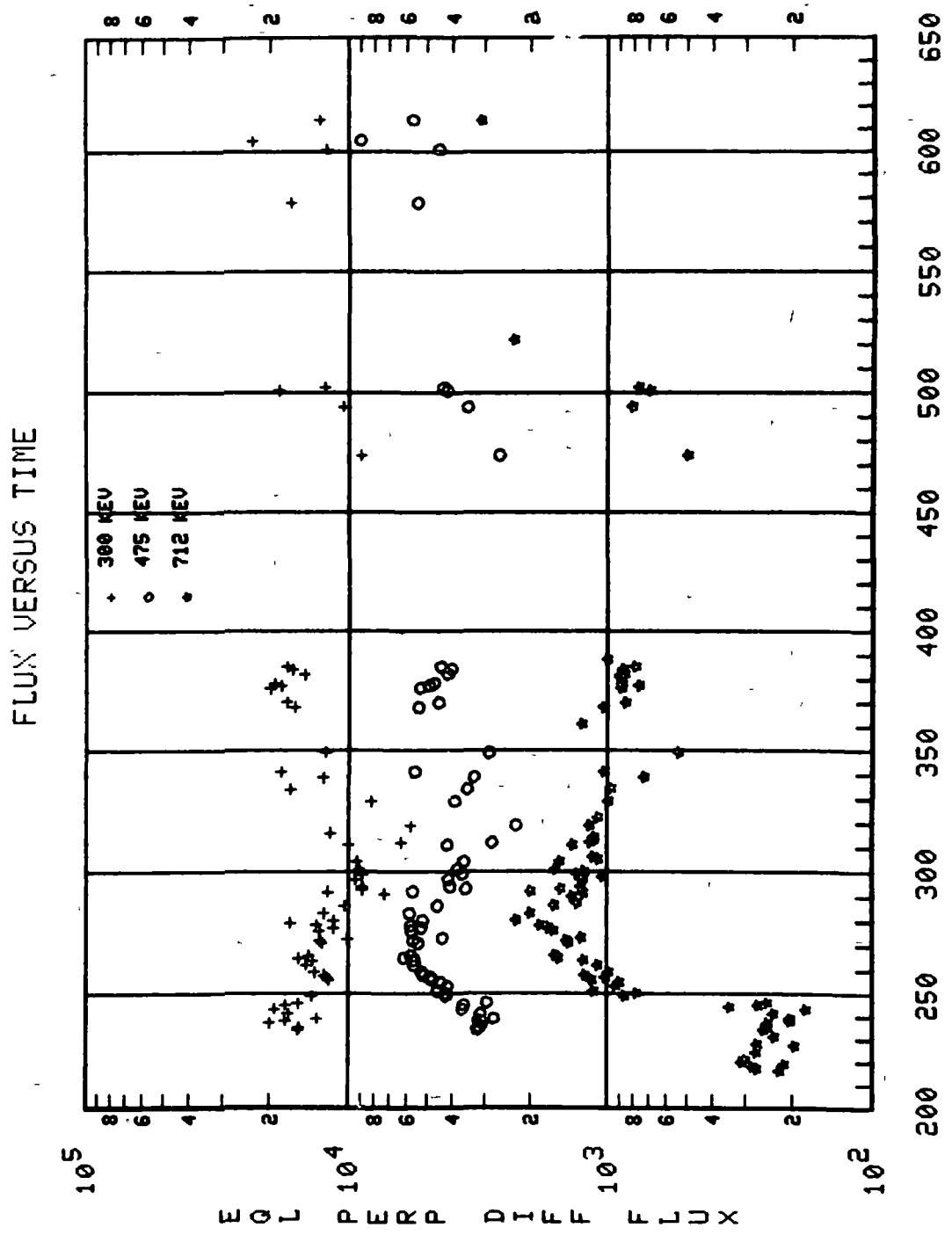
FLUX VERSUS TIME
300 KEV
475 KEV
712 KEV
EQL PERP DIFF FLUX
DAY OF YEAR 1966
OV3-3 L=1.80

Figure 57

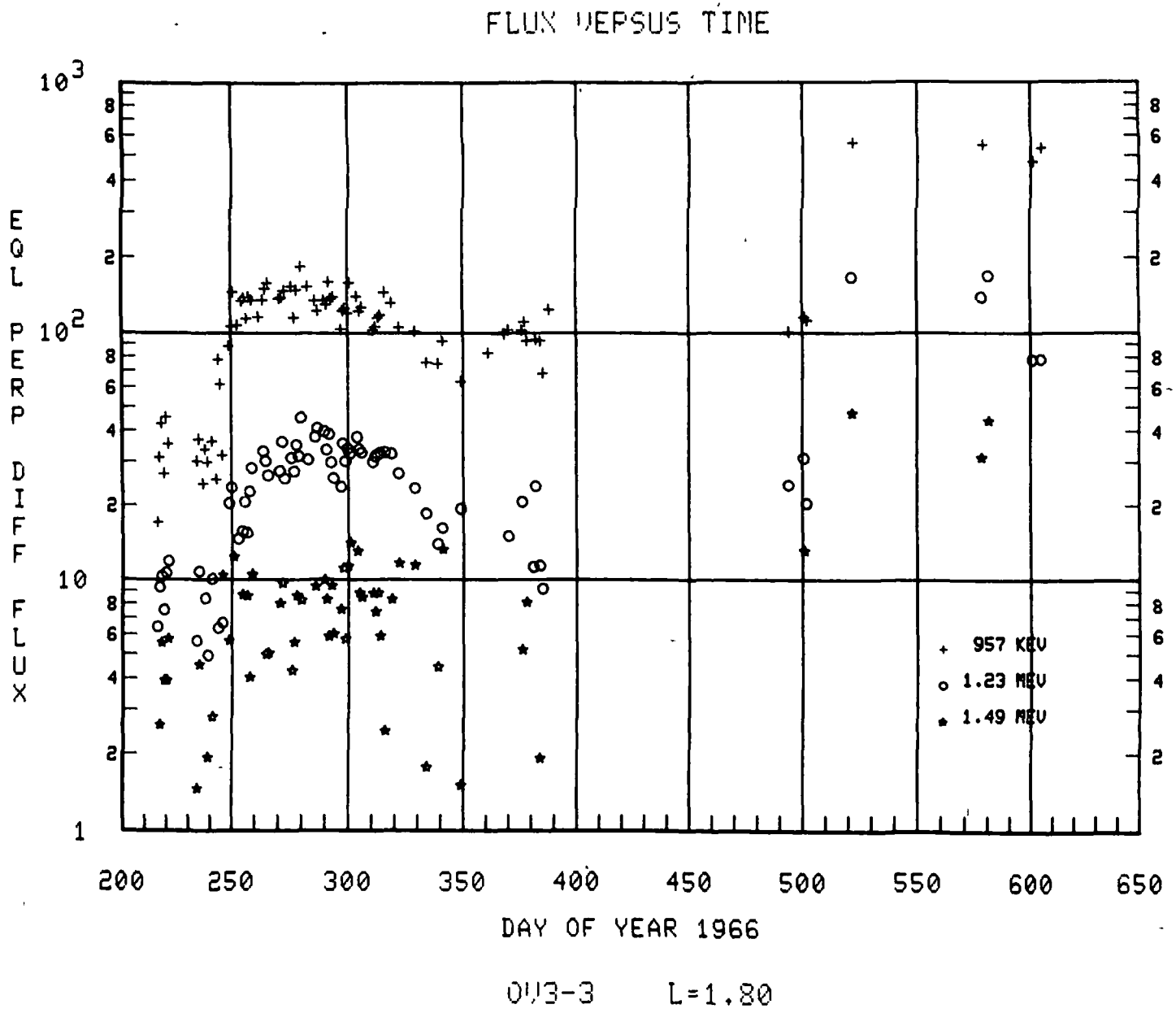

Figure 57 (continued)

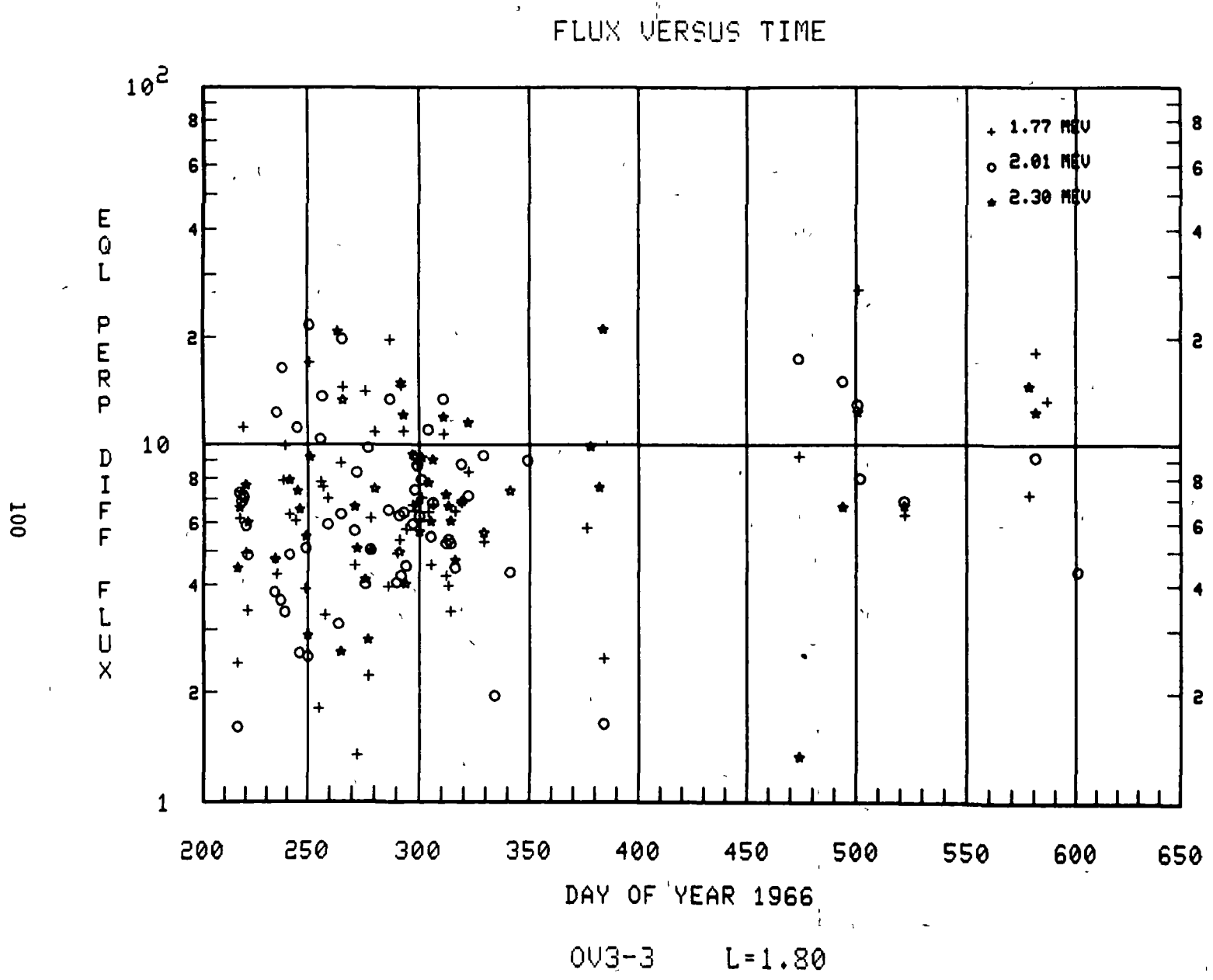

Figure 57 (concluded)

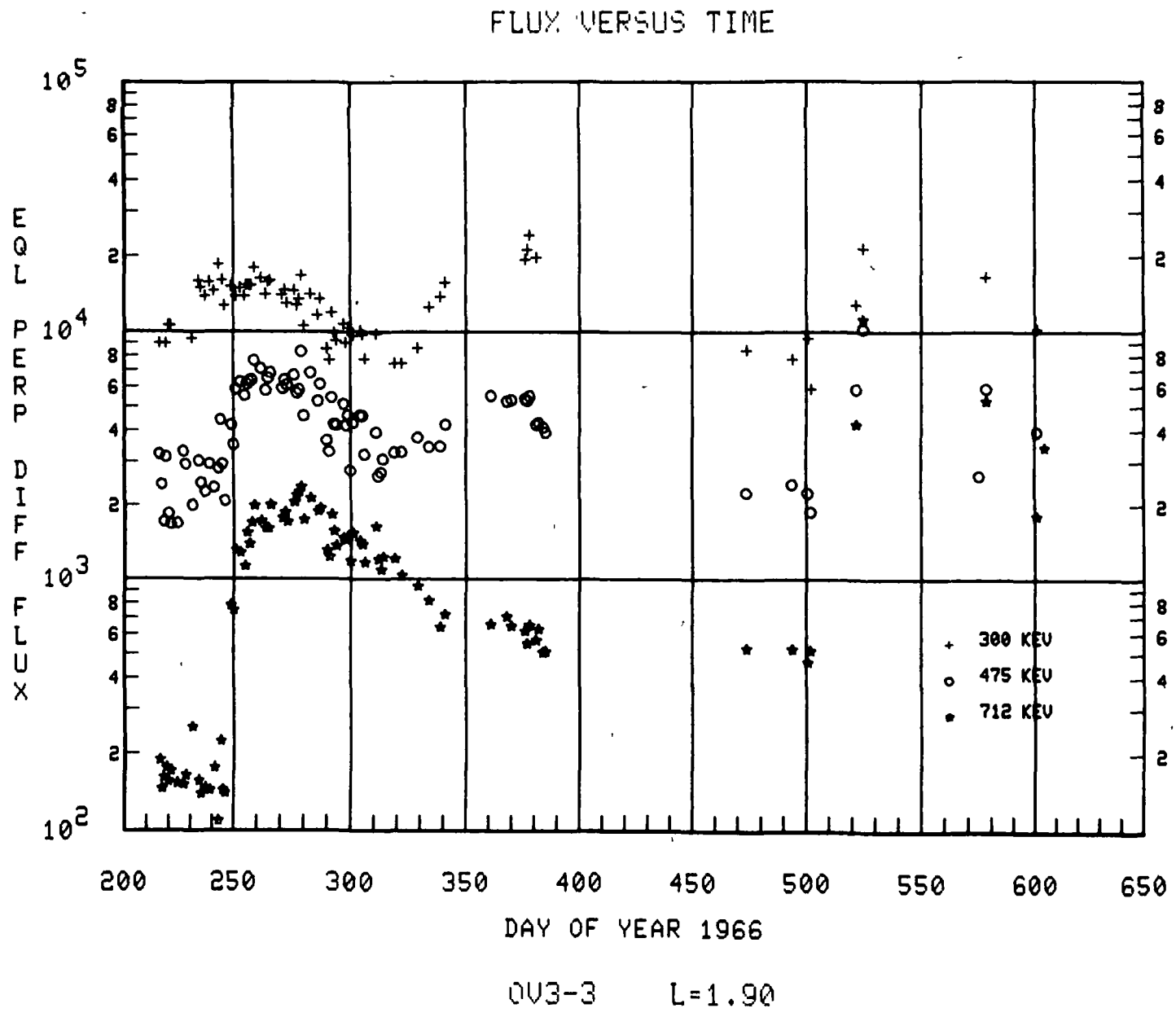
FLUX VERSUS TIME
EQL PERP DIFF FLUX
10^5
10^4
10^3
10^2
8
6
4
2
200
250
300
350
400
450
500
550
600
650
DAY OF YEAR 1966
300 KEV
475 KEV
712 KEV
OV3-3 L=1.90

Figure 58

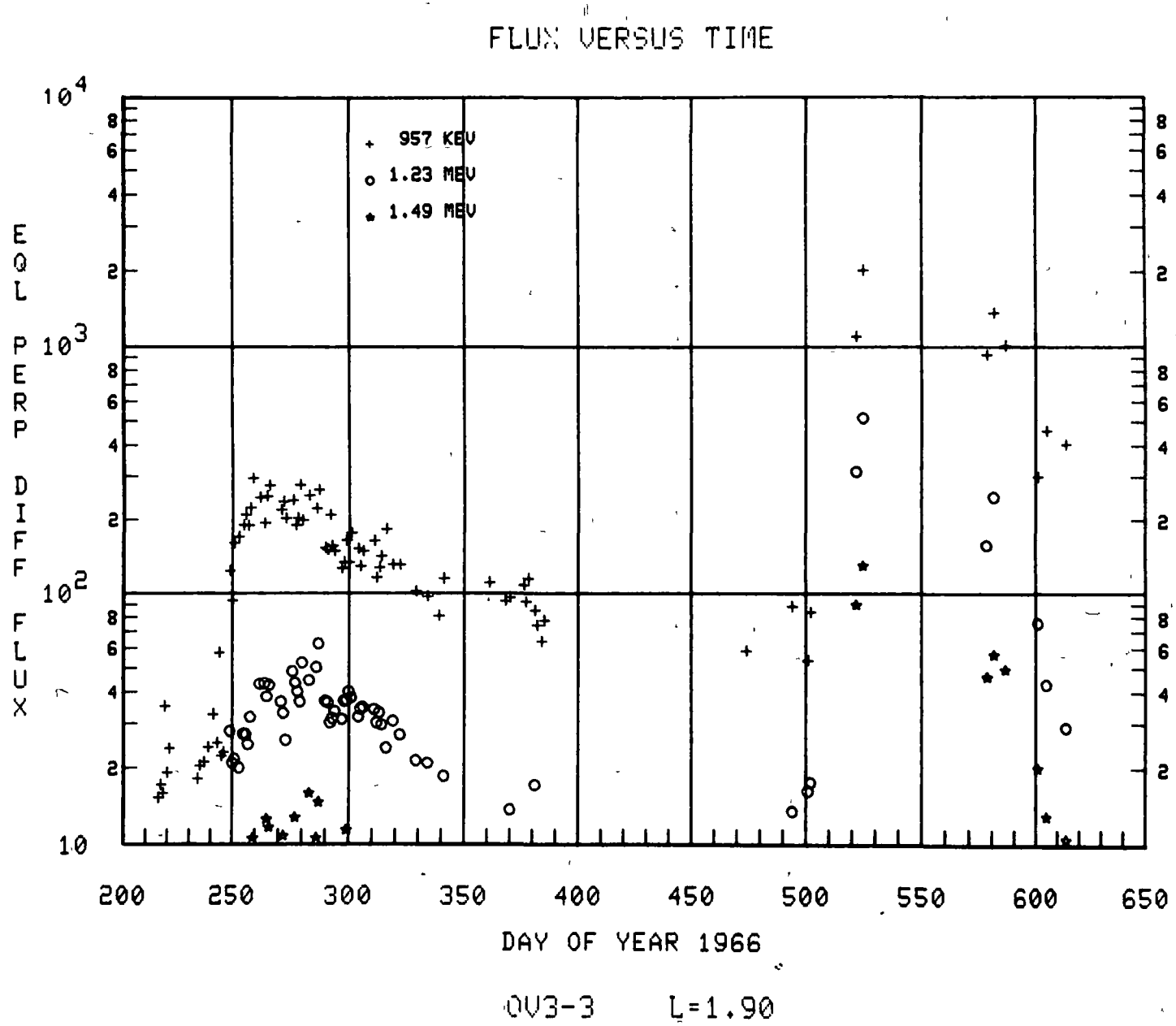

Figure 58 (continued)

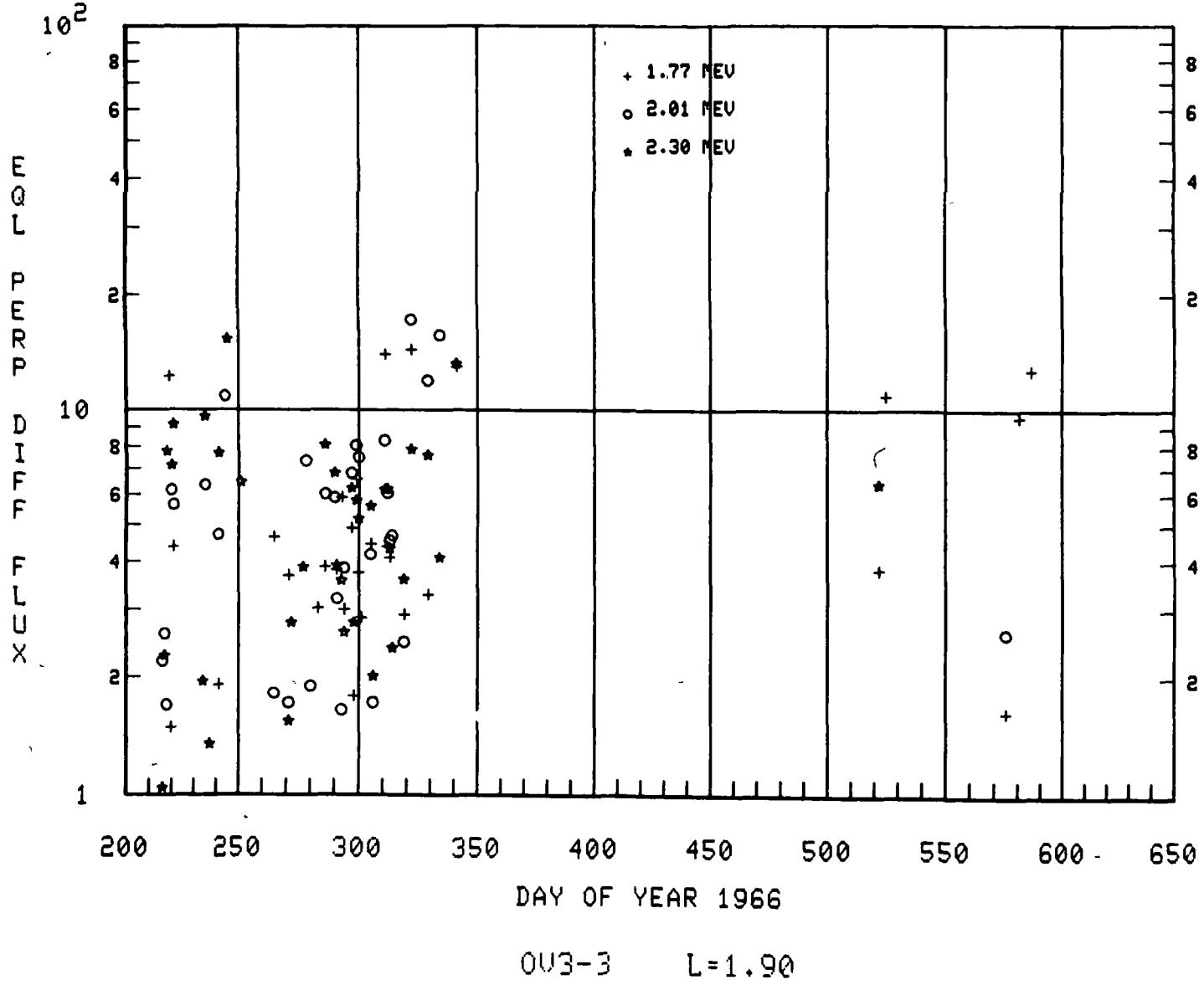
FLUX VERSUS TIME
+ 1.77 MEV
o 2.01 MEV
★ 2.30 MEV
EQL PERP DIFF FLUX
10^2
8
6
4
2
10
8
6
4
2
1
200
250
300
350
400
450
500
550
600
650
DAY OF YEAR 1966
OV3-3 L=1.90

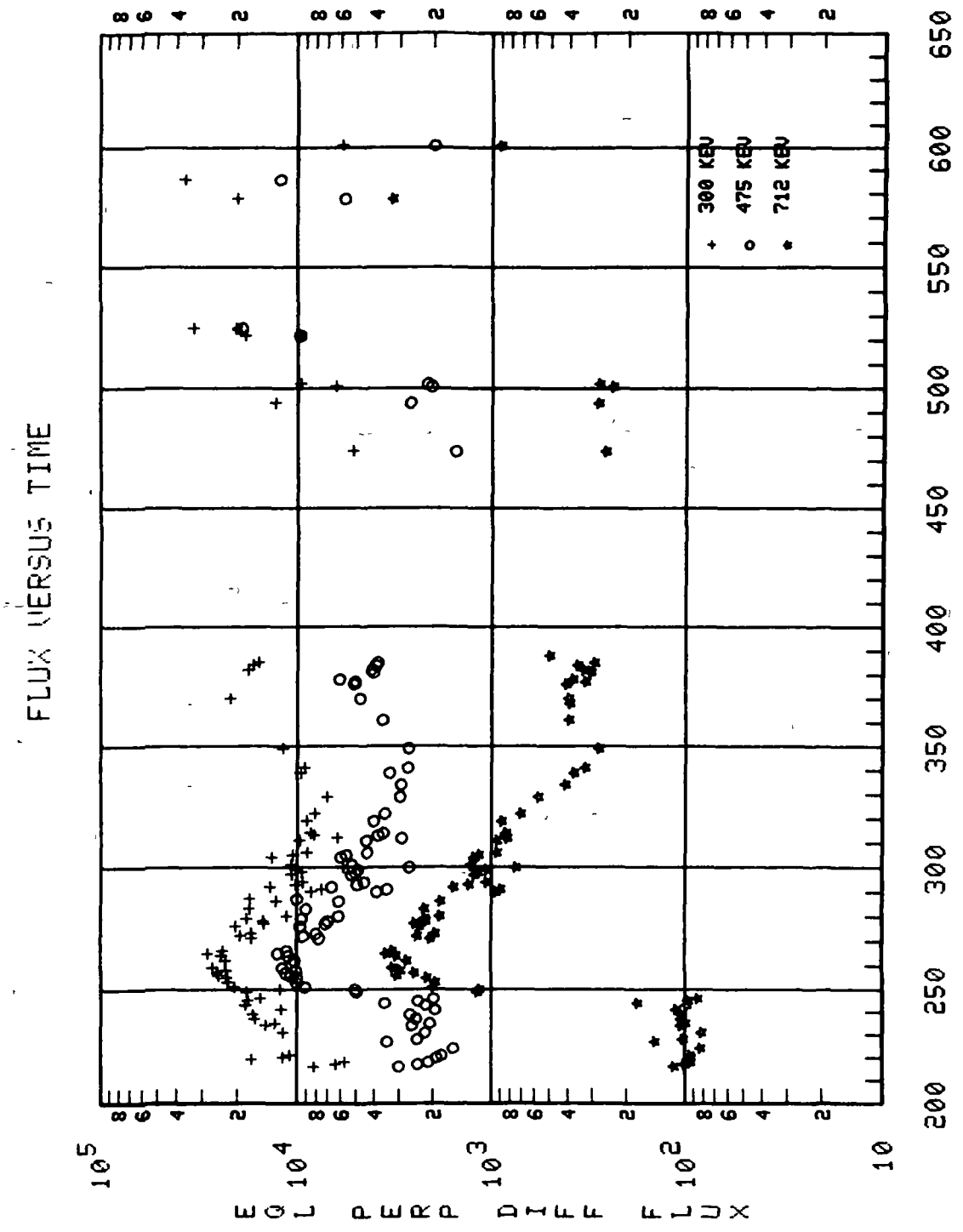
FLUX VERSUS TIME
EQL PERP DIFF FLUX
DAY OF YEAR 1966
OV3-3 L=2.00
300 KEV
475 KEV
712 KEV

Figure 59

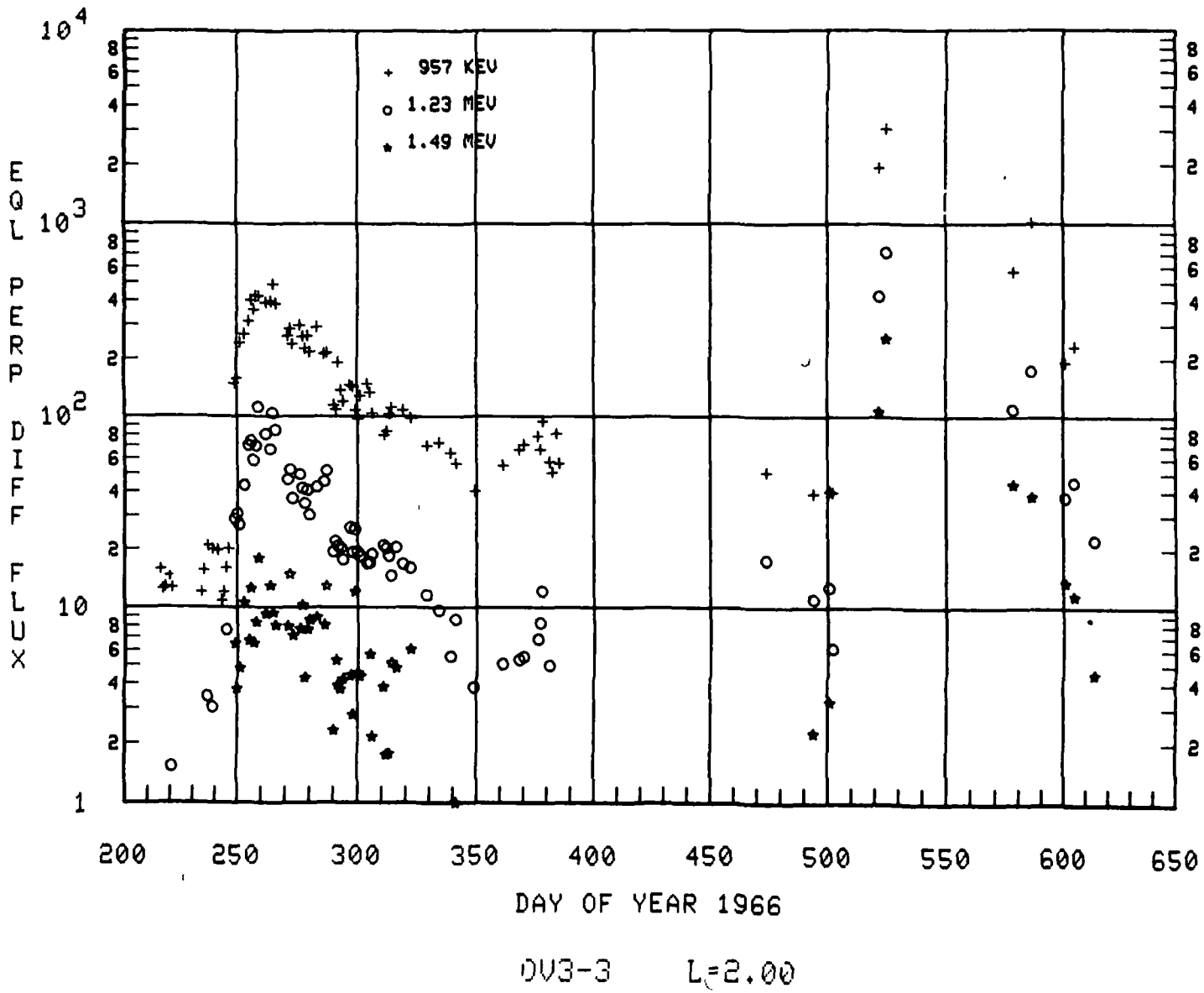

Figure 59 (continued)

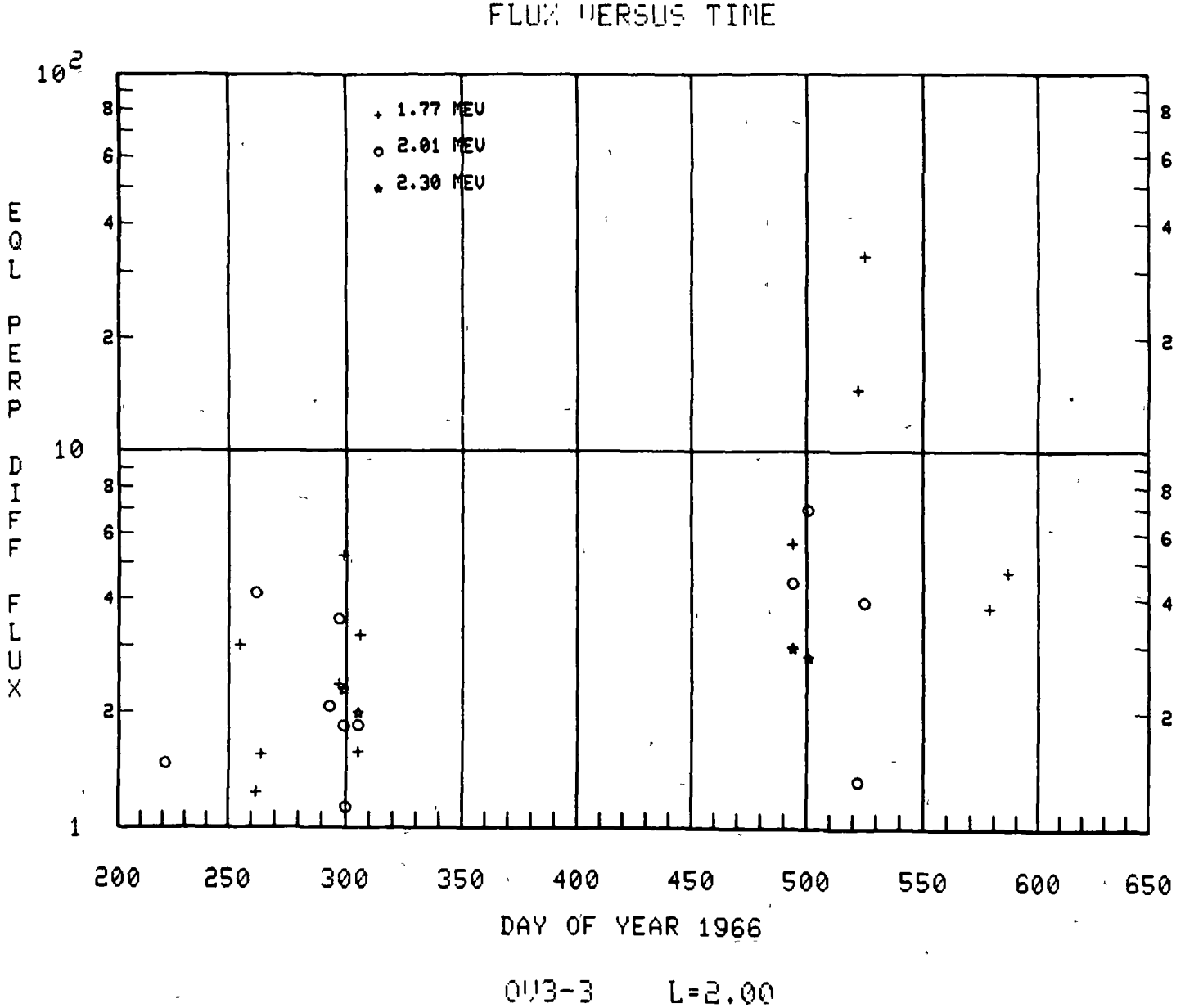

Figure 59 (concluded)

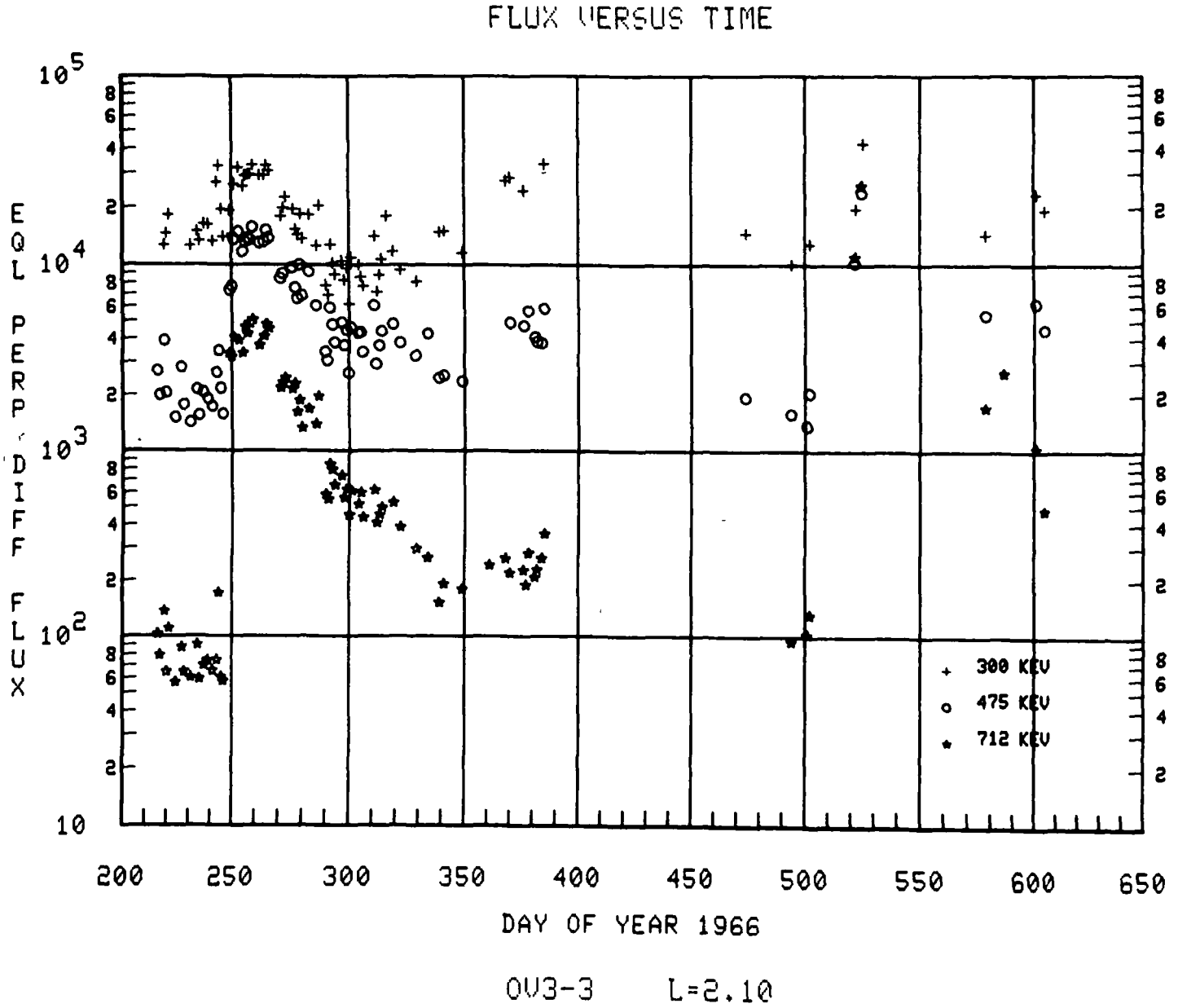
FLUX VERSUS TIME
EQL PERP DIFF FLUX
10^5
10^4
10^3
10^2
10
8
6
4
2
200
250
300
350
400
450
500
550
600
650
DAY OF YEAR 1966
300 KEV
475 KEV
712 KEV
OV3-3 L=2.10

Figure 60

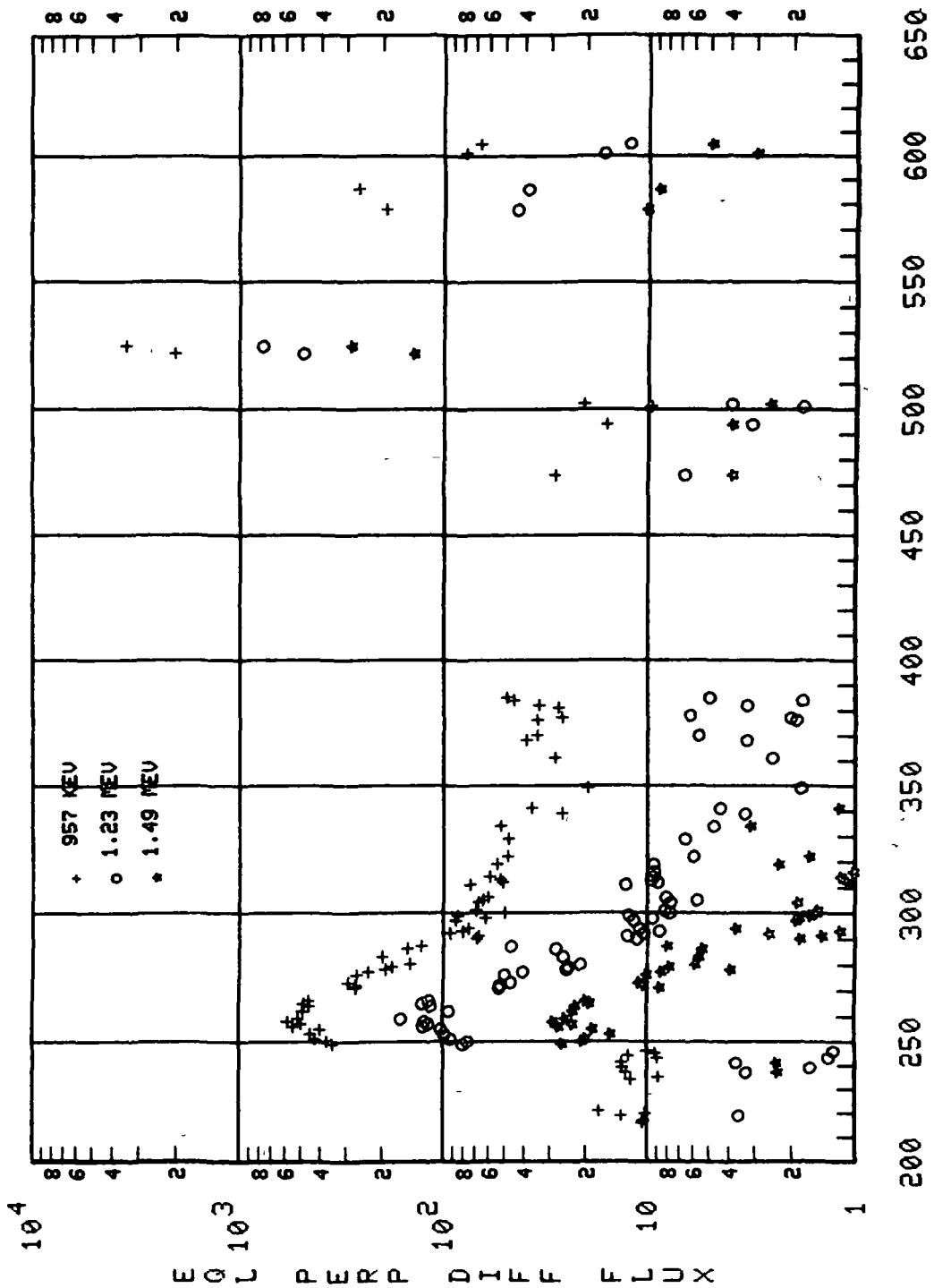

Figure 60 (continued)

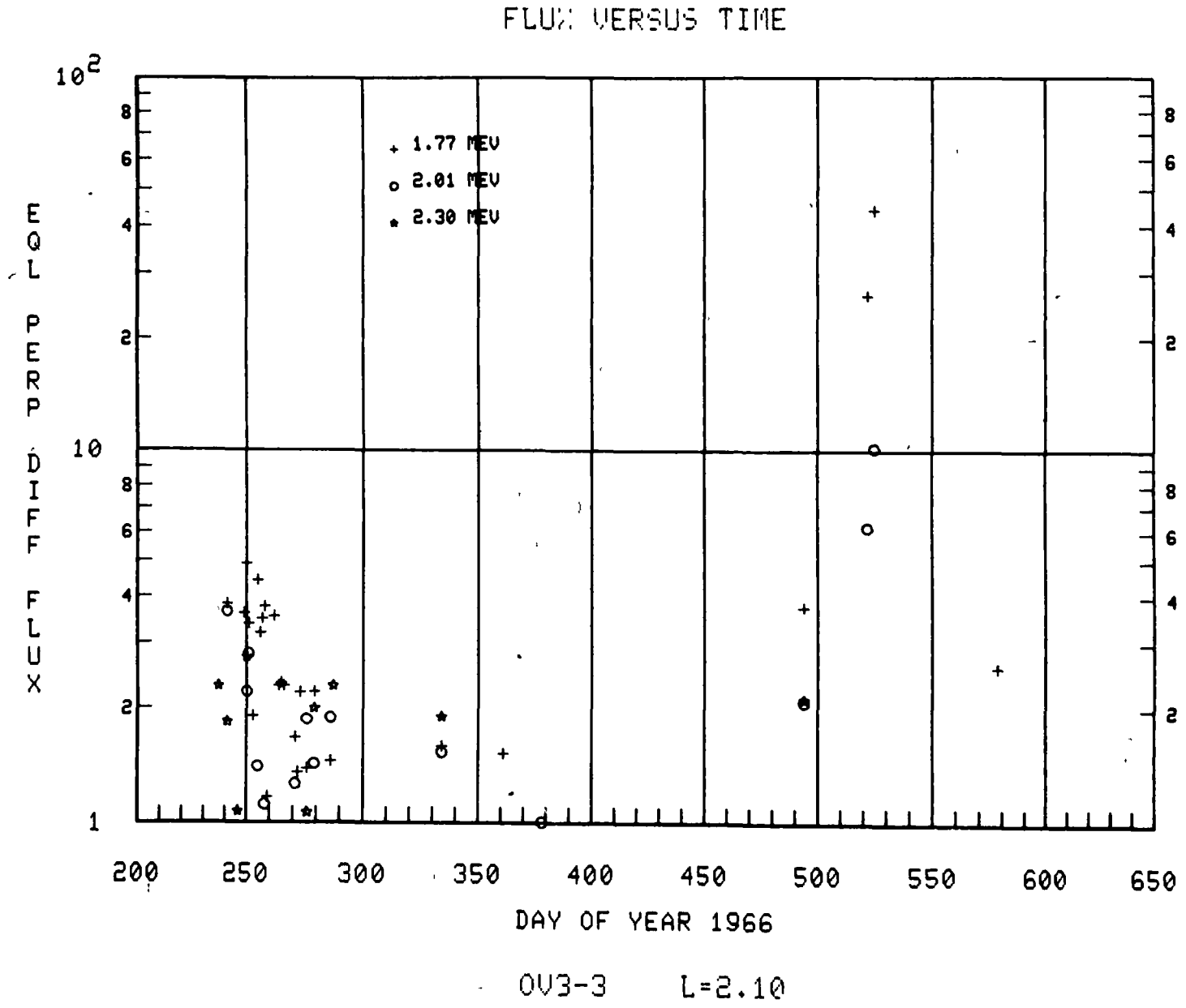

Figure 60 (concluded)

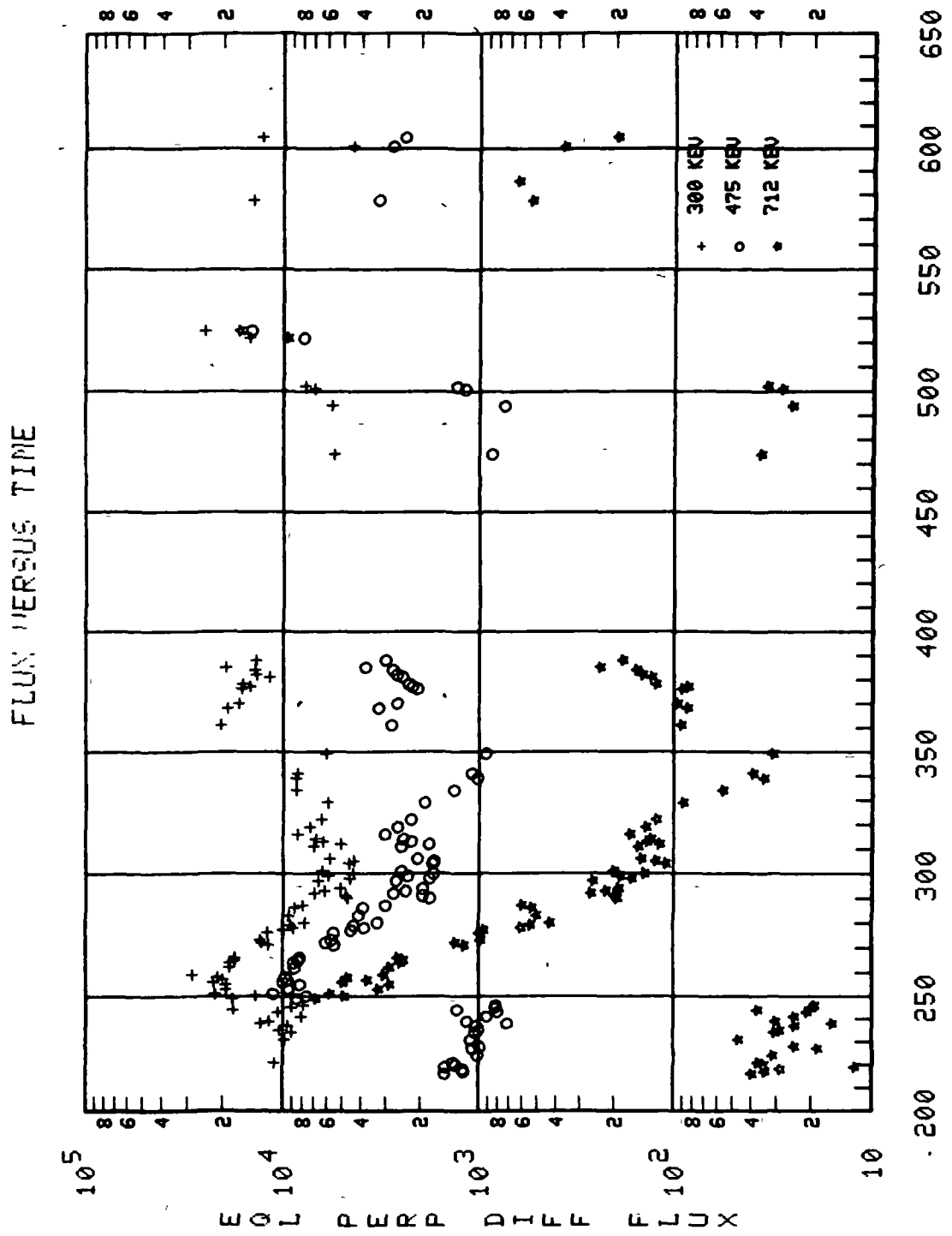
FLUX VERSUS TIME
300 KEV
475 KEV
712 KEV
EQ L PERP DIFF FLUX
DAY OF YEAR 1966
0113-3 L=2.20

Figure 61

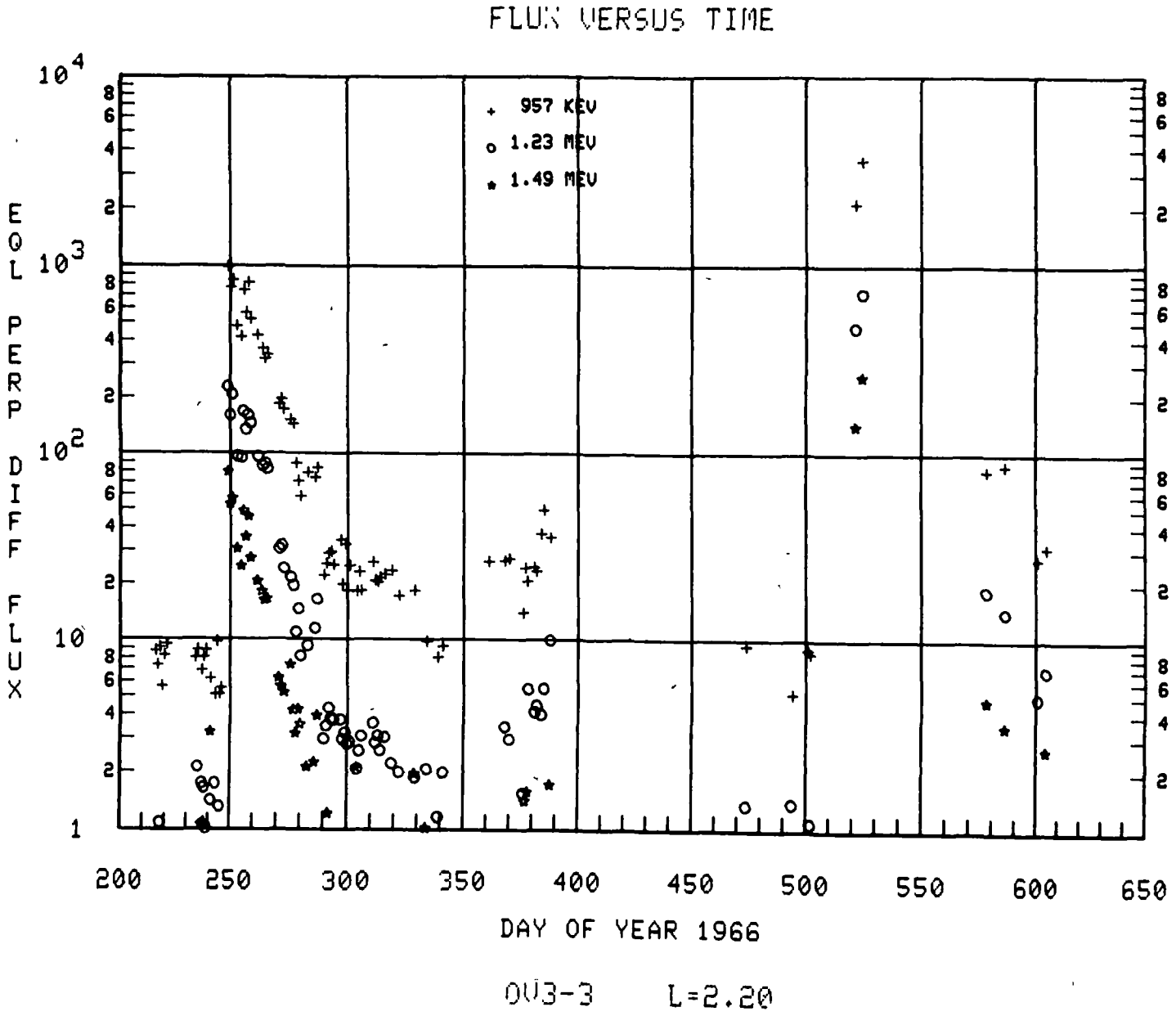

Figure 61 (continued)

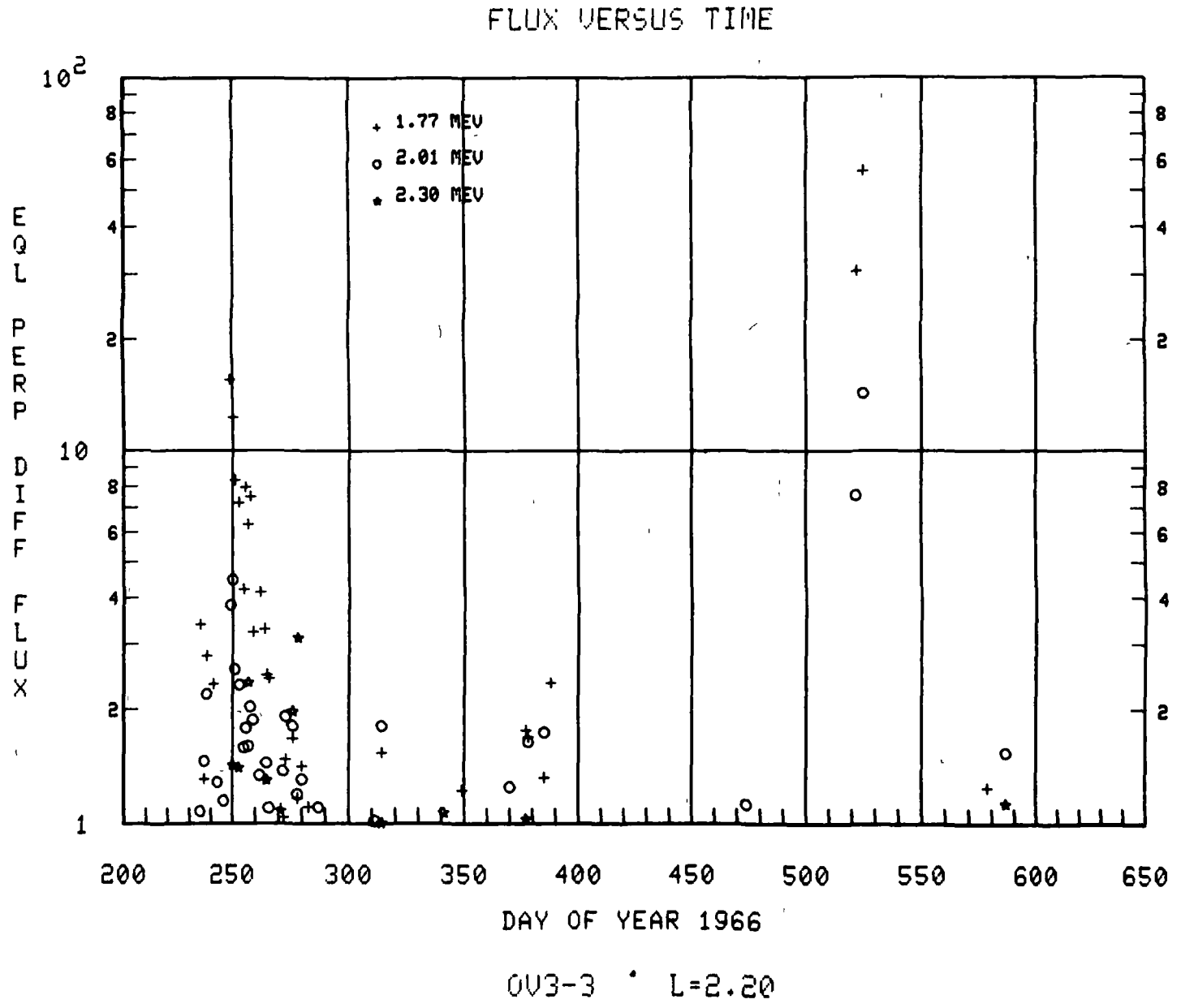

Figure 61 (concluded)

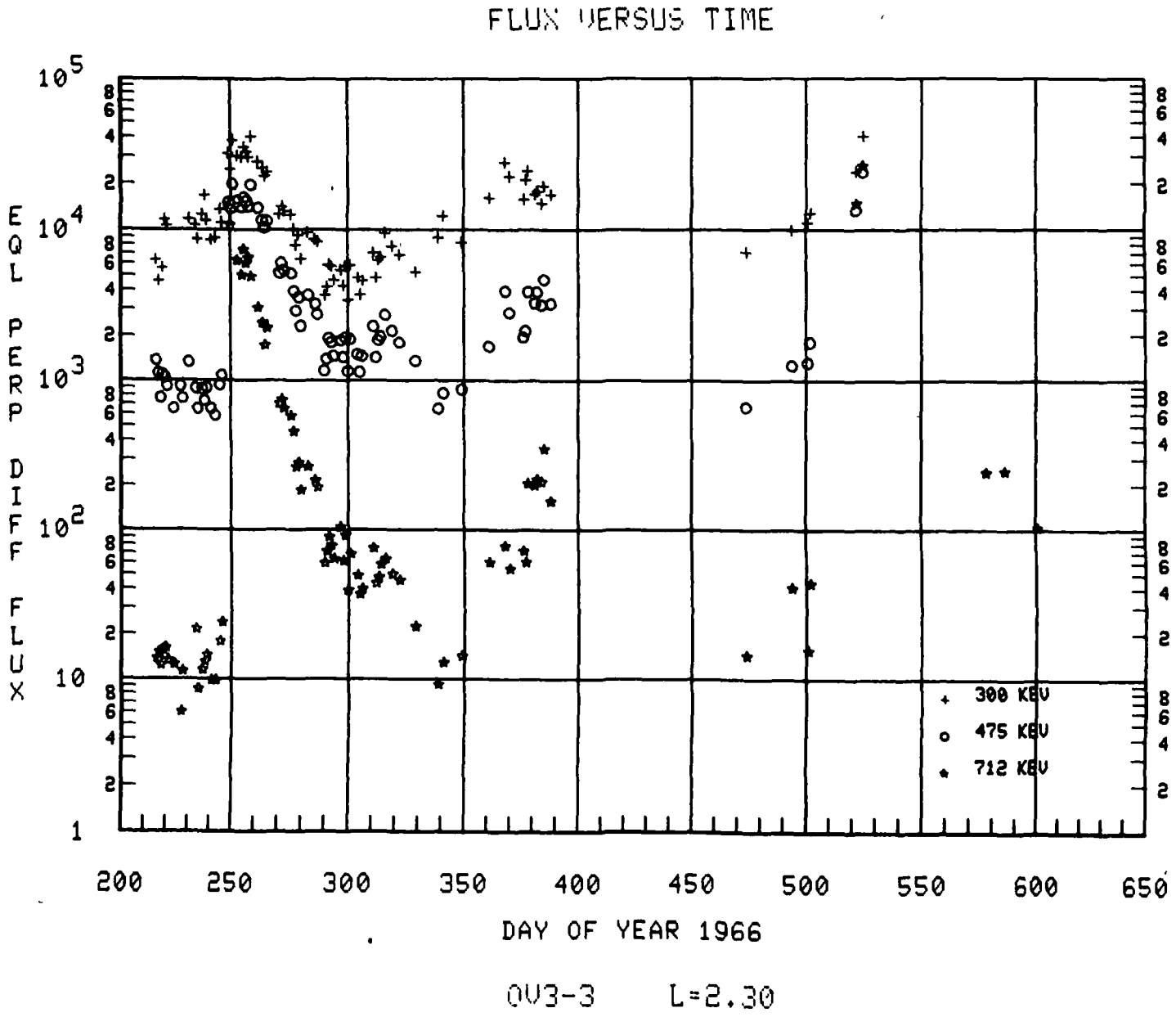
FLUX VERSUS TIME
EQL PERP DIFF FLUX
DAY OF YEAR 1966
300 KEV
475 KEV
712 KEV
OV3-3 L=2.30

Figure 62

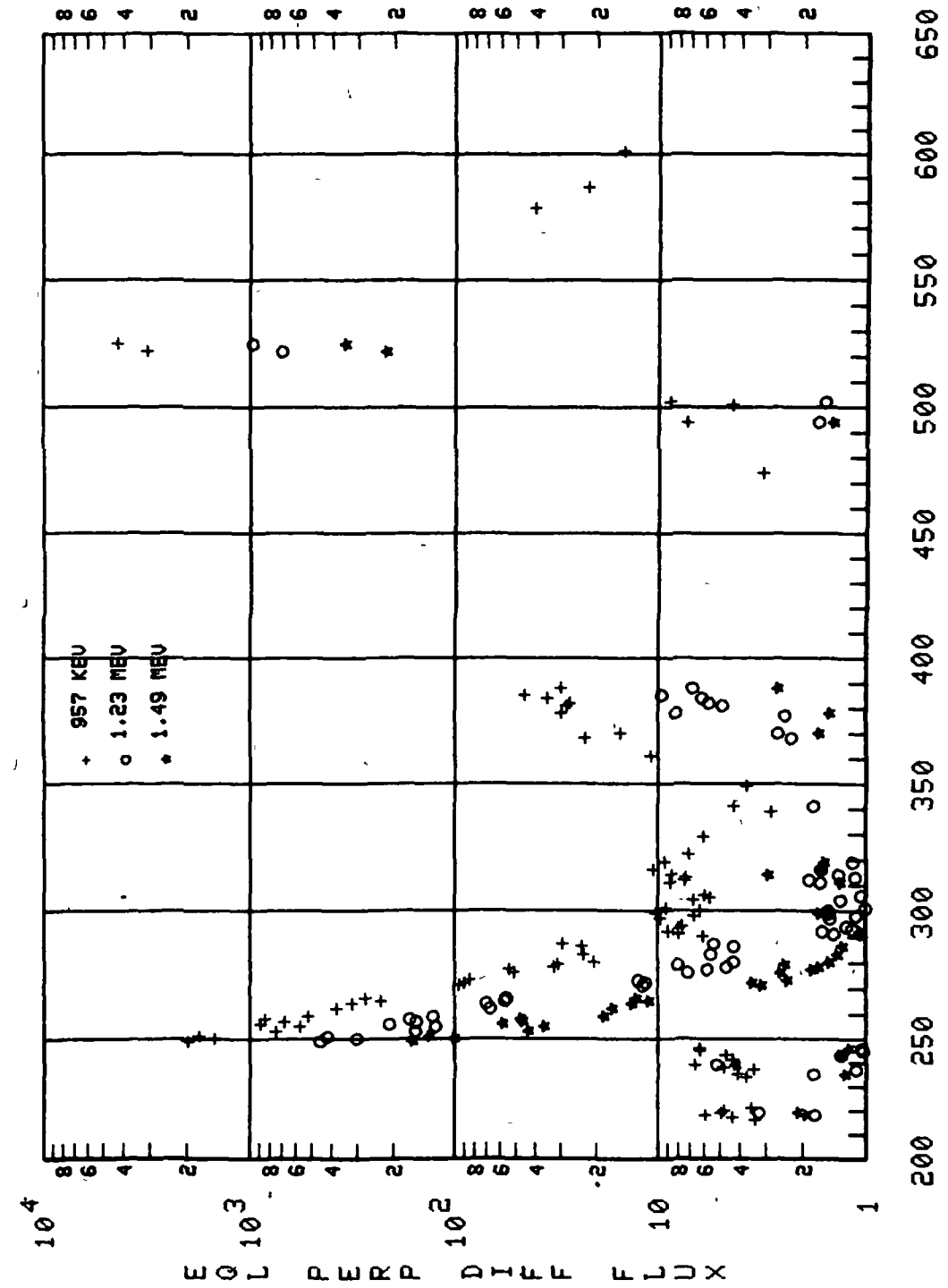

Figure 62 (continued)

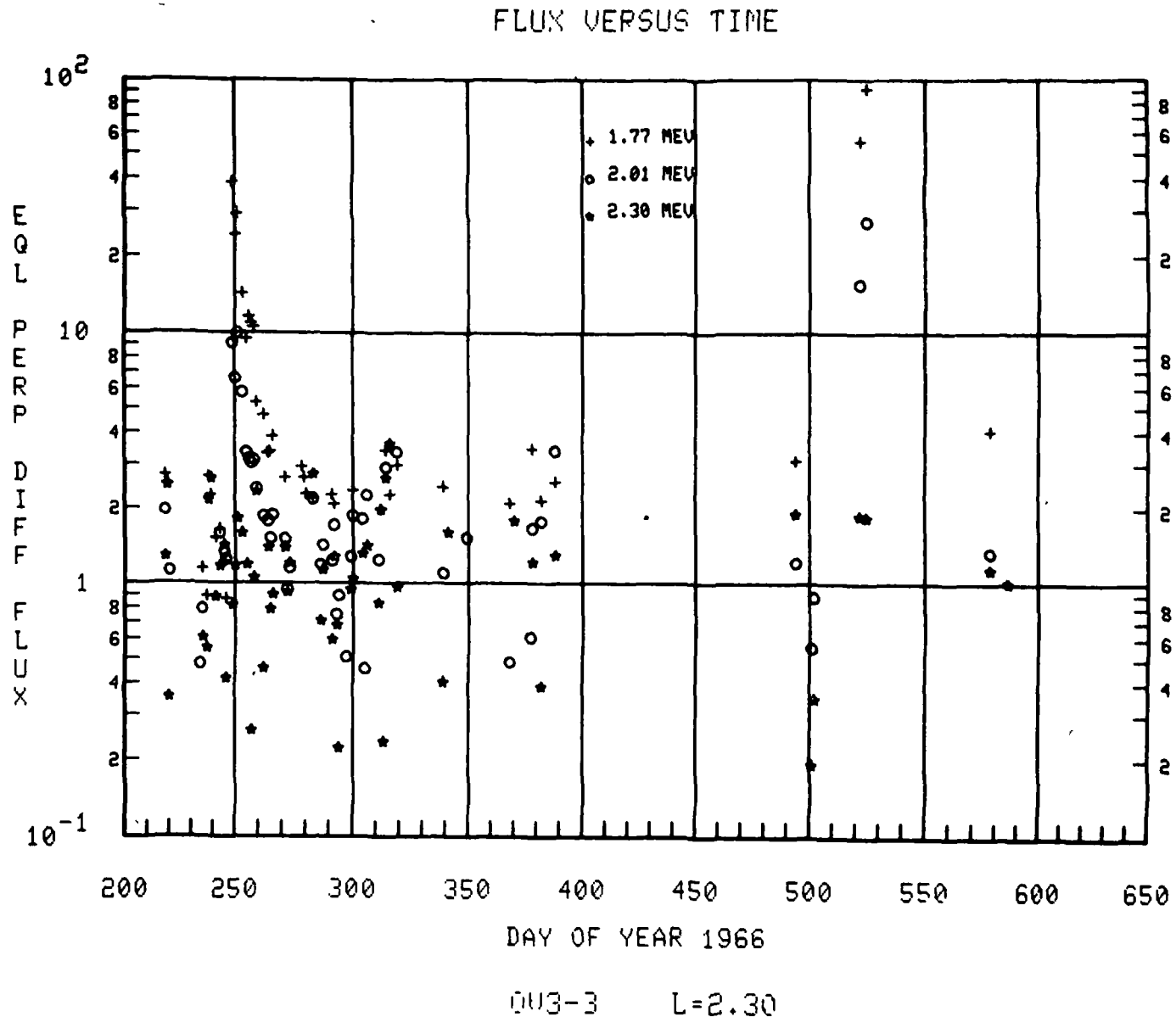

Figure 62 (concluded)

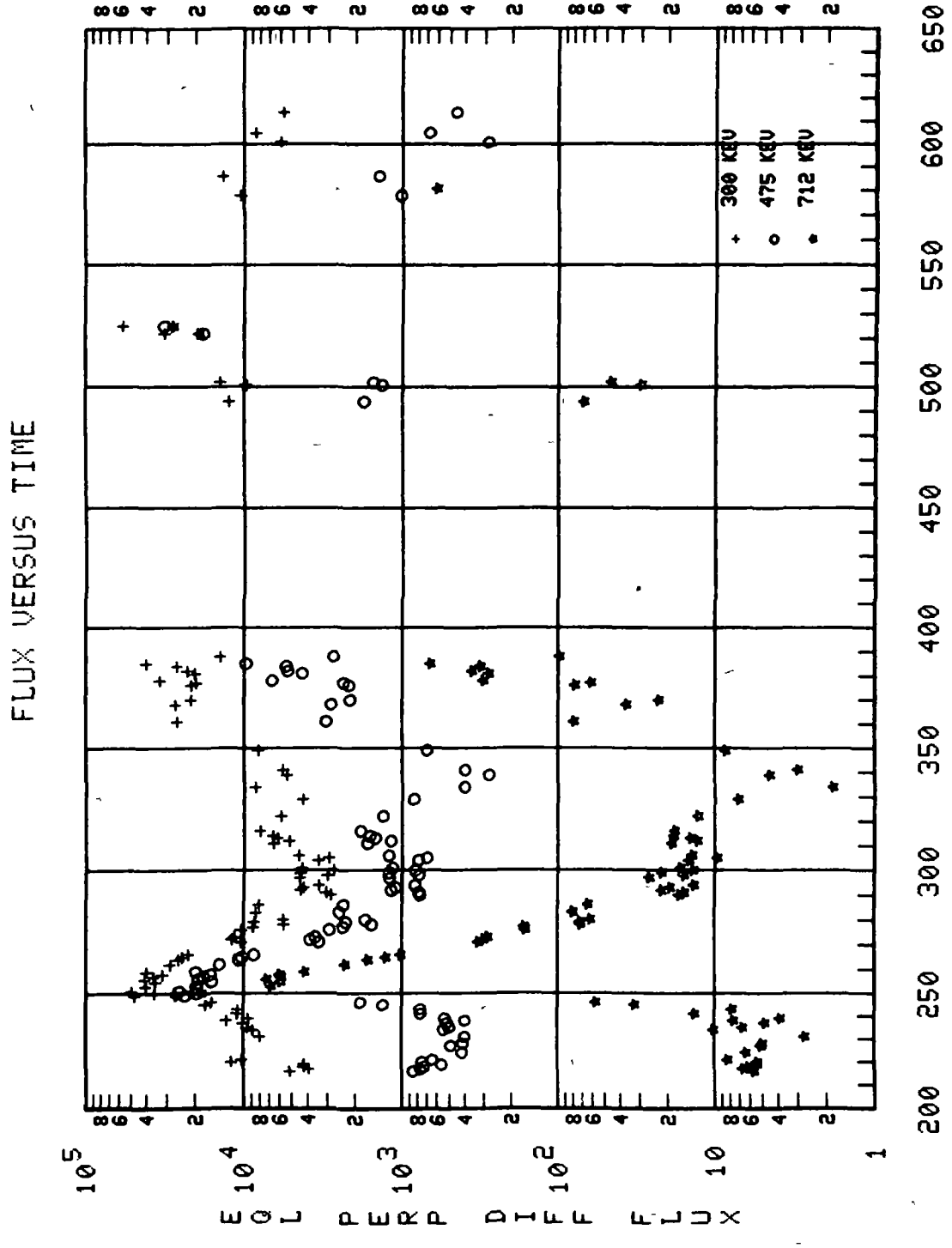
FLUX VERSUS TIME
EQL PERP DIFF FLUX
DAY OF YEAR 1966
DV3-3 L=2.40
300 KEV
475 KEV
712 KEV

Figure 63

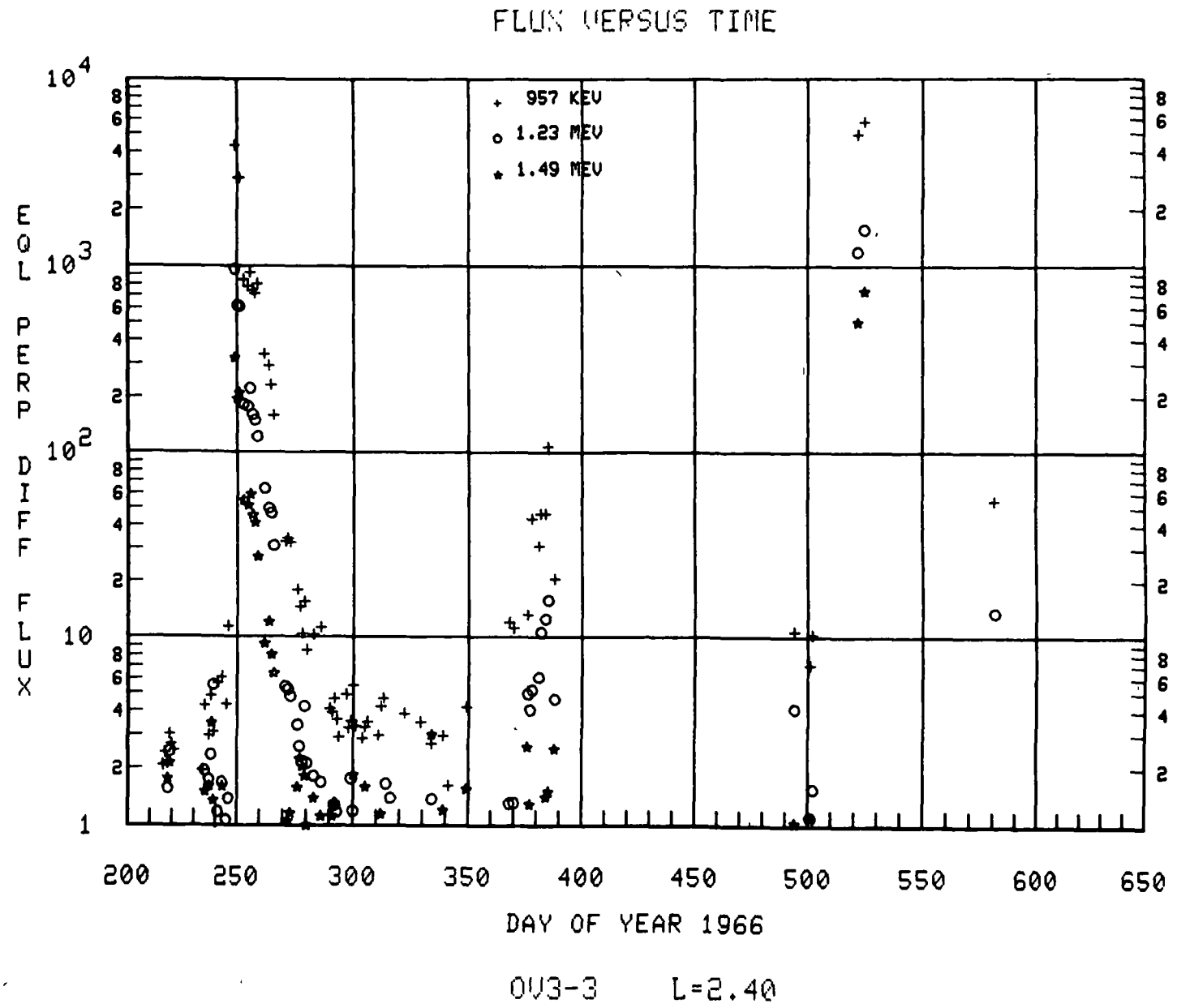

Figure 63 (continued)

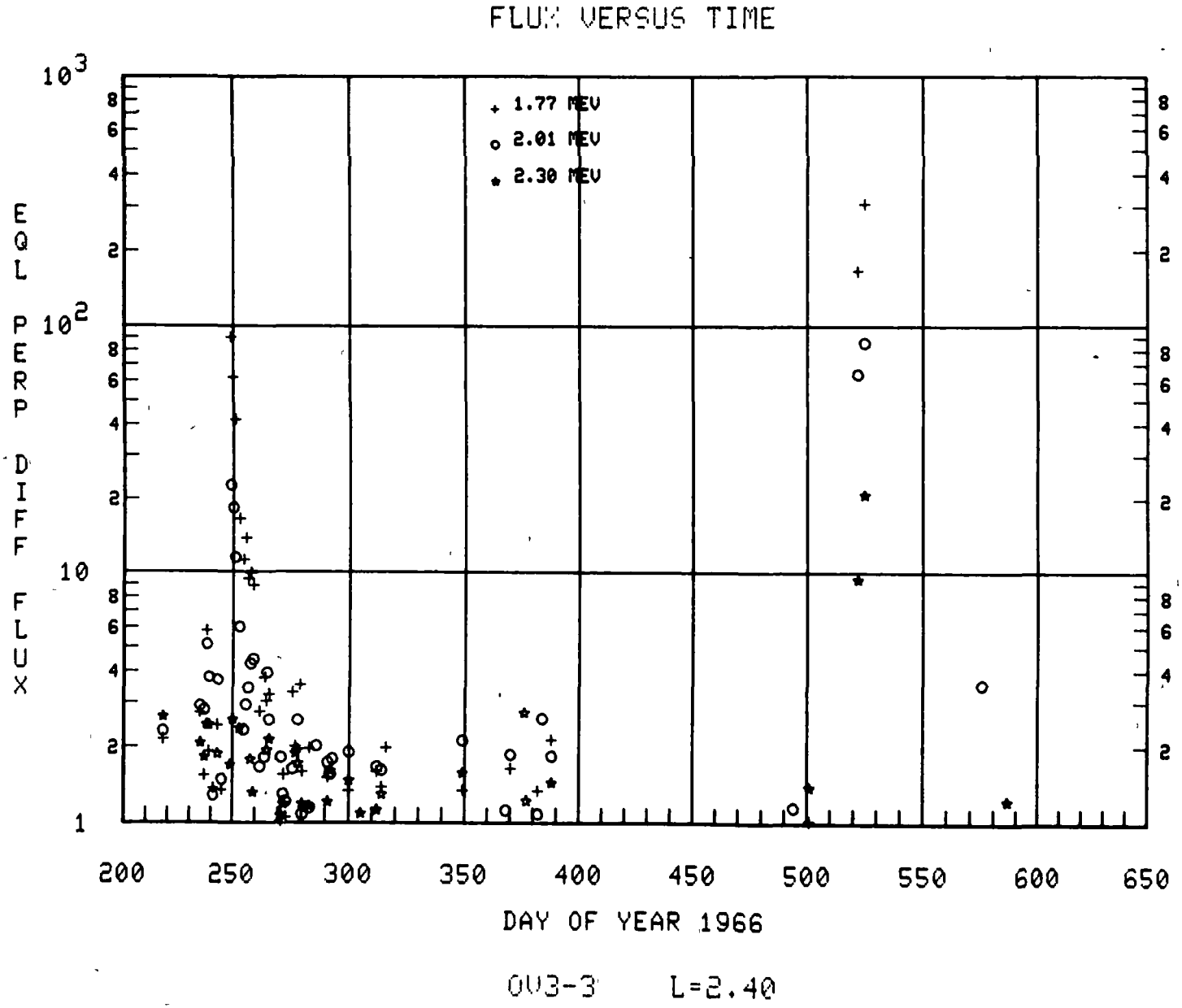

Figure 63 (concluded)

FLUX VERSUS TIME

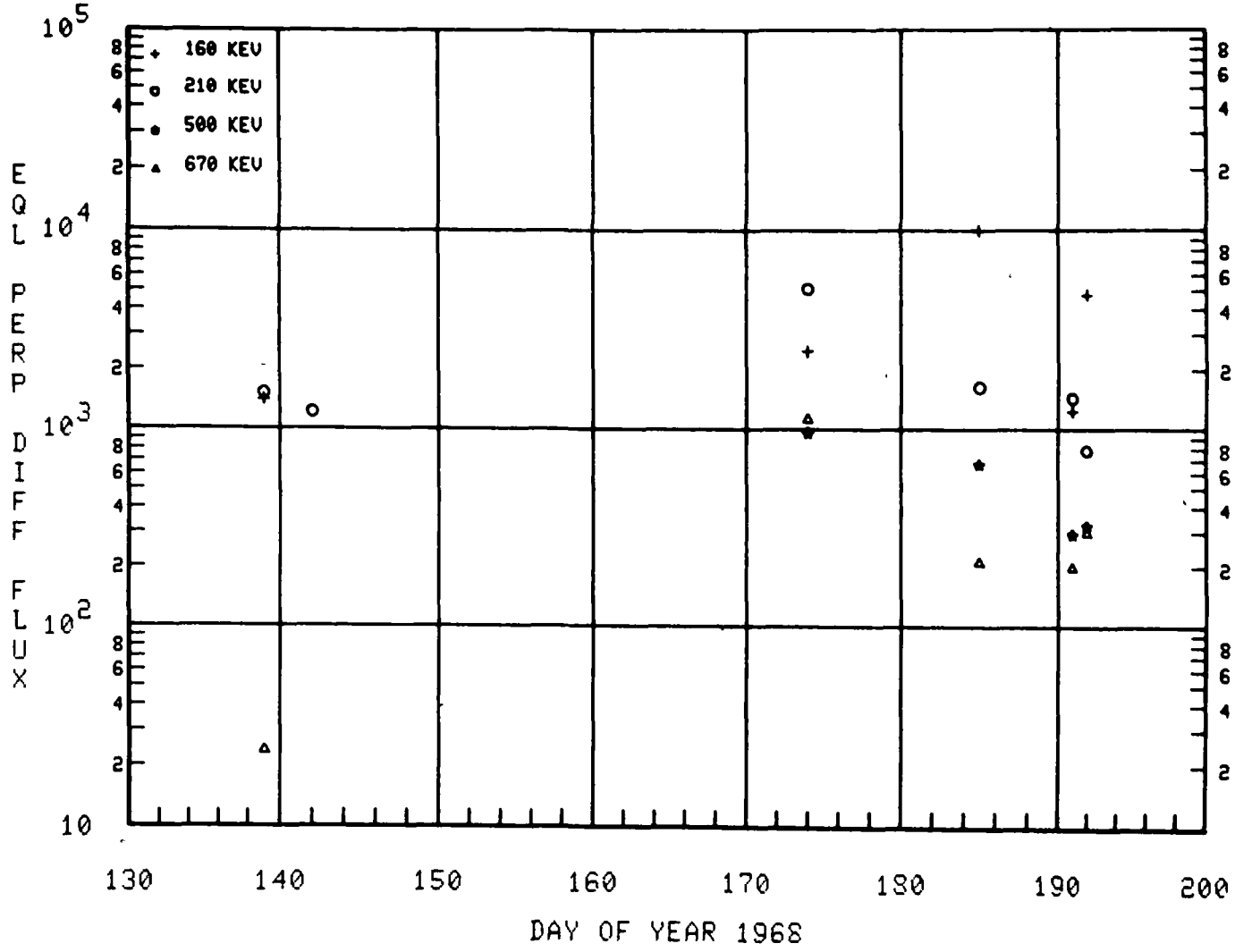

OU1-13 L=1.20

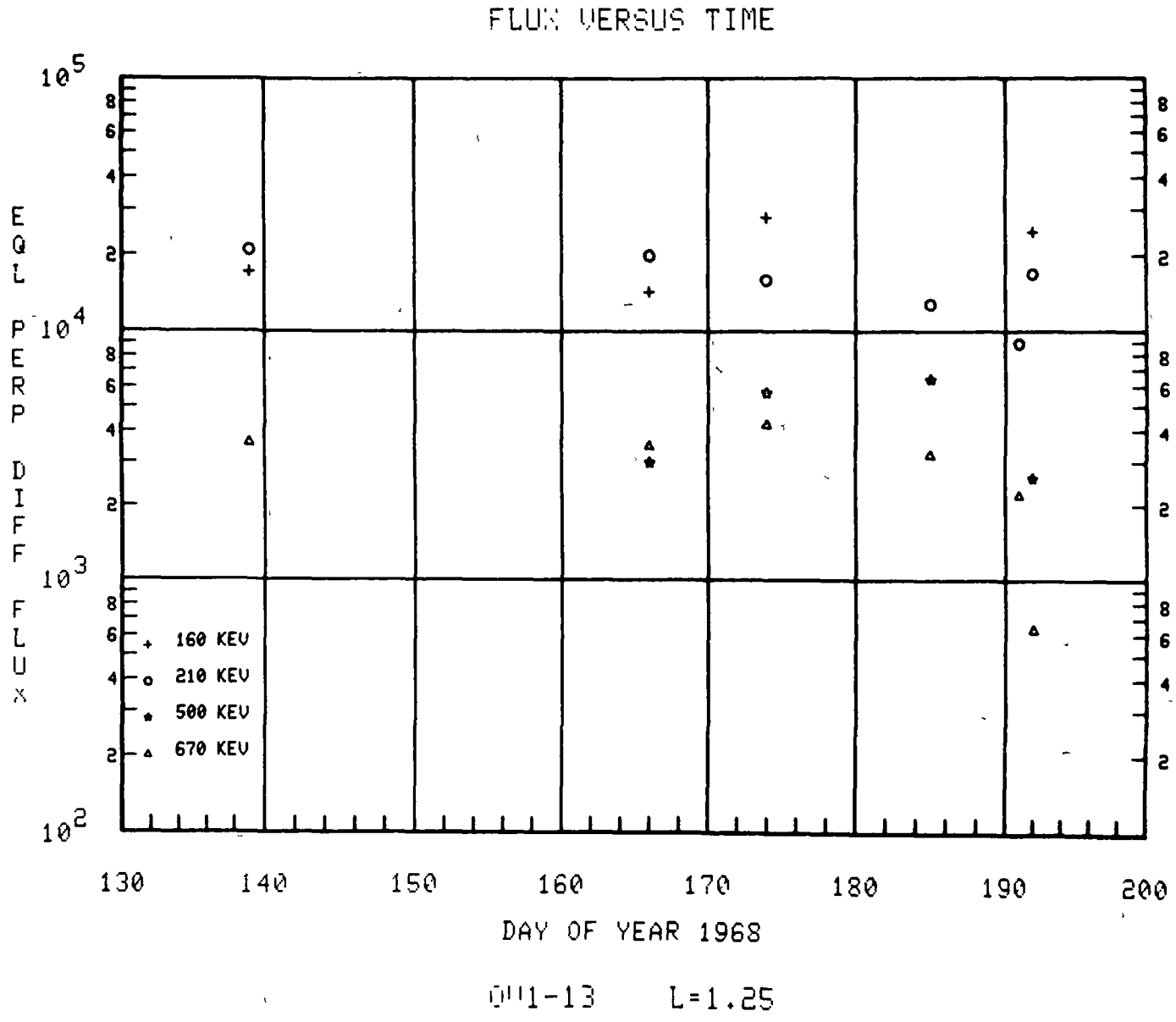
FLUX VERSUS TIME
EQUIV PERP DIFF FLUX
10^5
10^4
10^3
10^2
8
6
4
2
160 KEV
210 KEV
500 KEV
670 KEV
130
140
150
160
170
180
190
200
DAY OF YEAR 1968
OV1-13 L=1.25

Figure 65

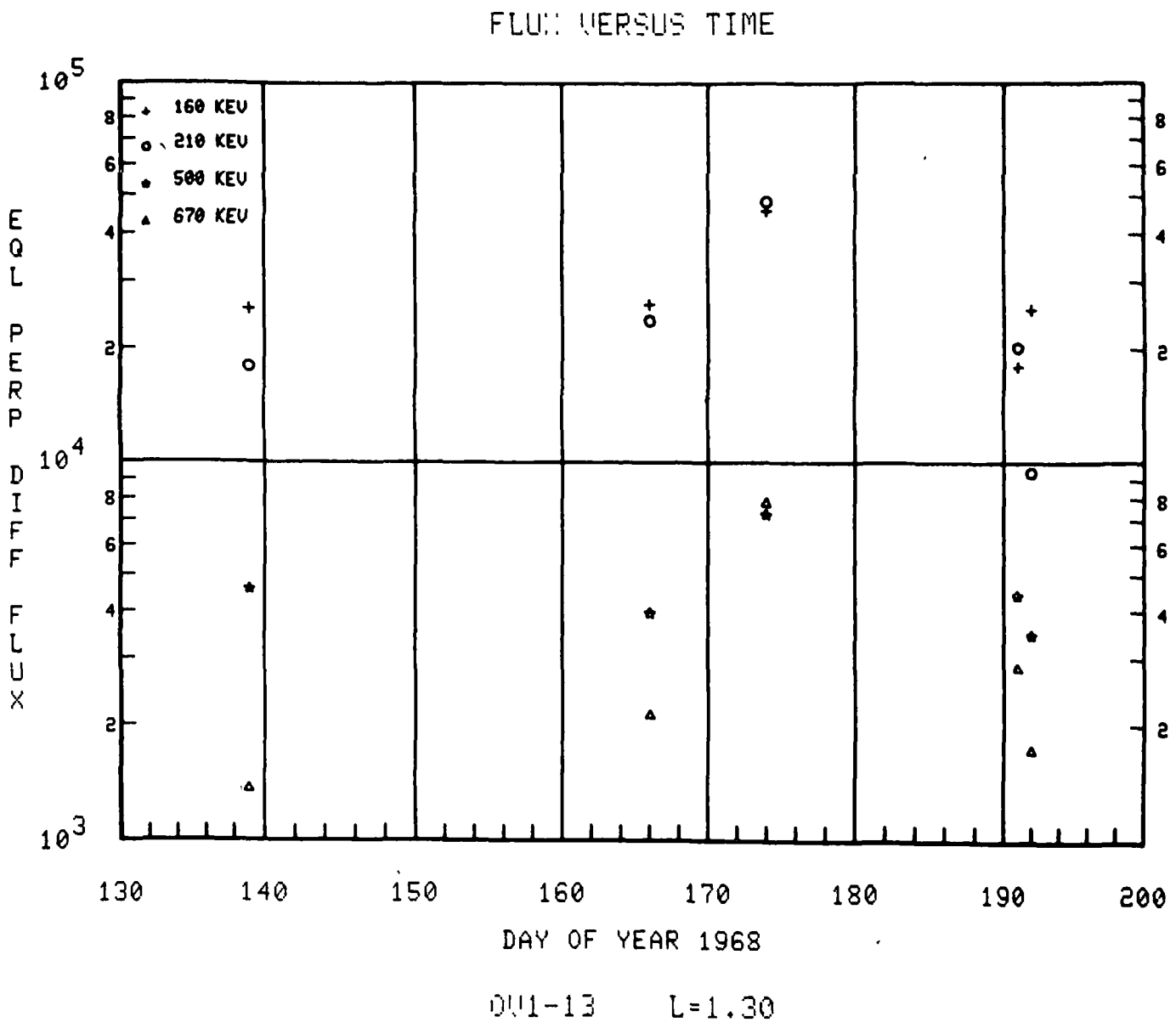
FLUX VERSUS TIME
160 KEV
210 KEV
500 KEV
670 KEV
EQL PERP DIFF FLUX
10^5
10^4
10^3
8
6
4
2
130
140
150
160
170
180
190
200
DAY OF YEAR 1968
OU1-13 L=1.30

Figure 66

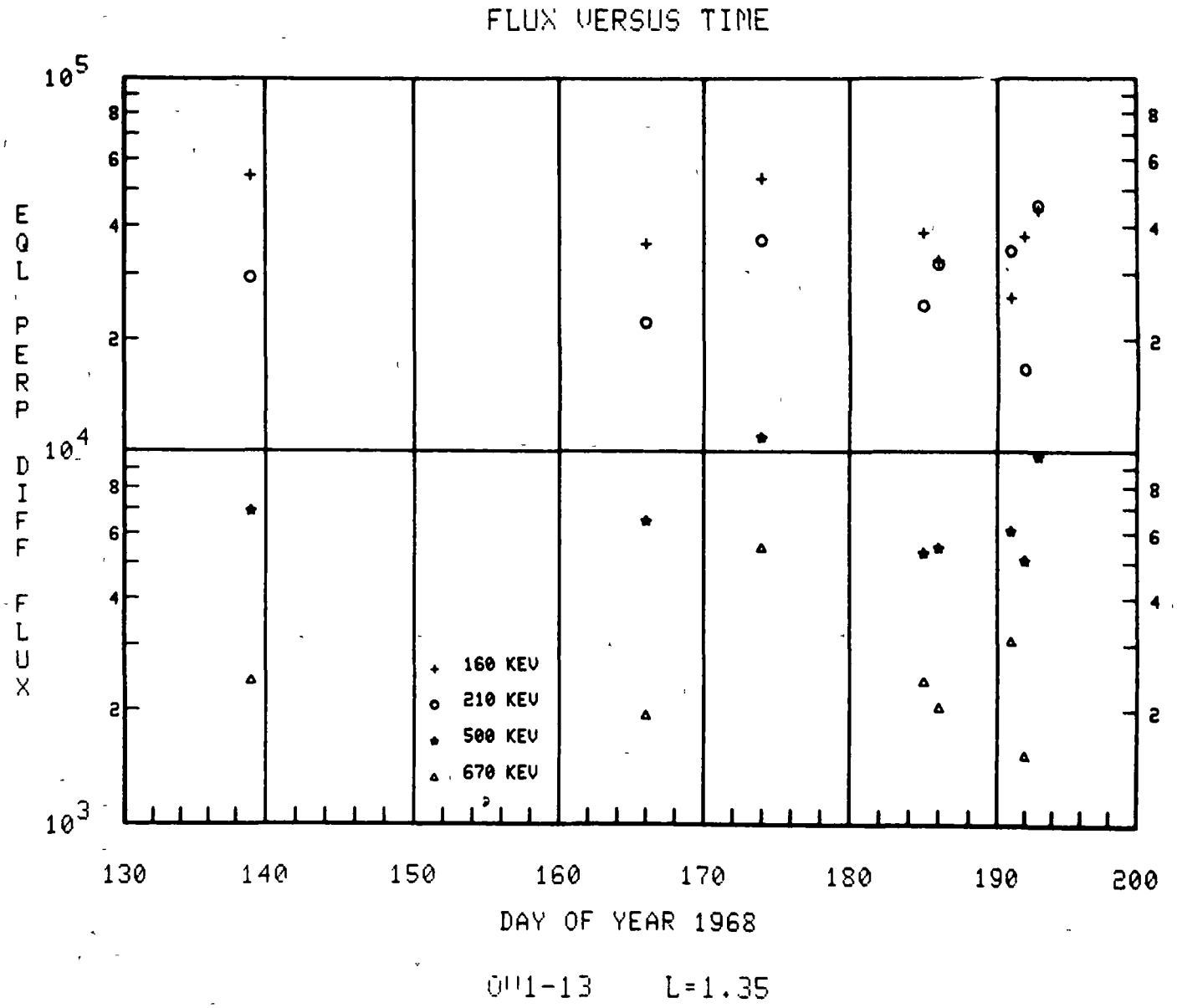
FLUX VERSUS TIME
EQL PERP DIFF FLUX
10^5
8
6
4
2
10^4
8
6
4
2
10^3
160 KEV
210 KEV
500 KEV
670 KEV
130
140
150
160
170
180
190
200
DAY OF YEAR 1968
OGO1-13 L=1.35

Figure 67

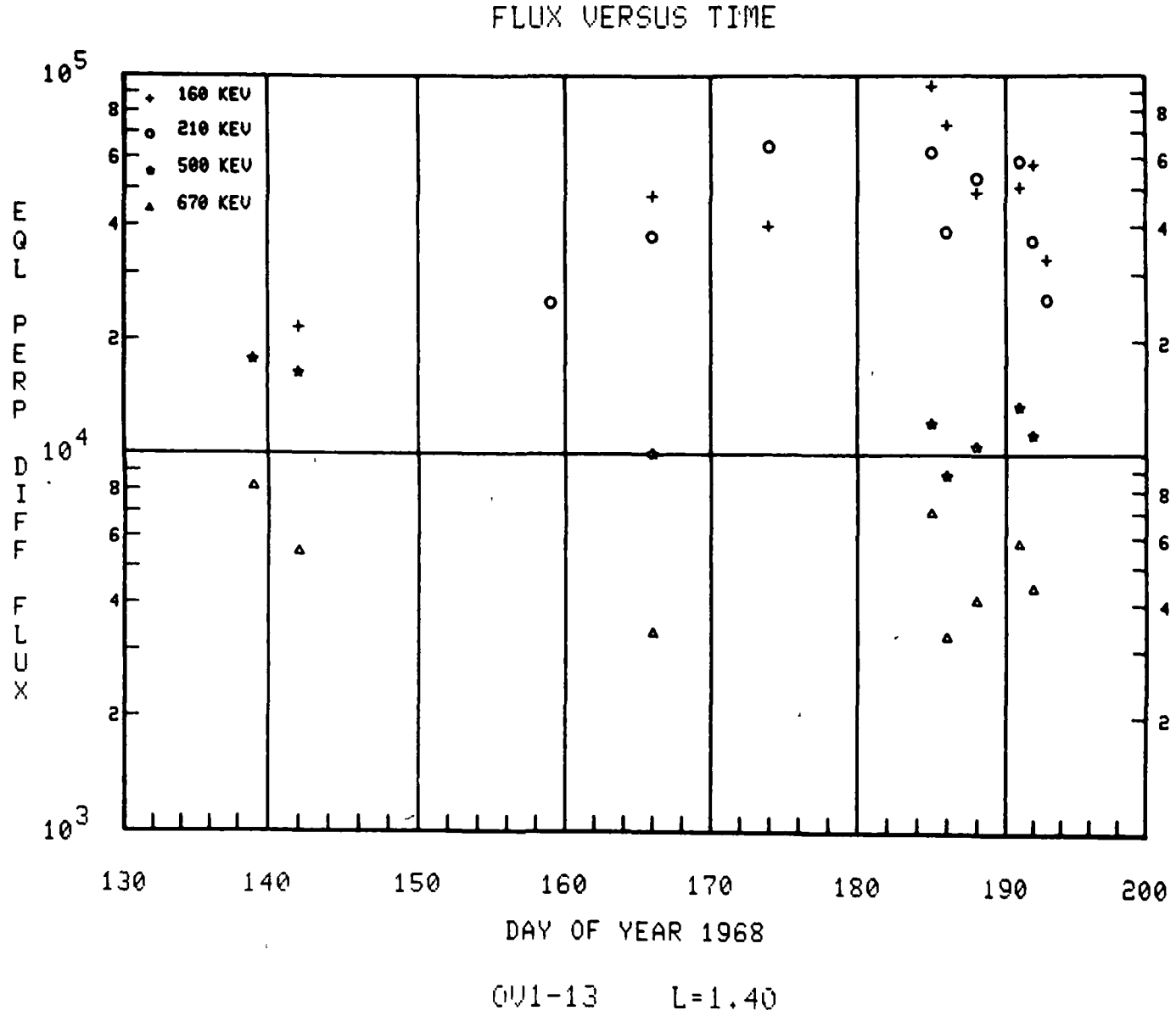
FLUX VERSUS TIME
160 KEV
210 KEV
500 KEV
670 KEV
EQL PERP DIFF FLUX
10^5
10^4
10^3
8
6
4
2
130
140
150
160
170
180
190
200
DAY OF YEAR 1968
OV1-13 L=1.40

Figure 68

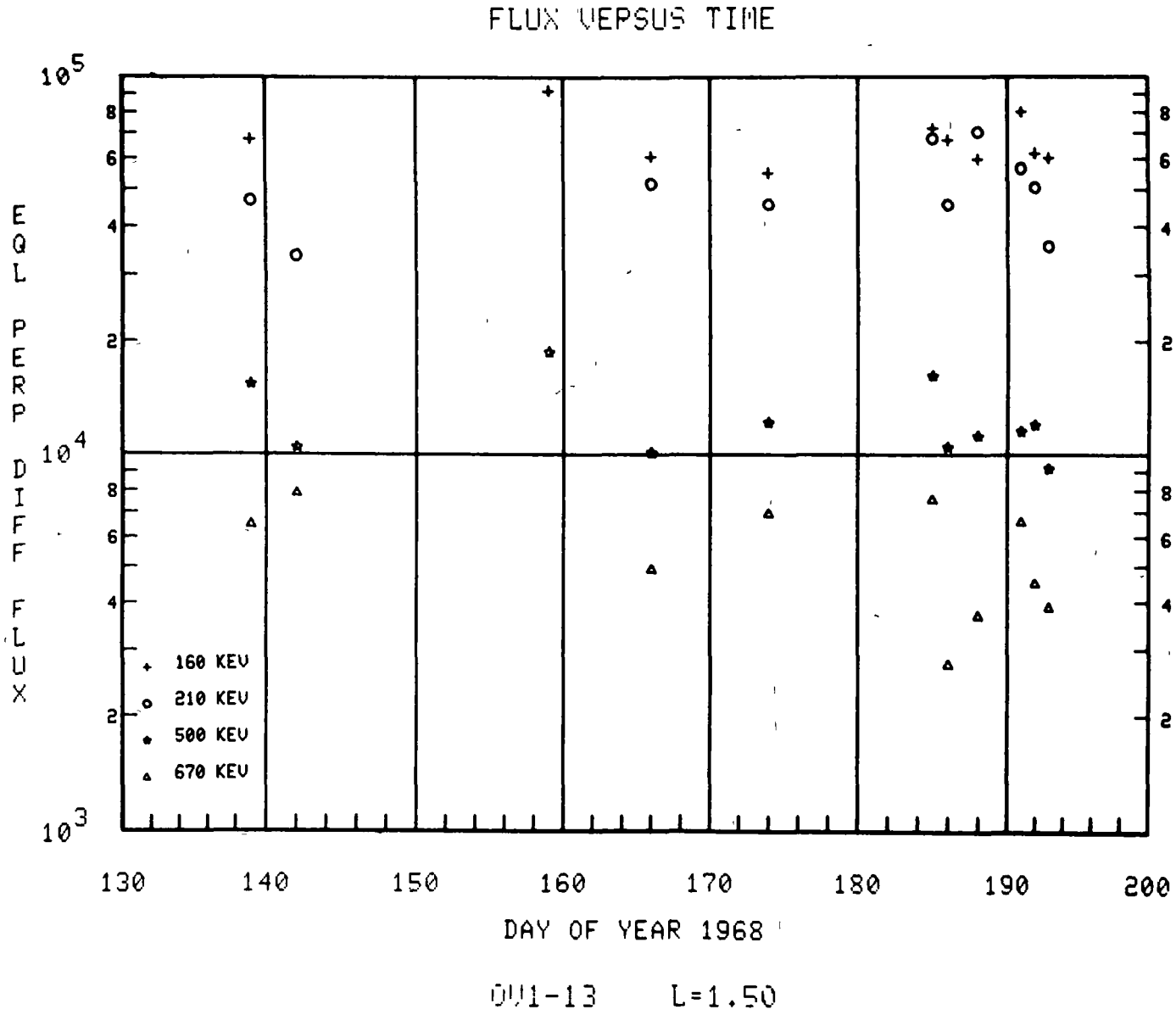
FLUX VERSUS TIME
EQL PERP DIFF FLUX
10^5
10^4
10^3
8
6
4
2
160 KEV
210 KEV
500 KEV
670 KEV
130
140
150
160
170
180
190
200
DAY OF YEAR 1968
OU1-13 L=1.50

Figure 69

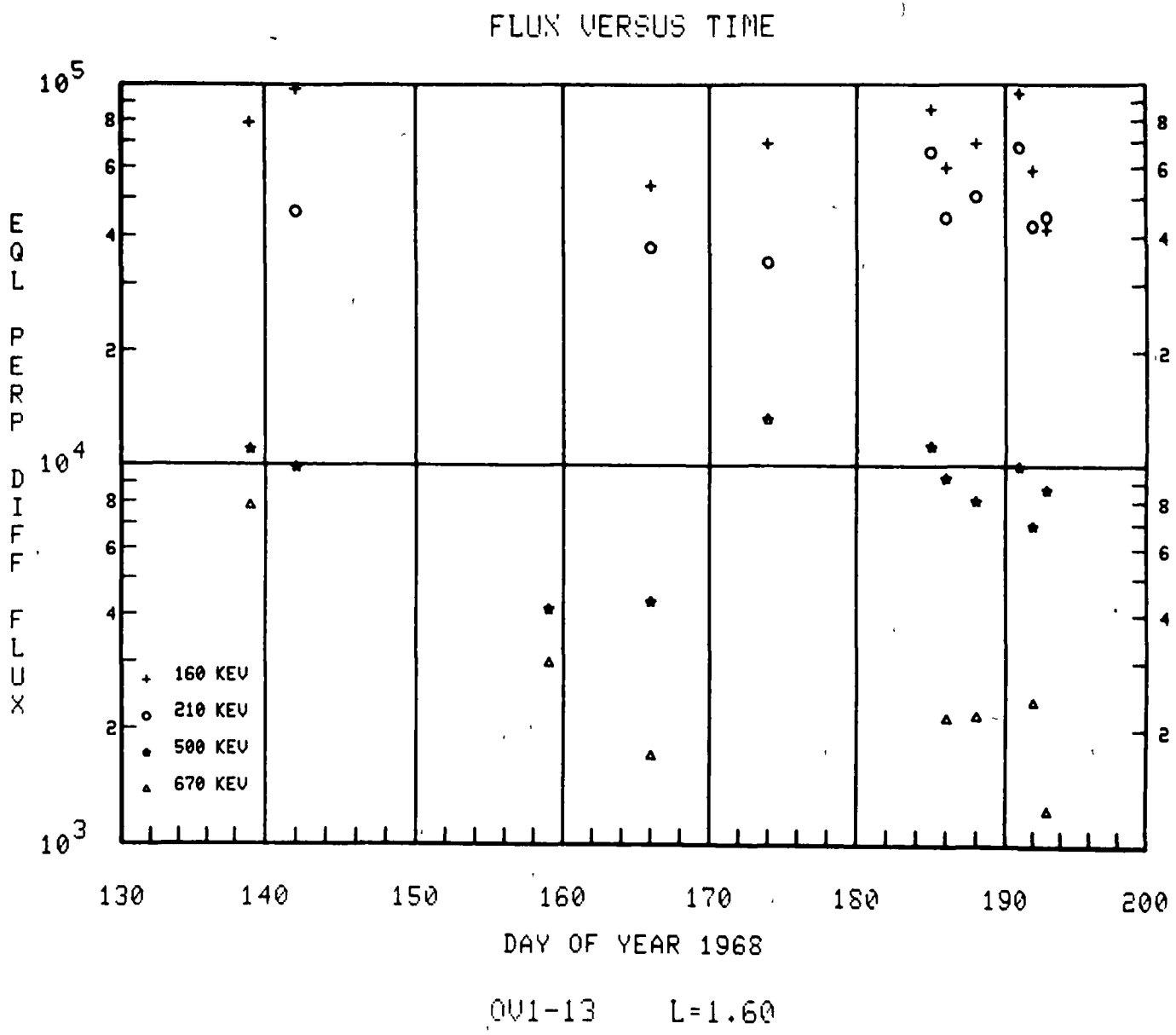
FLUX VERSUS TIME
EQL PERP DIFF FLUX
10^5
8
6
4
2
10^4
8
6
4
2
10^3
160 KEV
210 KEV
500 KEV
670 KEV
130
140
150
160
170
180
190
200
DAY OF YEAR 1968
OV1-13 L=1.60

Figure 70

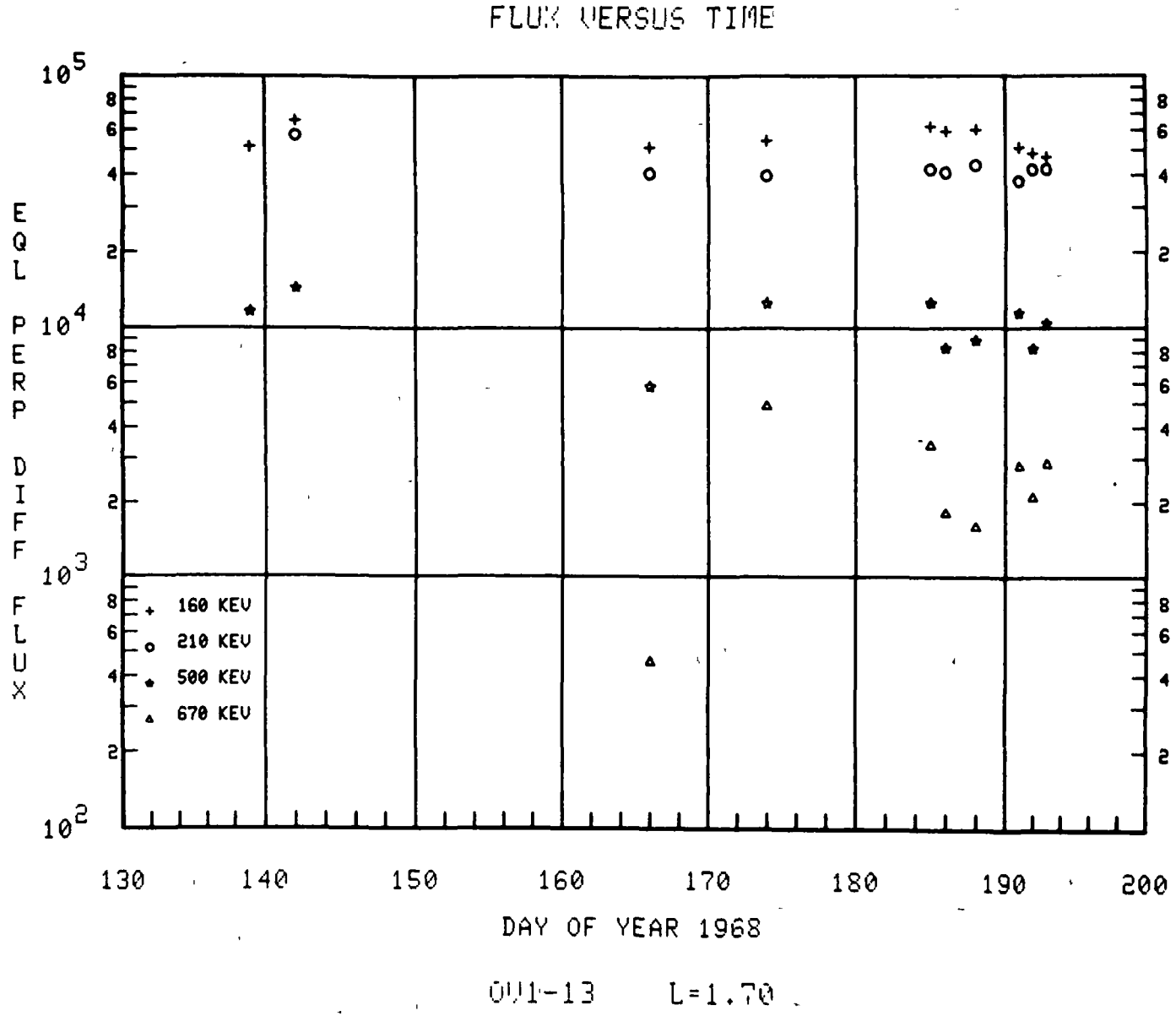
FLUX VERSUS TIME
EQL PERP DIFF FLUX
160 KEV
210 KEV
500 KEV
670 KEV
DAY OF YEAR 1968
OV1-13 L=1.70

Figure 71

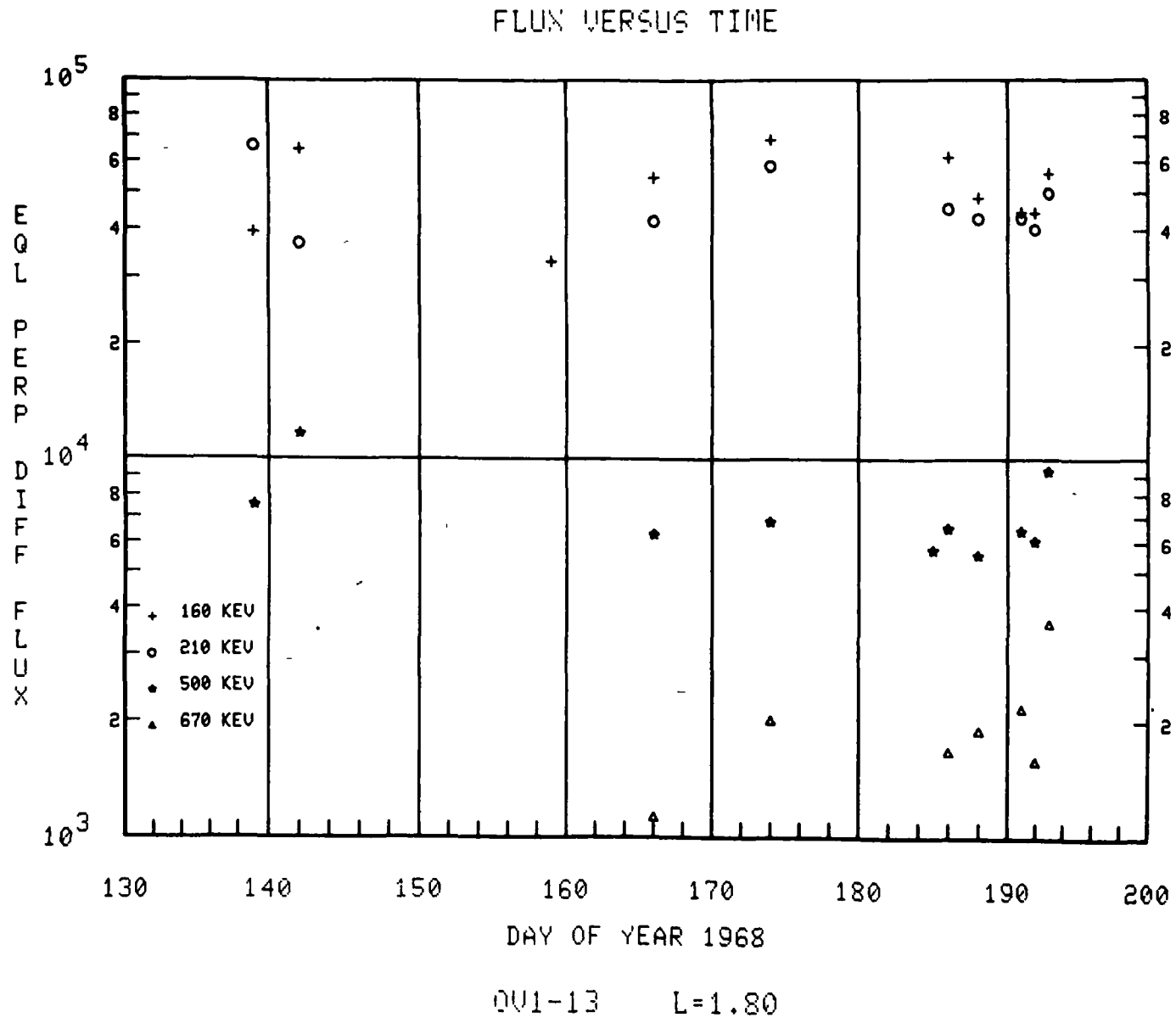
FLUX VERSUS TIME
EQL PERP DIFF FLUX
10^5
10^4
10^3
8
6
4
2
160 KEV
210 KEV
500 KEV
670 KEV
130
140
150
160
170
180
190
200
DAY OF YEAR 1968
OV1-13 L=1.80

Figure 72

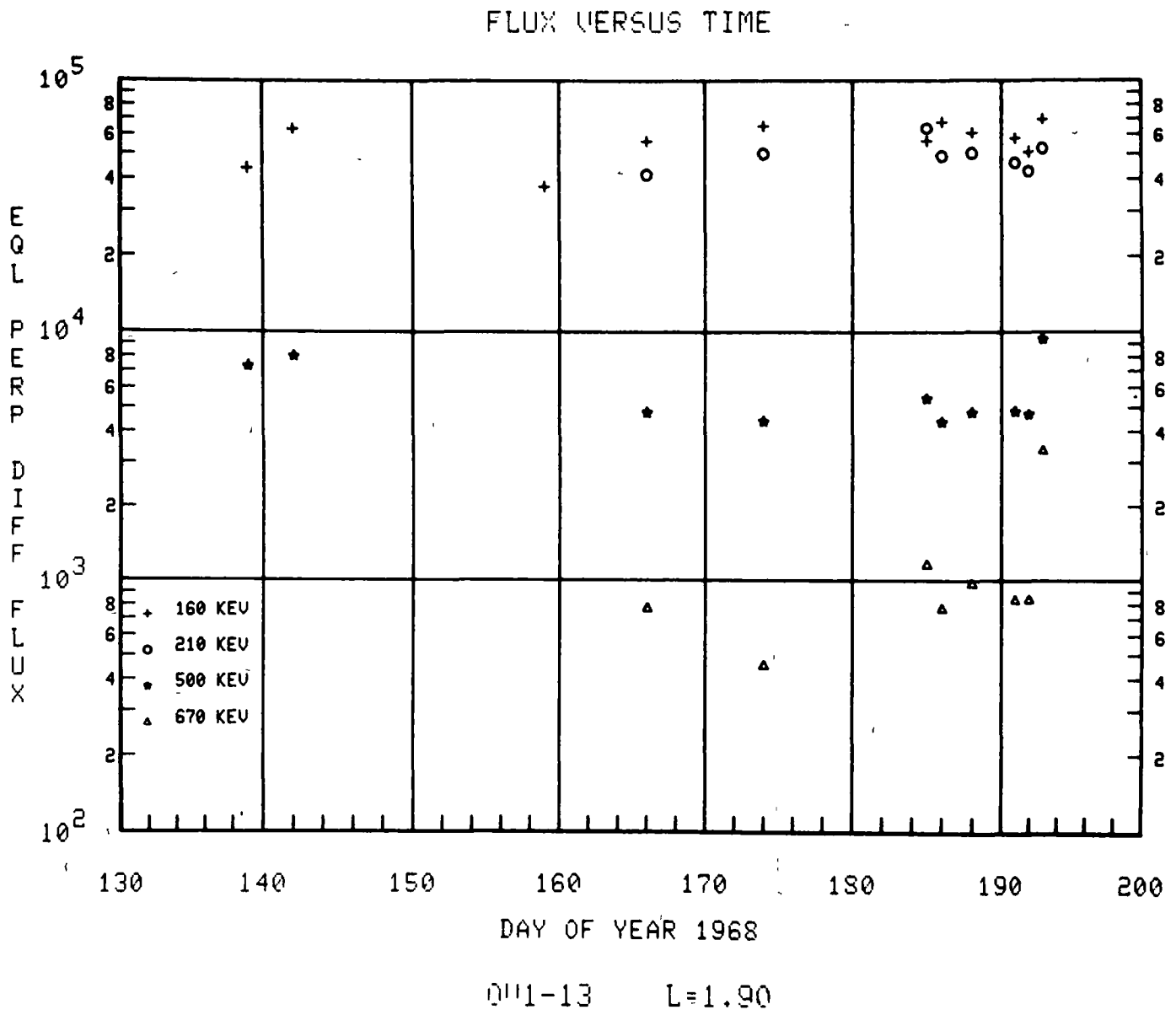
FLUX VERSUS TIME
EQL PERP DIFF FLUX
10^5
10^4
10^3
10^2
160 KEV
210 KEV
500 KEV
670 KEV
130
140
150
160
170
180
190
200
DAY OF YEAR 1968
0111-13 L=1.90

Figure 73

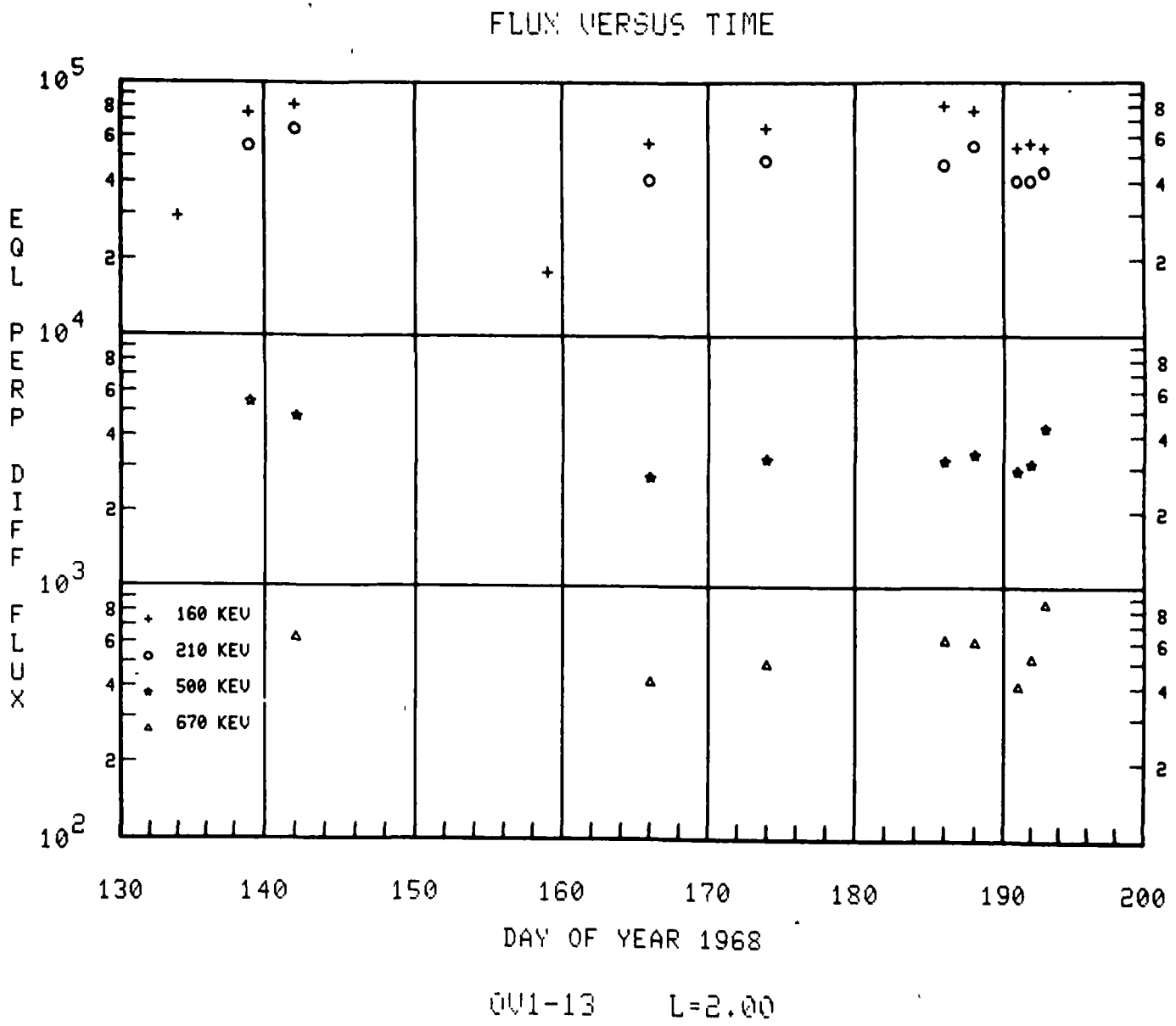
FLUX VERSUS TIME
EQL PERP DIFF FLUX
160 KEV
210 KEV
500 KEV
670 KEV
DAY OF YEAR 1968
OV1-13 L=2.00

Figure 74

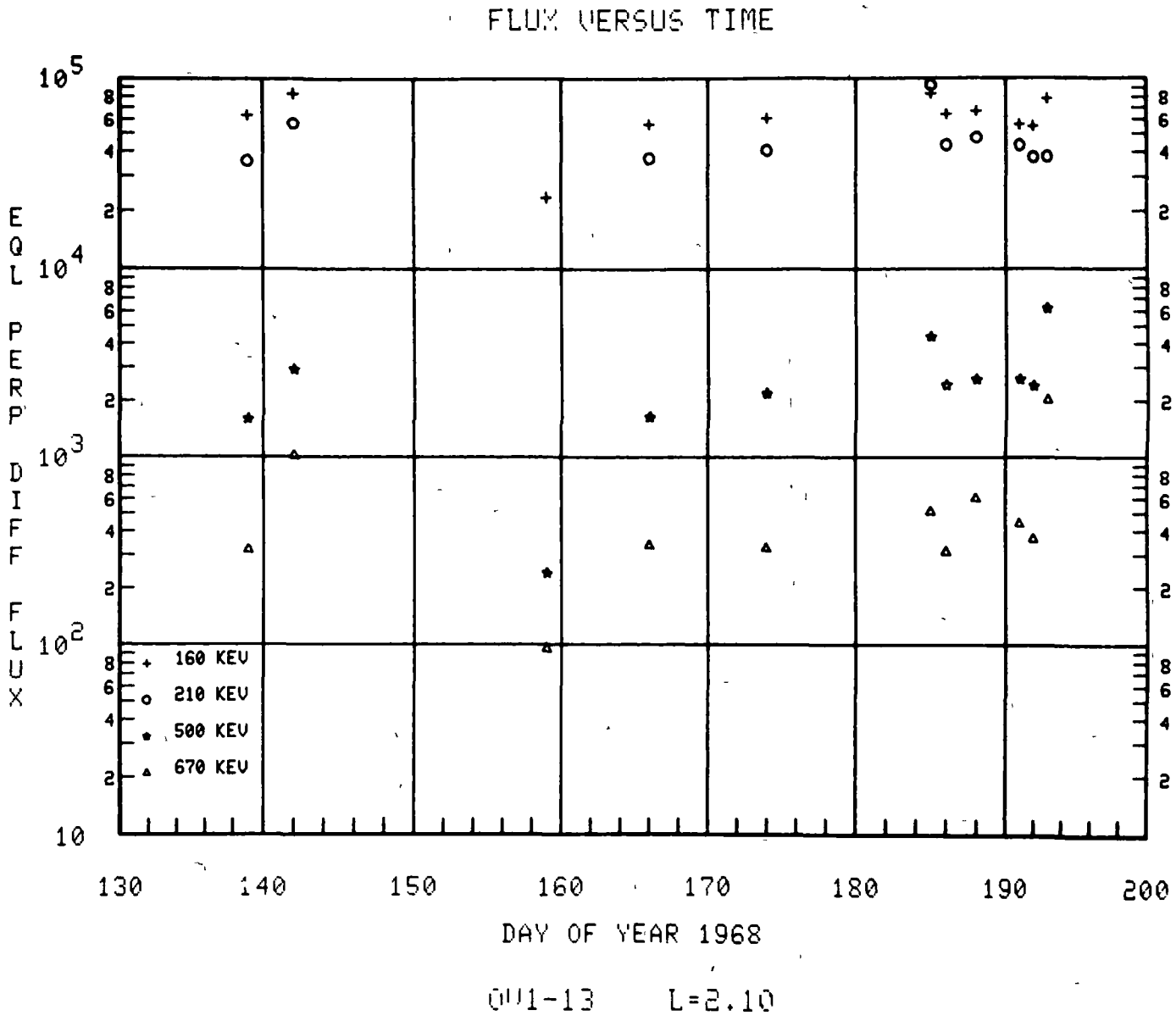
FLUX VERSUS TIME
EQL PERP DIFF FLUX
10^5
10^4
10^3
10^2
10
8
6
4
2
160 KEV
210 KEV
500 KEV
670 KEV
130
140
150
160
170
180
190
200
DAY OF YEAR 1968
OV1-13 L=2.10

Figure 75

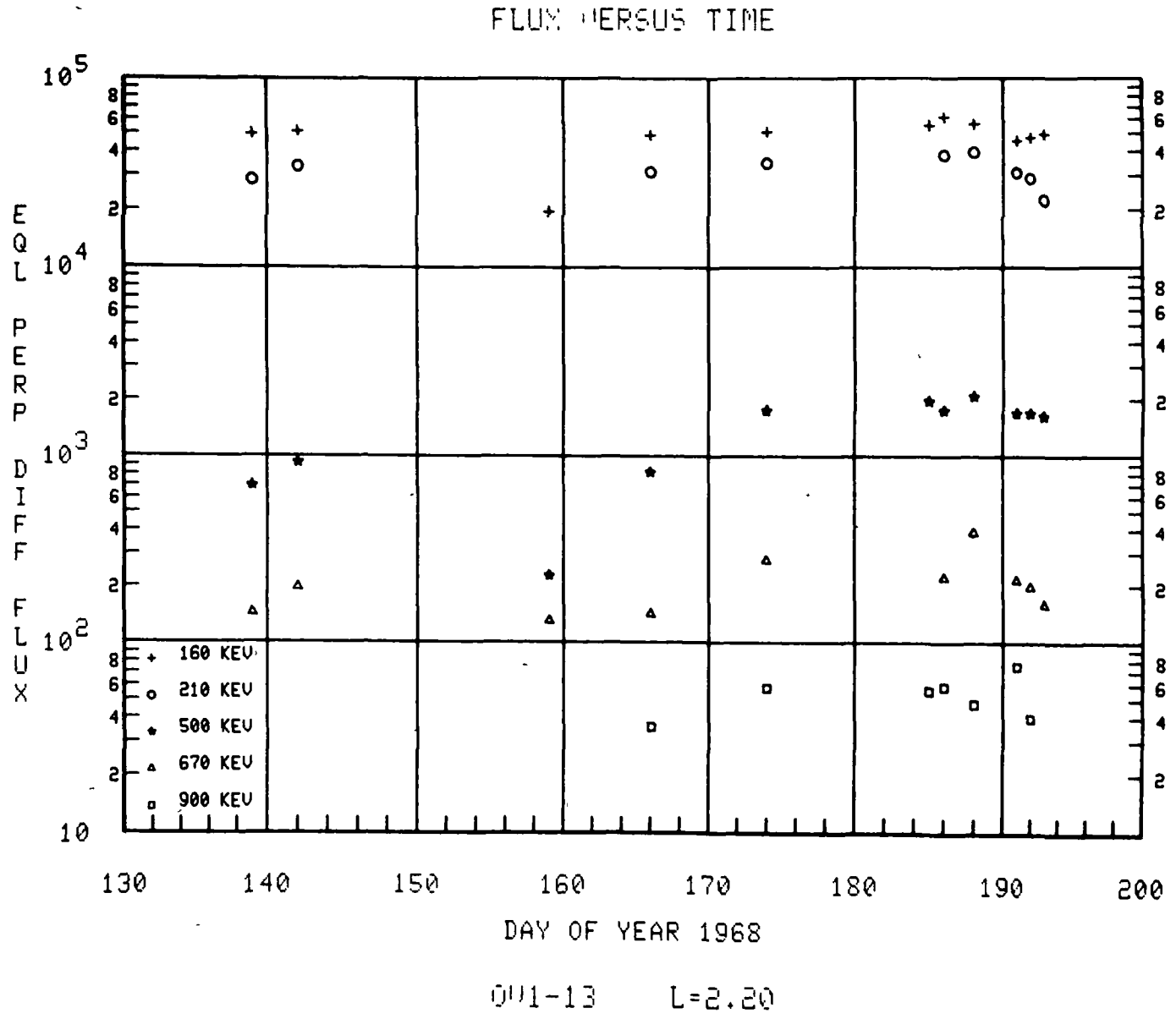
FLUX VERSUS TIME
EQL PERP DIFF FLUX
10^5
10^4
10^3
10^2
10
160 KEV
210 KEV
500 KEV
670 KEV
900 KEV
130
140
150
160
170
180
190
200
DAY OF YEAR 1968
OU1-13 L=2.20

Figure 76

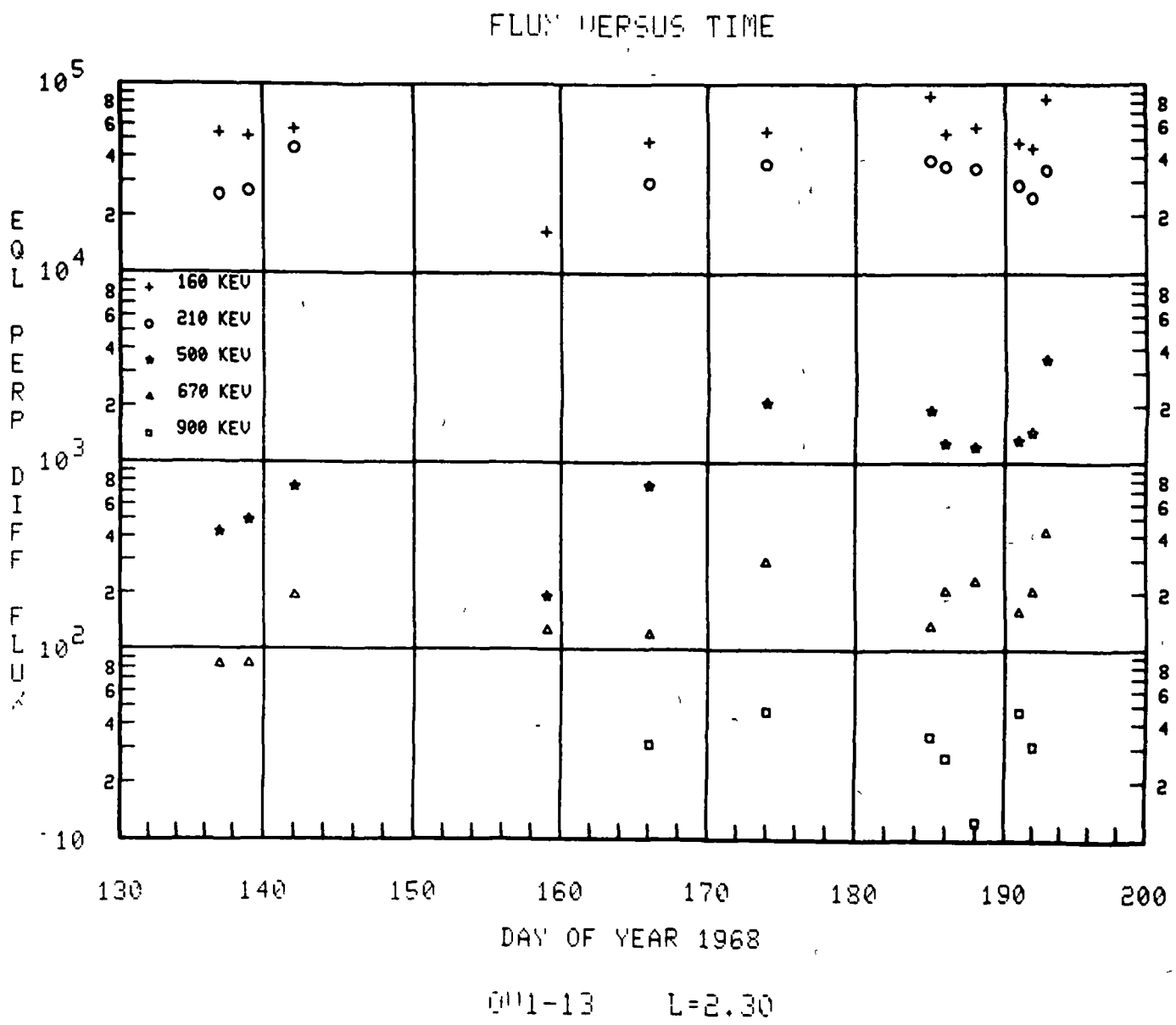
FLUX VERSUS TIME
EQL PERP DIFF FLUX
160 KEV
210 KEV
500 KEV
670 KEV
900 KEV
DAY OF YEAR 1968
0001-13 L=2.30

Figure 77

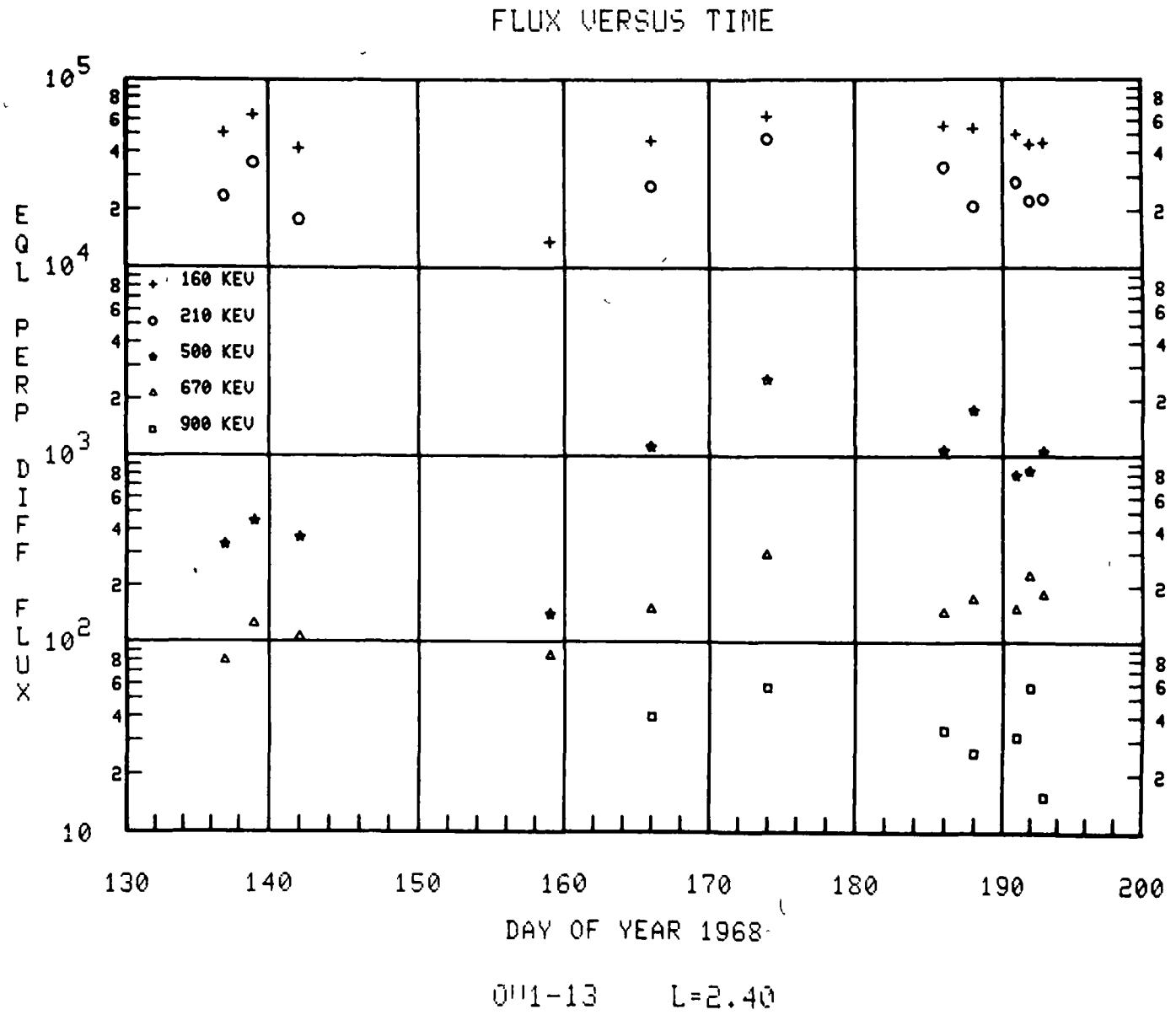
FLUX VERSUS TIME
EQL PERP DIFF FLUX
160 KEV
210 KEV
500 KEV
670 KEV
900 KEV
DAY OF YEAR 1968
0111-13 L=2.40

Figure 78

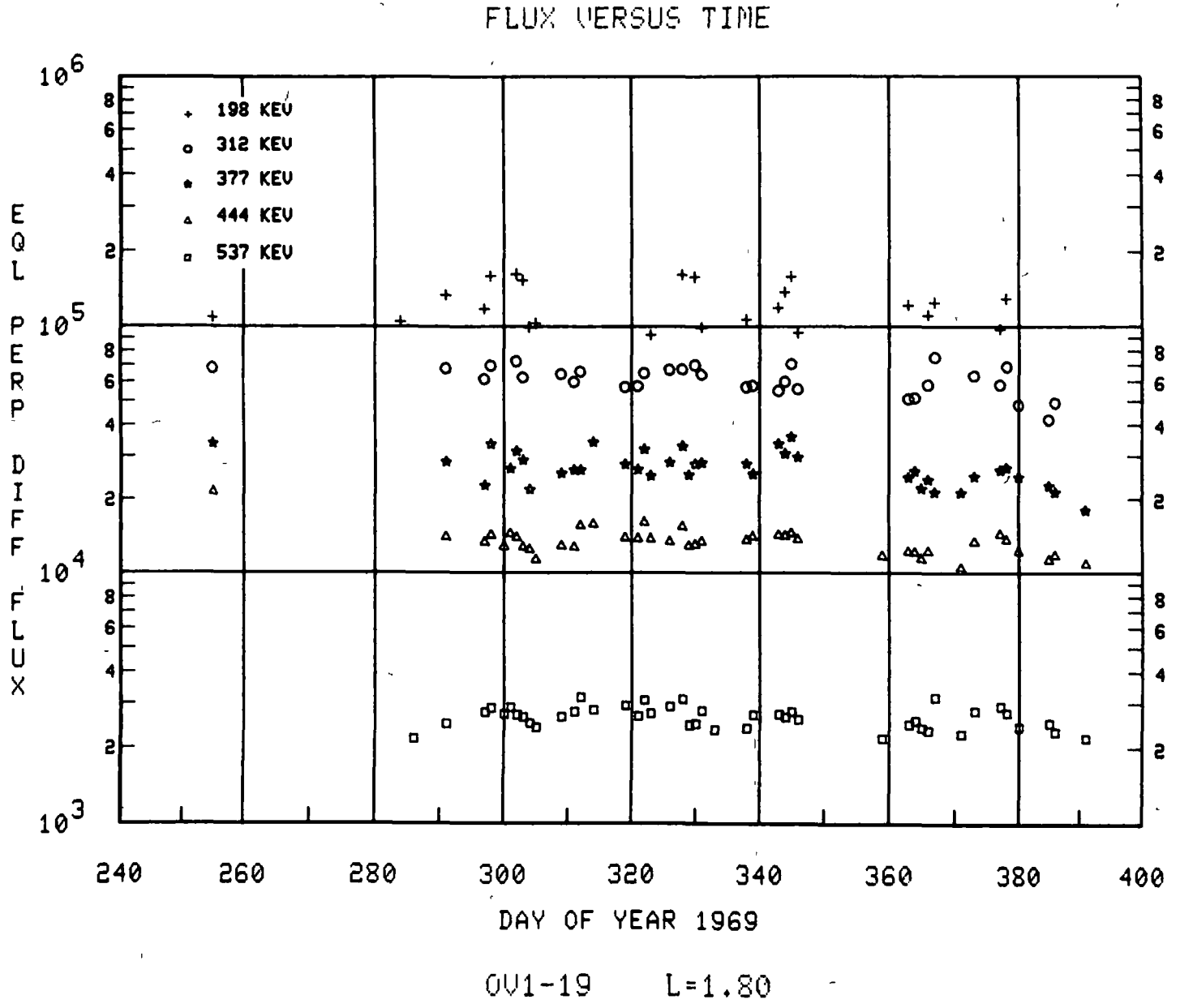
FLUX VERSUS TIME
198 KEV
312 KEV
377 KEV
444 KEV
537 KEV
EQL PER DIFF FLUX
DAY OF YEAR 1969
OV1-19 L=1.80

Figure 79

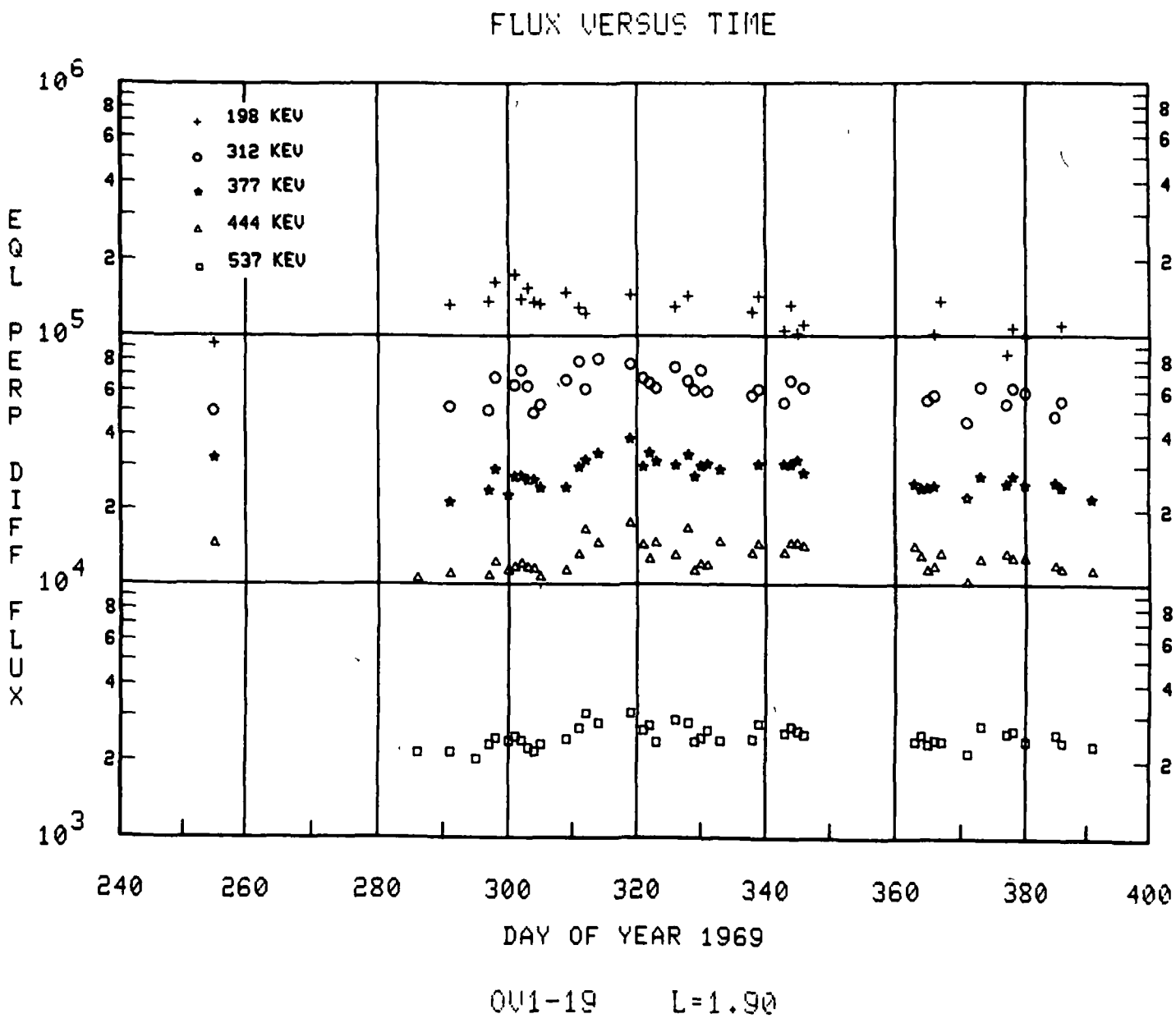
FLUX VERSUS TIME
198 KEV
312 KEV
377 KEV
444 KEV
537 KEV
EQL PERP DIFF FLUX
DAY OF YEAR 1969
OV1-19 L=1.90

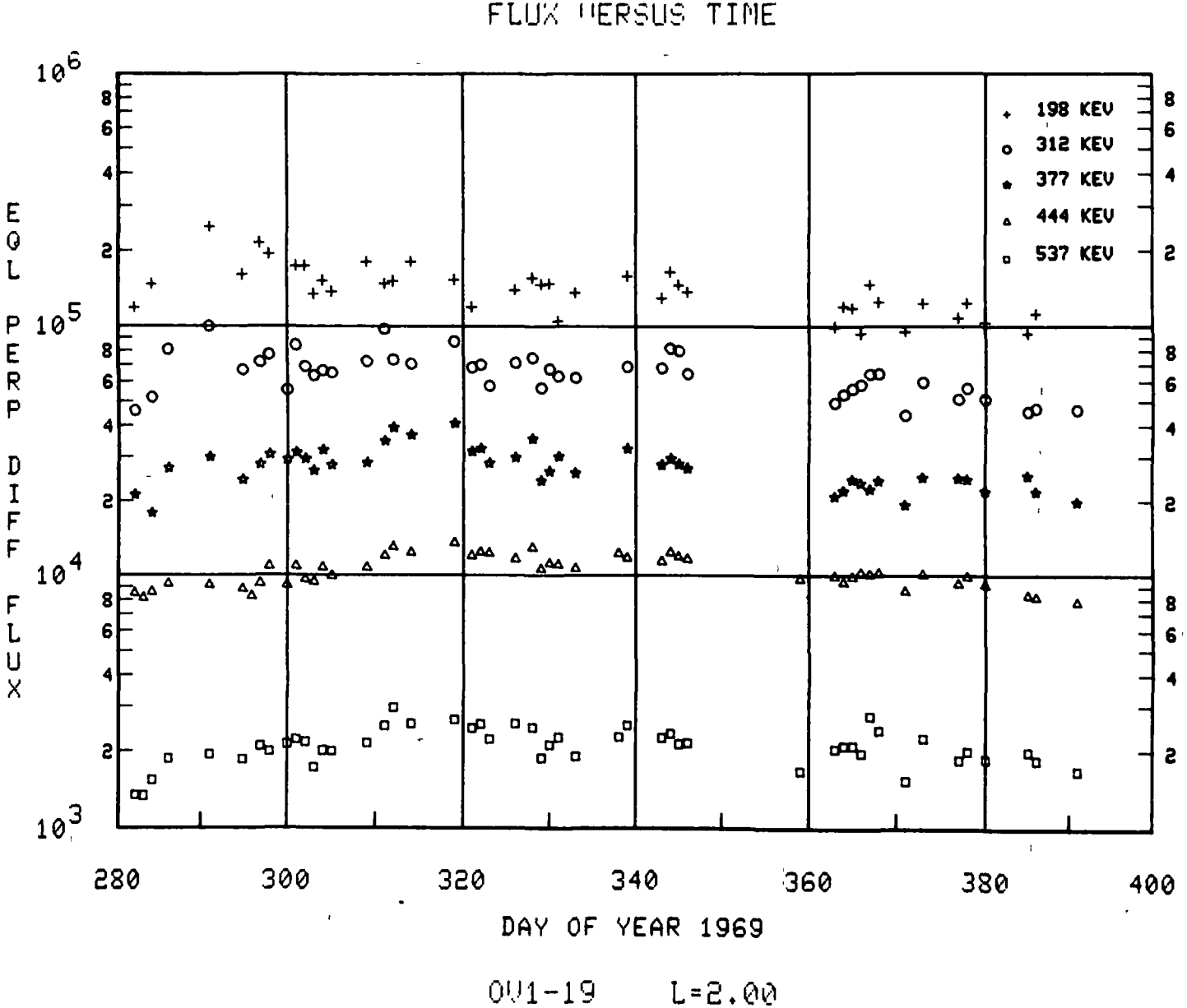
FLUX VERSUS TIME
EQL PERP DIFF FLUX
198 KEV
312 KEV
377 KEV
444 KEV
537 KEV
DAY OF YEAR 1969
OV1-19 L=2.00

Figure 81

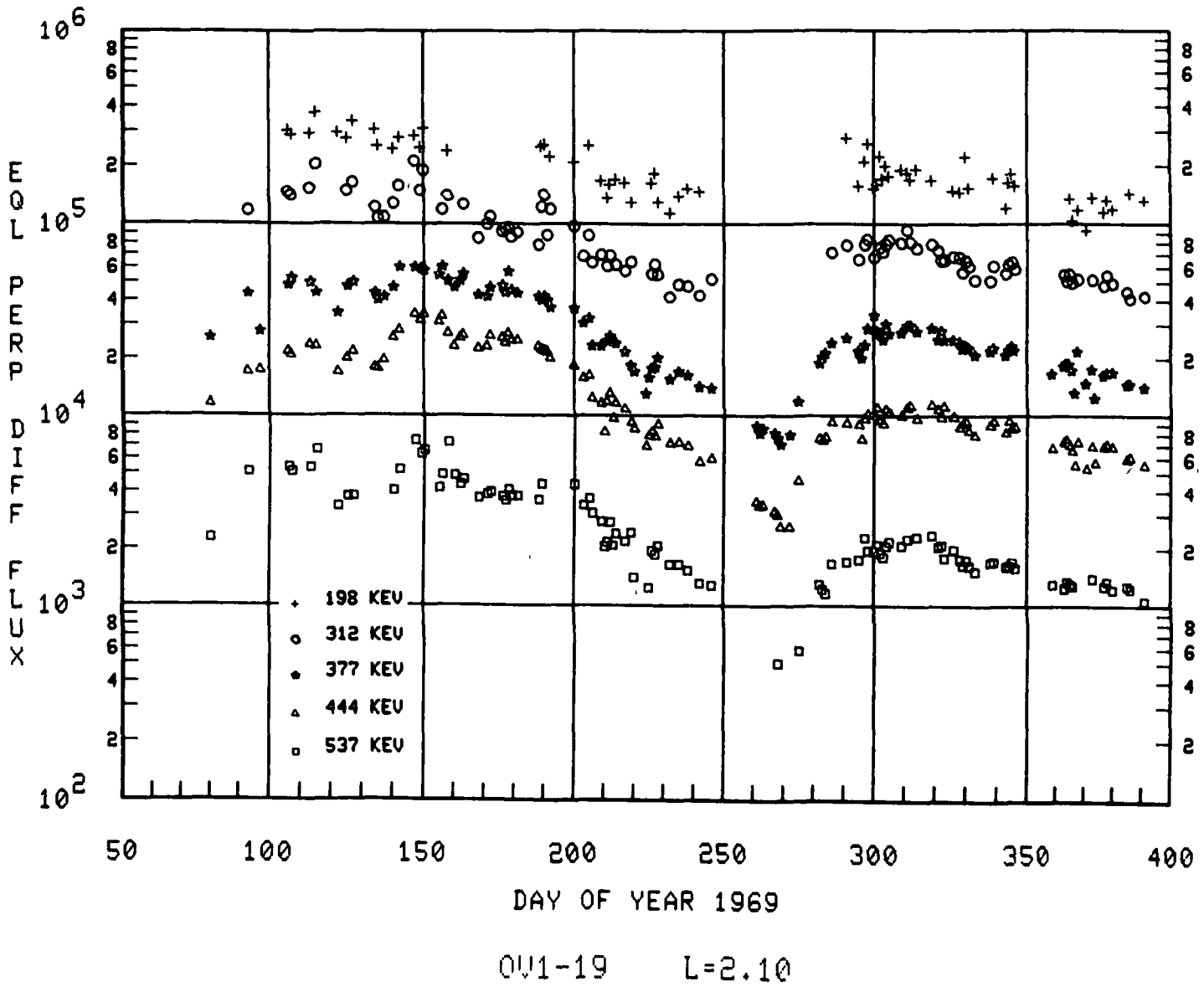
FLUX VERSUS TIME
EQL PERP DIFF FLUX
198 KEV
312 KEV
377 KEV
444 KEV
537 KEV
DAY OF YEAR 1969
OV1-19 L=2.10

Figure 82

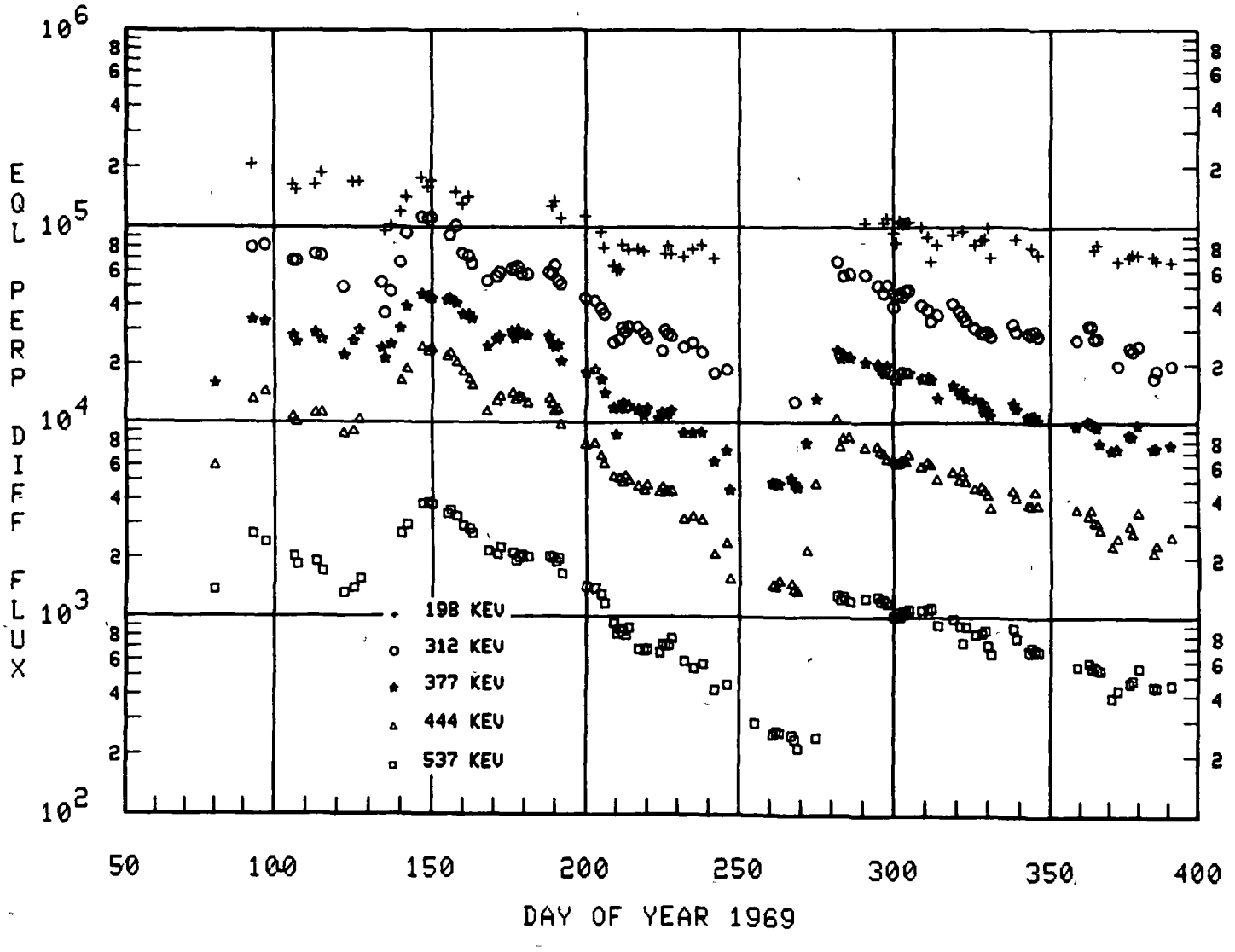
FLUX VERSUS TIME
EQL PERP DIFF FLUX
198 KEV
312 KEV
377 KEV
444 KEV
537 KEV
DAY OF YEAR 1969
OV1-19 L=2.20

Figure 83

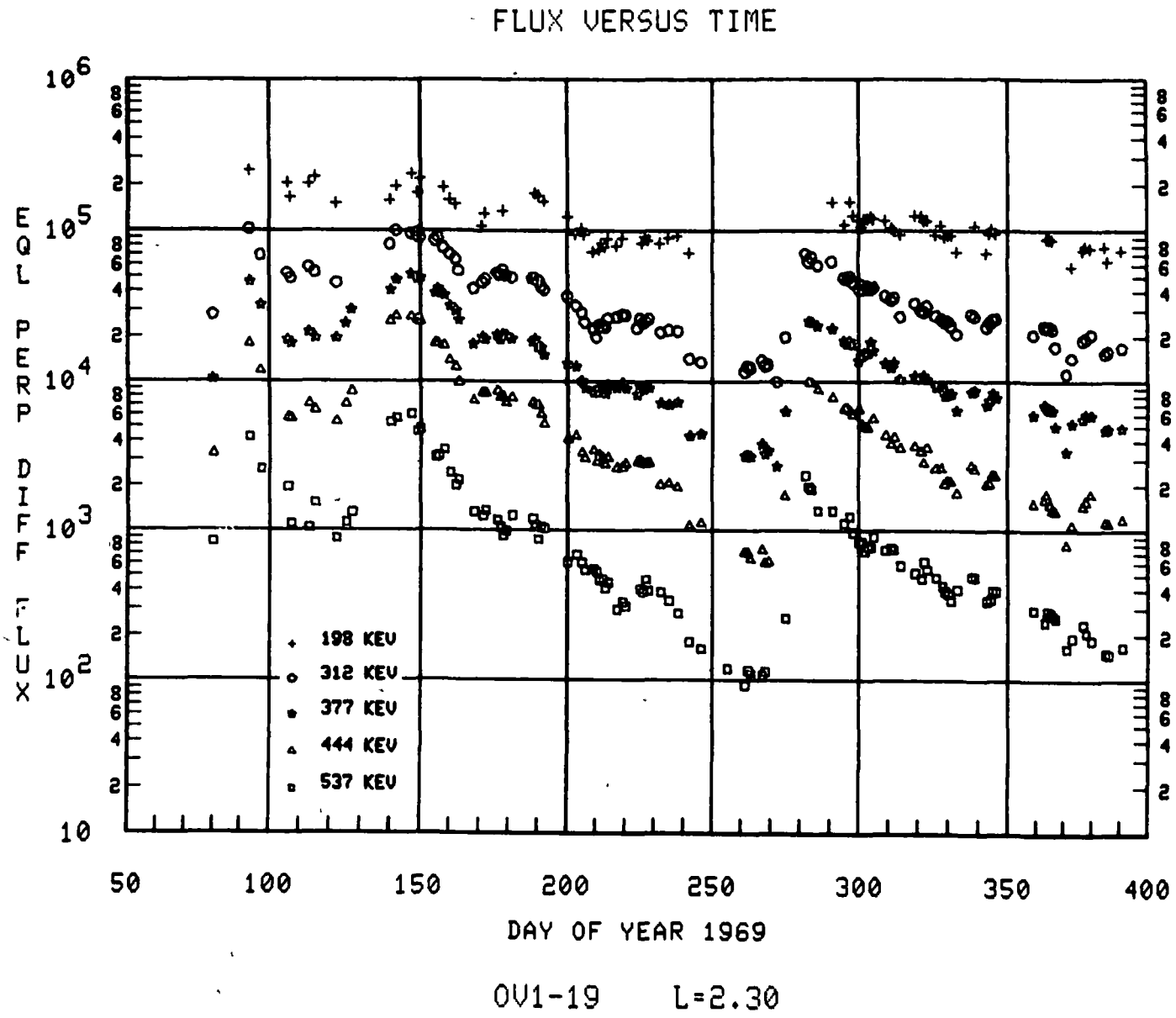
FLUX VERSUS TIME
EQ PERP DIFF FLUX
198 KEV
312 KEV
377 KEV
444 KEV
537 KEV
DAY OF YEAR 1969
OV1-19 L=2.30

Figure 84

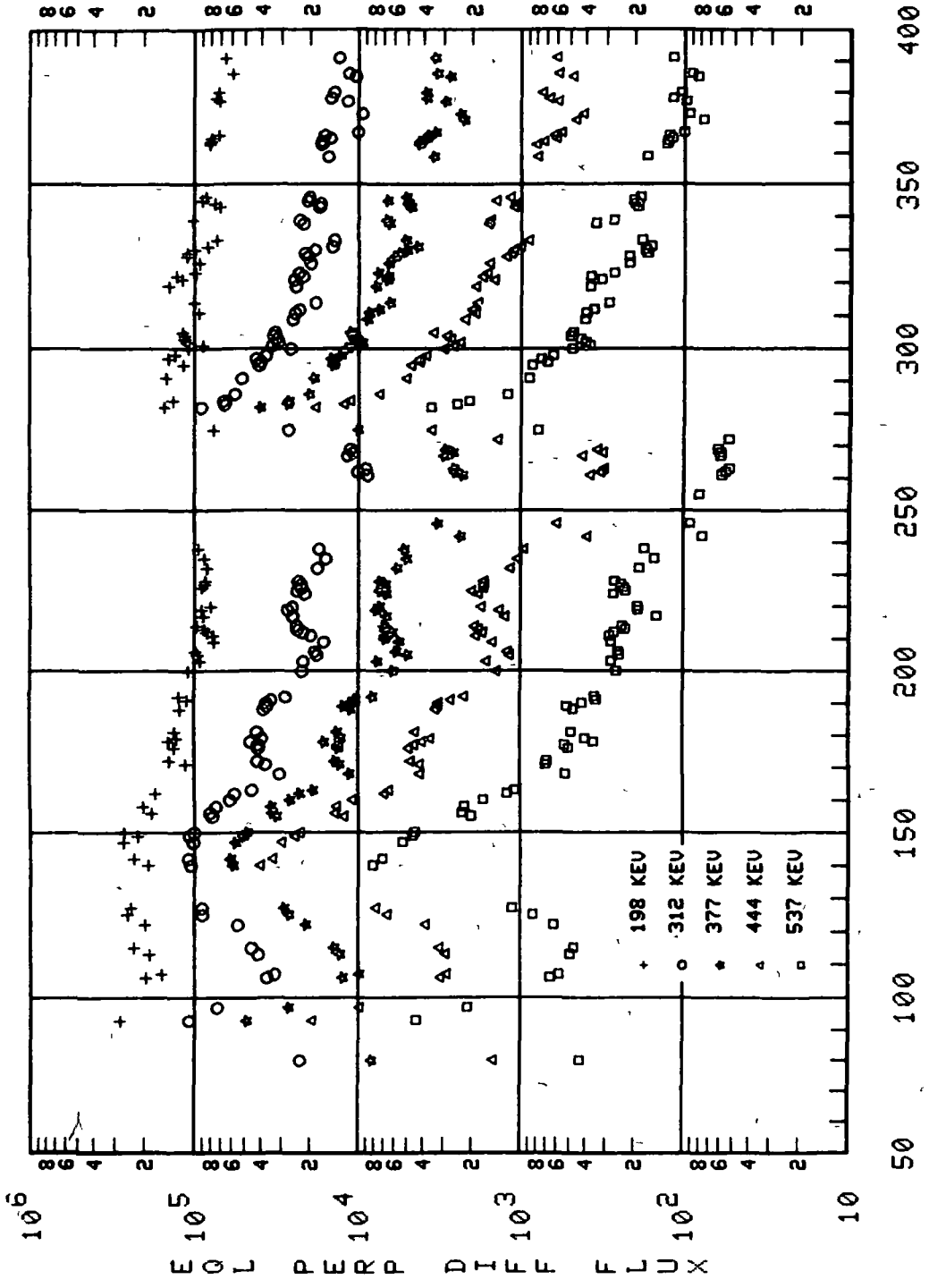
FLUX VERSUS TIME
EQL PERP DIFF FLUX
DAY OF YEAR 1969
OV1-19 L=2.40
198 KEV
312 KEV
377 KEV
444 KEV
537 KEV

Figure 85

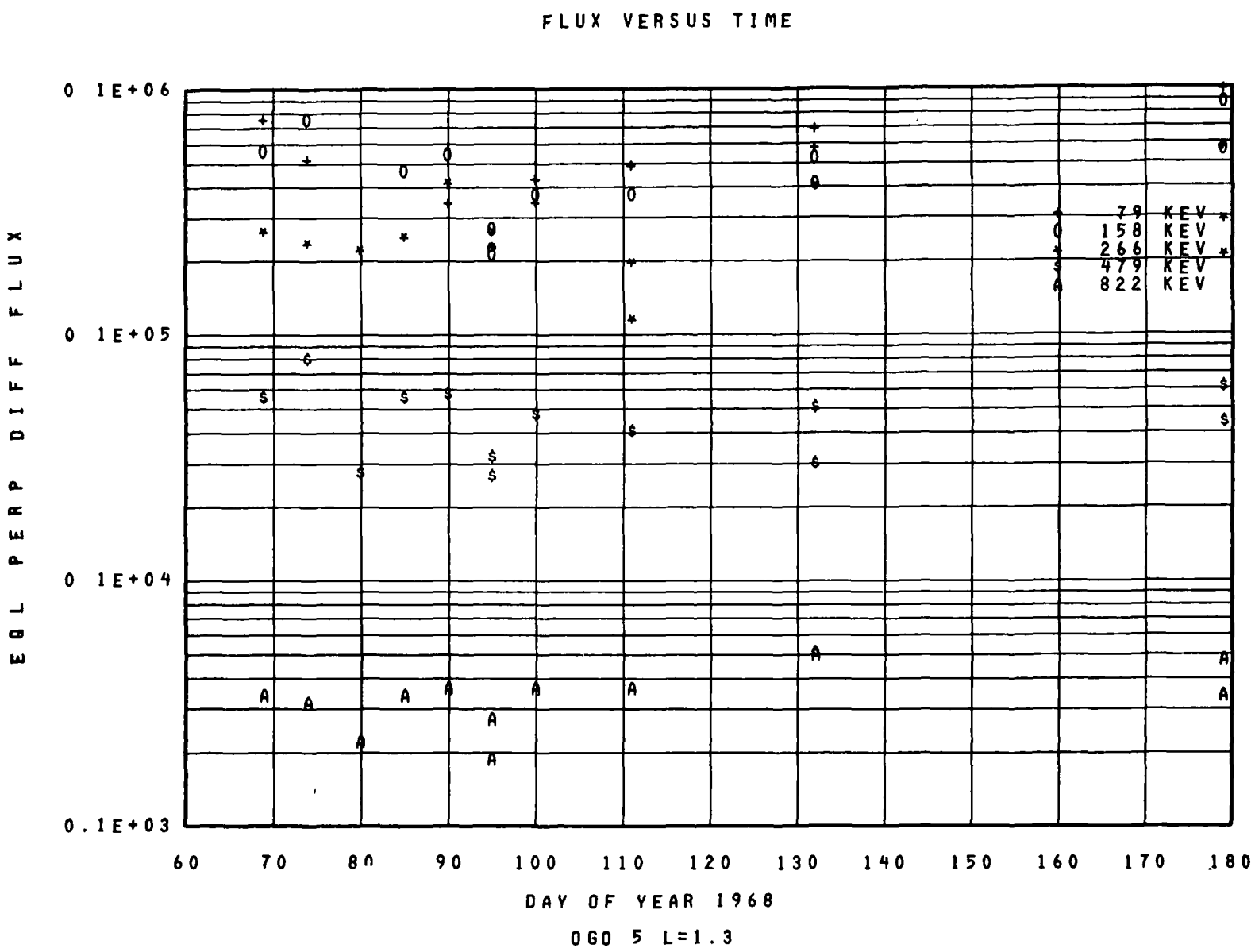
FLUX VERSUS TIME
EQL PERP DIFF FLUX
0 1E+06
0 1E+05
0 1E+04
0.1E+03
79 KEV
158 KEV
266 KEV
479 KEV
822 KEV
60
70
80
90
100
110
120
130
140
150
160
170
180
DAY OF YEAR 1968
OGO 5 L=1.3

Figure 86

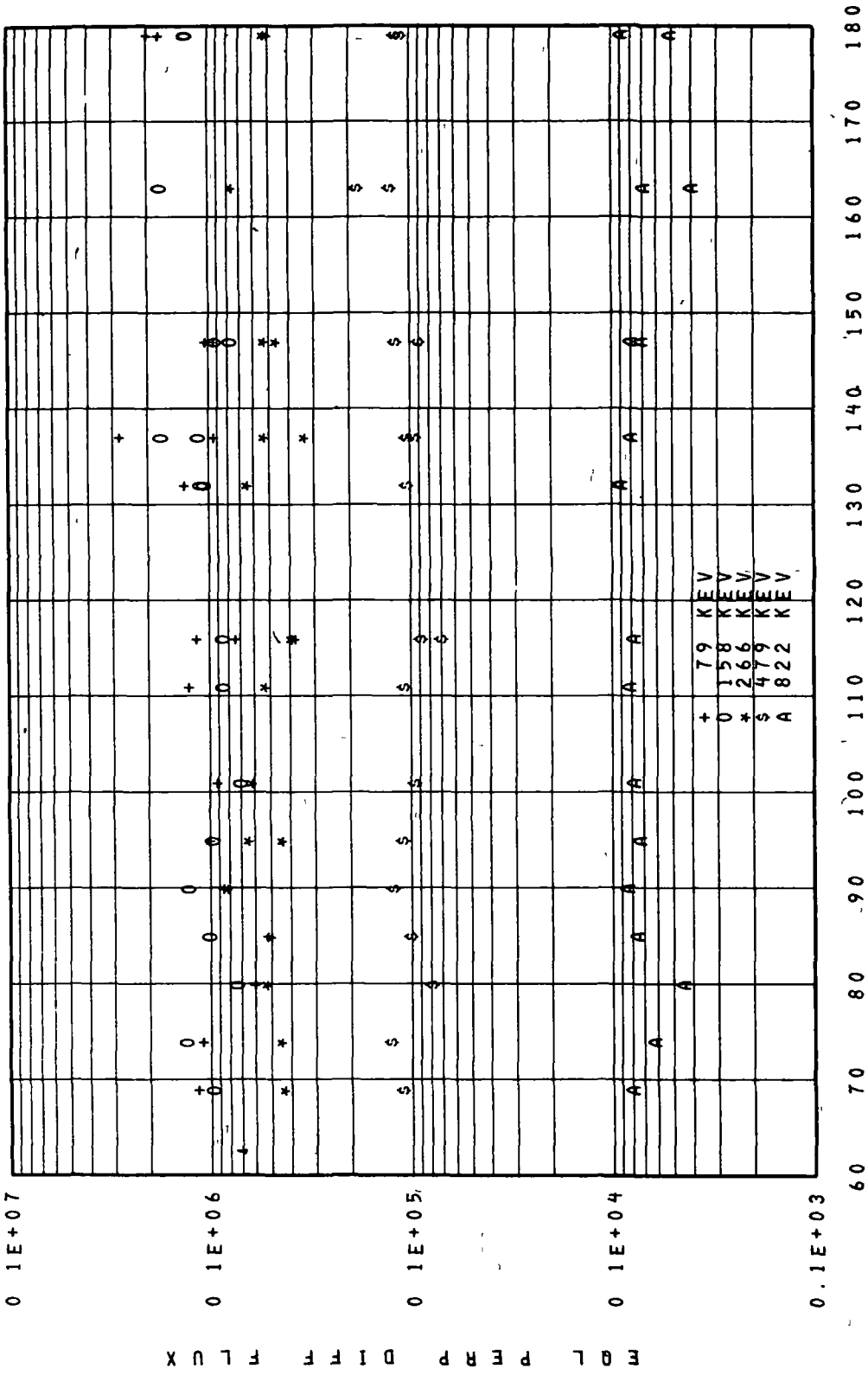
FLUX VERSUS TIME
EQL PERP DIFF FLUX
0 1E+07
0 1E+06
0 1E+05
0 1E+04
0.1E+03
60
70
80
90
100
110
120
130
140
150
160
170
180
DAY OF YEAR 1968
OGO 5 L=1.35
+ 79 KEV
0 158 KEV
* 266 KEV
$ 479 KEV
A 822 KEV

Figure 87

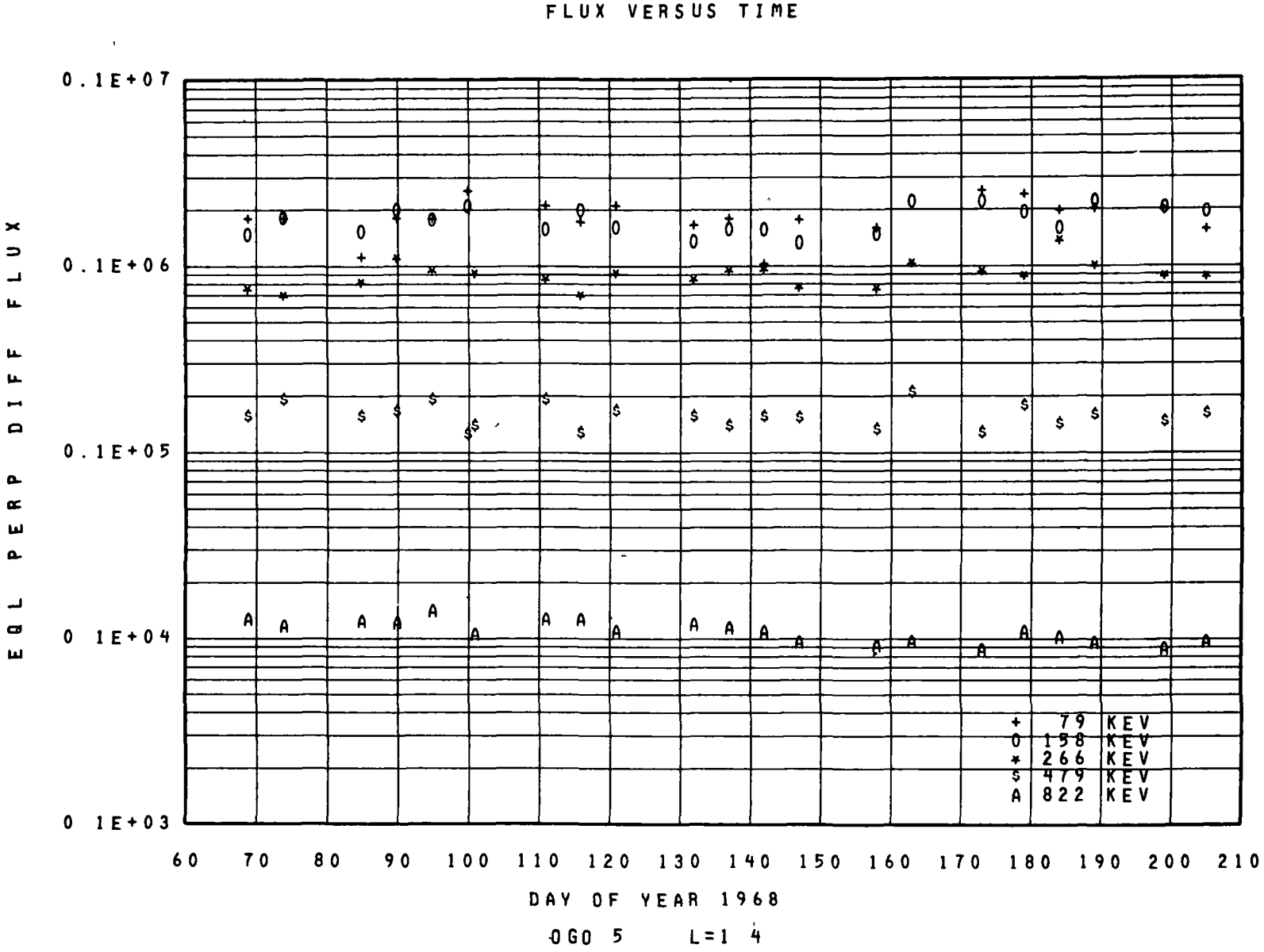
FLUX VERSUS TIME
EQL PERP DIFF FLUX
0.1E+07
0.1E+06
0.1E+05
0 1E+04
0 1E+03
60 70 80 90 100 110 120 130 140 150 160 170 180 190 200 210
DAY OF YEAR 1968
OGO 5 L=1 4
+ 79 KEV
0 158 KEV
* 266 KEV
$ 479 KEV
A 822 KEV

Figure 88

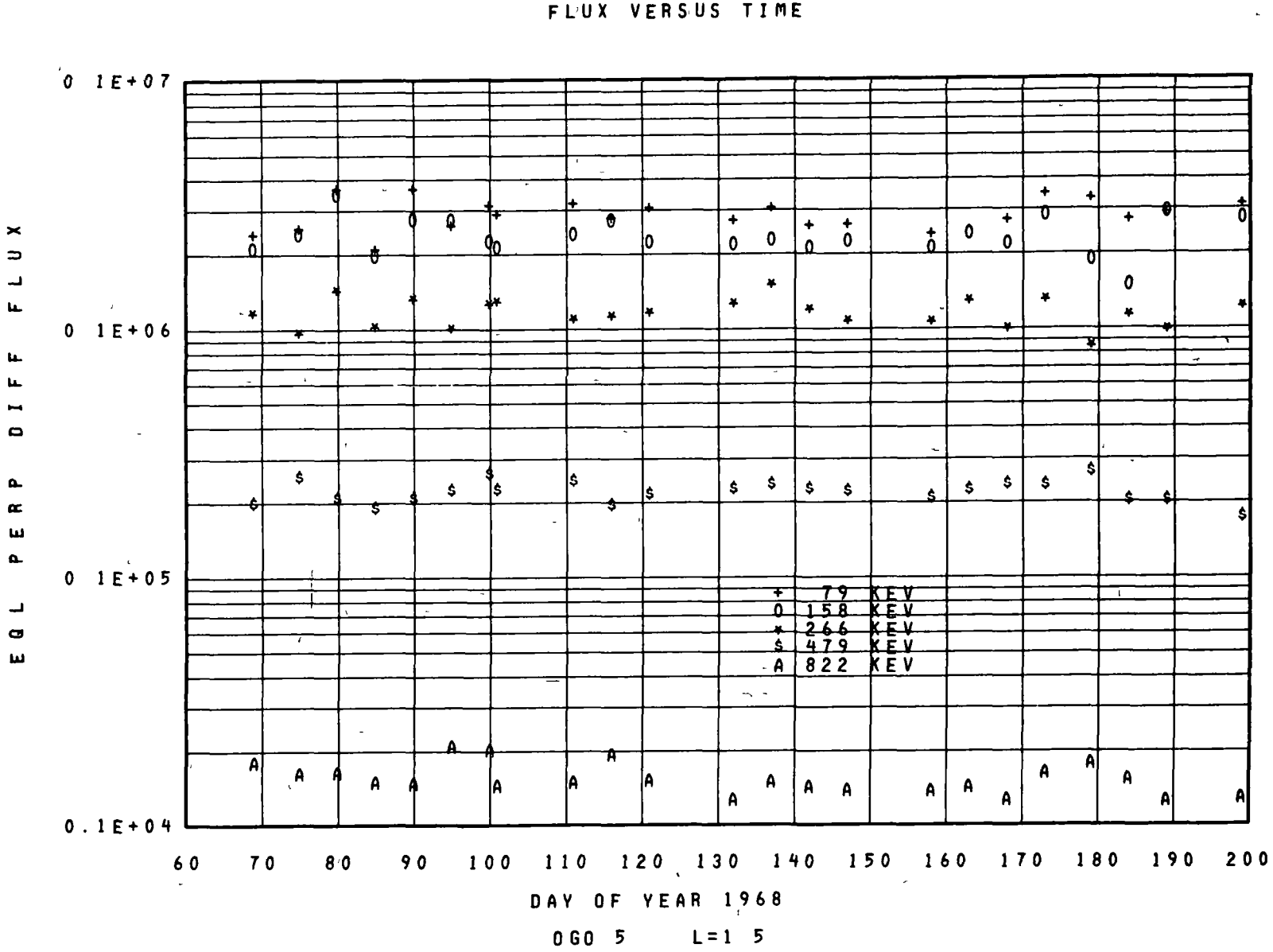
FLUX VERSUS TIME
EQL PERP DIFF FLUX
0 1E+07
0 1E+06
0 1E+05
0.1E+04
60
70
80
90
100
110
120
130
140
150
160
170
180
190
200
DAY OF YEAR 1968
OGO 5 L=1 5
+ 79 KEV
0 158 KEV
* 266 KEV
$ 479 KEV
A 822 KEV

Figure 89

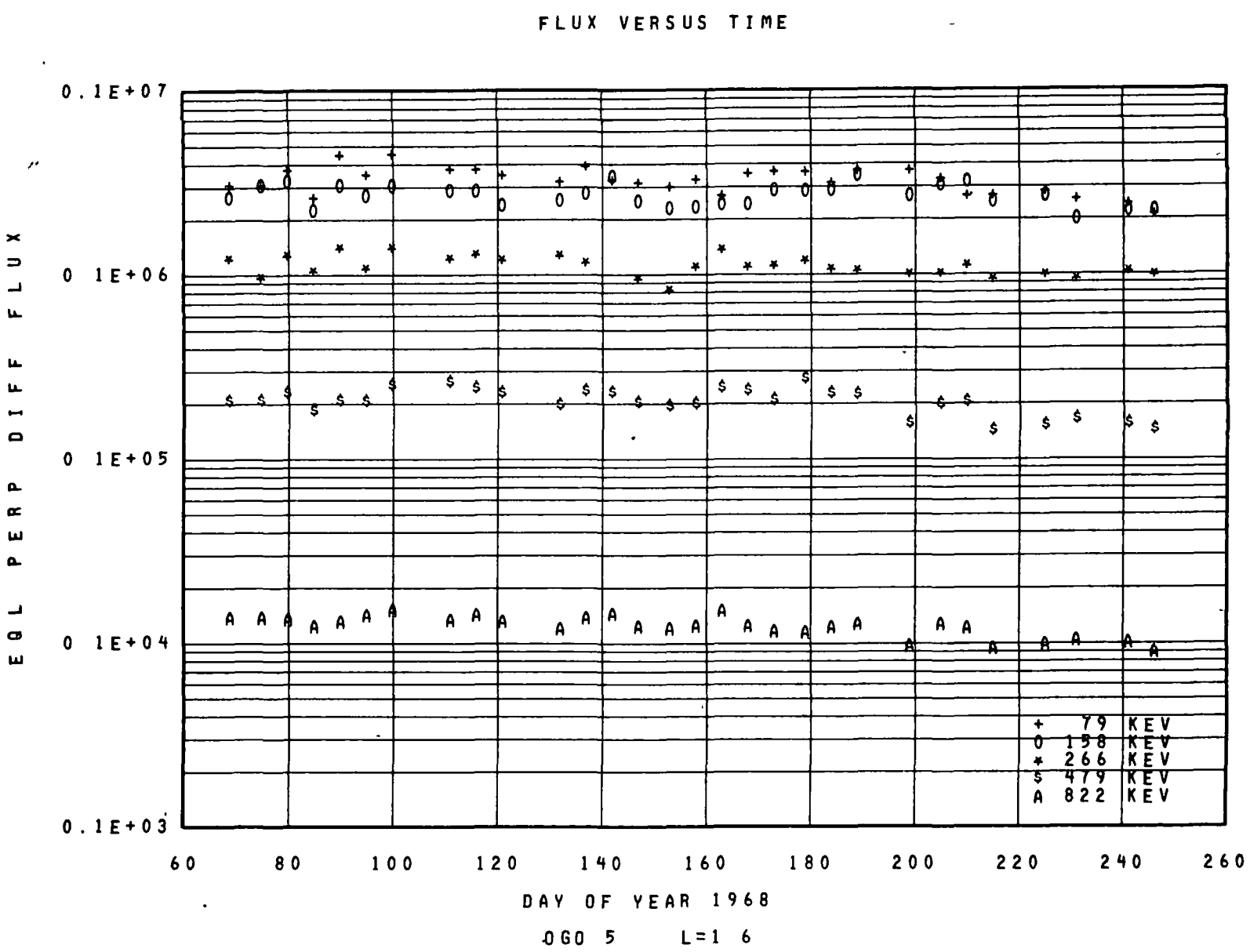
FLUX VERSUS TIME
EQL PERP DIFF FLUX
0.1E+07
0 1E+06
0 1E+05
0 1E+04
0.1E+03
60
80
100
120
140
160
180
200
220
240
260
DAY OF YEAR 1968
OGO 5 L=1 6
+ 79 KEV
0 158 KEV
* 266 KEV
$ 479 KEV
A 822 KEV

Figure 90

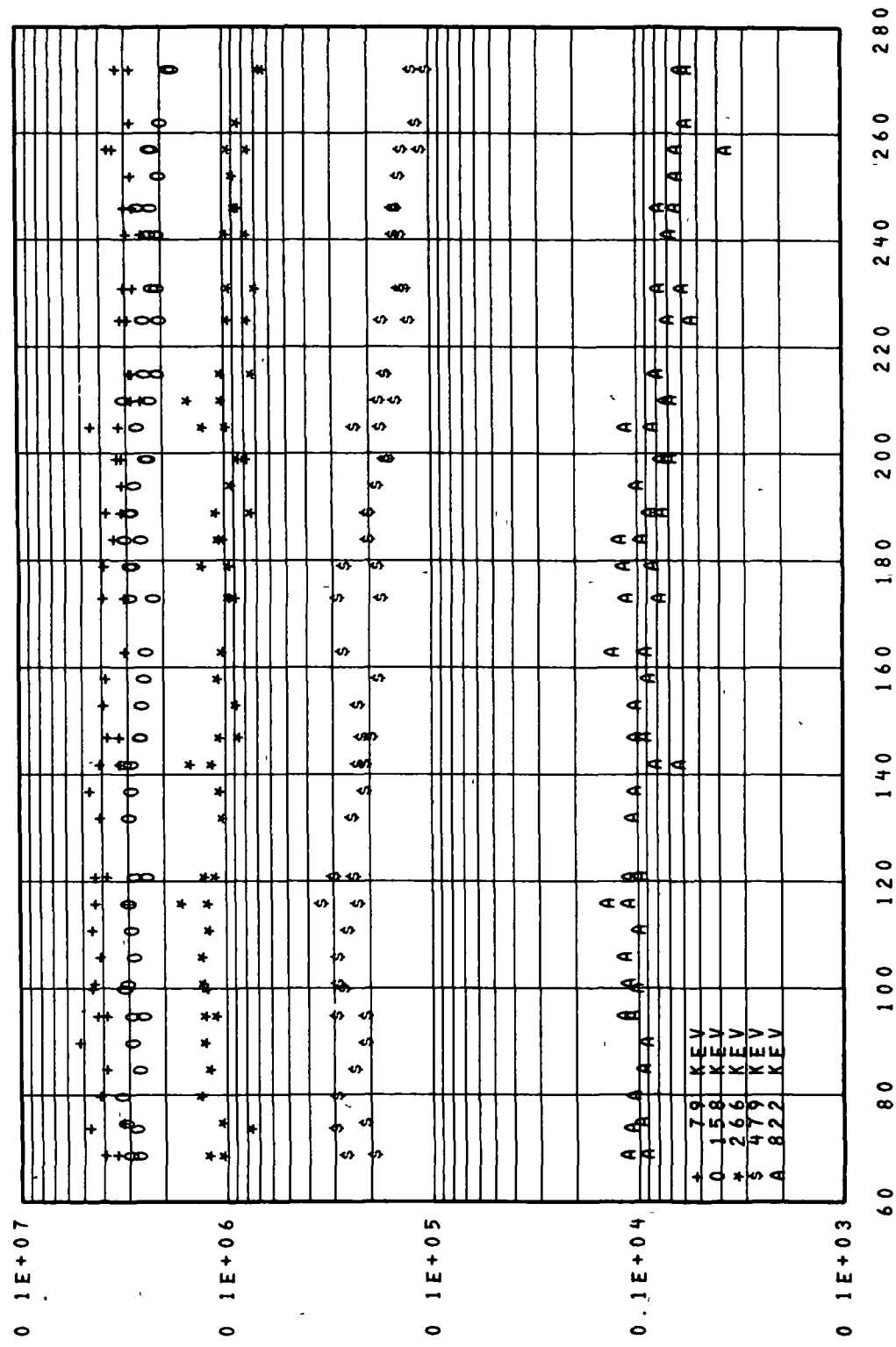
FLUX VERSUS TIME
EQL PERP DIFF FLUX
0 1E+07
0 1E+06
0 1E+05
0.1E+04
0 1E+03
60
80
100
120
140
160
180
200
220
240
260
280
DAY OF YEAR 1968
OGO 5 L=1 7
+ 79 KEV
0 158 KEV
* 266 KEV
$ 479 KEV
A 822 KEV

Figure 91

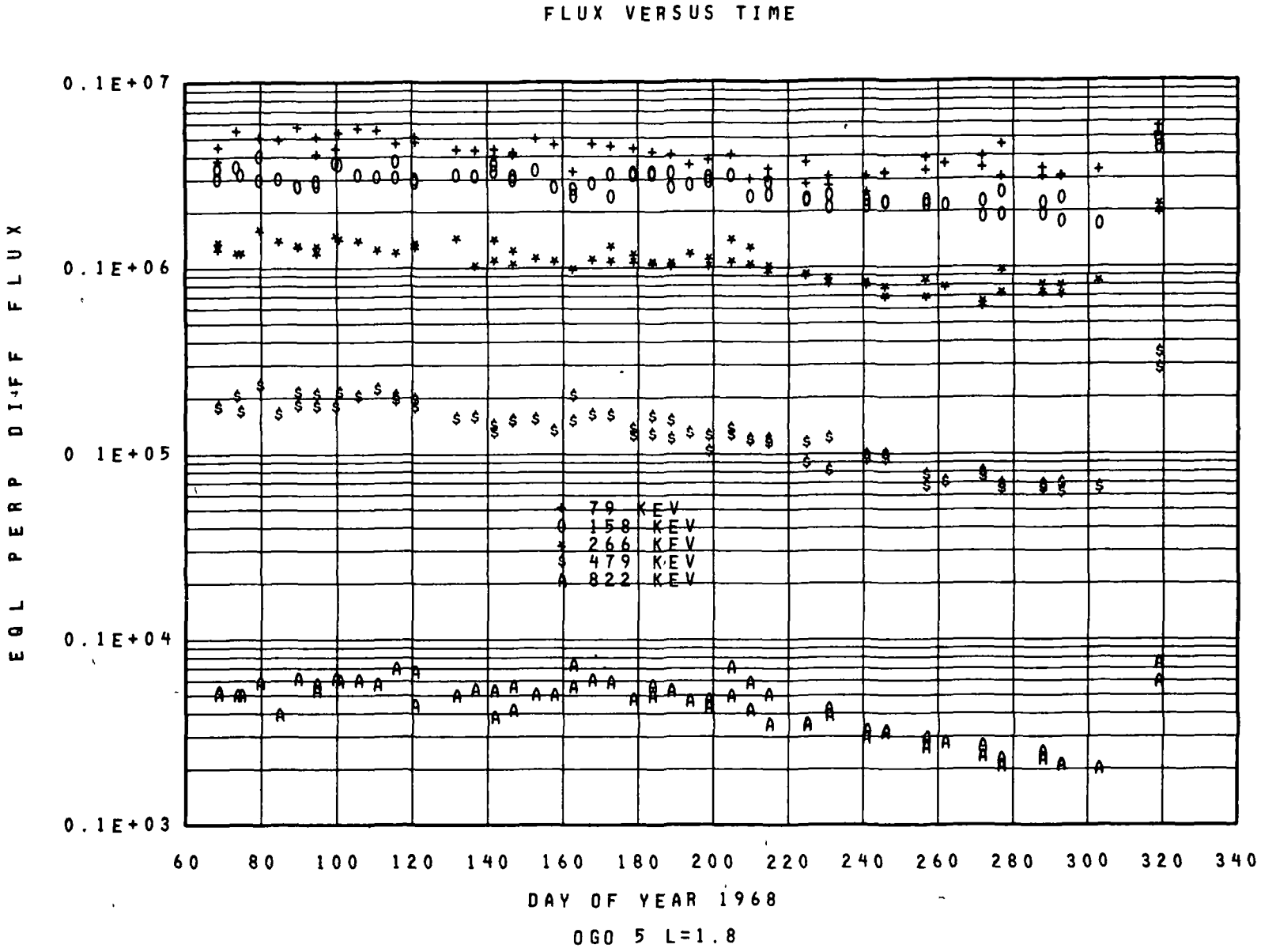
FLUX VERSUS TIME
EQL PERP DIFF FLUX
0.1E+07
0.1E+06
0 1E+05
0.1E+04
0.1E+03
79 KEV
158 KEV
266 KEV
479 KEV
822 KEV
60
80
100
120
140
160
180
200
220
240
260
280
300
320
340
DAY OF YEAR 1968
OGO 5 L=1.8

Figure 92

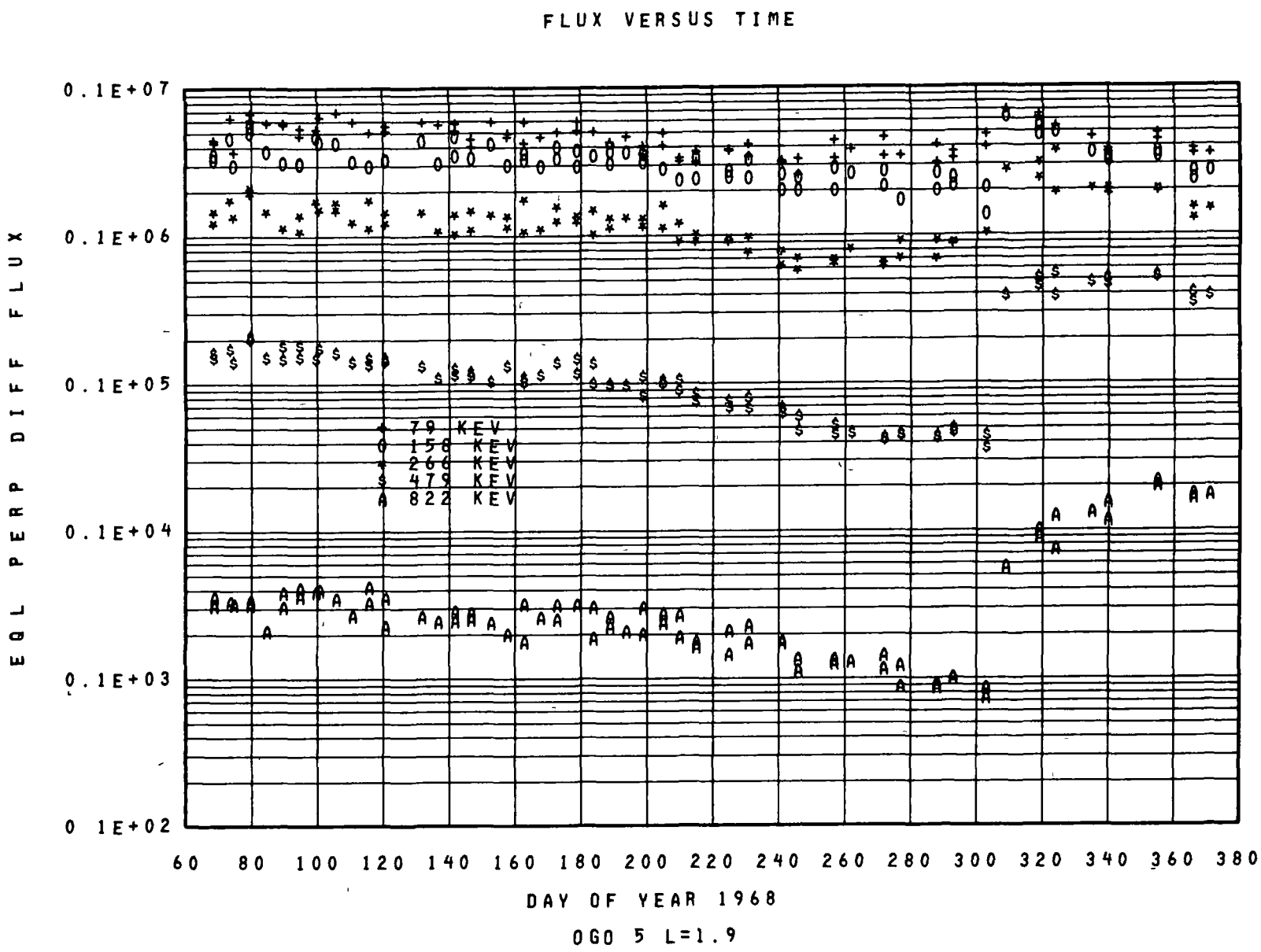
FLUX VERSUS TIME
EQL PERP DIFF FLUX
0.1E+07
0.1E+06
0.1E+05
0.1E+04
0.1E+03
0 1E+02
79 KEV
158 KEV
266 KEV
479 KEV
822 KEV
60 80 100 120 140 160 180 200 220 240 260 280 300 320 340 360 380
DAY OF YEAR 1968
OGO 5 L=1.9

Figure 93

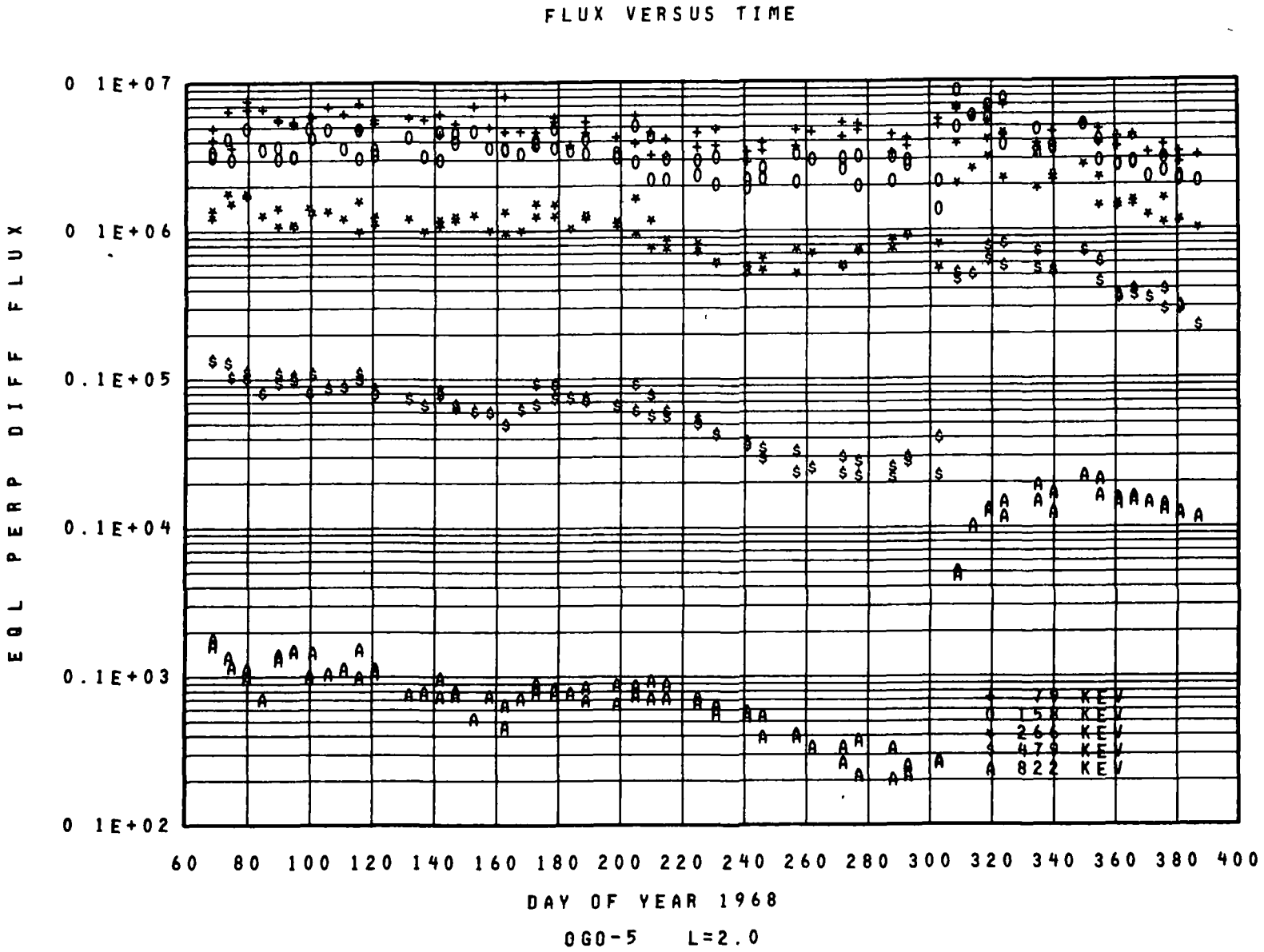
FLUX VERSUS TIME
EQL PERP DIFF FLUX
0 1E+07
0 1E+06
0.1E+05
0.1E+04
0.1E+03
0 1E+02
60 80 100 120 140 160 180 200 220 240 260 280 300 320 340 360 380 400
DAY OF YEAR 1968
OGO-5 L=2.0
79 KEV
152 KEV
266 KEV
479 KEV
822 KEV

Figure 94

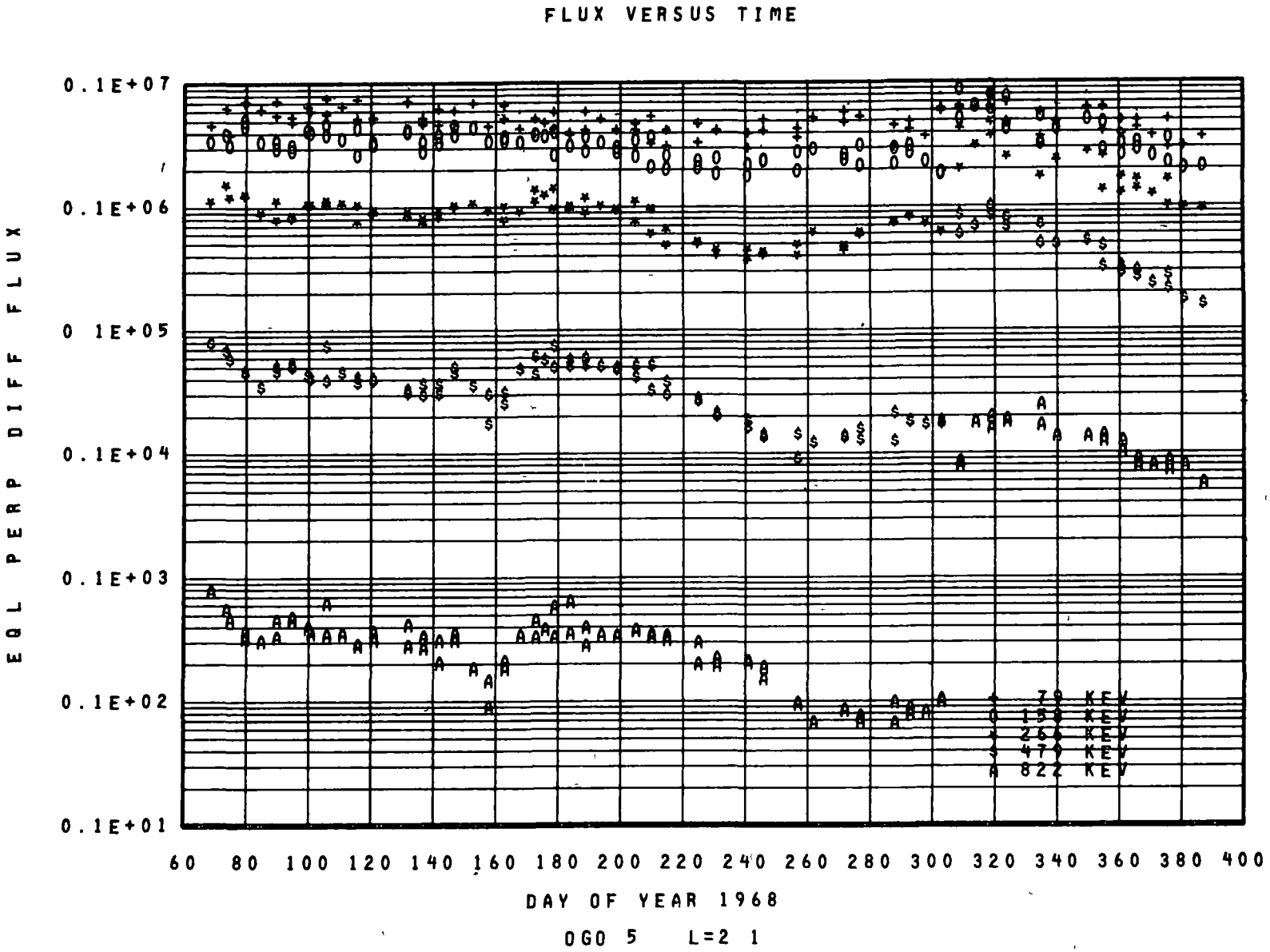
FLUX VERSUS TIME
EQL PERP DIFF FLUX
0.1E+07
0.1E+06
0 1E+05
0.1E+04
0.1E+03
0.1E+02
0.1E+01
60 80 100 120 140 160 180 200 220 240 260 280 300 320 340 360 380 400
DAY OF YEAR 1968
OGO 5 L=2 1
79 KEV
KEV
KEV
KEV
822 KEV

Figure 95

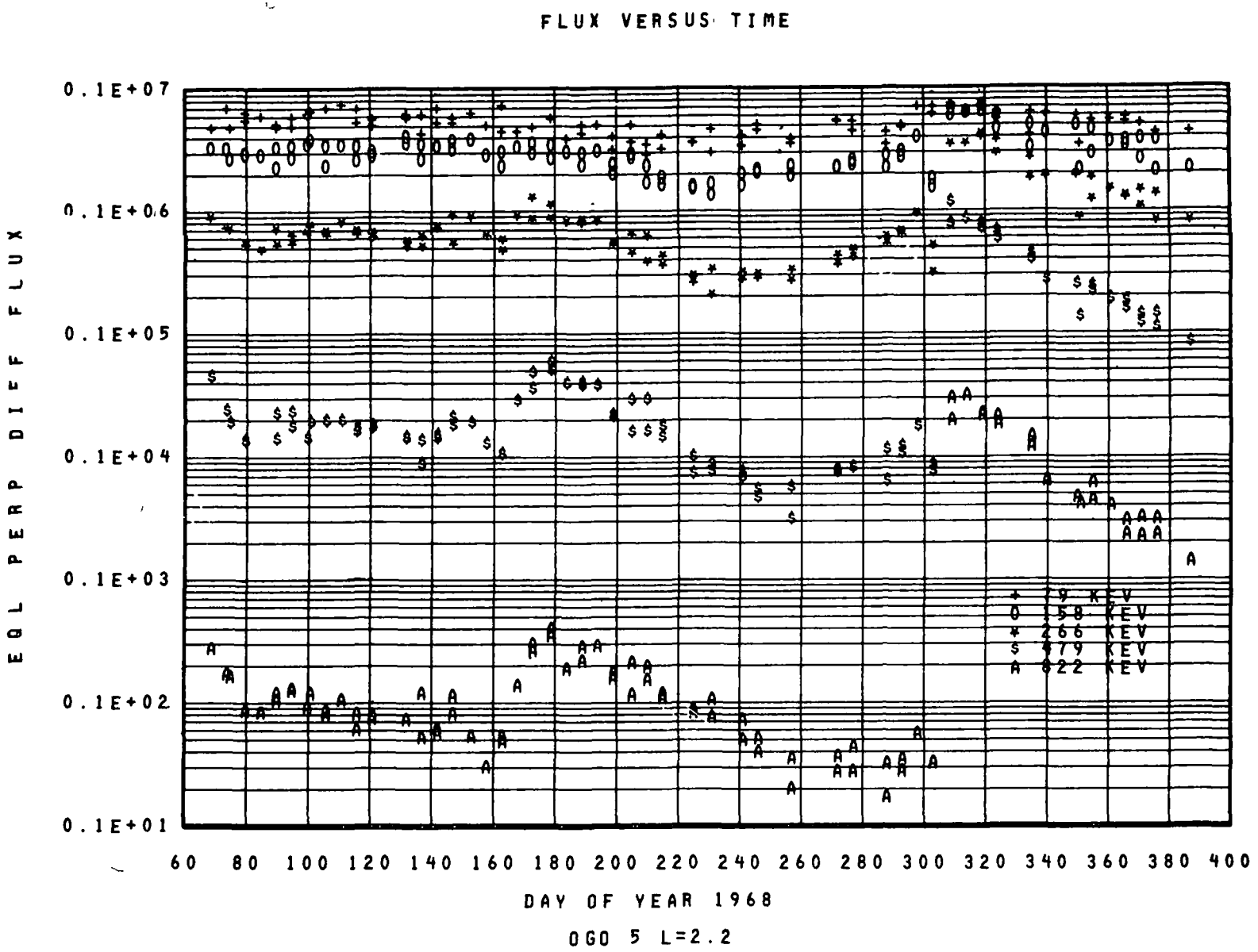
FLUX VERSUS TIME
EQL PERP DIFF FLUX
0.1E+07
0.1E+06
0.1E+05
0.1E+04
0.1E+03
0.1E+02
0.1E+01
60 80 100 120 140 160 180 200 220 240 260 280 300 320 340 360 380 400
DAY OF YEAR 1968
OGO 5 L=2.2
79 KEV
158 KEV
266 KEV
479 KEV
822 KEV

Figure 96

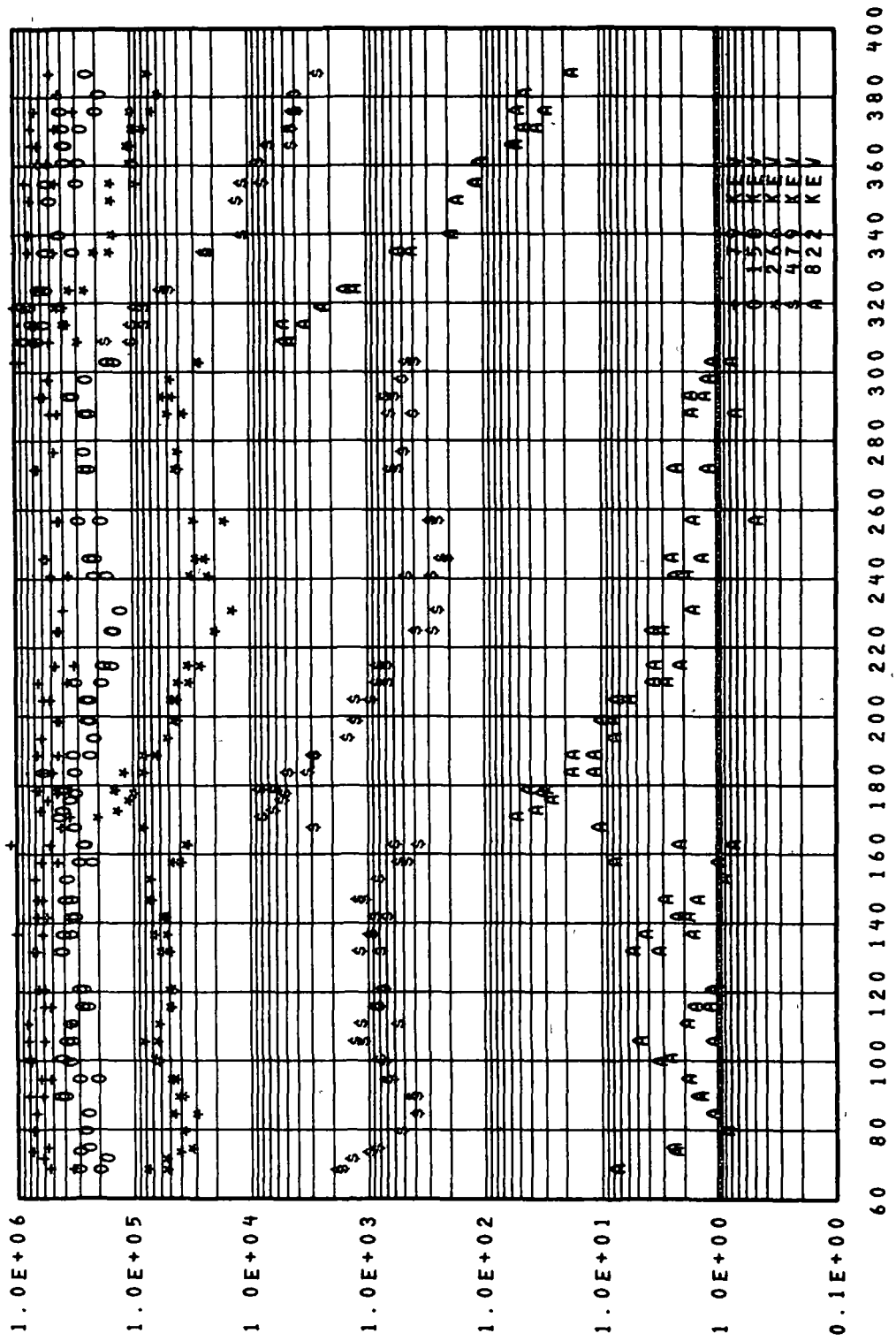
FLUX VERSUS TIME
EQL PERP DIFF FLUX
1.0E+06
1.0E+05
1 0E+04
1.0E+03
1.0E+02
1.0E+01
1 0E+00
0.1E+00
60 80 100 120 140 160 180 200 220 240 260 280 300 320 340 360 380 400
DAY OF YEAR 1968
OGO 5 L=2.3
150 KEV
266 KEV
479 KEV
822 KEV

Figure 97

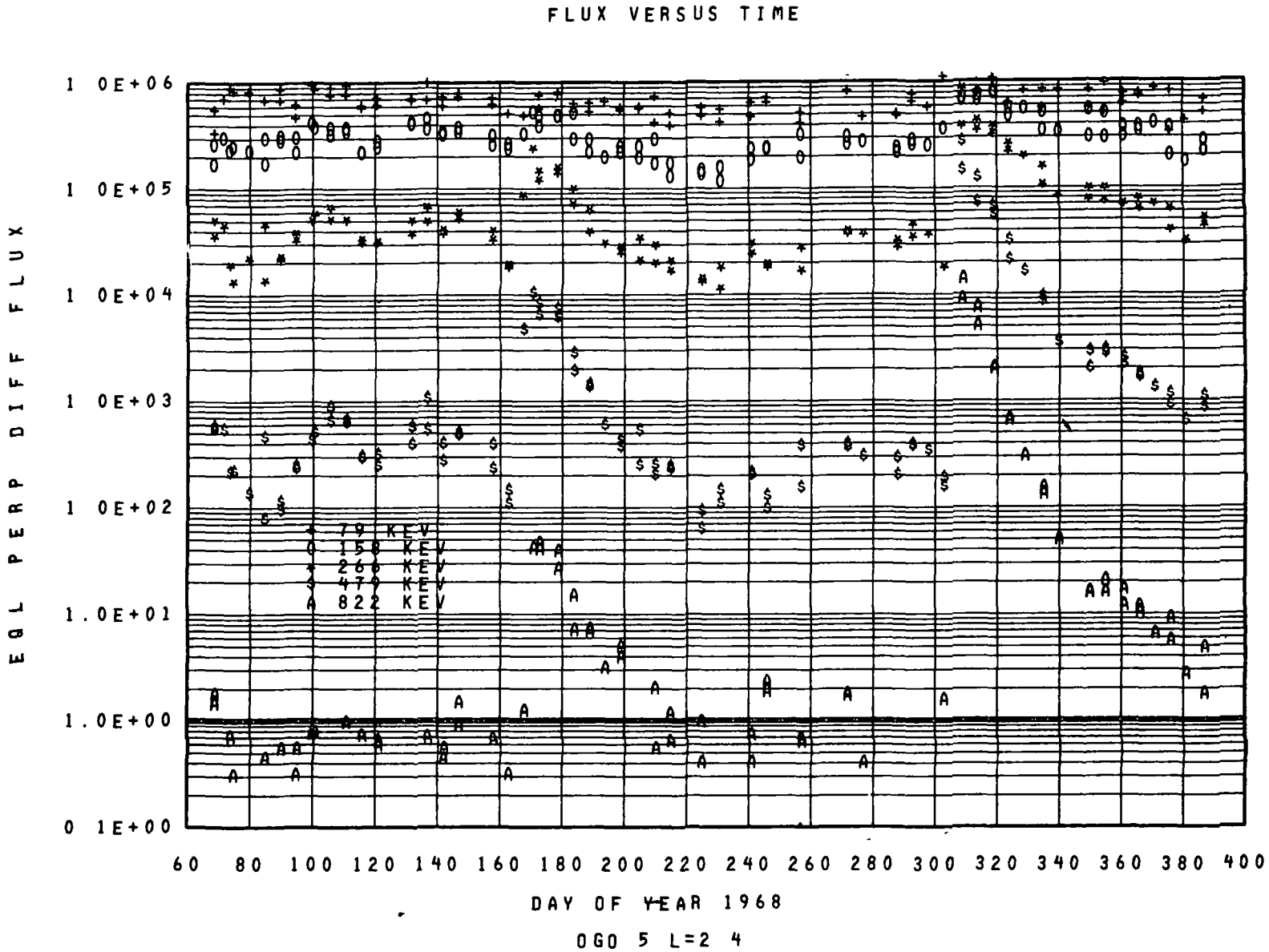
FLUX VERSUS TIME
EQL PERP DIFF FLUX
1 0E+06
1 0E+05
1 0E+04
1 0E+03
1 0E+02
1.0E+01
1.0E+00
0 1E+00
79 KEV
158 KEV
266 KEV
479 KEV
822 KEV
60 80 100 120 140 160 180 200 220 240 260 280 300 320 340 360 380 400
DAY OF YEAR 1968
OGO 5 L=2 4

Figure 98

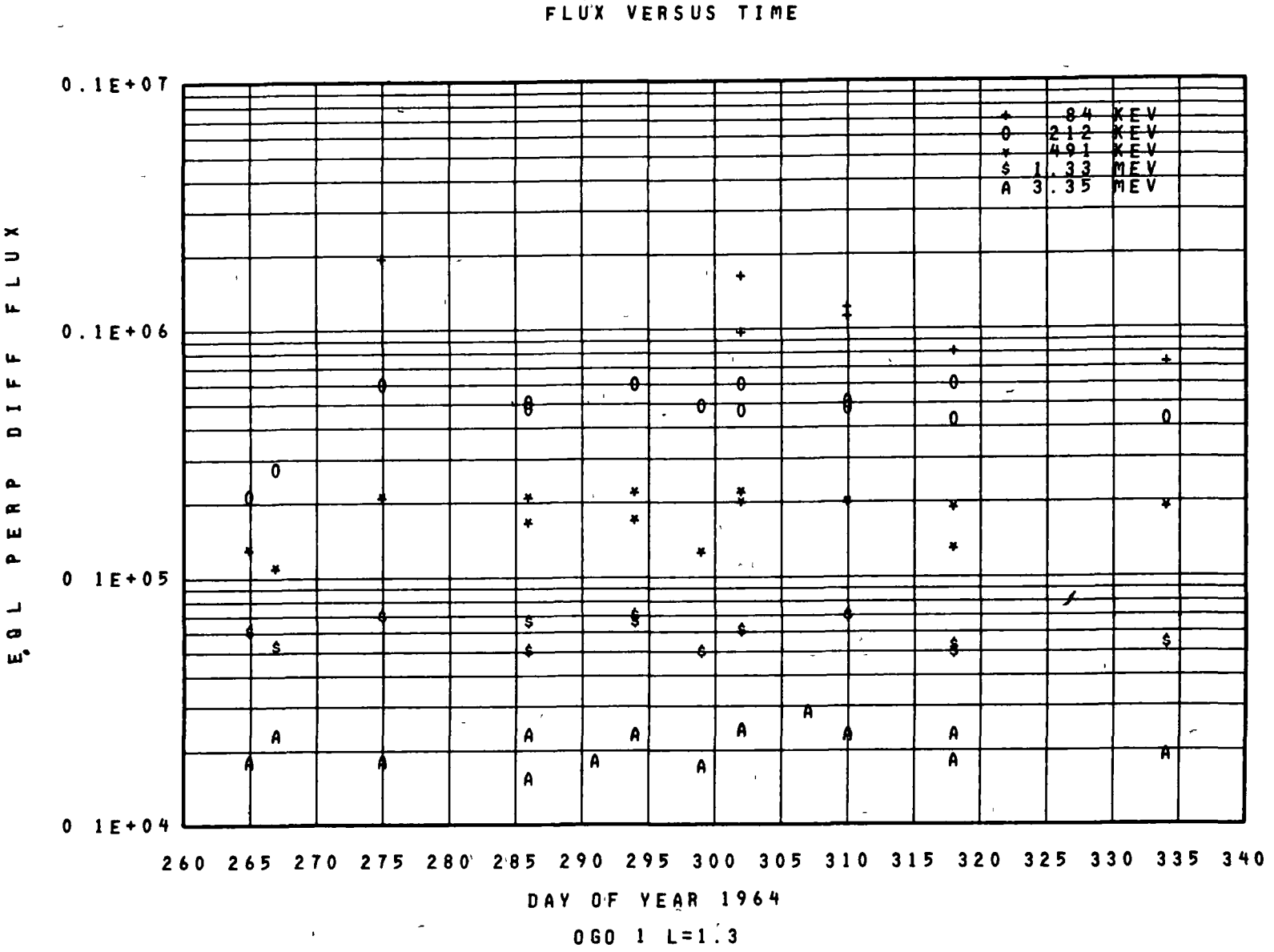
FLUX VERSUS TIME
0.1E+07
0.1E+06
0 1E+05
0 1E+04
EQL PERP DIFF FLUX
+ 84 KEV
0 212 KEV
* 491 KEV
$ 1.33 MEV
A 3.35 MEV
260 265 270 275 280 285 290 295 300 305 310 315 320 325 330 335 340
DAY OF YEAR 1964
OGO 1 L=1.3

Figure 99

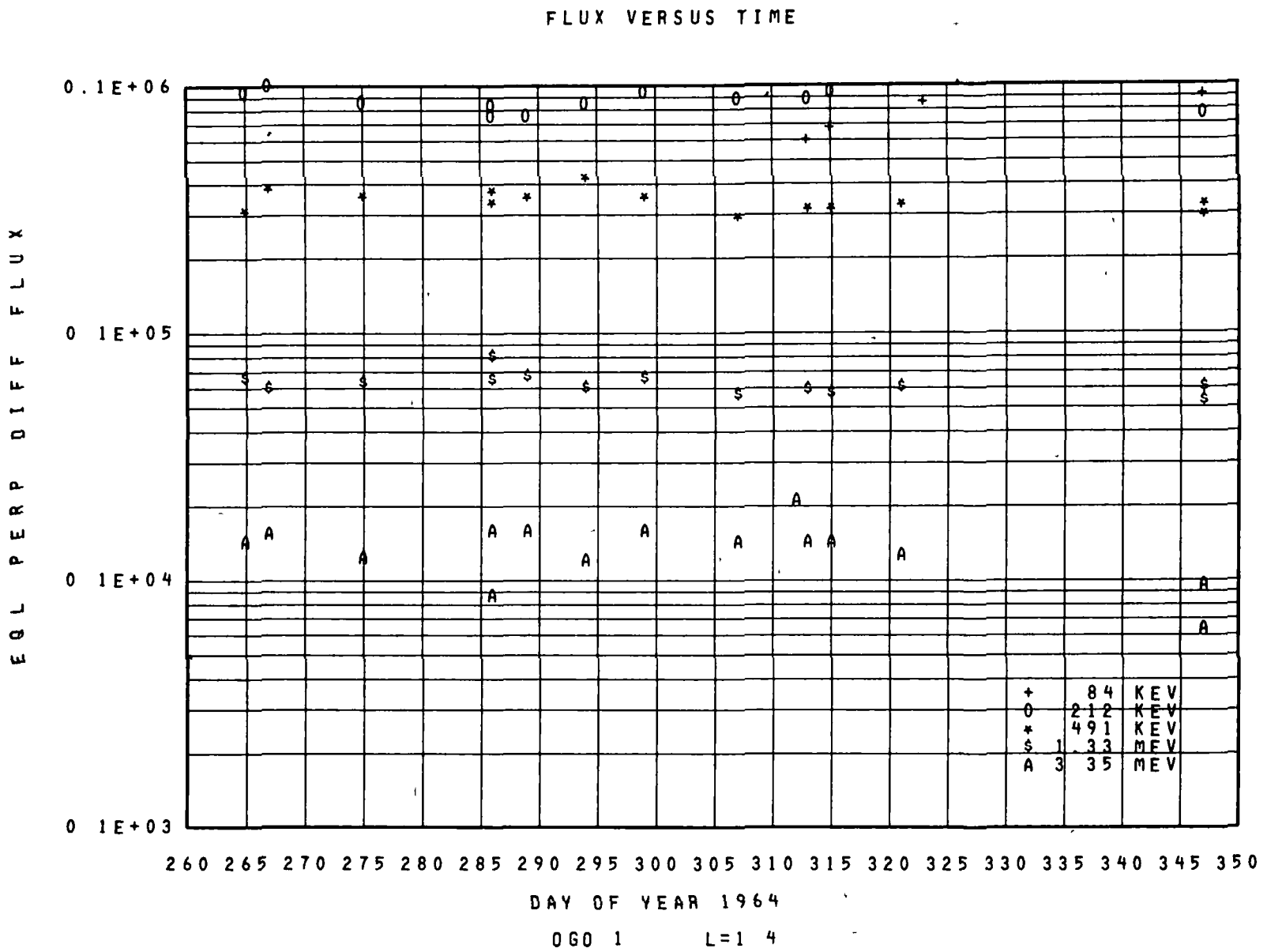
FLUX VERSUS TIME
EQL PERP DIFF FLUX
0.1E+06
0 1E+05
0 1E+04
0 1E+03
260 265 270 275 280 285 290 295 300 305 310 315 320 325 330 335 340 345 350
DAY OF YEAR 1964
OGO 1 L=1 4
+ 84 KEV
0 212 KEV
* 491 KEV
$ 1.33 MEV
A 3 35 MEV

Figure 100

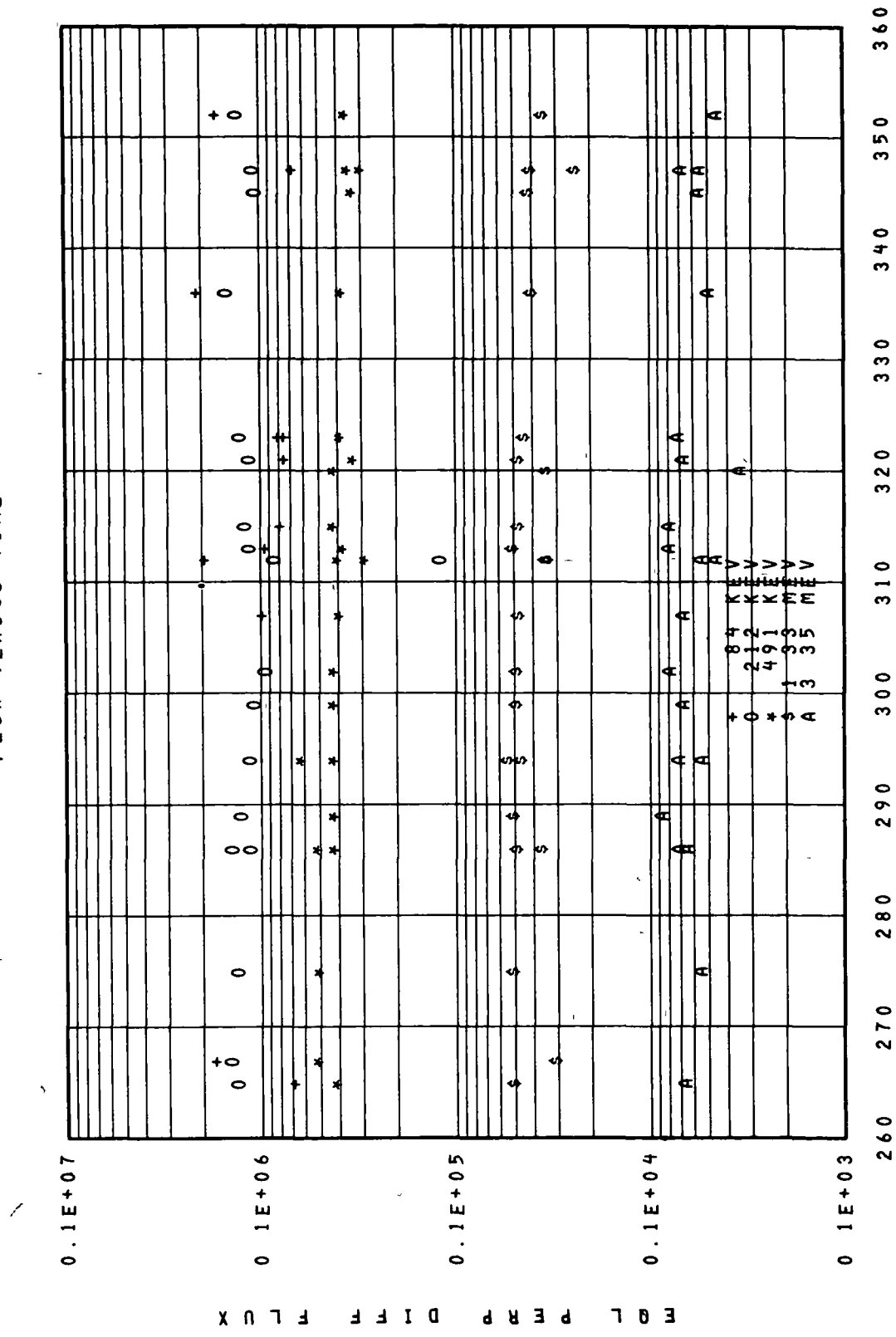
FLUX VERSUS TIME
EQL PERP DIFF FLUX
0.1E+07
0 1E+06
0.1E+05
0.1E+04
0 1E+03
260
270
280
290
300
310
320
330
340
350
360
DAY OF YEAR 1964
OGO 1 L=1.5
84 KEV
212 KEV
491 KEV
1 33 MEV
3 35 MEV

Figure 101

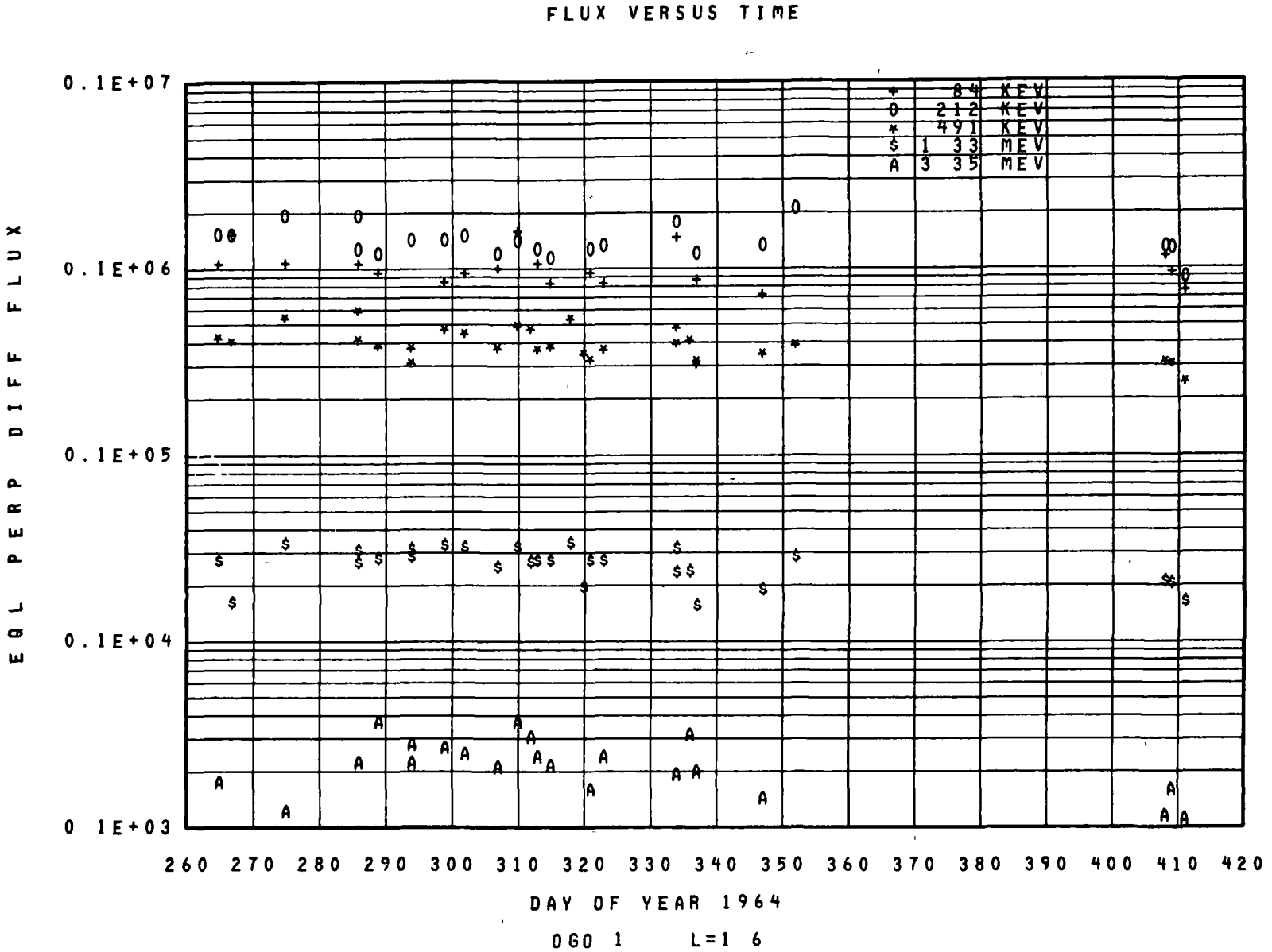
FLUX VERSUS TIME
+ 84 KEV
0 212 KEV
* 491 KEV
$ 1 33 MEV
A 3 35 MEV
EQL PERP DIFF FLUX
0.1E+07
0.1E+06
0.1E+05
0.1E+04
0 1E+03
260 270 280 290 300 310 320 330 340 350 360 370 380 390 400 410 420
DAY OF YEAR 1964
OGO 1 L=1 6

Figure 102

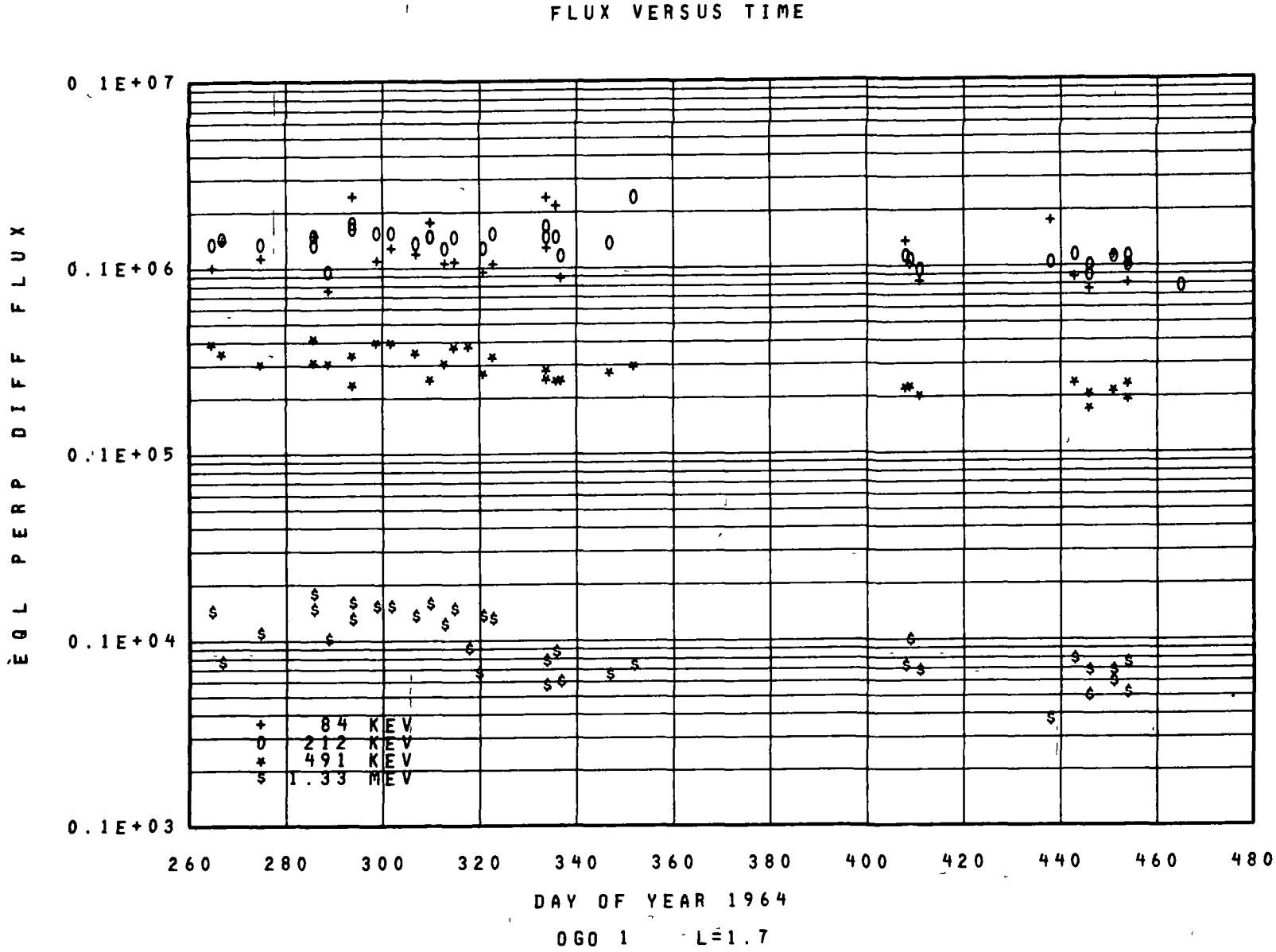
FLUX VERSUS TIME
0.1E+07
0.1E+06
0.1E+05
0.1E+04
0.1E+03
EQL PERP DIFF FLUX
84 KEV
212 KEV
491 KEV
1.33 MEV
260
280
300
320
340
360
380
400
420
440
460
480
DAY OF YEAR 1964
OGO 1 L=1.7

Figure 103

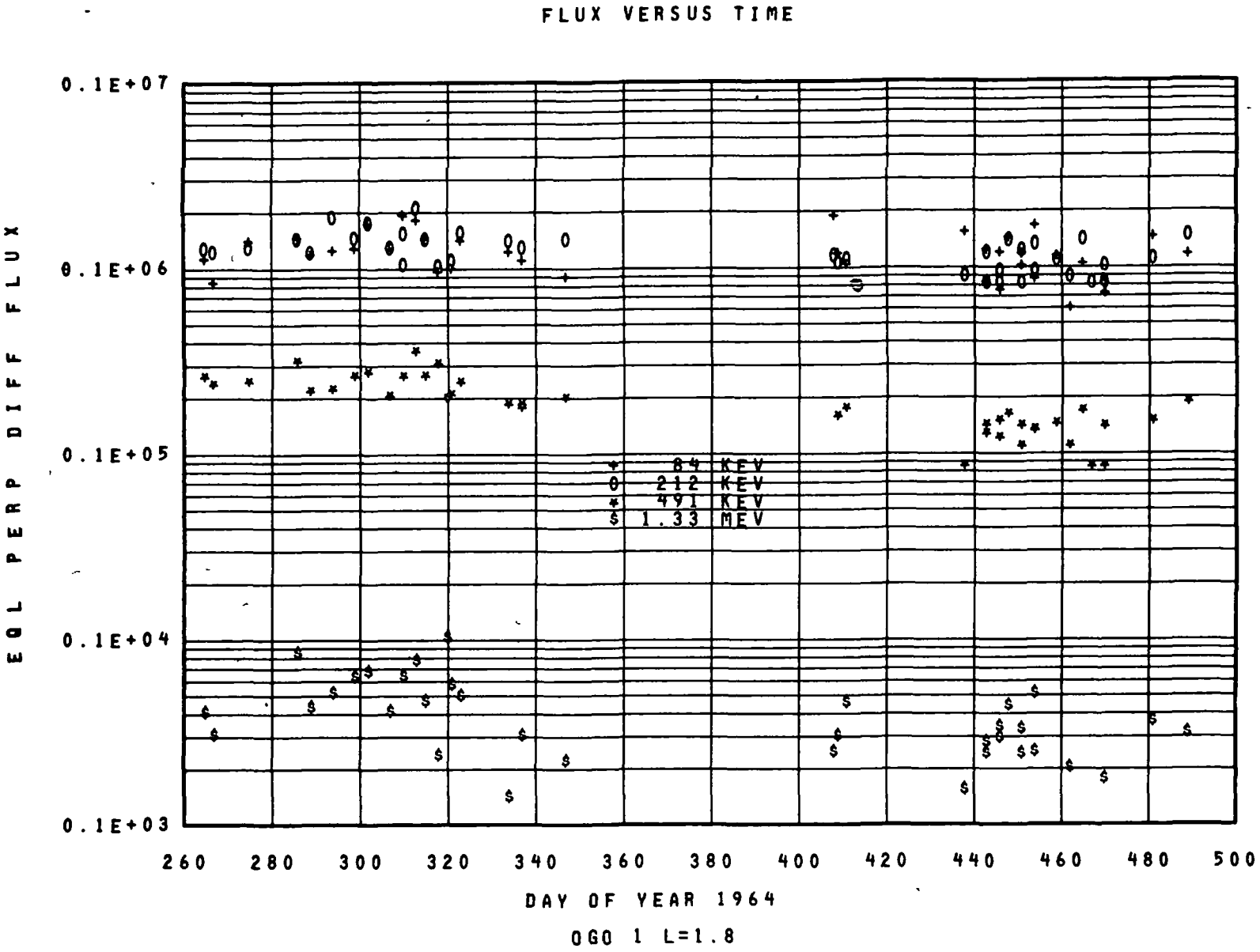
FLUX VERSUS TIME
EQL PERP DIFF FLUX
0.1E+07
0.1E+06
0.1E+05
0.1E+04
0.1E+03
84 KEV
212 KEV
491 KEV
1.33 MEV
260
280
300
320
340
360
380
400
420
440
460
480
500
DAY OF YEAR 1964
OGO 1 L=1.8

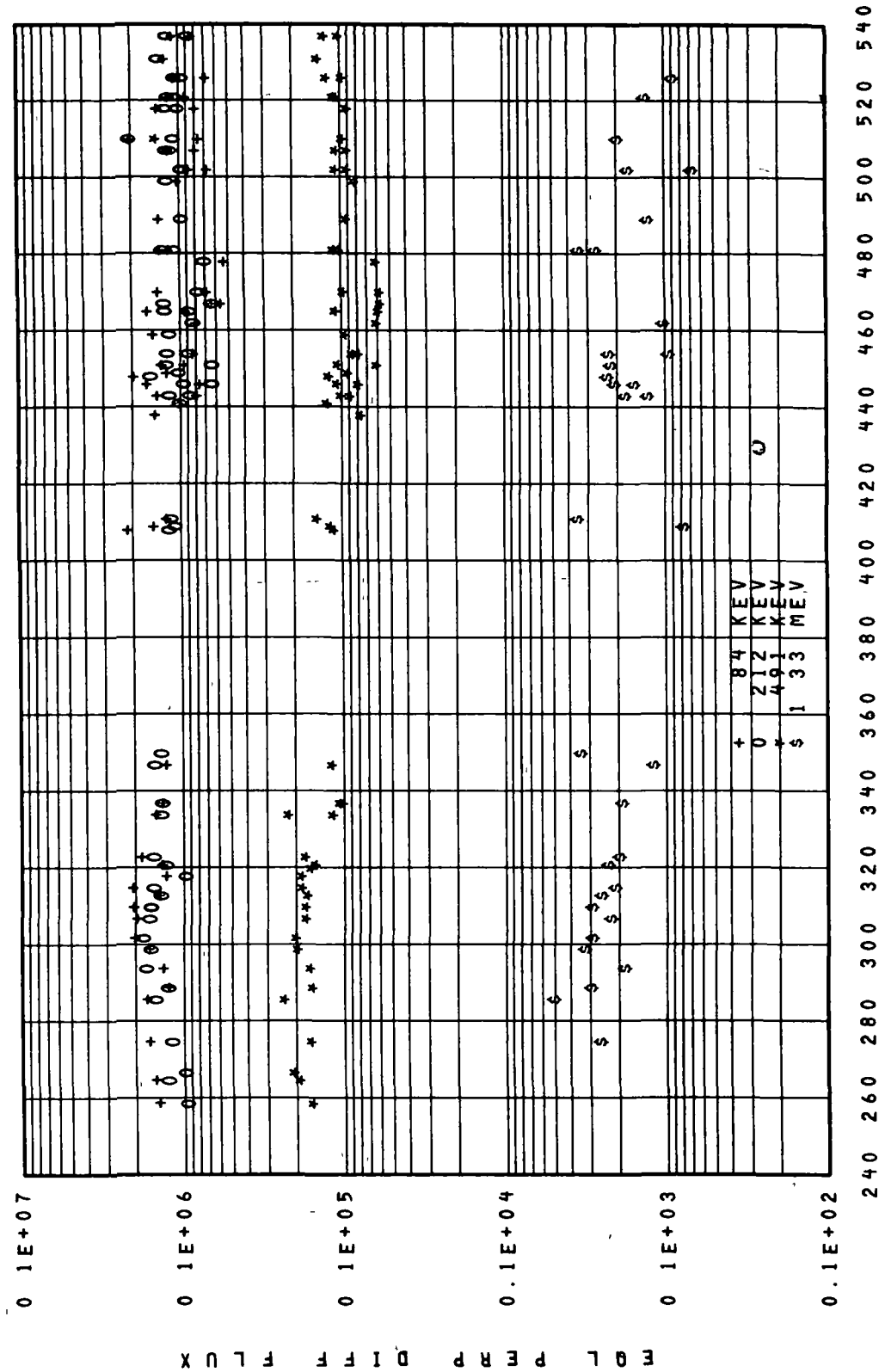
FLUX VERSUS TIME
EQL PERP DIFF FLUX
0 1E+07
0 1E+06
0 1E+05
0.1E+04
0 1E+03
0.1E+02
240 260 280 300 320 340 360 380 400 420 440 460 480 500 520 540
DAY OF YEAR 1964
OGO 1 L=1 9
+ 84 KEV
0 212 KEV
* 491 KEV
$ 1 33 MEV

Figure 105

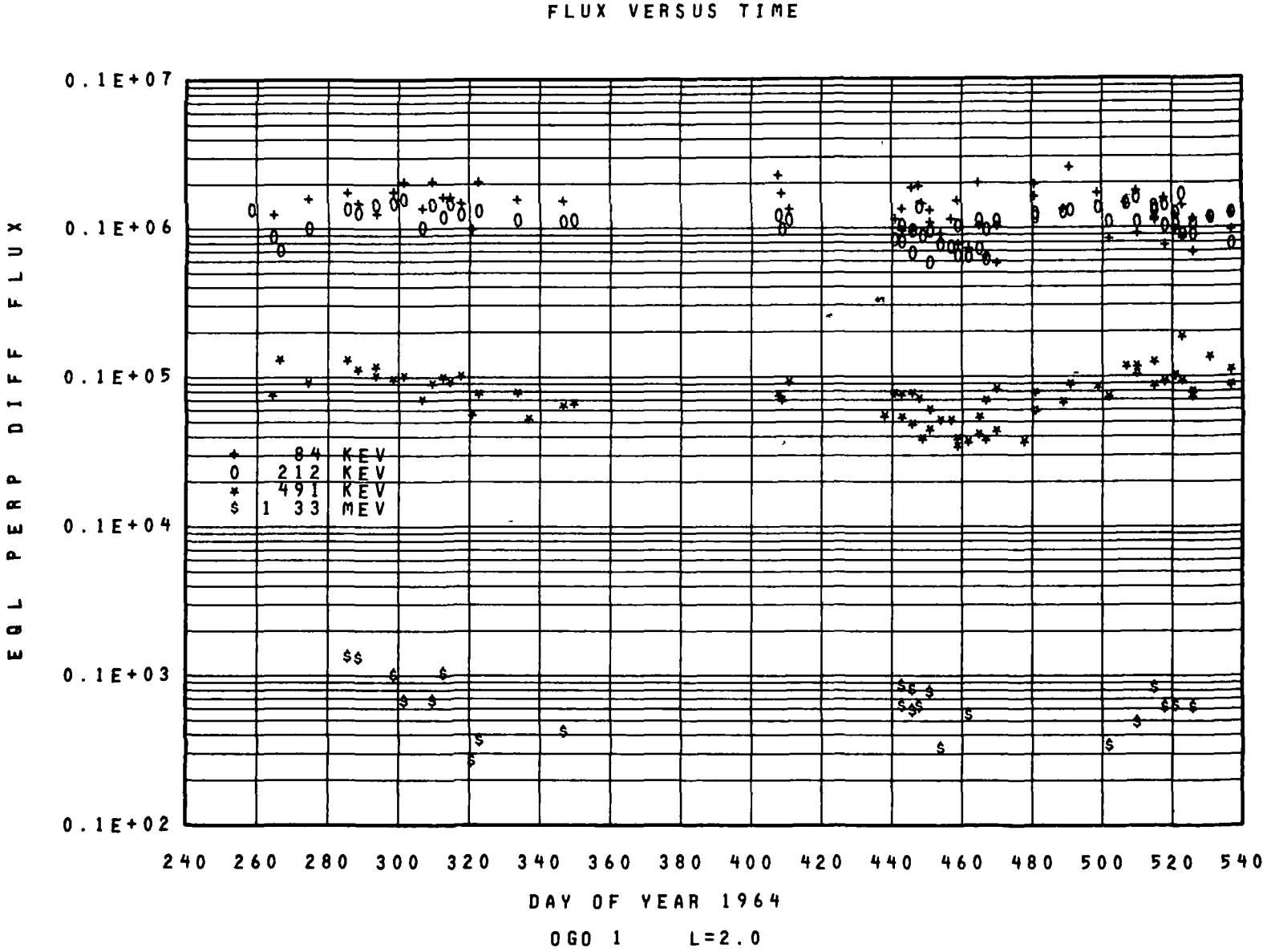
FLUX VERSUS TIME
EQL PERP DIFF FLUX
0.1E+07
0.1E+06
0.1E+05
0.1E+04
0.1E+03
0.1E+02
84 KEV
212 KEV
491 KEV
1 33 MEV
240 260 280 300 320 340 360 380 400 420 440 460 480 500 520 540
DAY OF YEAR 1964
OGO 1 L=2.0

Figure 106

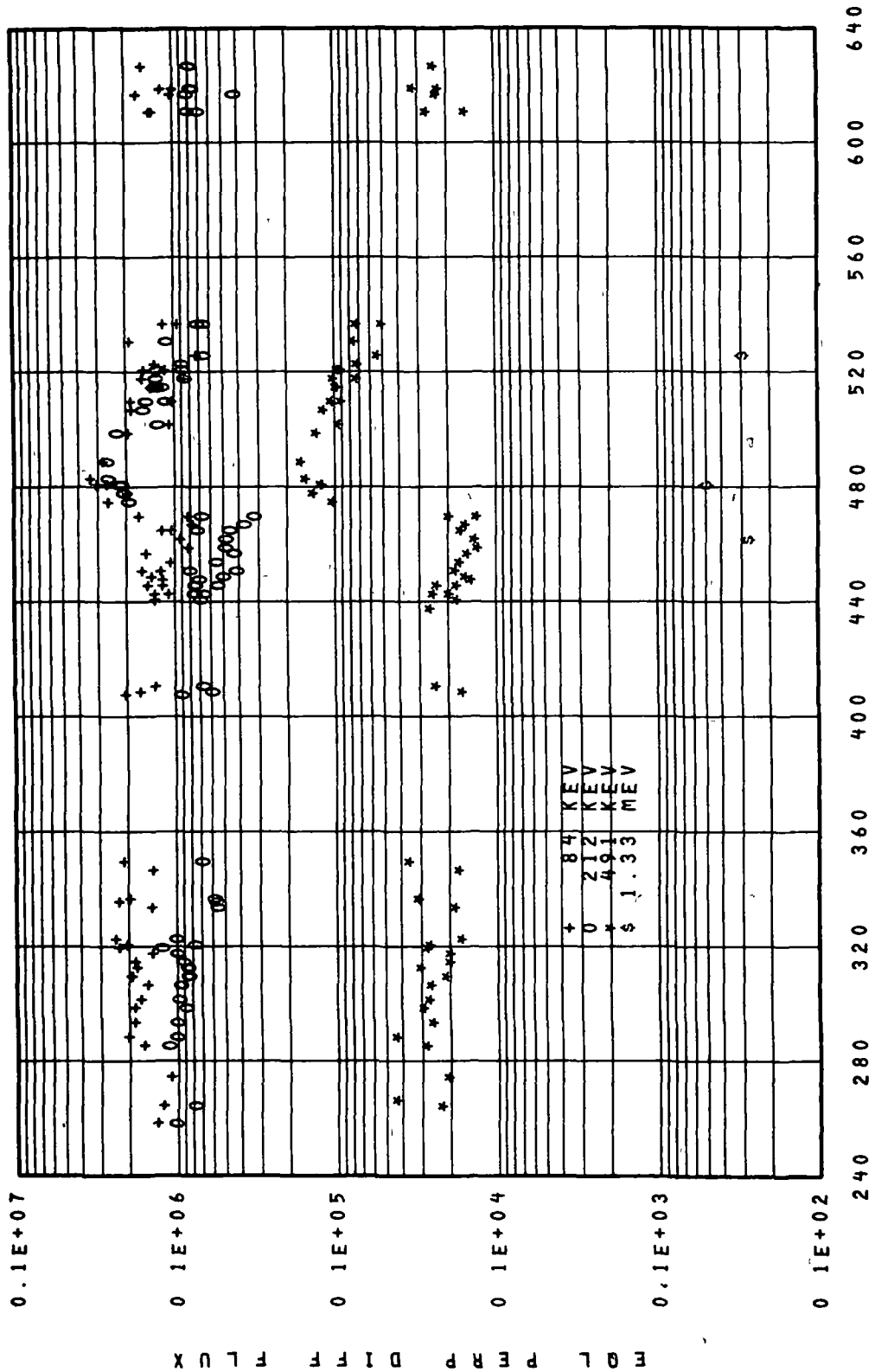
FLUX VERSUS TIME
EQL PERP DIFF FLUX
0.1E+07
0 1E+06
0 1E+05
0 1E+04
0.1E+03
0 1E+02
240
280
320
360
400
440
480
520
560
600
640
DAY OF YEAR 1964
OGO 1 L=2.2
+ 84 KEV
0 212 KEV
* 491 KEV
$ 1.33 MEV

Figure 107

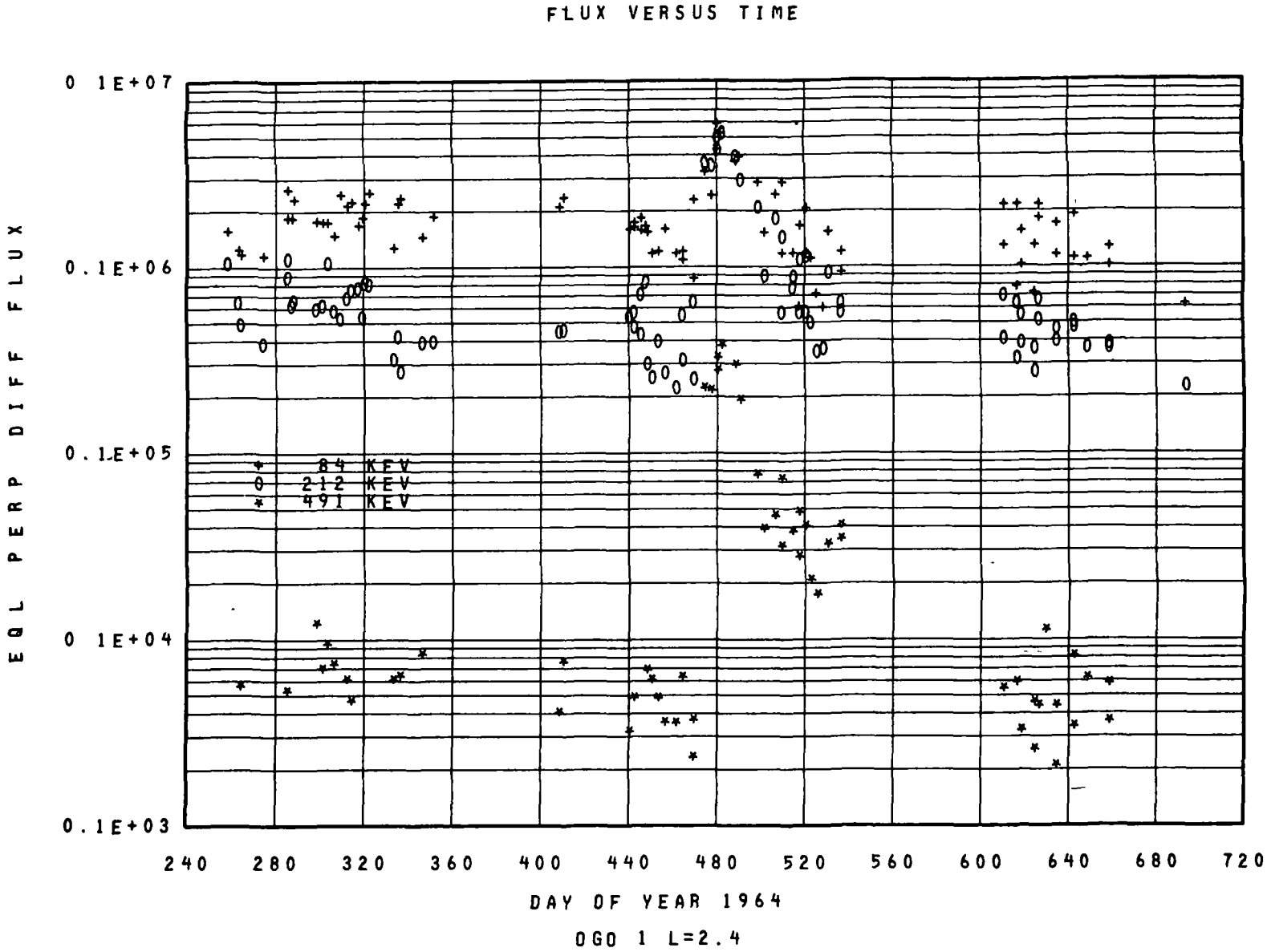
FLUX VERSUS TIME
EQL PERP DIFF FLUX
0 1E+07
0.1E+06
0.1E+05
0 1E+04
0.1E+03
84 KEV
212 KEV
491 KEV
240
280
320
360
400
440
480
520
560
600
640
680
720
DAY OF YEAR 1964
OGO 1 L=2.4

Figure 108

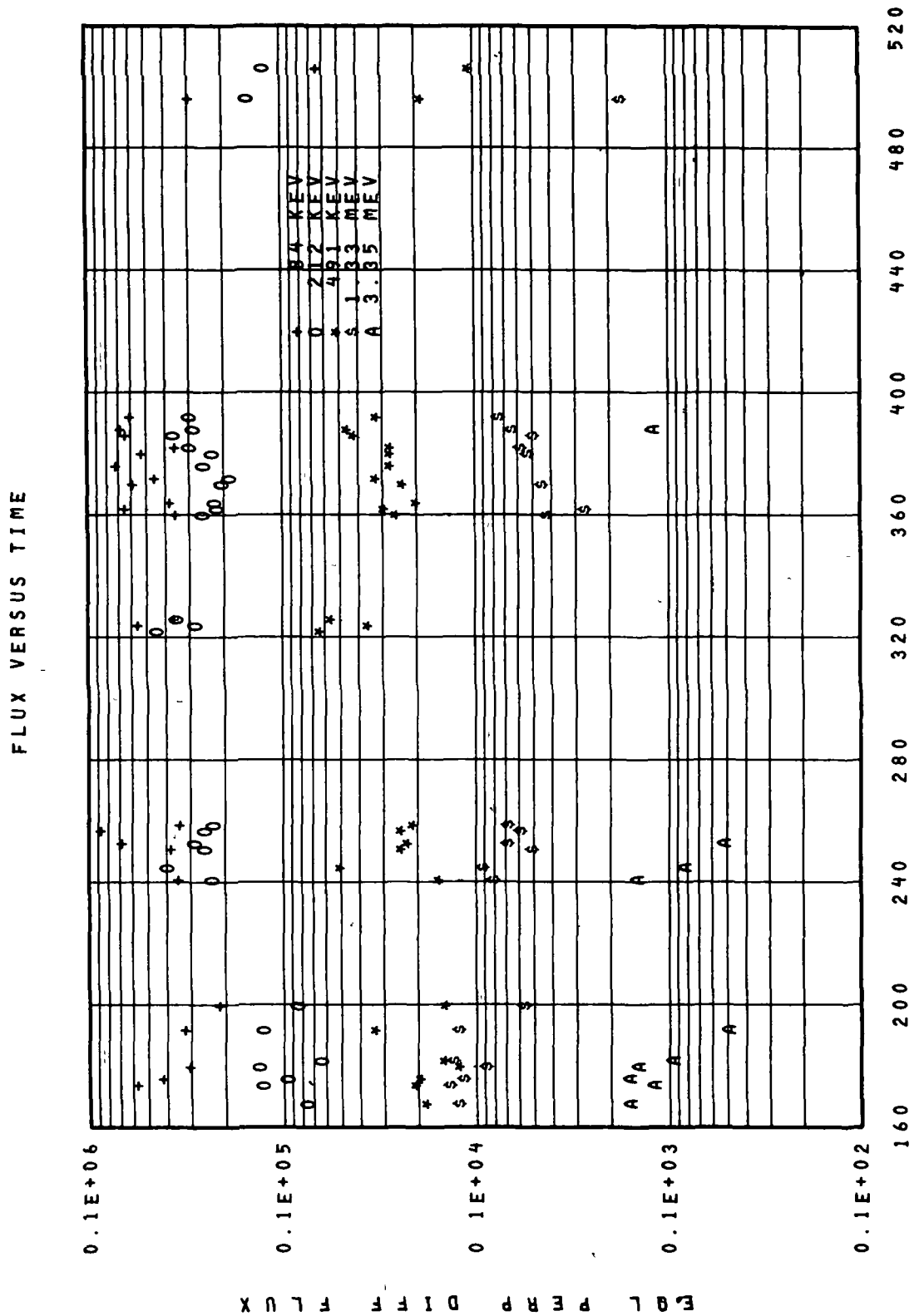
FLUX VERSUS TIME
EQL PERP DIFF FLUX
0.1E+06
0.1E+05
0.1E+04
0.1E+03
0.1E+02
160
200
240
280
320
360
400
440
480
520
DAY OF YEAR 1966
OGO 3 L=1.3
84 KEV
212 KEV
491 KEV
1.33 MEV
3.35 MEV

Figure 109

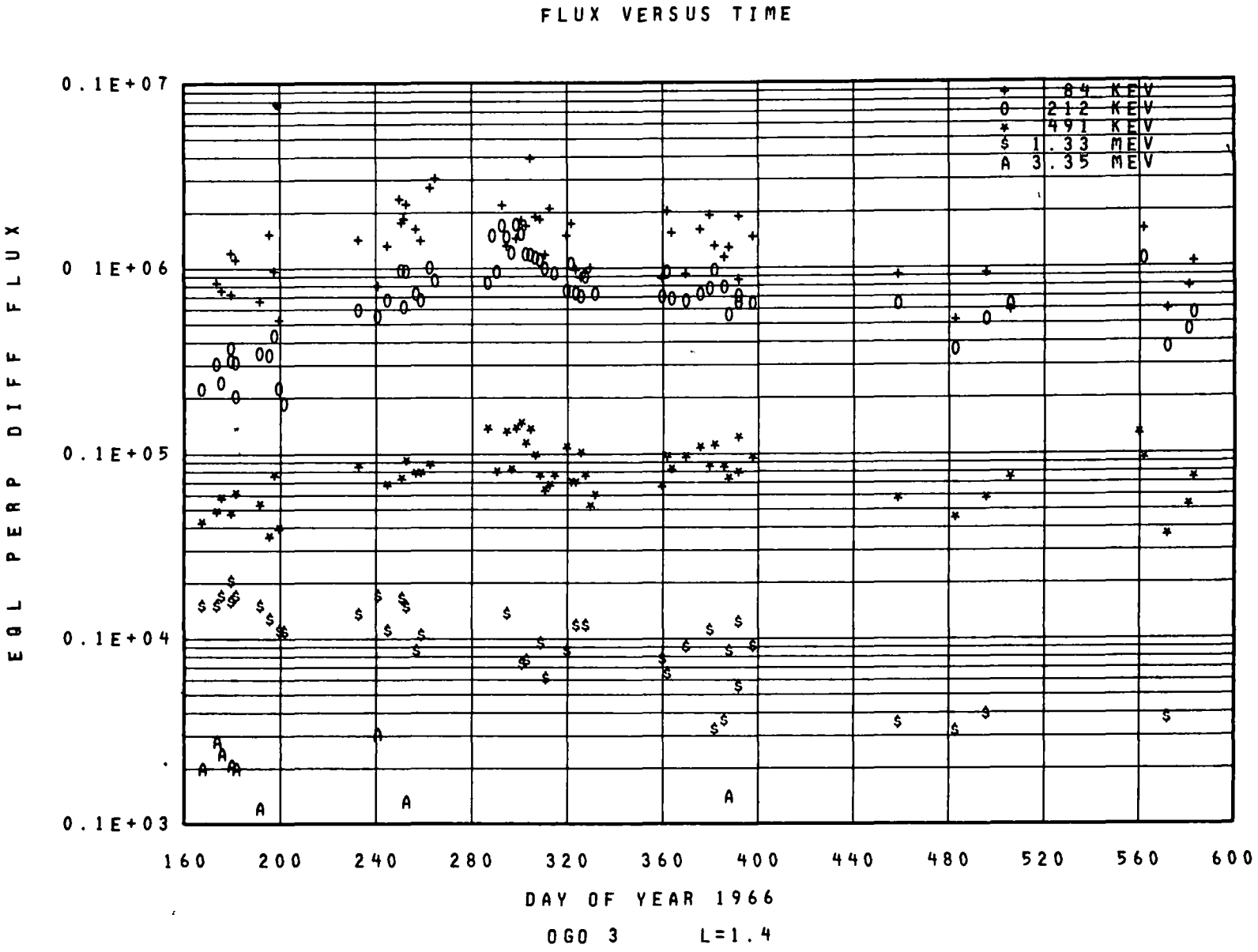
FLUX VERSUS TIME
0.1E+07
0 1E+06
0.1E+05
0.1E+04
0.1E+03
EQL PERP DIFF FLUX
+ 84 KEV
0 212 KEV
* 491 KEV
$ 1.33 MEV
A 3.35 MEV
160
200
240
280
320
360
400
440
480
520
560
600
DAY OF YEAR 1966
OGO 3 L=1.4

Figure 110

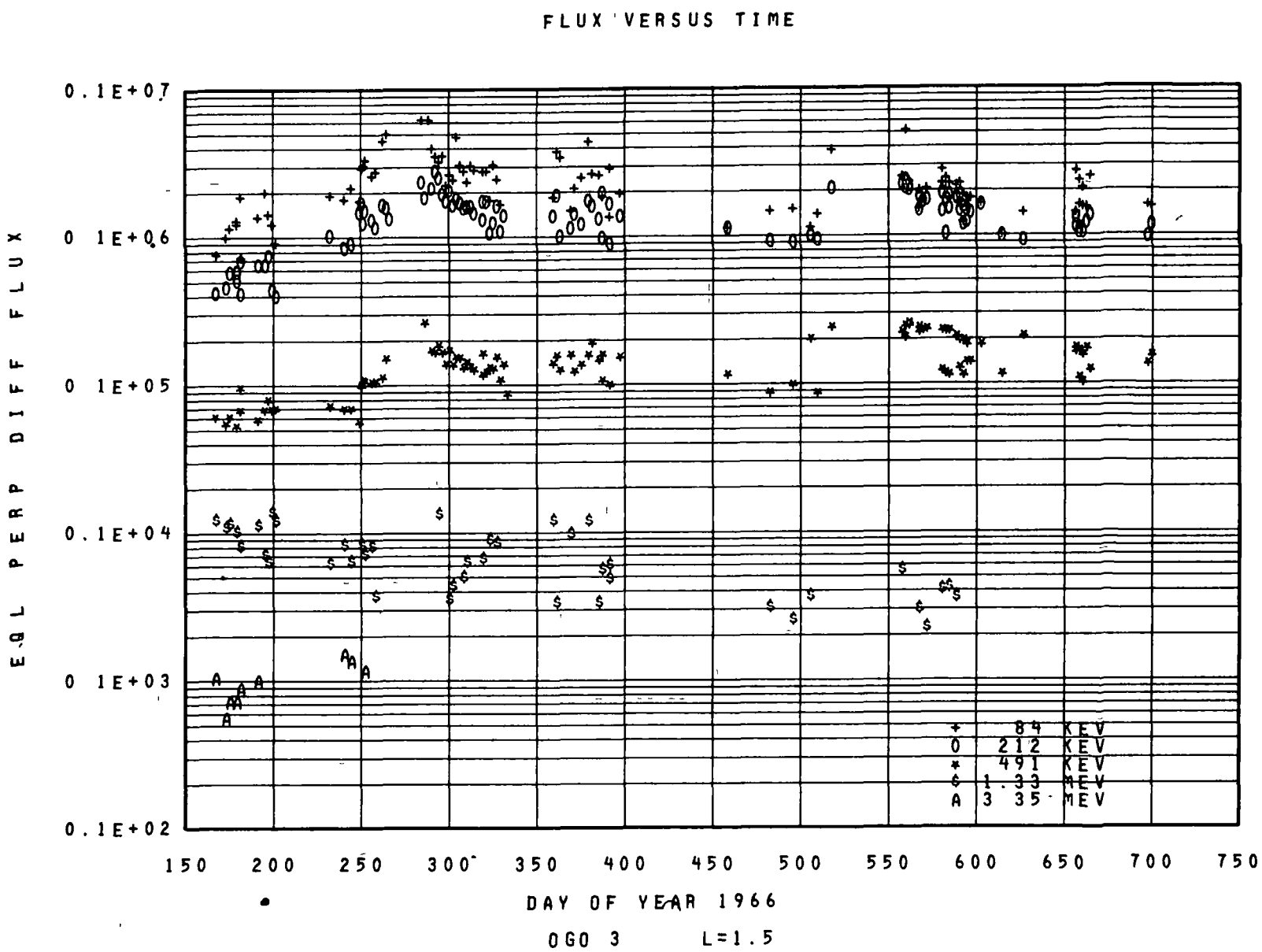
FLUX VERSUS TIME
EQL PERP DIFF FLUX
0.1E+07
0 1E+06
0 1E+05
0.1E+04
0 1E+03
0.1E+02
150
200
250
300
350
400
450
500
550
600
650
700
750
DAY OF YEAR 1966
OGO 3 L=1.5
+ 84 KEV
0 212 KEV
* 491 KEV
$ 1.33 MEV
A 3.35 MEV

Figure 111

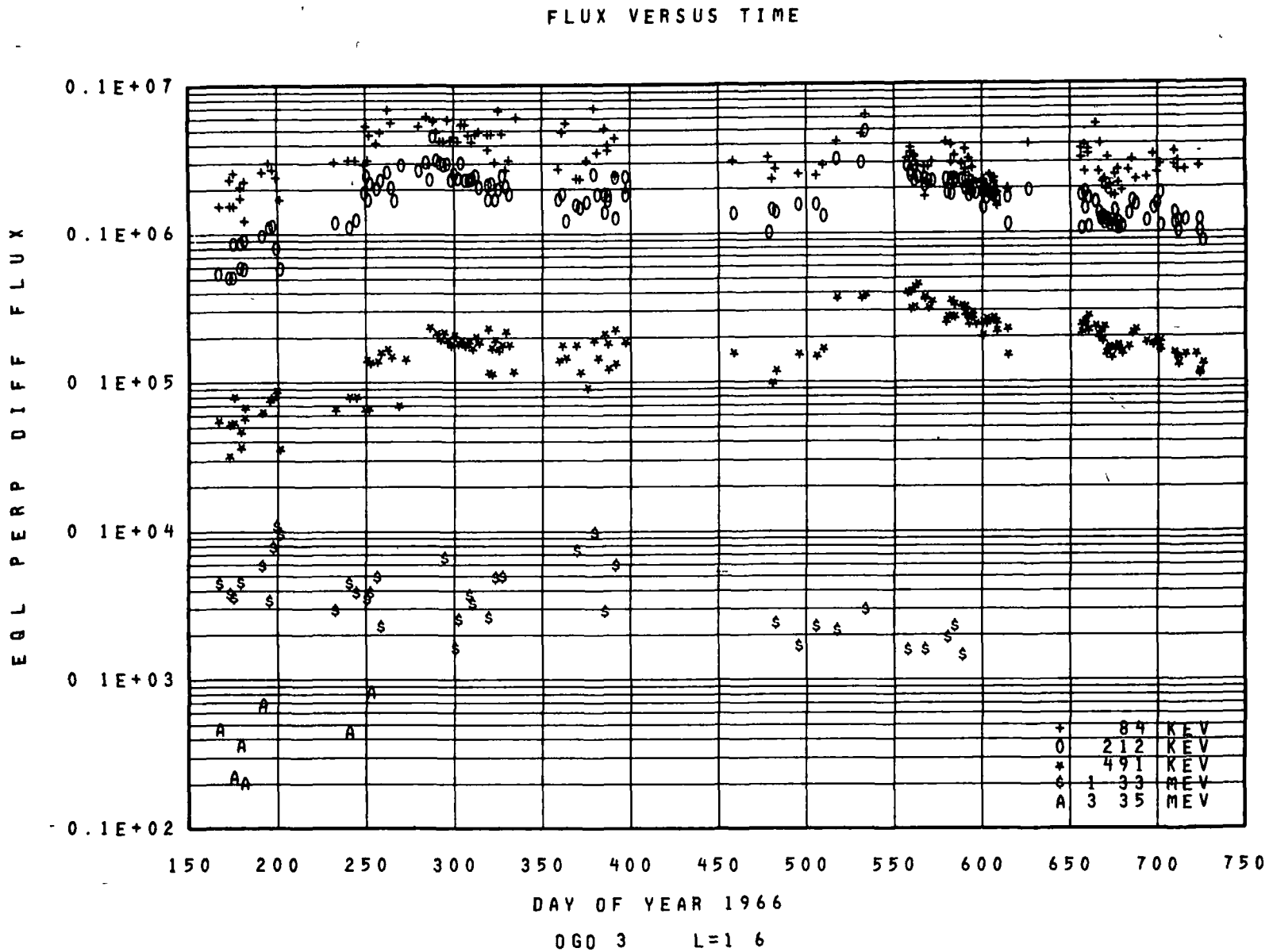
FLUX VERSUS TIME
EQL PERP DIFF FLUX
0.1E+07
0.1E+06
0 1E+05
0 1E+04
0 1E+03
0.1E+02
150
200
250
300
350
400
450
500
550
600
650
700
750
DAY OF YEAR 1966
OGO 3 L=1 6
+ 84 KEV
0 212 KEV
* 491 KEV
$ 1 33 MEV
A 3 35 MEV

Figure 112

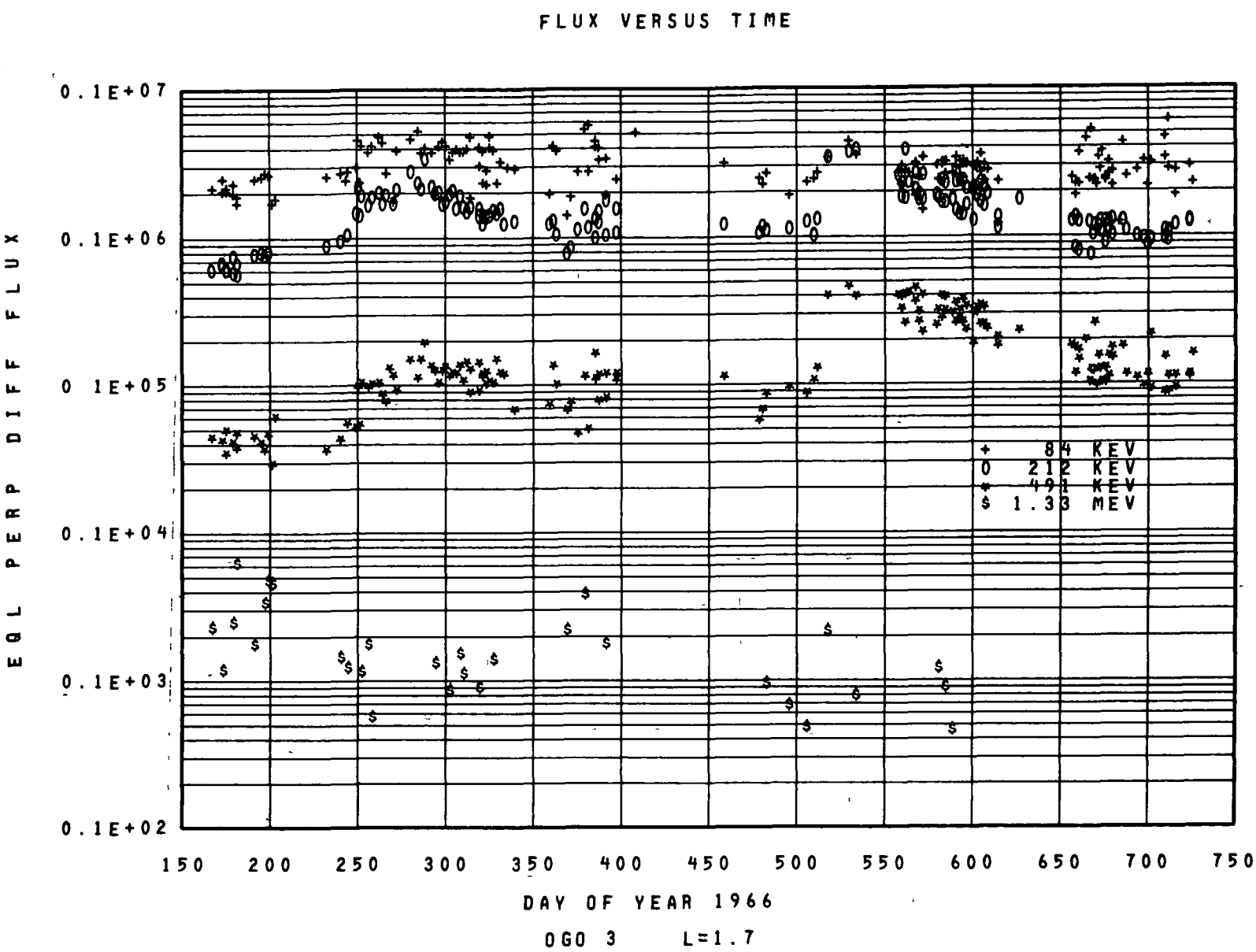
FLUX VERSUS TIME
EQL PERP DIFF FLUX
0.1E+07
0.1E+06
0 1E+05
0.1E+04
0.1E+03
0.1E+02
150
200
250
300
350
400
450
500
550
600
650
700
750
DAY OF YEAR 1966
OGO 3 L=1.7
+ 84 KEV
0 212 KEV
* 491 KEV
$ 1.33 MEV

Figure 113

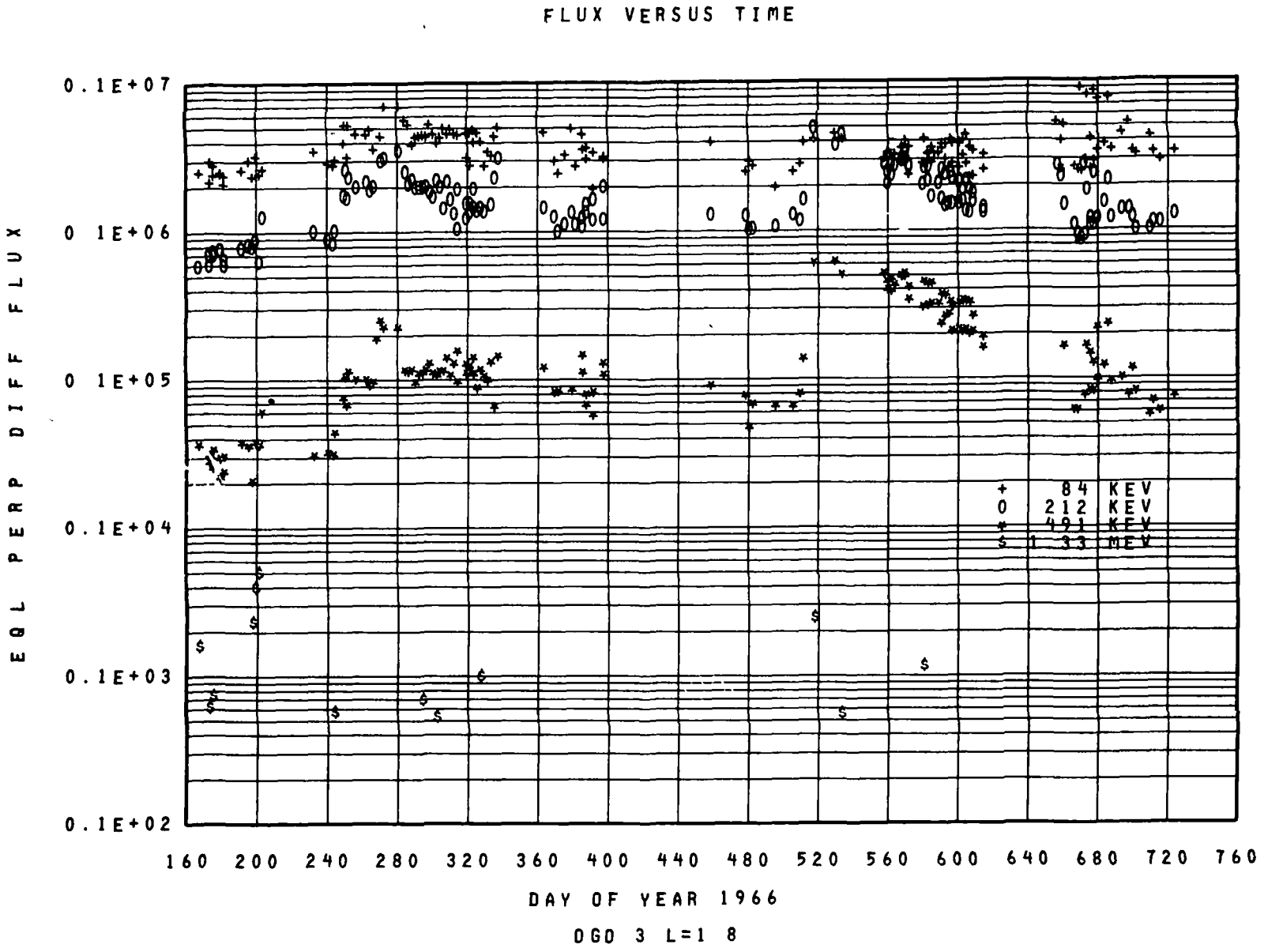
FLUX VERSUS TIME
EQL PERP DIFF FLUX
0.1E+07
0 1E+06
0 1E+05
0.1E+04
0.1E+03
0.1E+02
+ 84 KEV
0 212 KEV
* 491 KEV
$ 1 33 MEV
160 200 240 280 320 360 400 440 480 520 560 600 640 680 720 760
DAY OF YEAR 1966
DGO 3 L=1 8

Figure 114

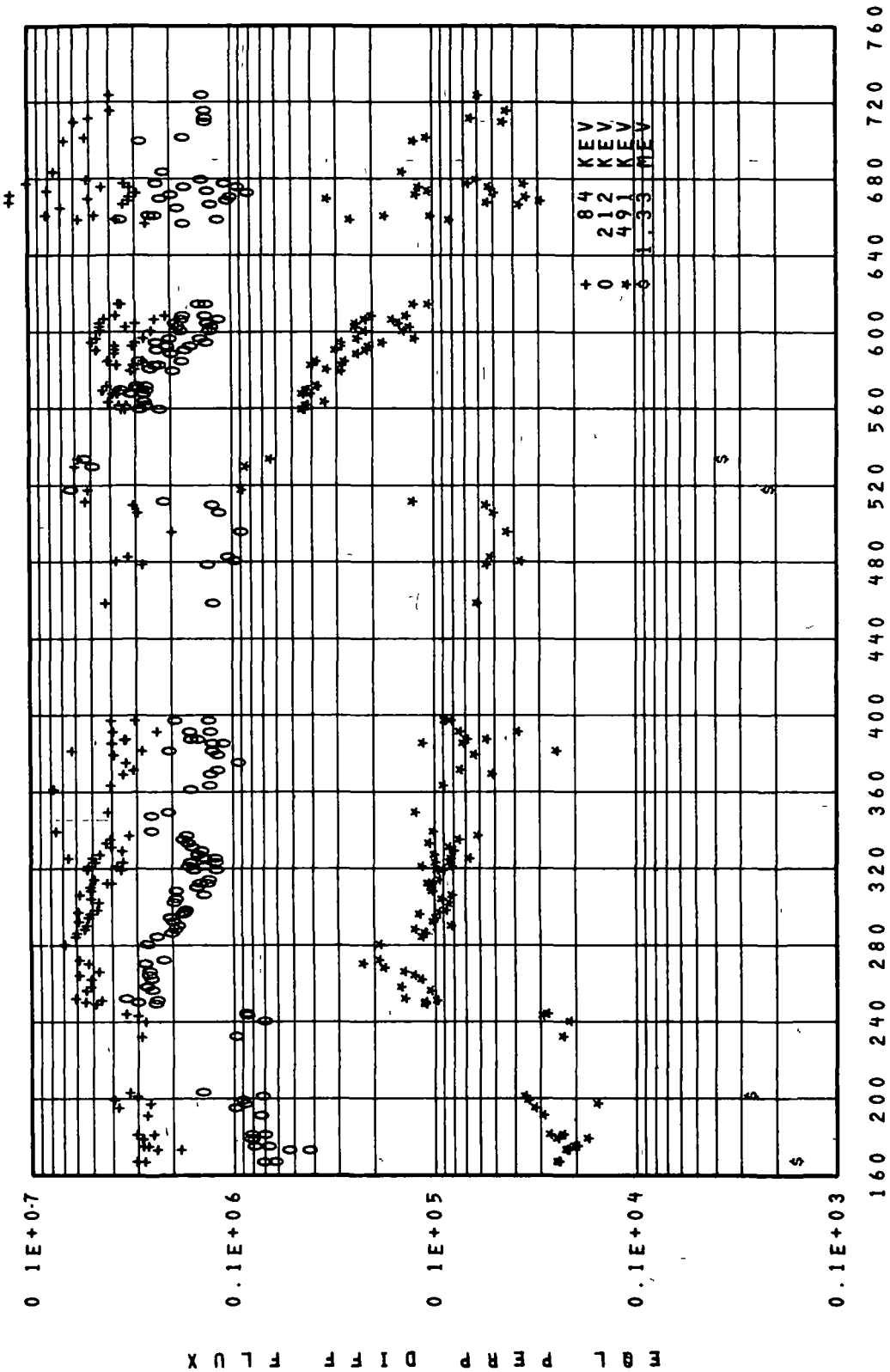
FLUX VERSUS TIME
EQL PERP DIFF FLUX
0.1E+07
0.1E+06
0.1E+05
0.1E+04
0.1E+03
160 200 240 280 320 360 400 440 480 520 560 600 640 680 720 760
DAY OF YEAR 1966
OGO 3 L=1.9
+ 84 KEV
0 212 KEV
* 491 KEV
$ 1.33 MEV

Figure 115

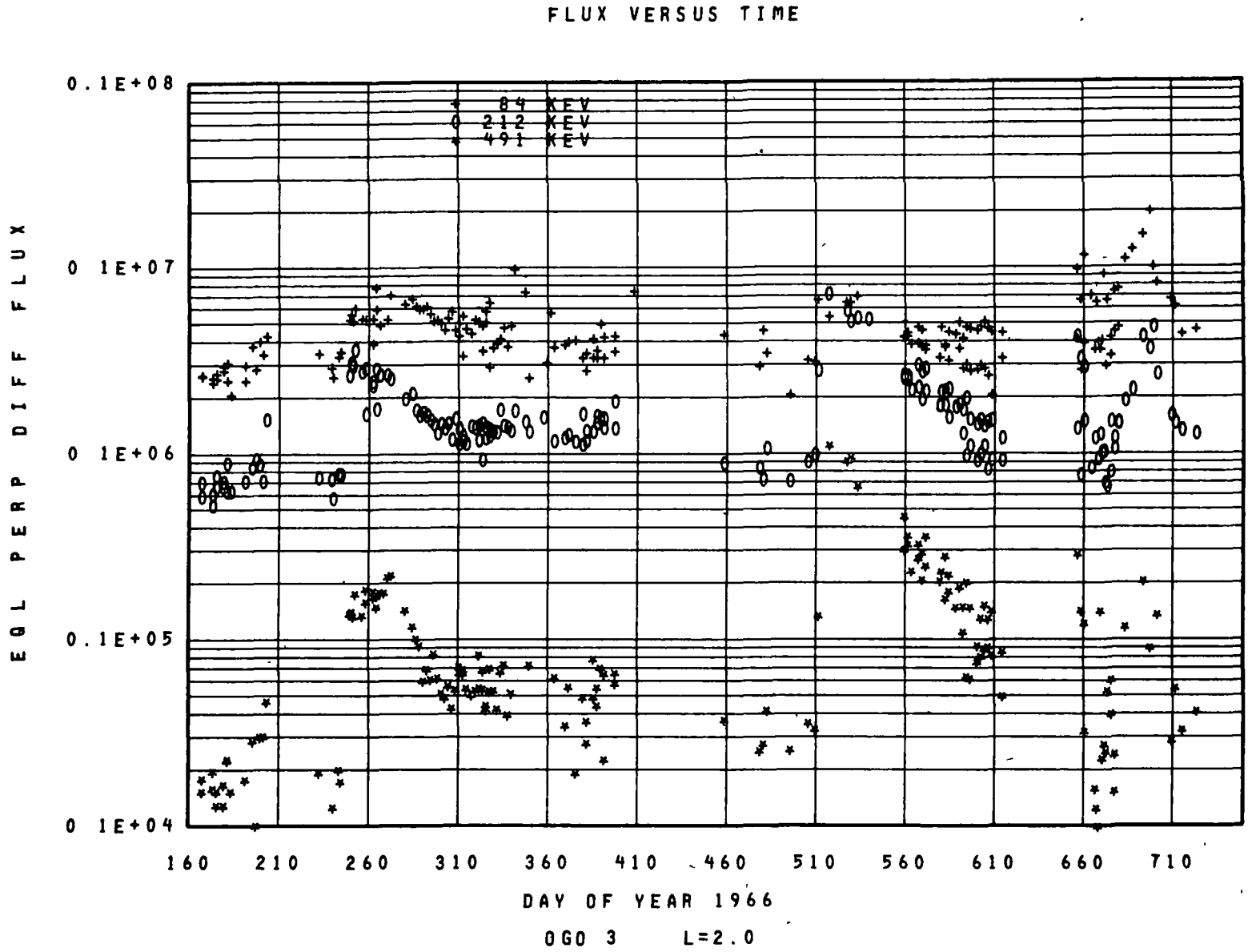
FLUX VERSUS TIME
84 KEV
212 KEV
491 KEV
0.1E+08
0 1E+07
0 1E+06
0.1E+05
0 1E+04
EQL PERP DIFF FLUX
160
210
260
310
360
410
460
510
560
610
660
710
DAY OF YEAR 1966
OGO 3 L=2.0

Figure 116

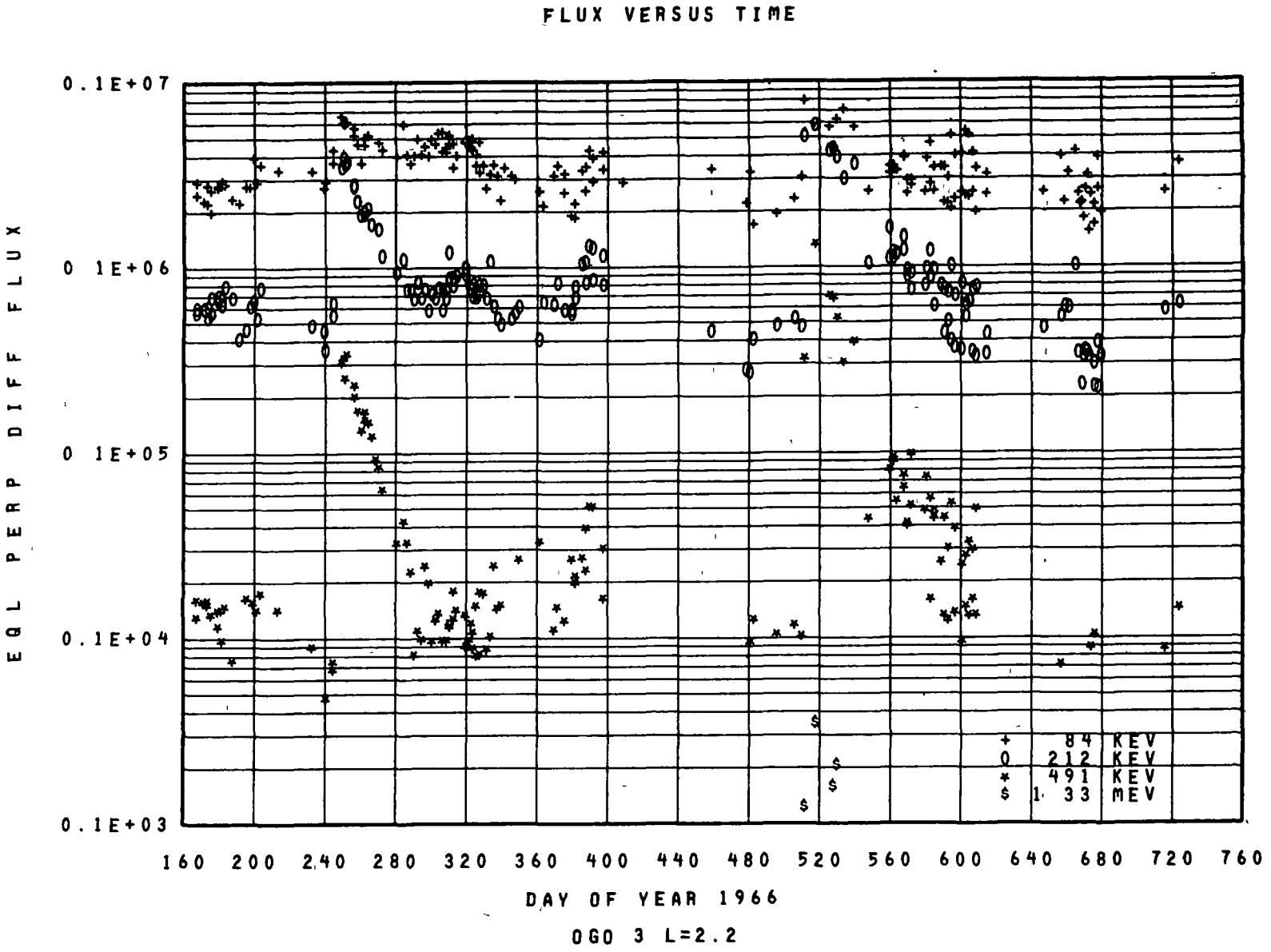
FLUX VERSUS TIME
EQL PERP DIFF FLUX
0.1E+07
0 1E+06
0 1E+05
0.1E+04
0.1E+03
160 200 240 280 320 360 400 440 480 520 560 600 640 680 720 760
DAY OF YEAR 1966
OGO 3 L=2.2
+ 84 KEV
0 212 KEV
* 491 KEV
$ 1.33 MEV

Figure 117

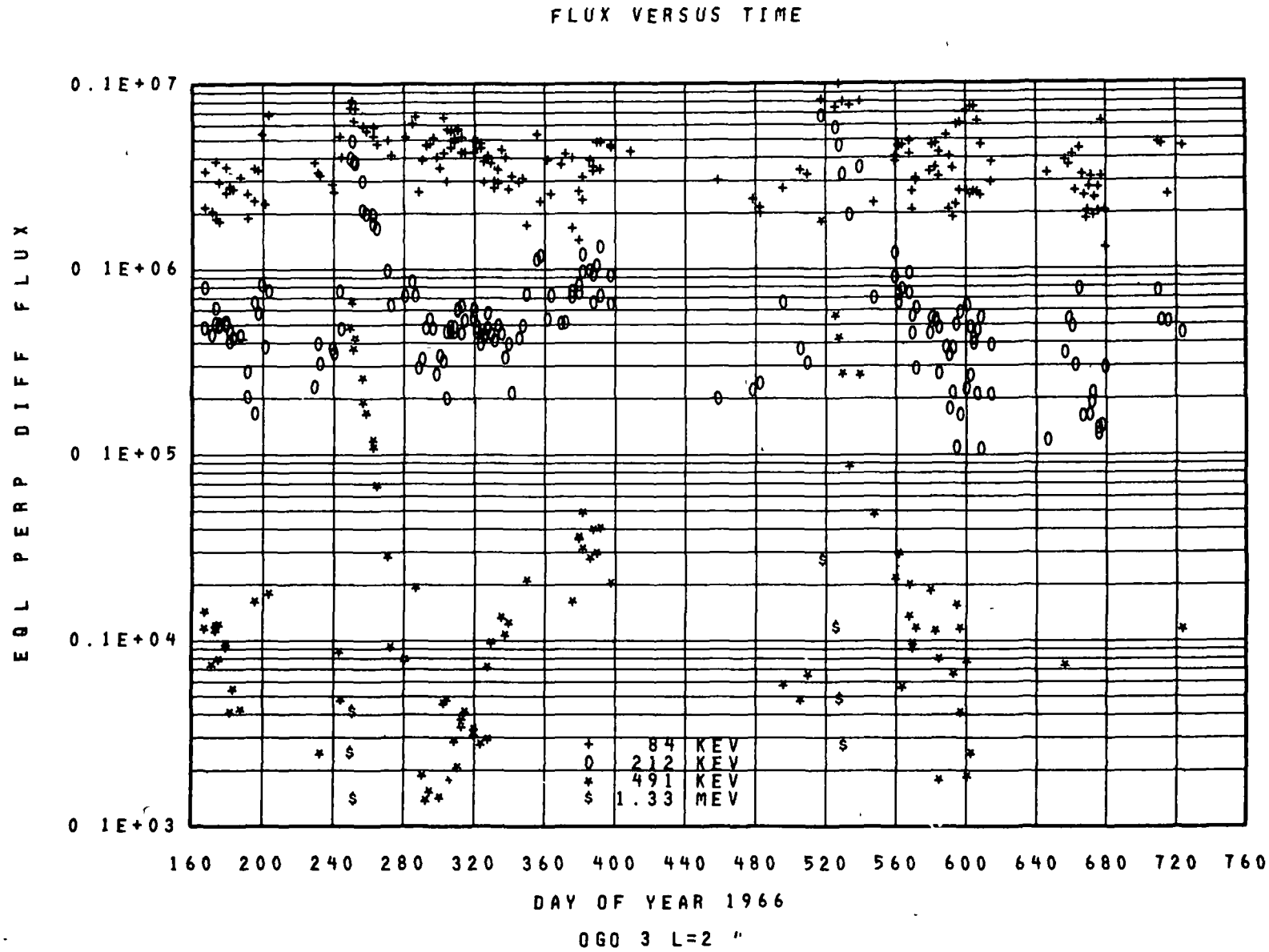
FLUX VERSUS TIME
0.1E+07
0 1E+06
0 1E+05
0.1E+04
0 1E+03
EQL PERP DIFF FLUX
84 KEV
212 KEV
491 KEV
1.33 MEV
160 200 240 280 320 360 400 440 480 520 560 600 640 680 720 760
DAY OF YEAR 1966
OGO 3 L=2 "

Figure 118

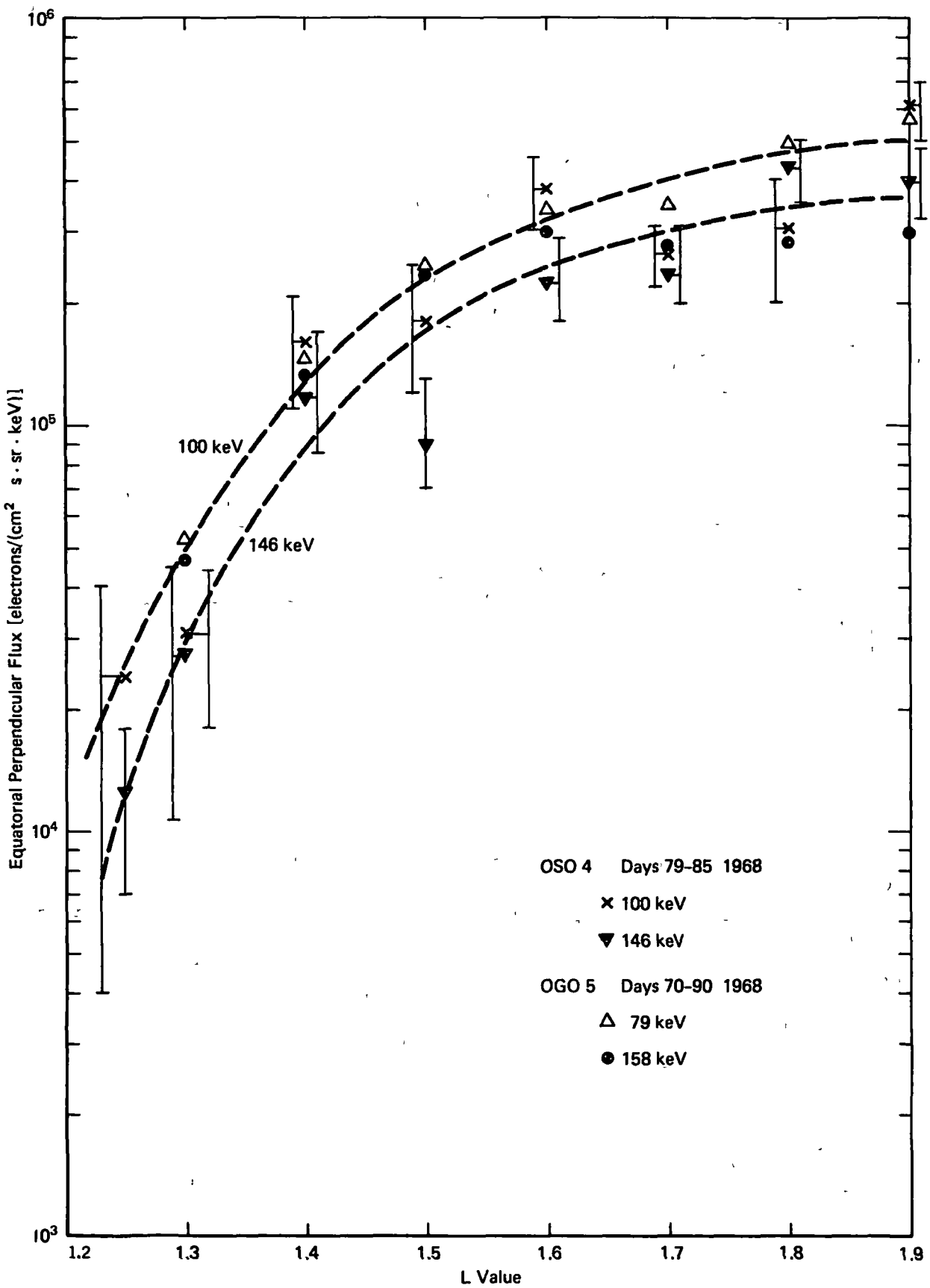

Figure 119. OSO 4 Equatorial Flux Radial Profiles

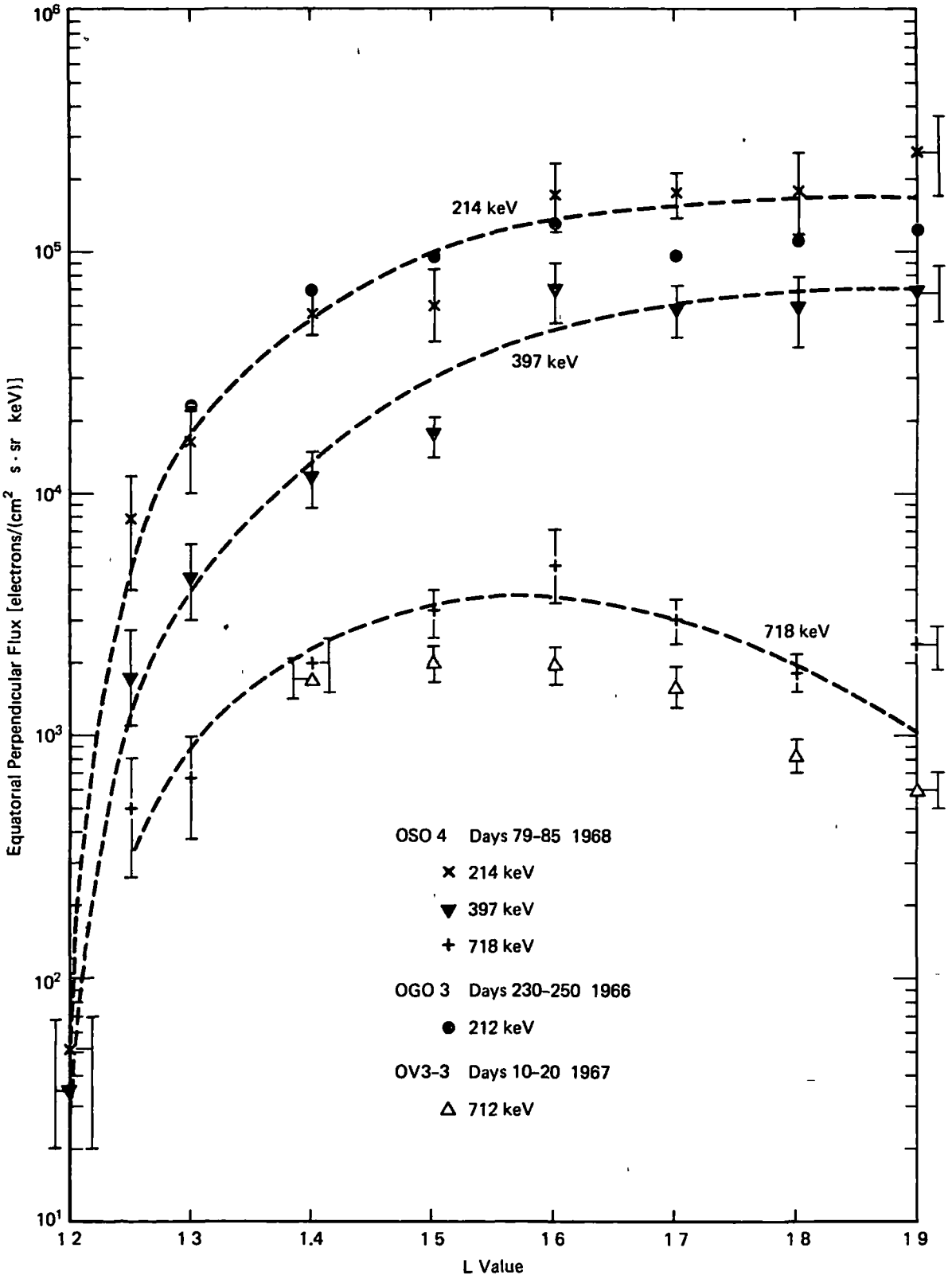

Figure 119. OSO 4 Equatorial Flux Radial Profiles (concluded)

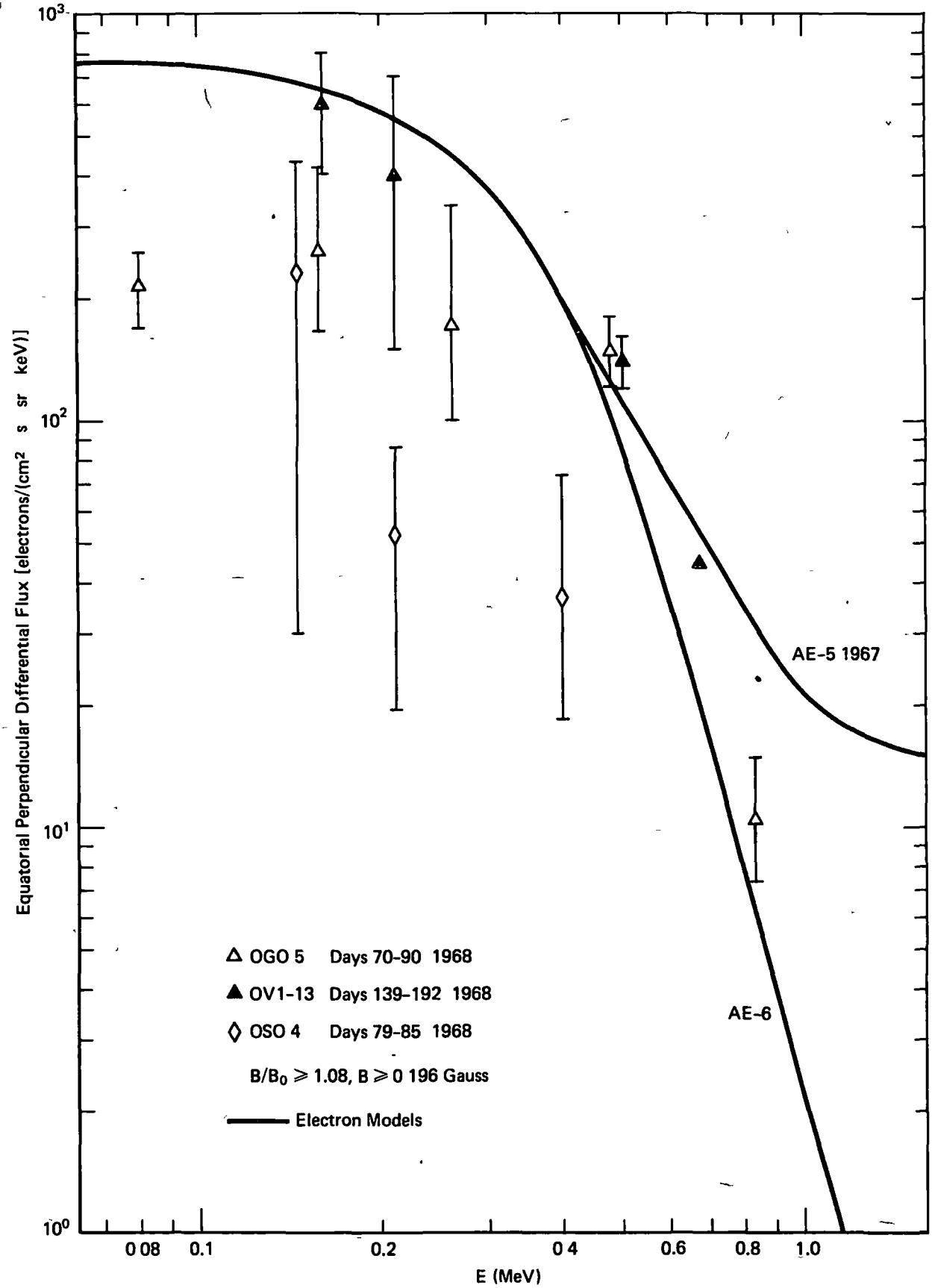

Figure 120. Quiet Time Inner Zone Spectra at L = 1.2

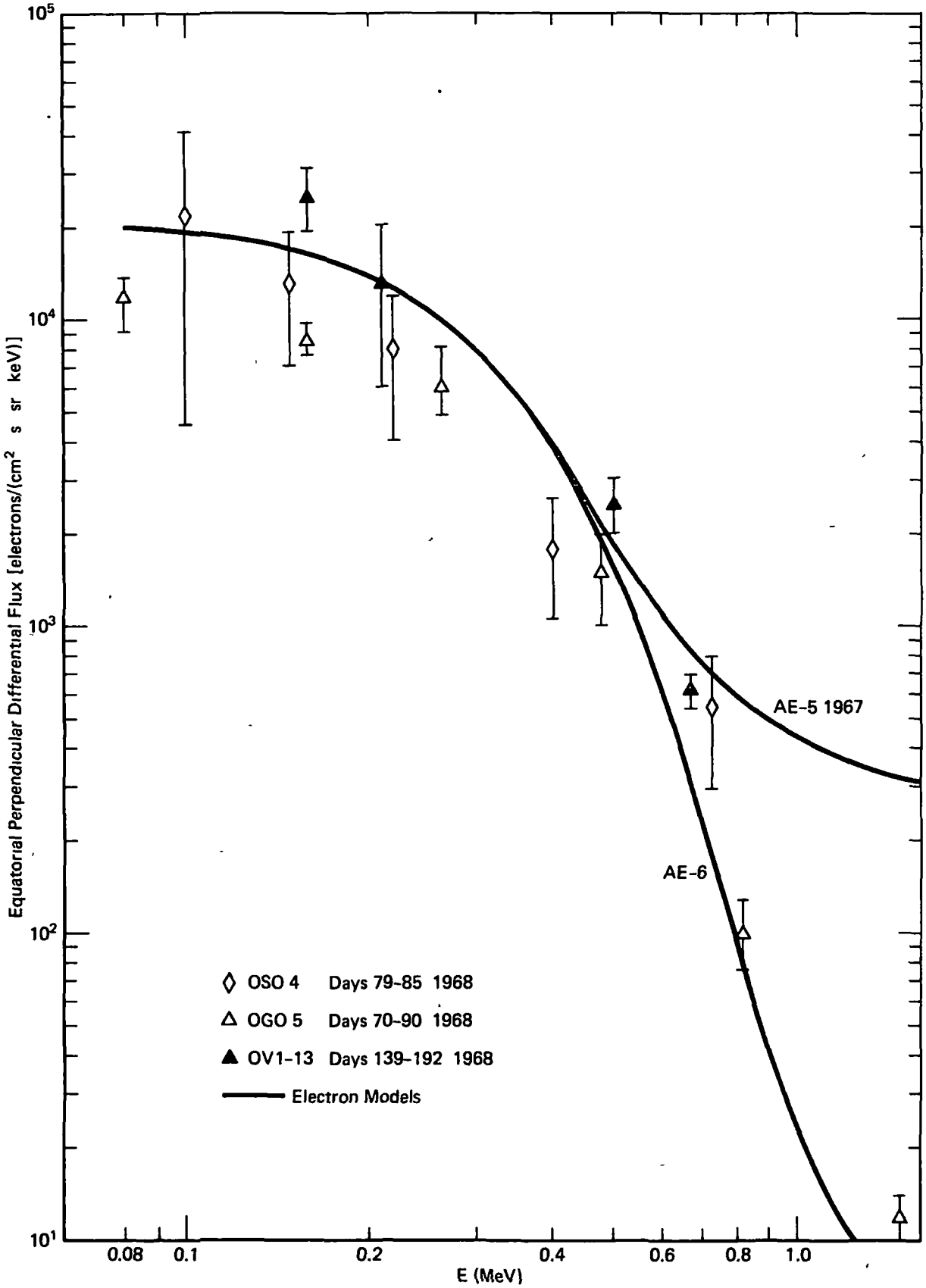

Figure 121. Quiet Time Inner Zone Spectra at L = 1.25

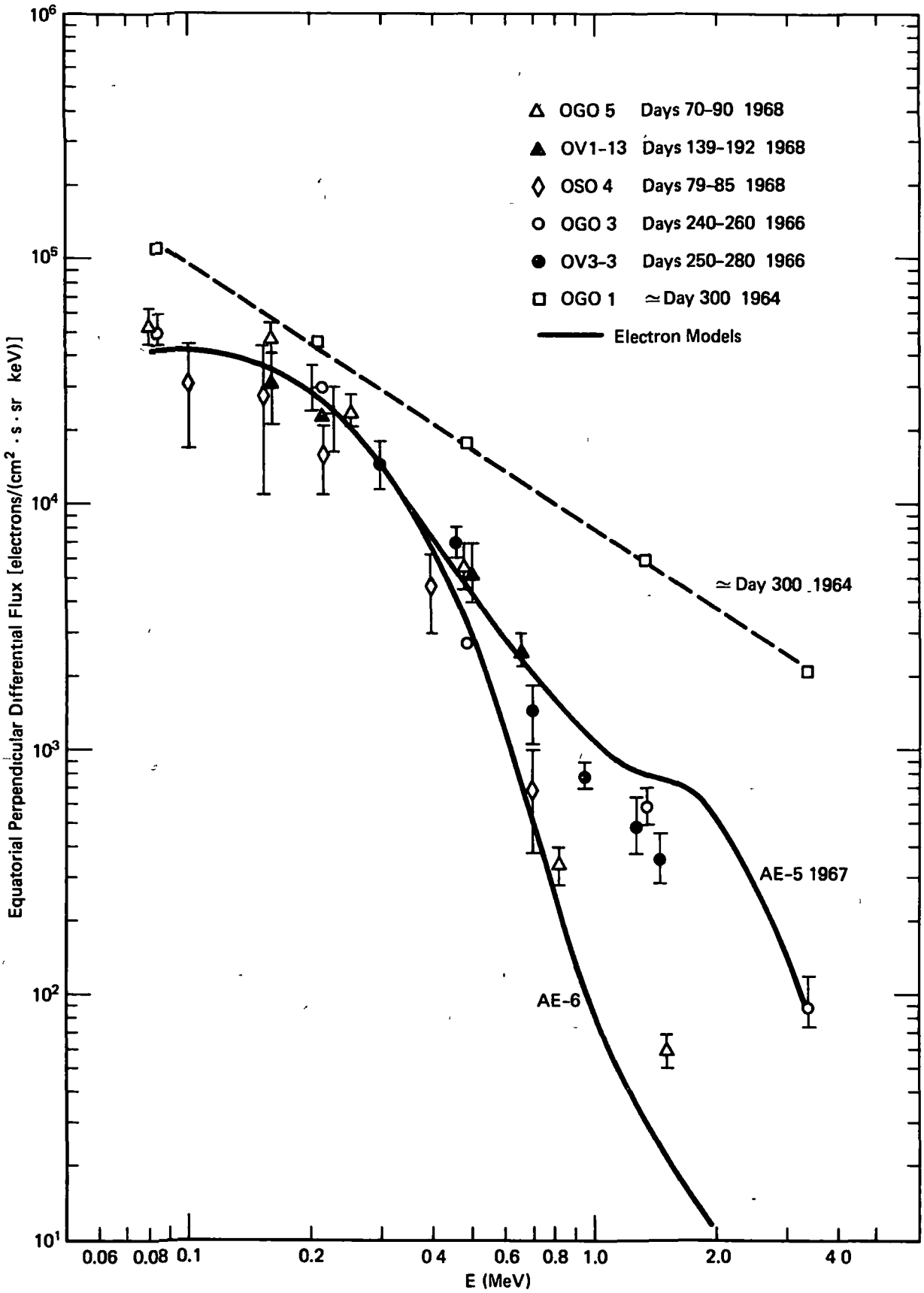

Figure 122. Quiet Time Inner Zone Spectra at L = 1.3

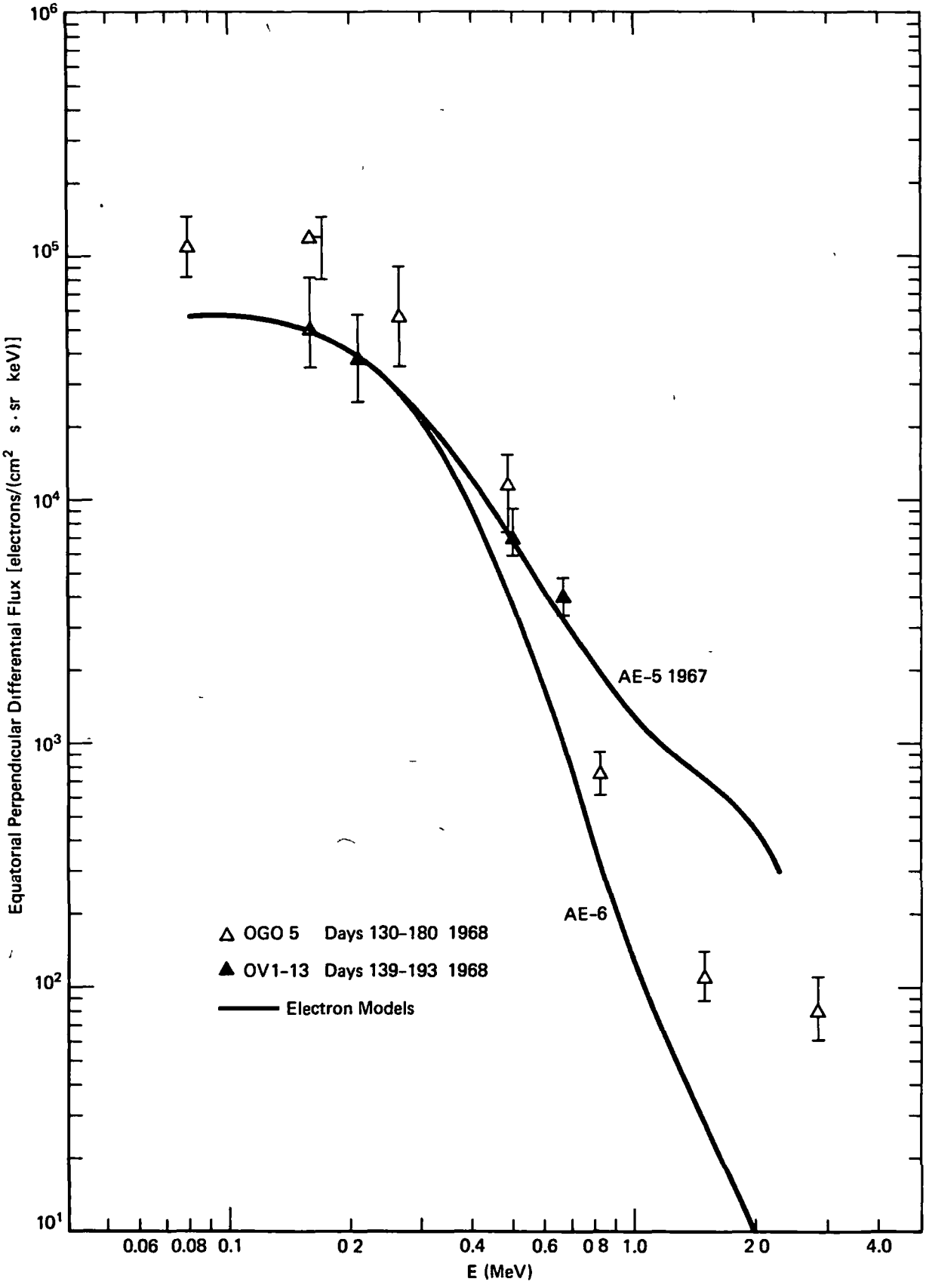

Figure 123. Quiet Time Inner Zone Spectra at L = 1.35

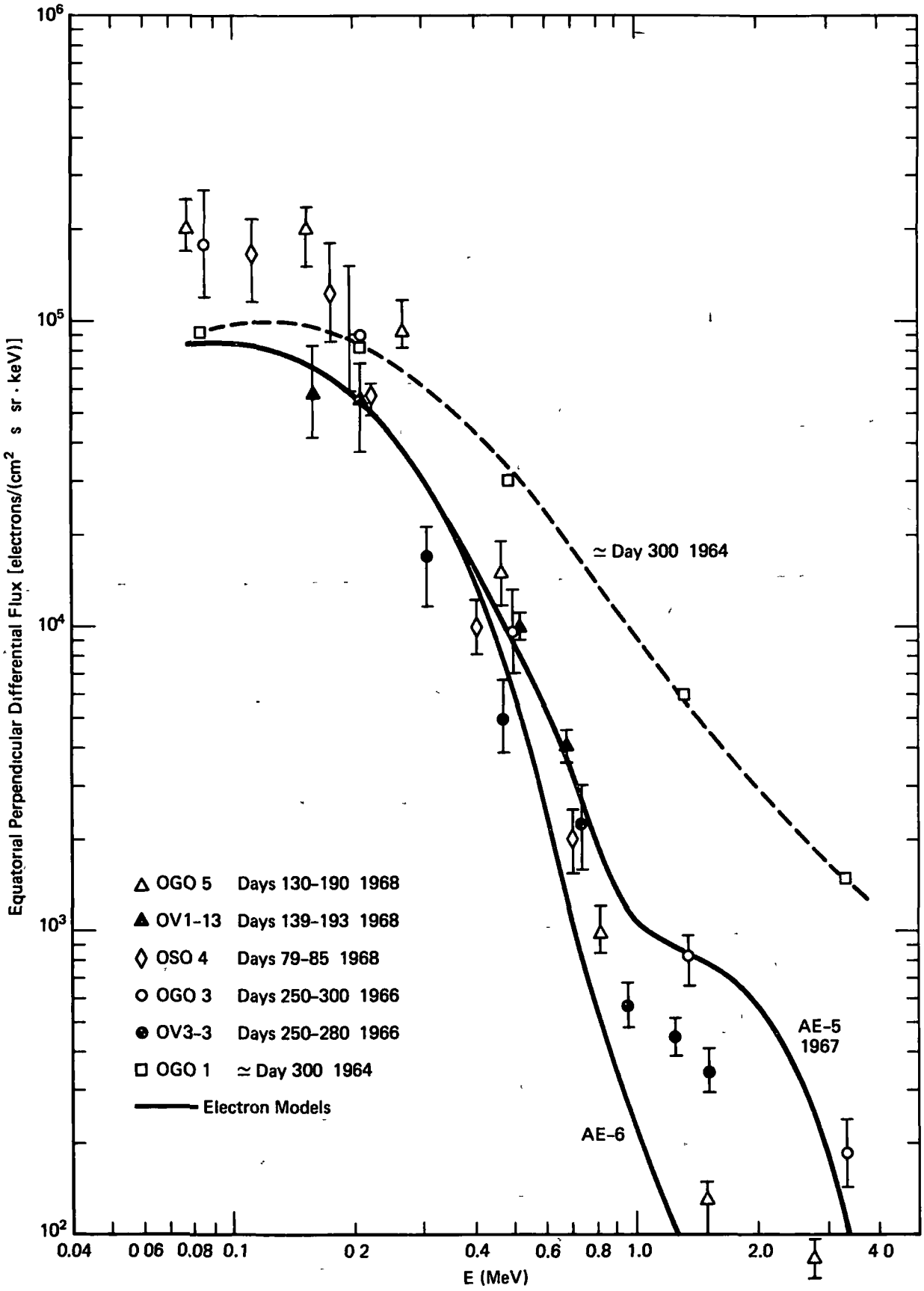

Figure 124. Quiet Time Inner Zone Spectra at L = 1.4

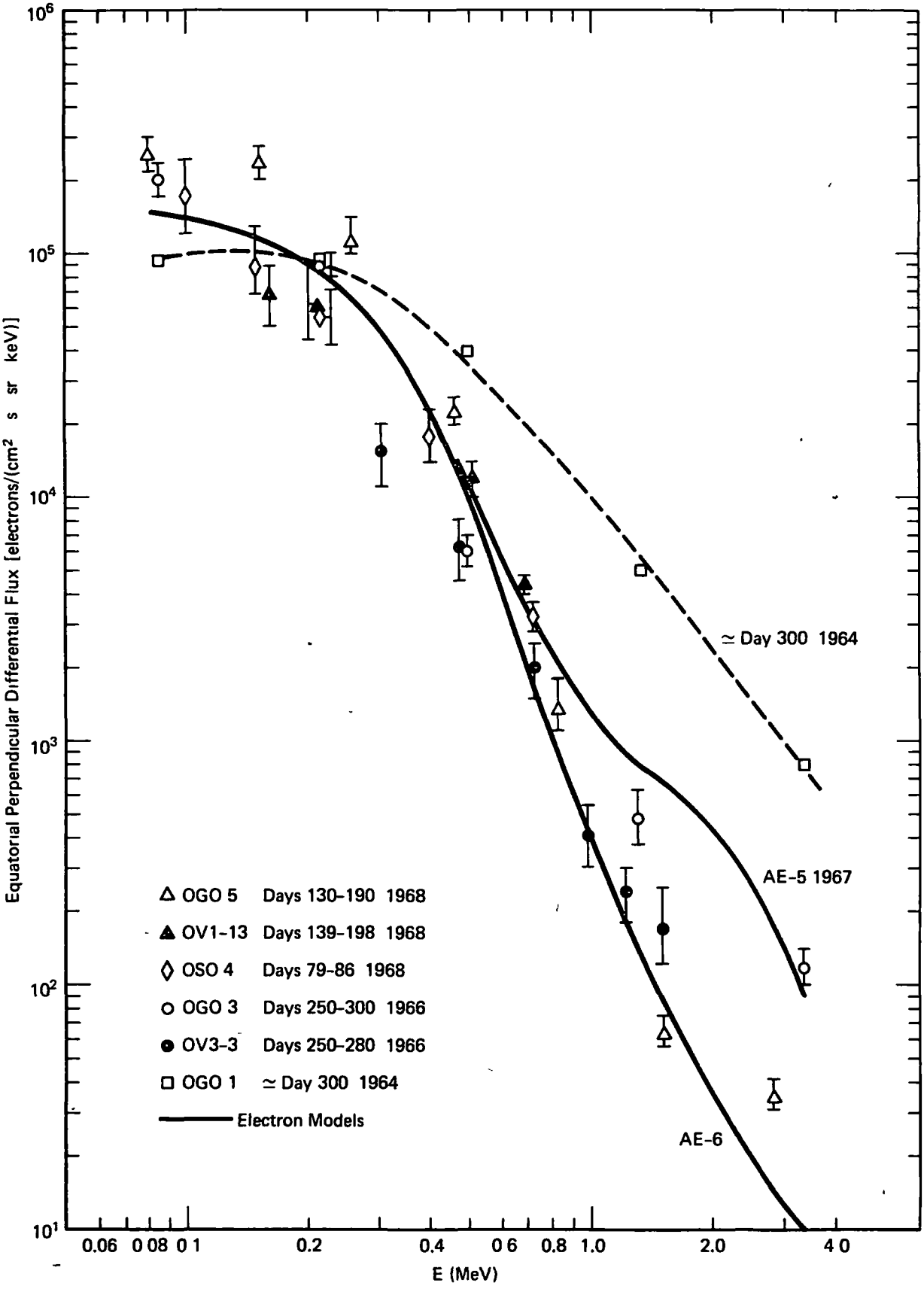

Figure 125. Quiet Time Inner Zone Spectra at L = 1.5

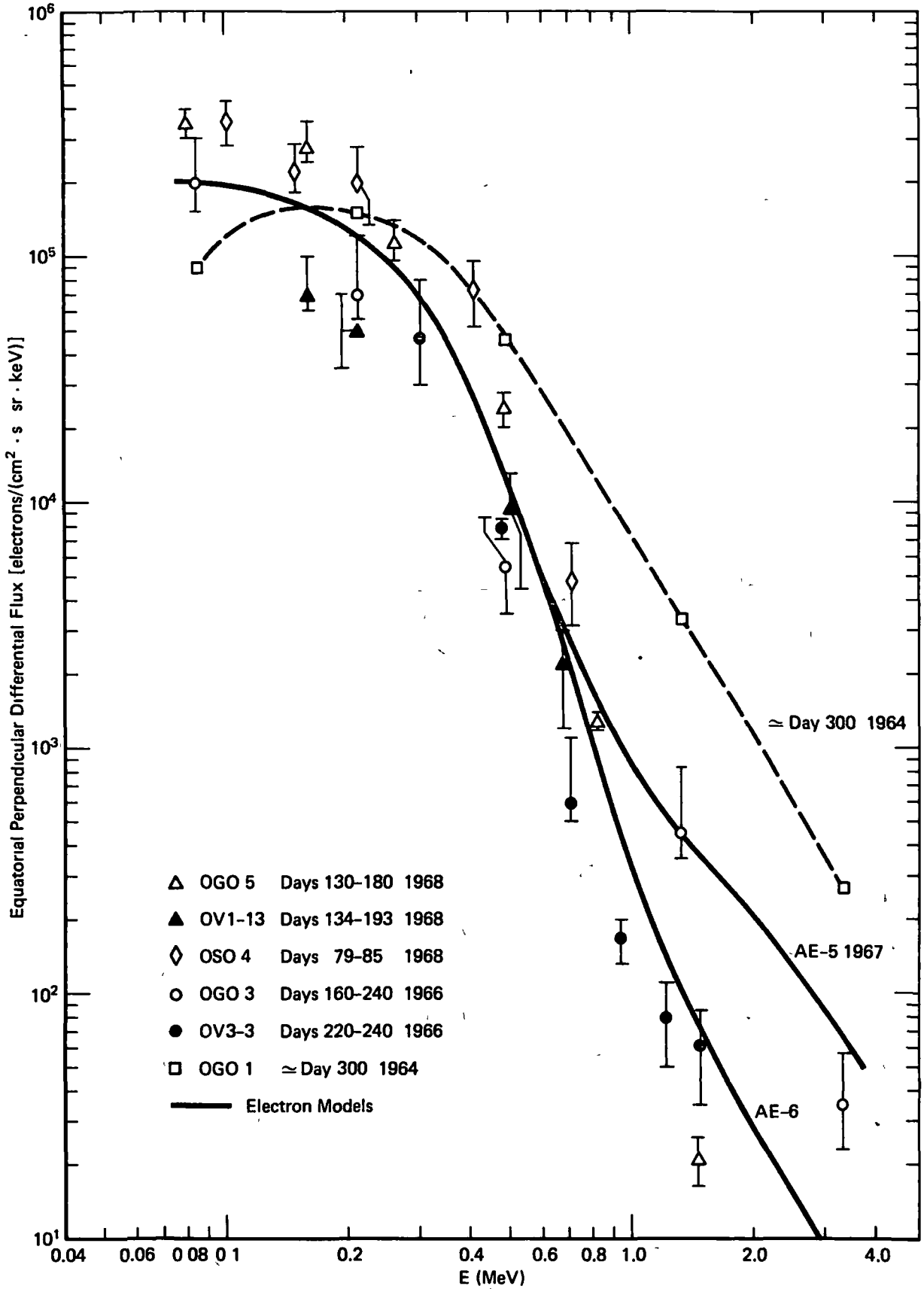

Figure 126. Quiet Time Inner Zone Spectra at L = 1.6

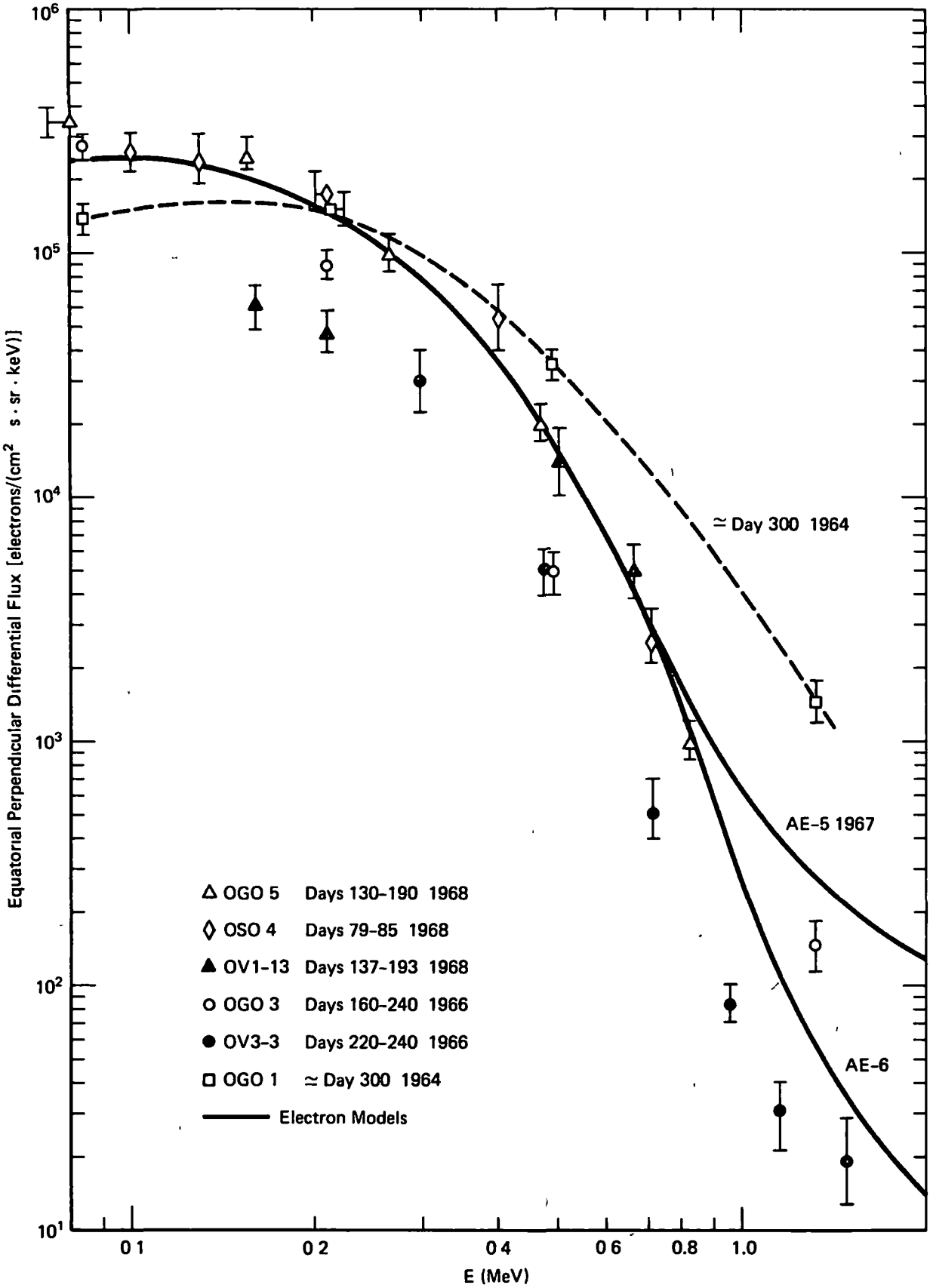

Figure 127. Quiet Time Inner Zone Spectra at L = 1.7

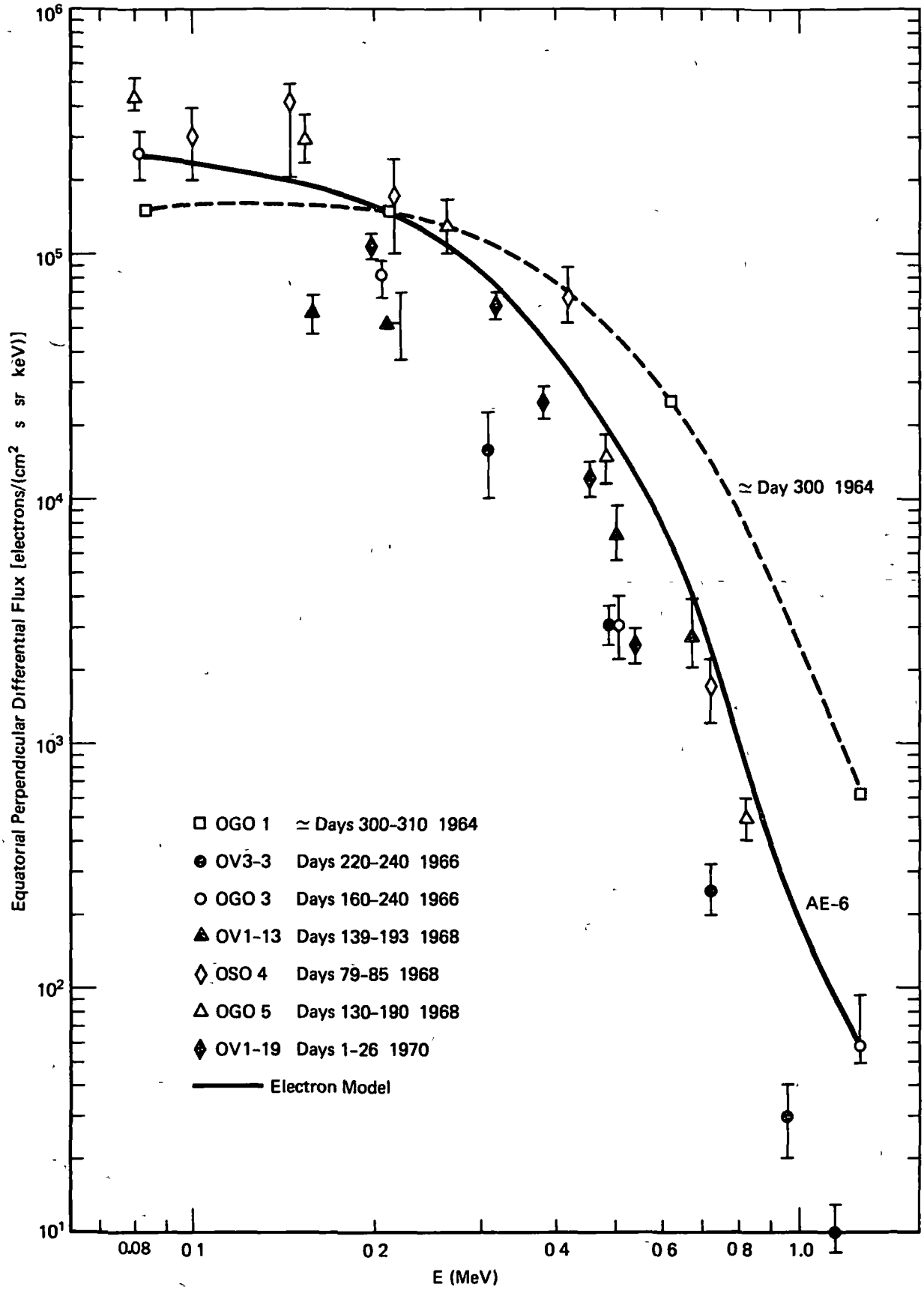

Figure 128. Quiet Time Inner Zone Spectra at L = 1.8

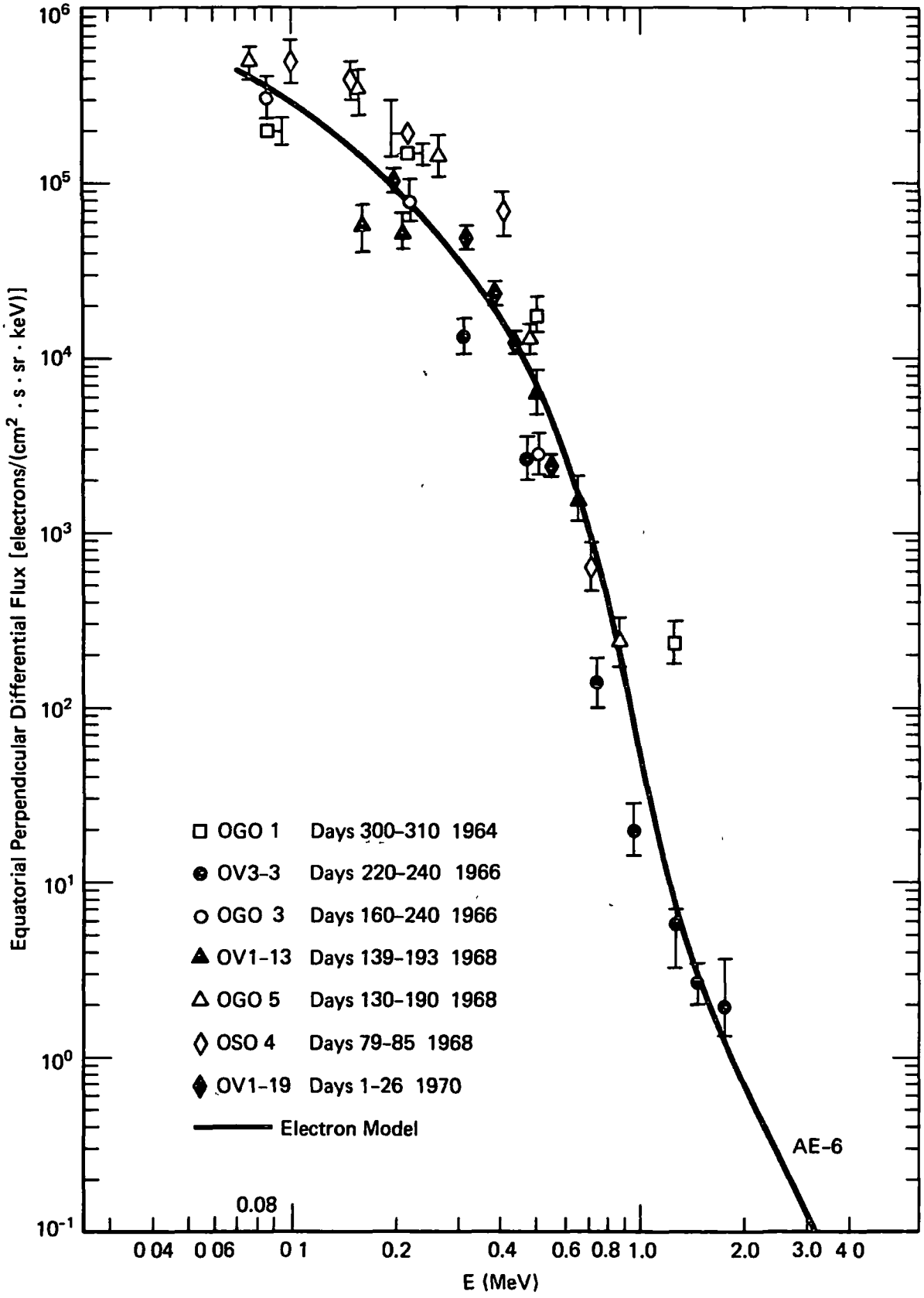

Figure 129. Quiet Time Inner Zone Spectra at L = 1.9

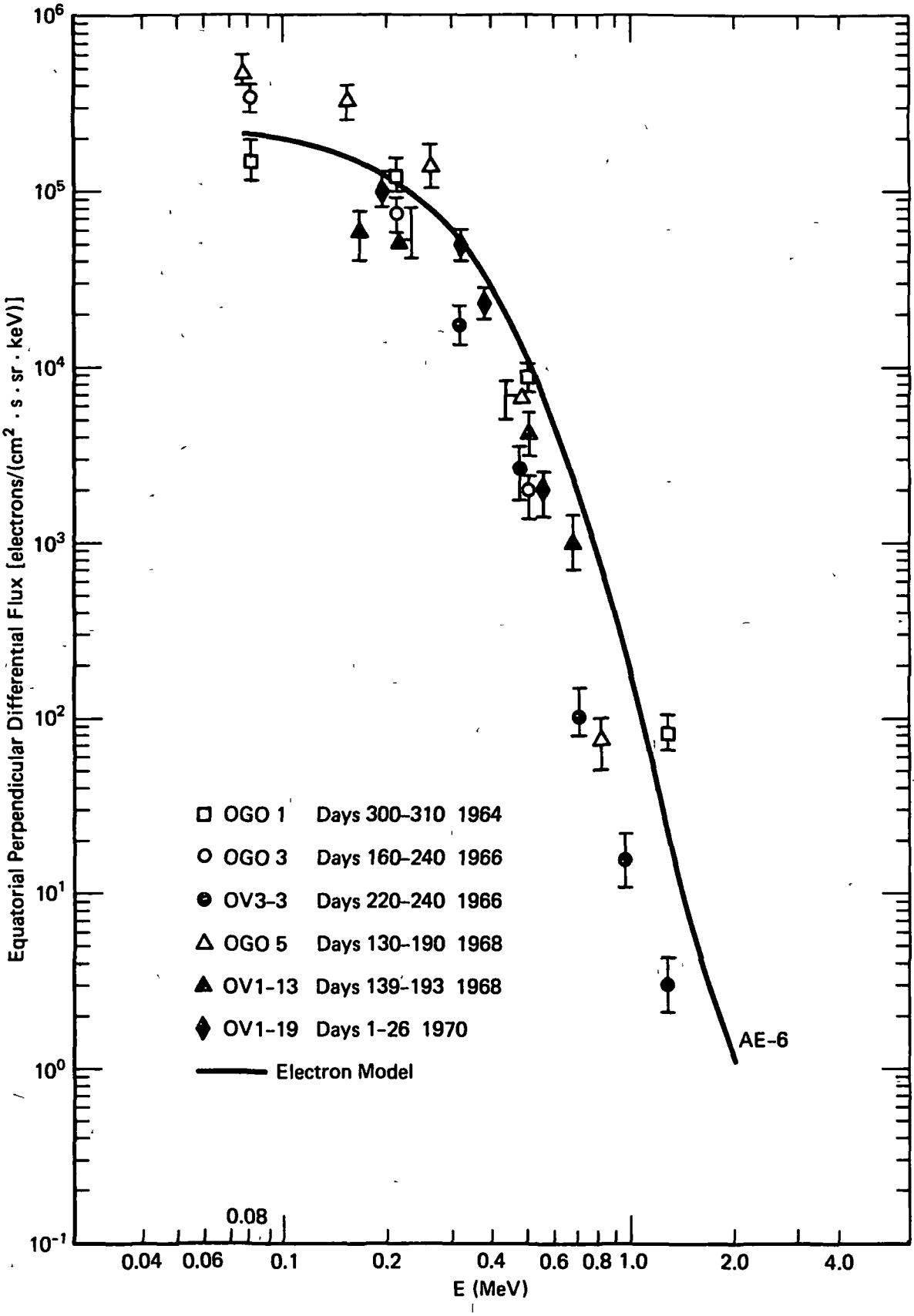

Figure 130. Quiet Time Inner Zone Spectra at L = 2.0

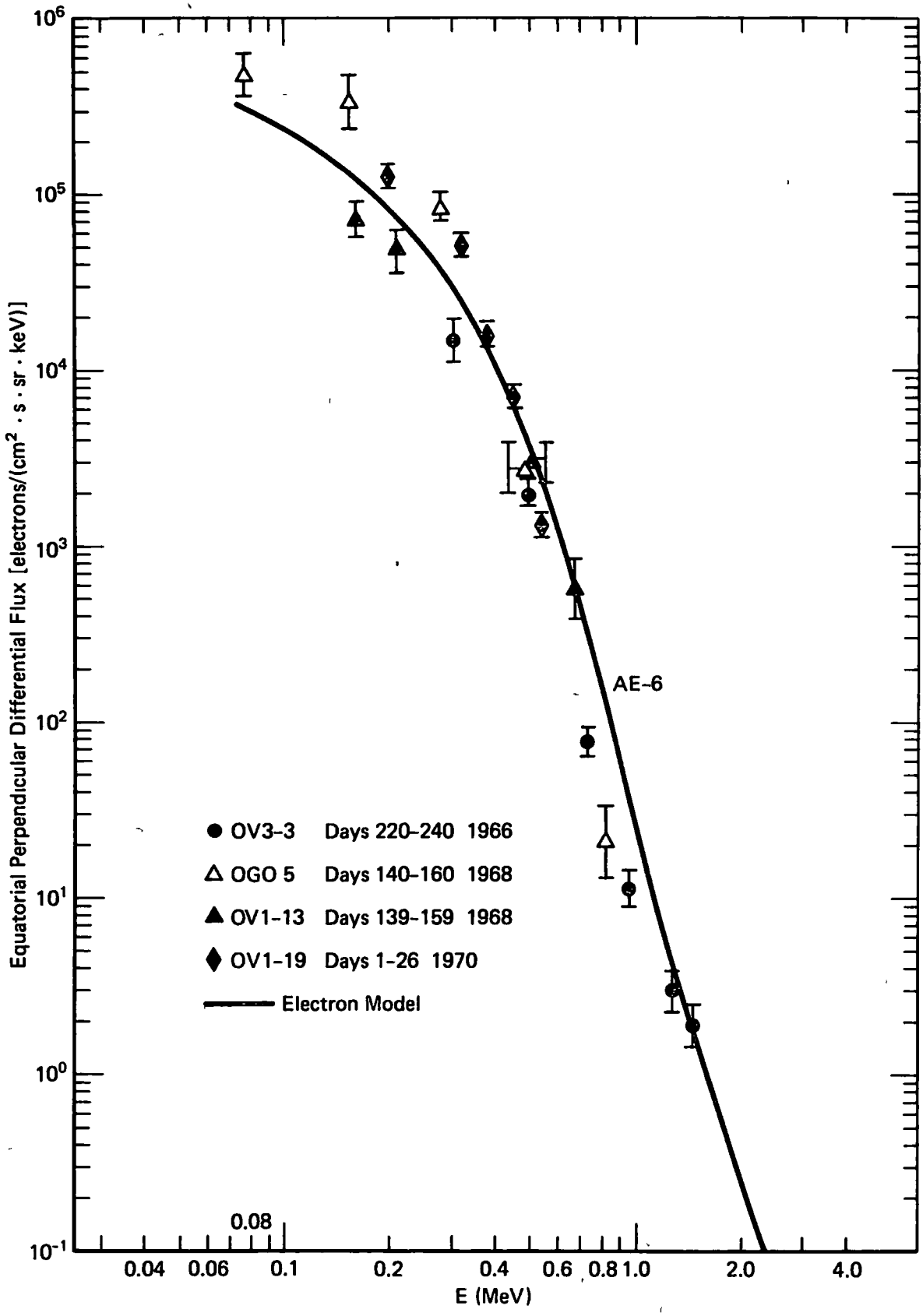

Figure 131. Quiet Time Inner Zone Spectra at L = 2.1

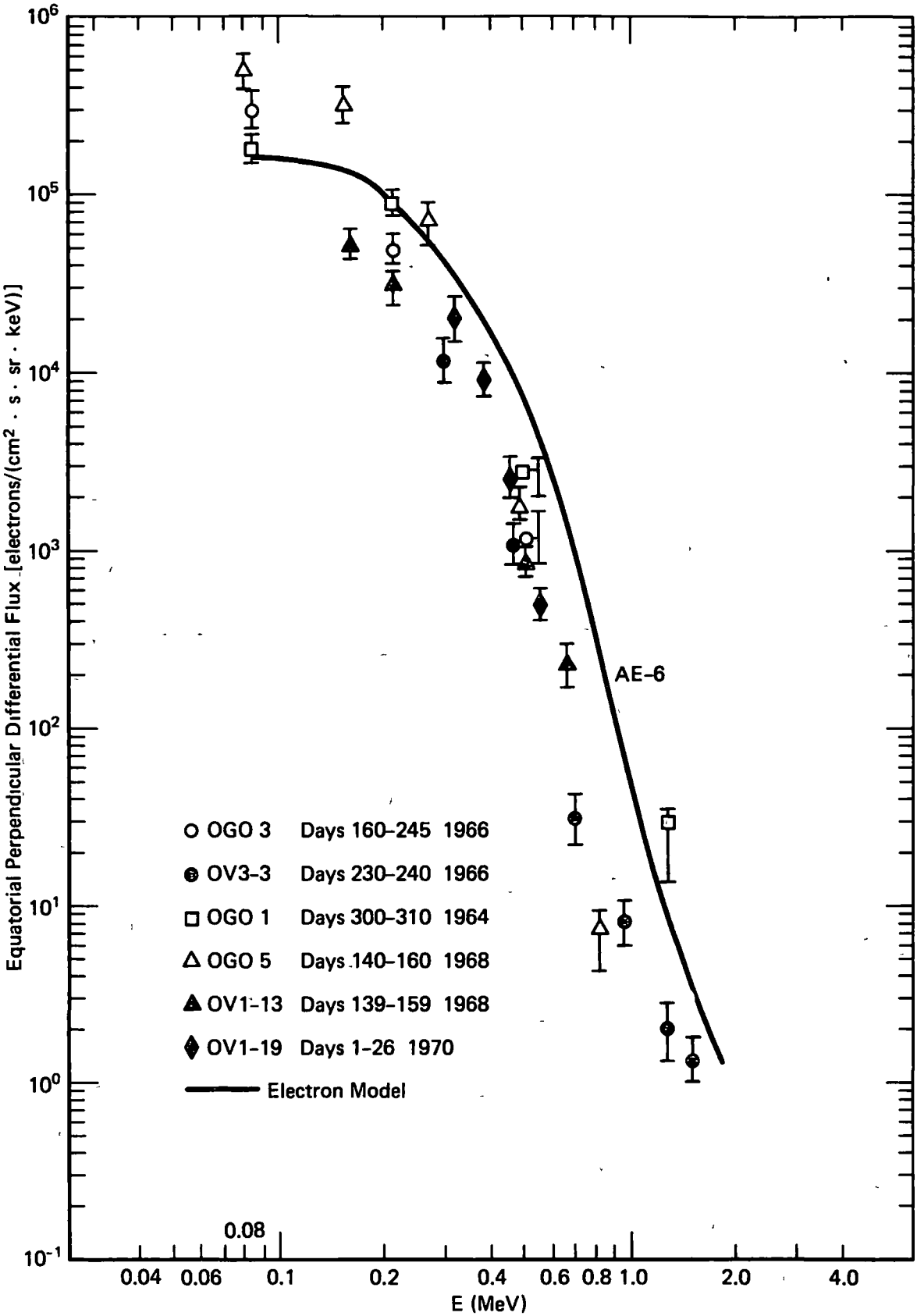

Figure 132. Quiet Time Inner Zone Spectra at L = 2.2

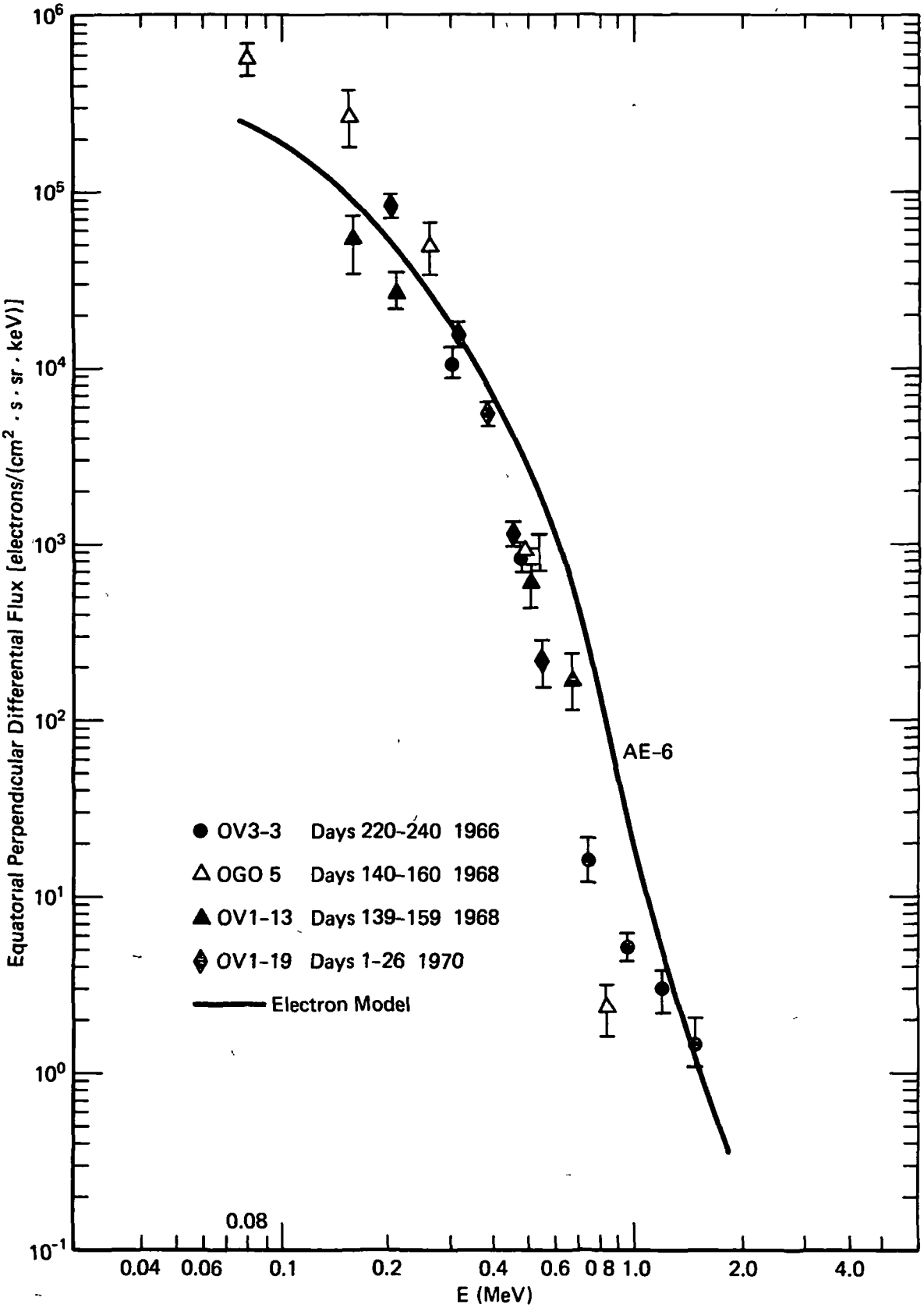

Figure 133. Quiet Time Inner Zone Spectra at L = 2.3

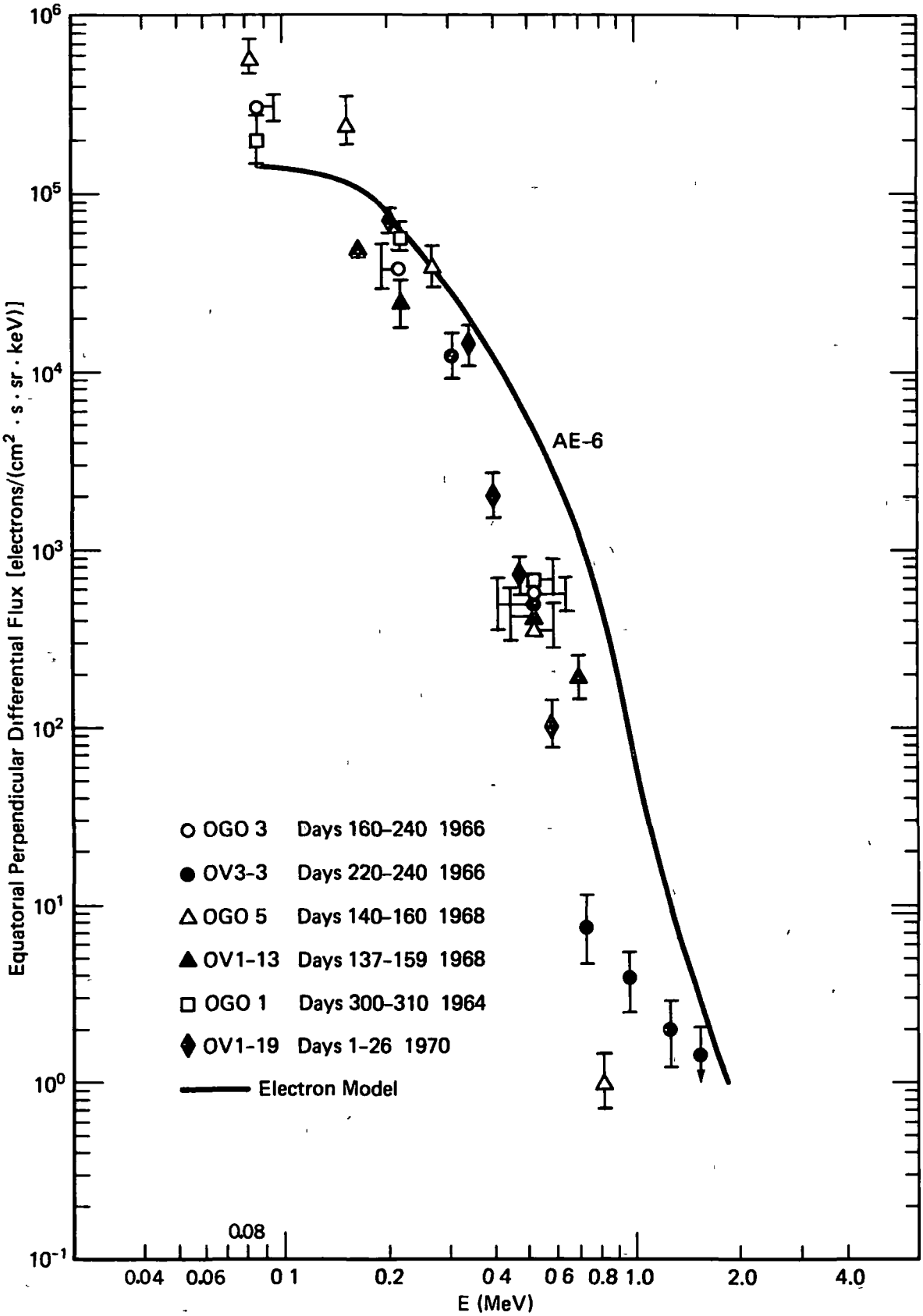

Figure 134. Quiet Time Inner Zone Spectra at L = 2.4

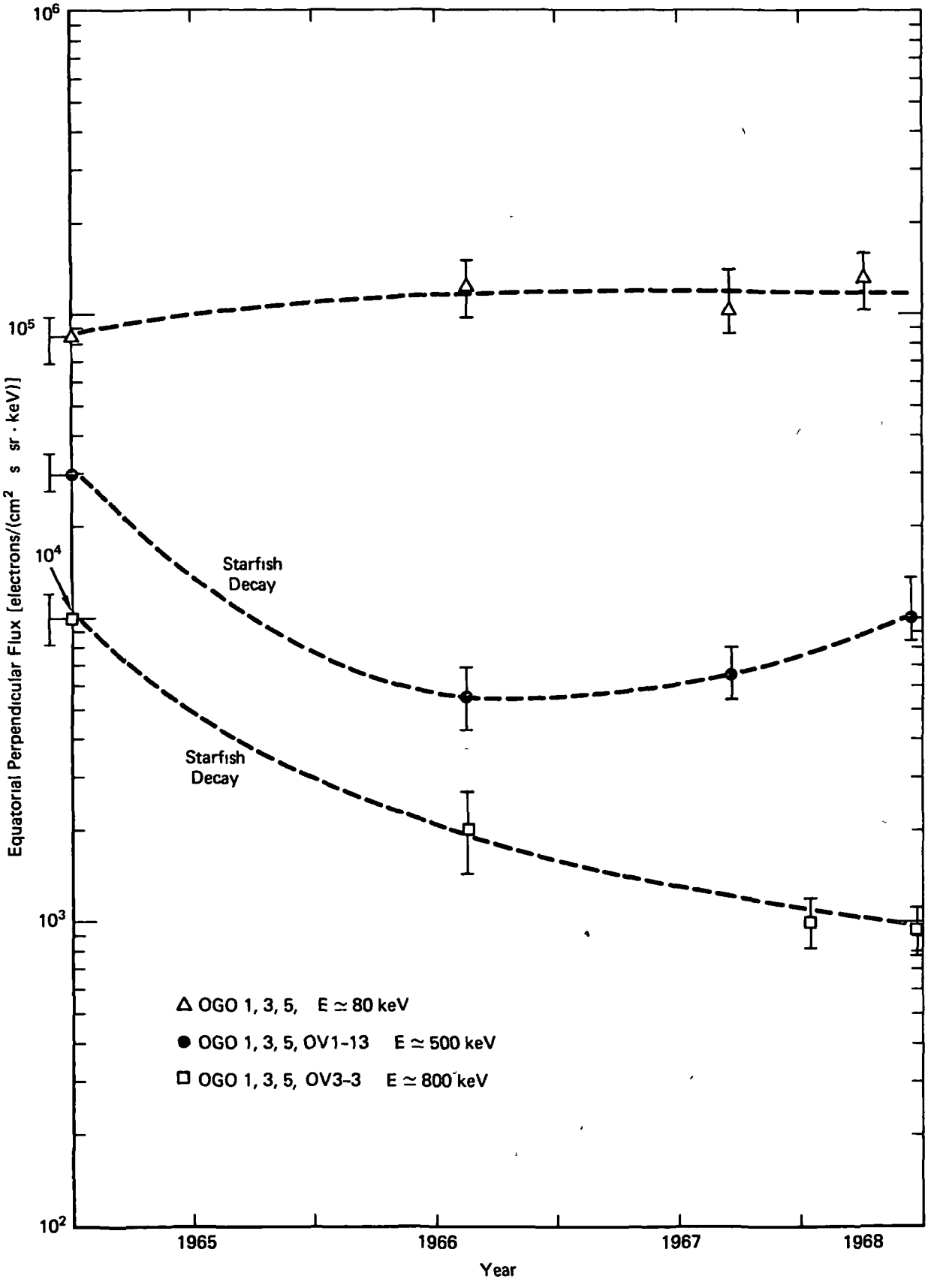

Figure 135. Variation of the Quiet Time Flux at L = 1.4

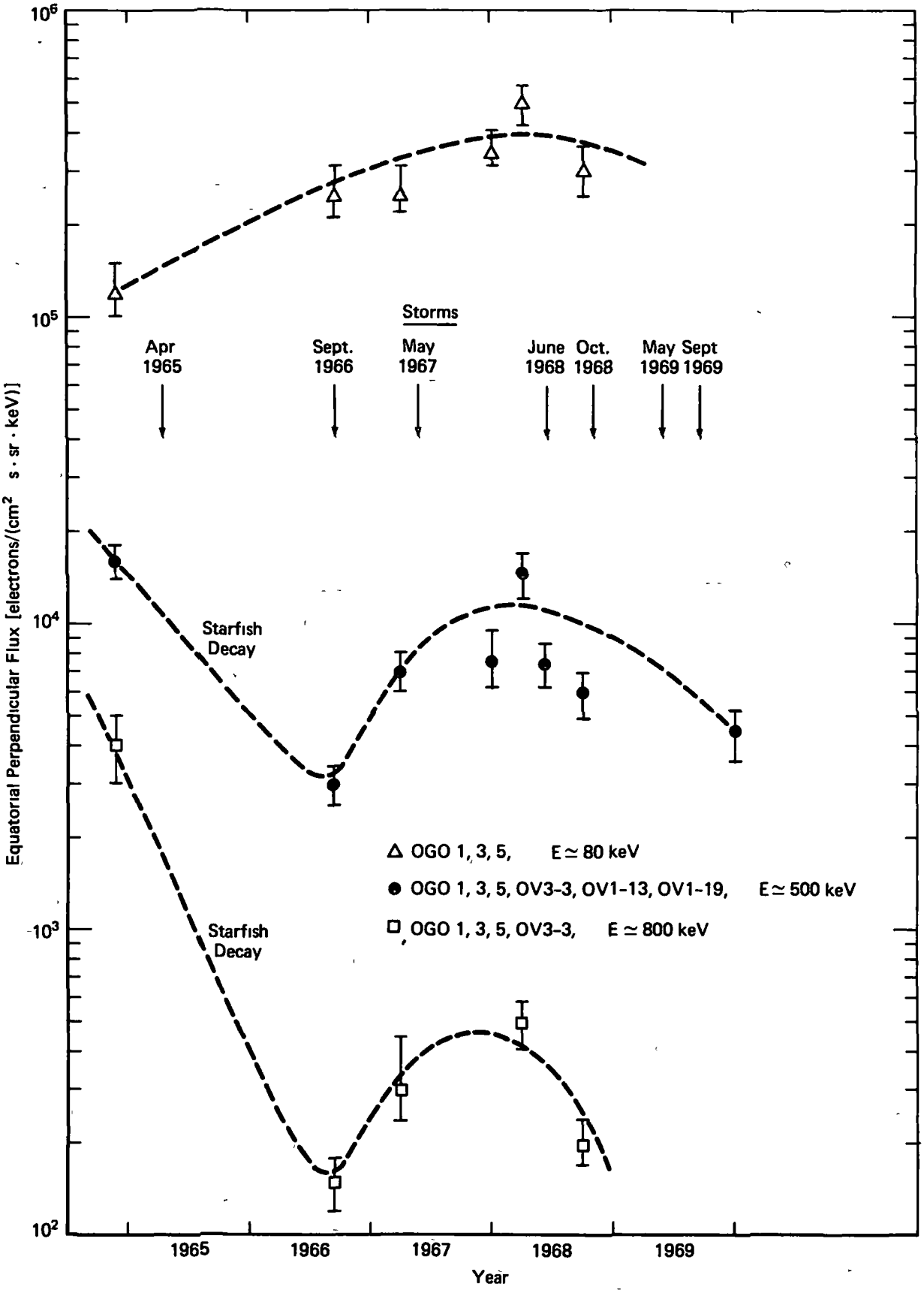

Figure 136. Variation of the Quiet Time Flux at L = 1.8

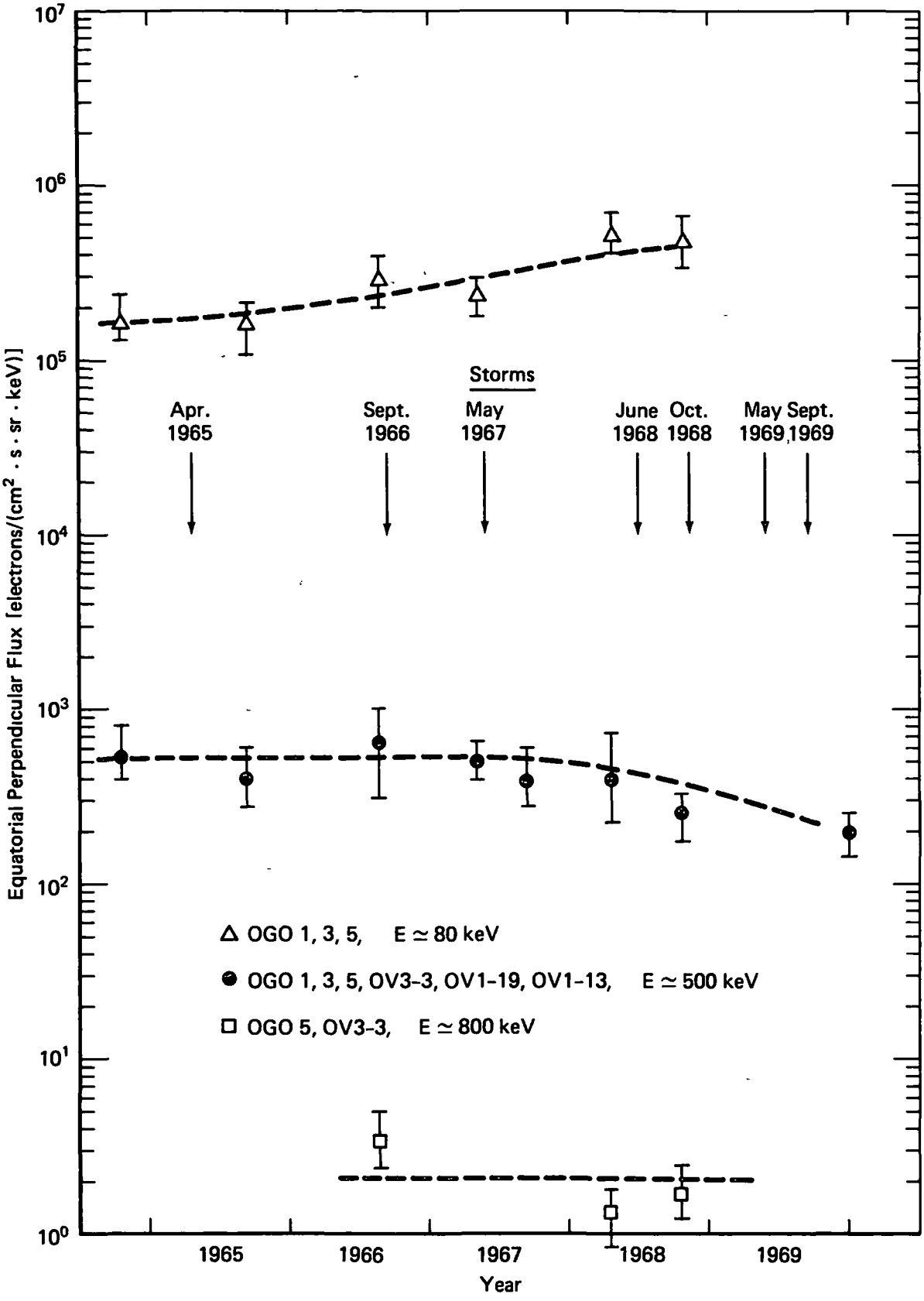

Figure 137. Variation of the Quiet Time Flux at L = 2.4

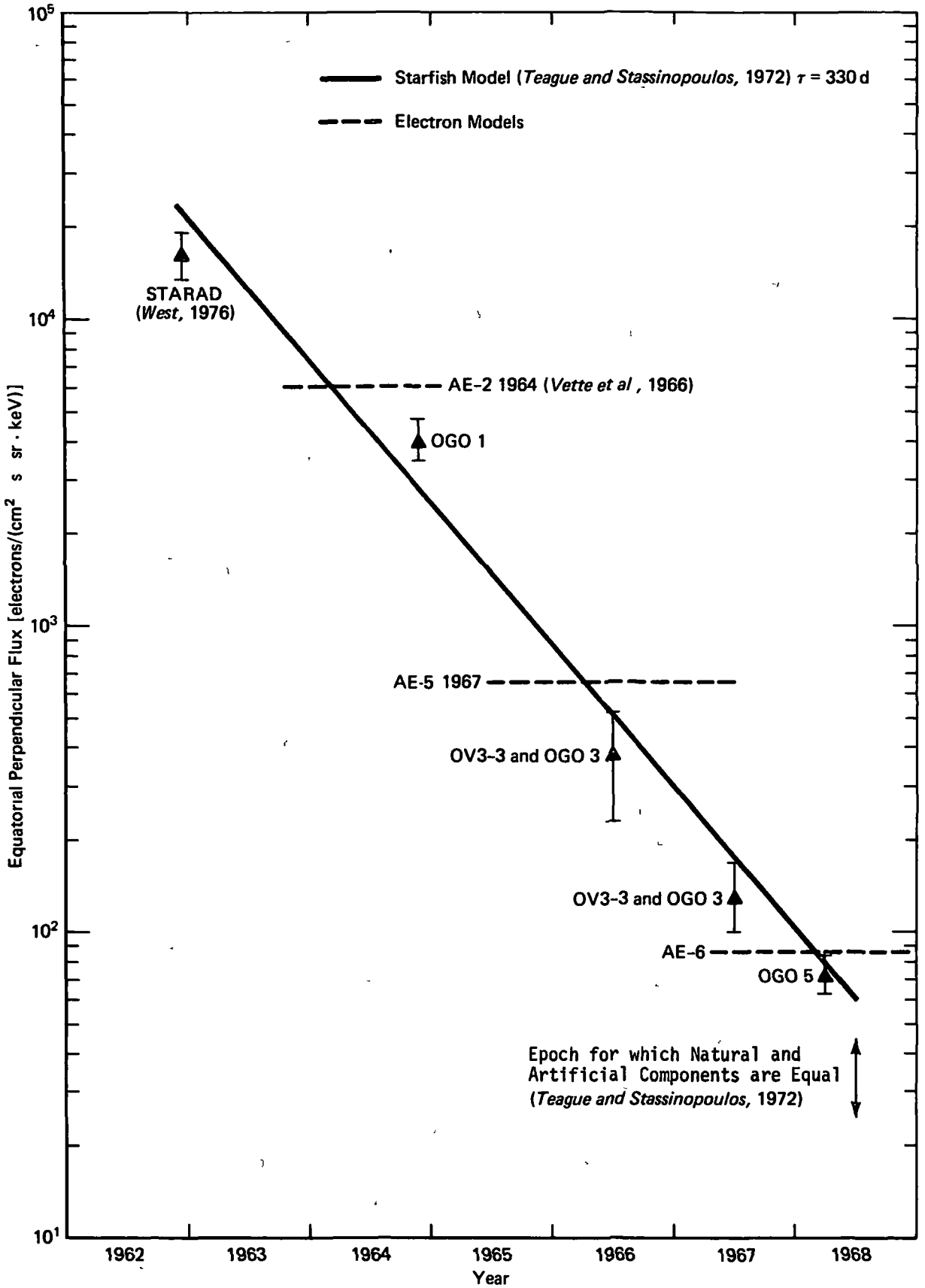

Figure 138. Decay of Starfish Electrons at L = 1.5, E ≃ 1.5 MeV

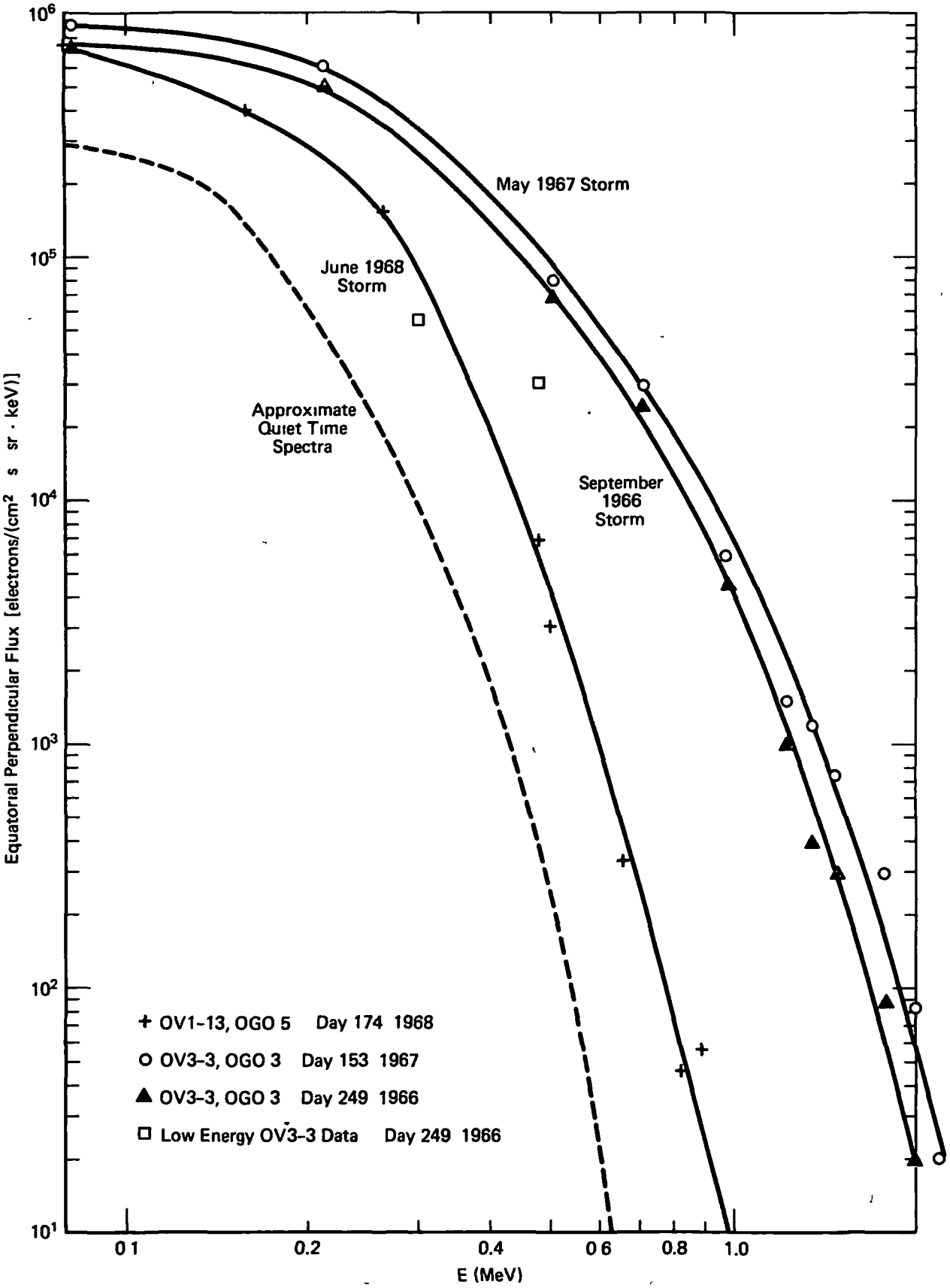

Figure 139. Peak Flux Storm Spectra at L = 2.4

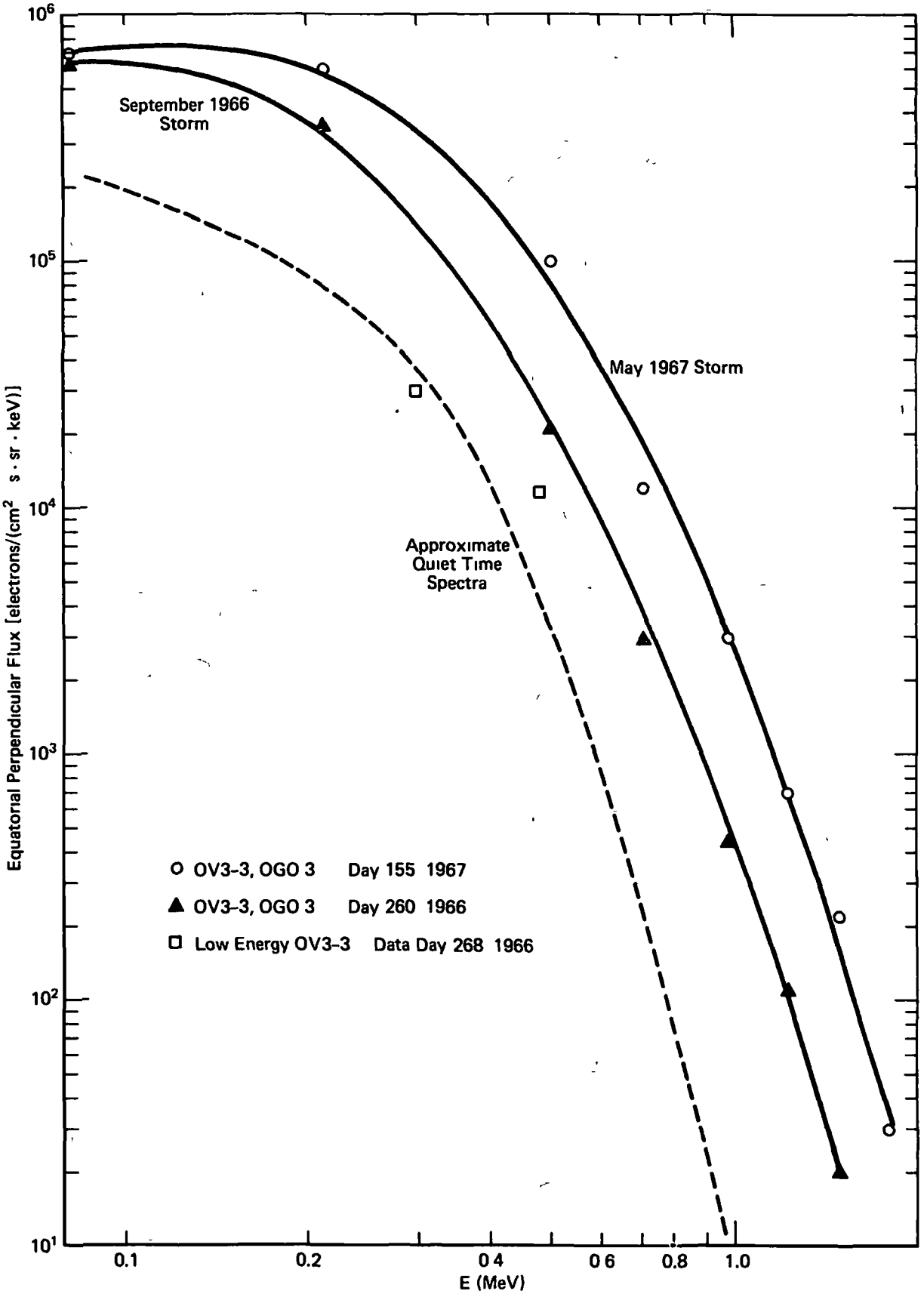

Figure 140. Peak Flux Storm Spectra at L = 2.0

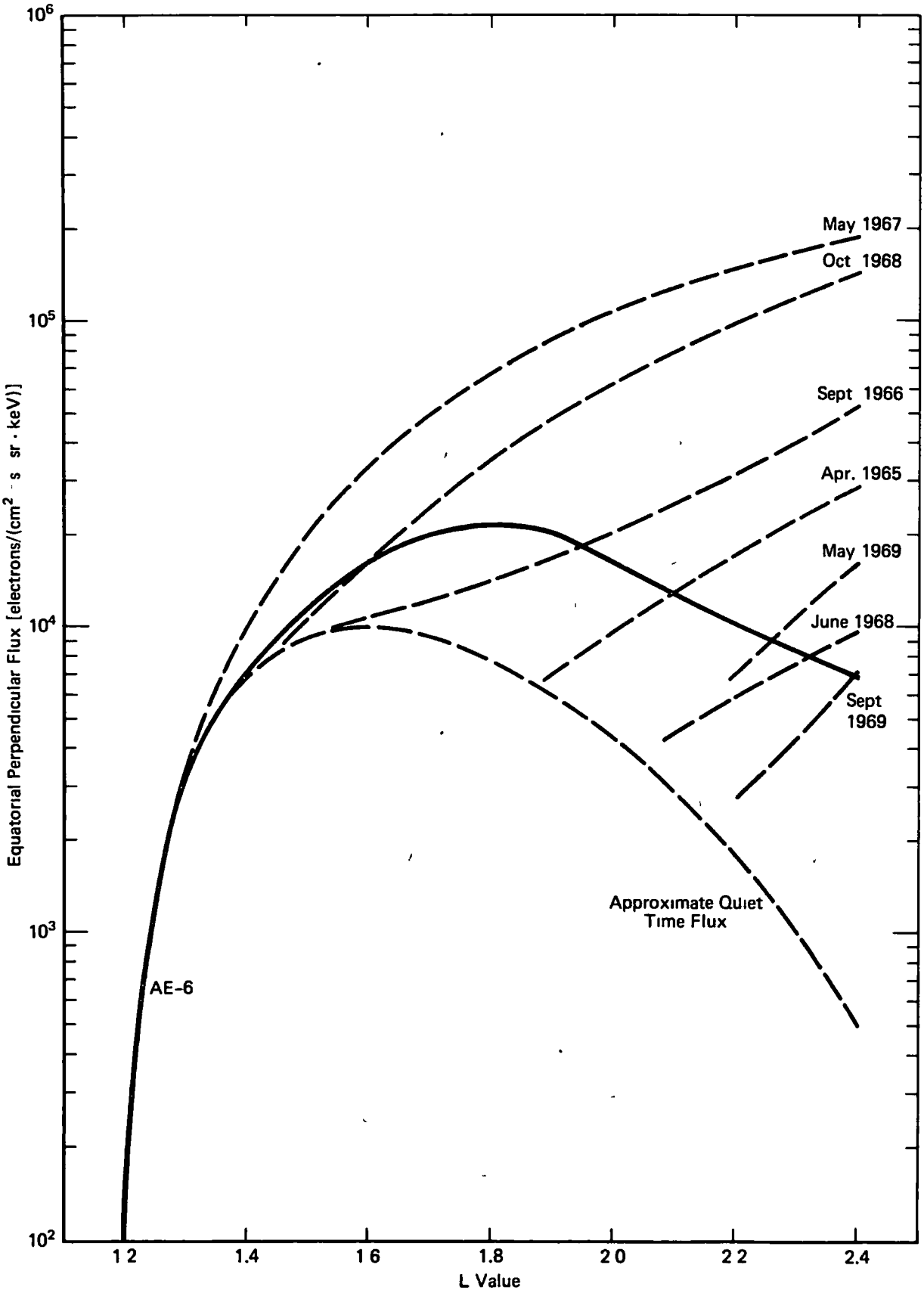

Figure 141. Peak Storm Radial Profiles for 500-keV Electrons

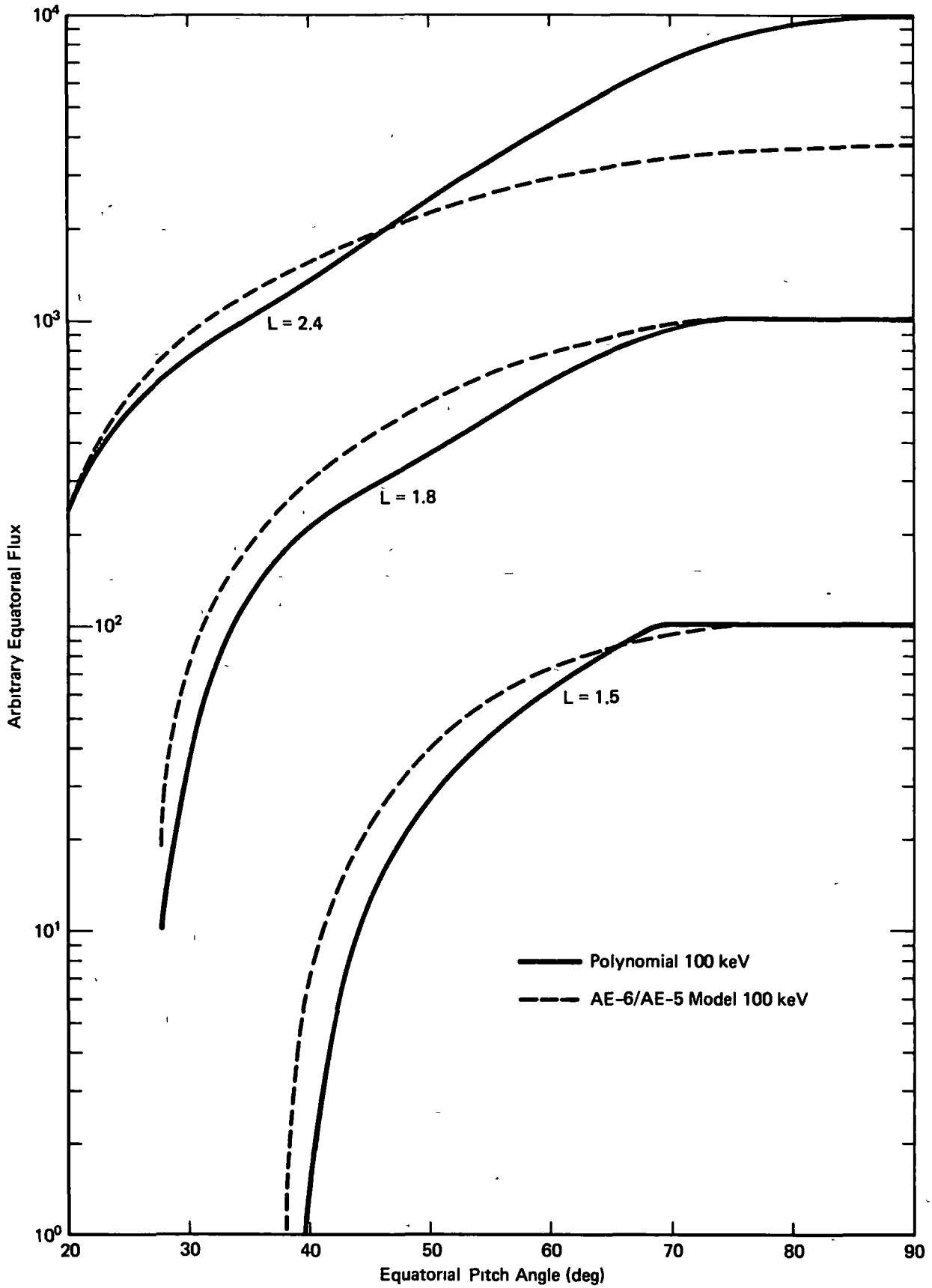

Figure 142. Comparison of Polynomial and AE-6 Pitch Angle Distributions

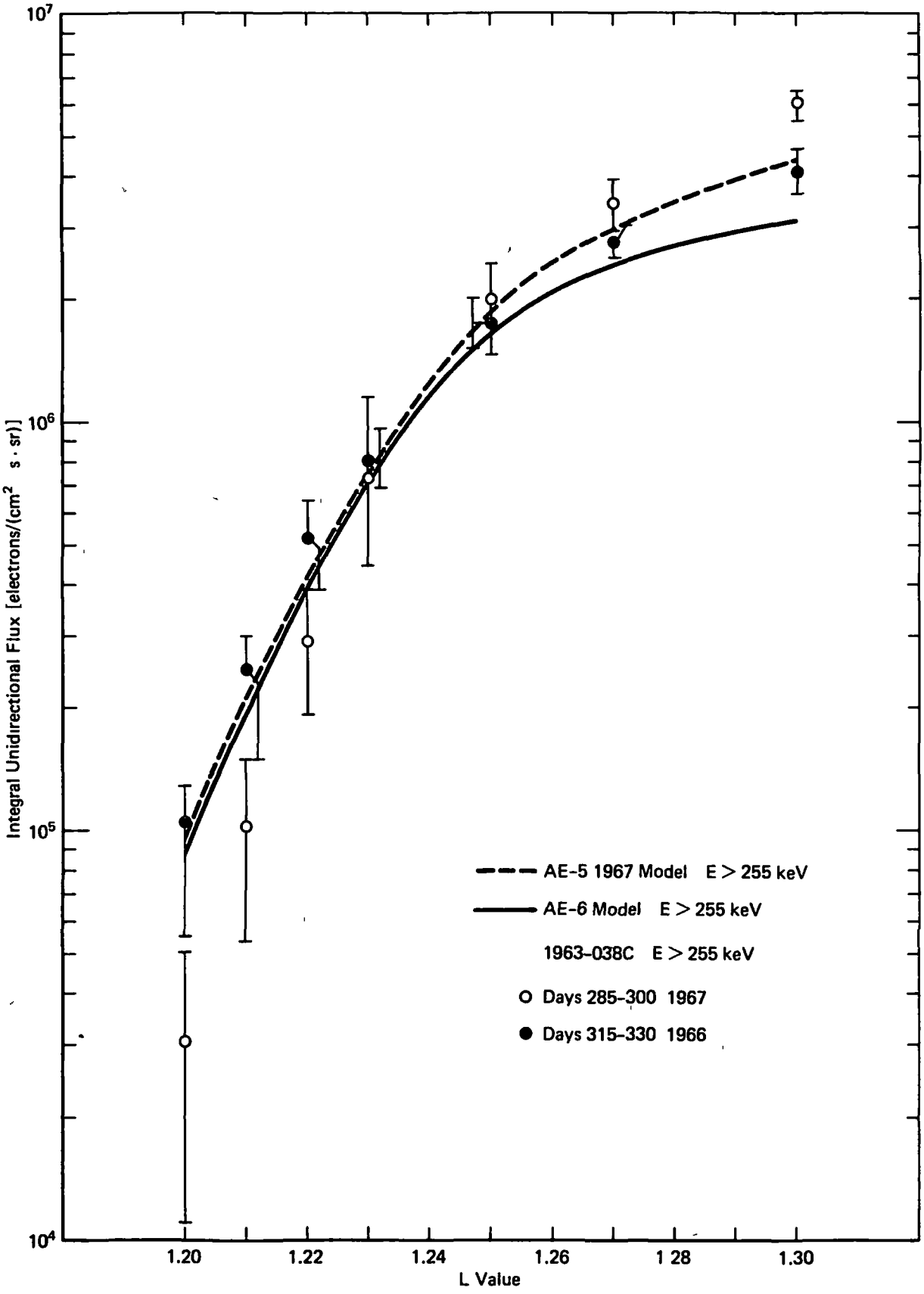

Figure 143. Comparison of Models AE-5 1967 and AE-6 with 1963-038C data

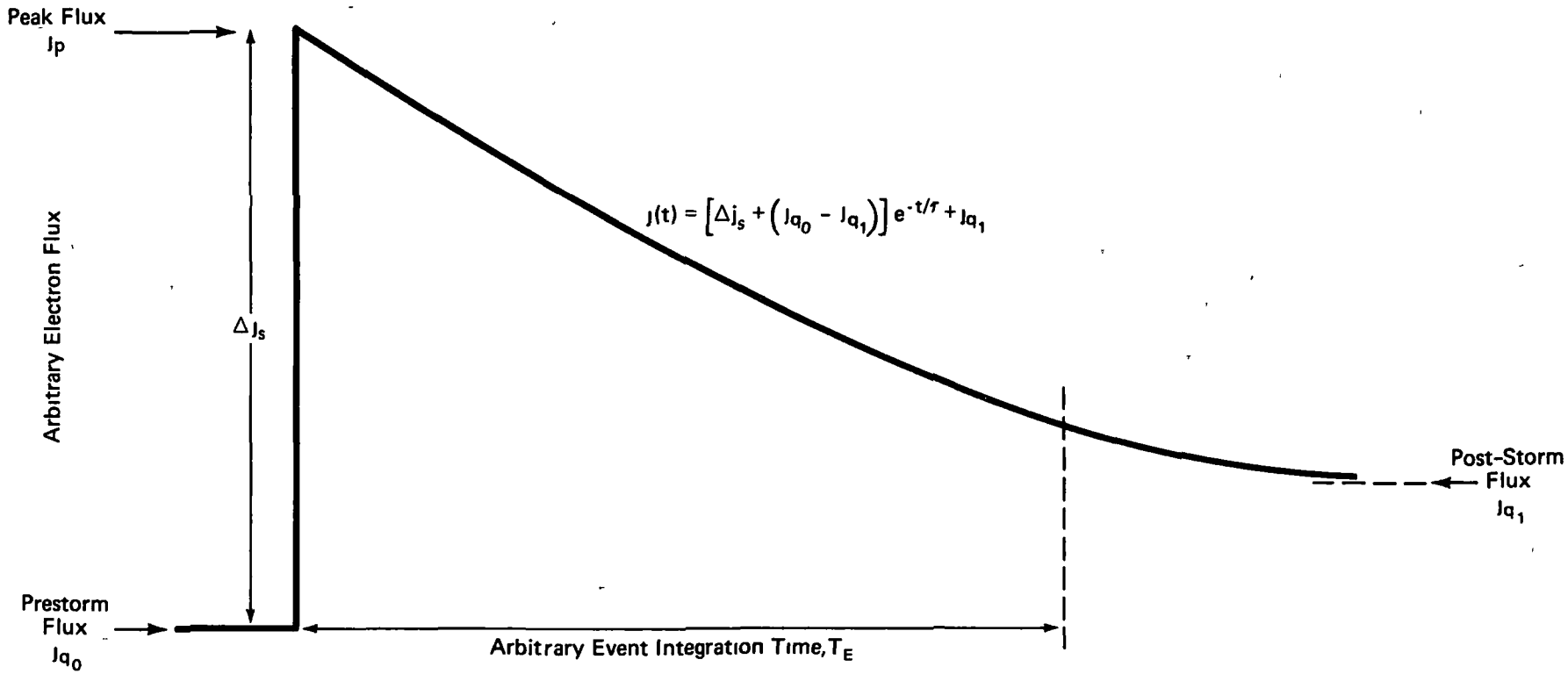

Figure 144. Storm Model

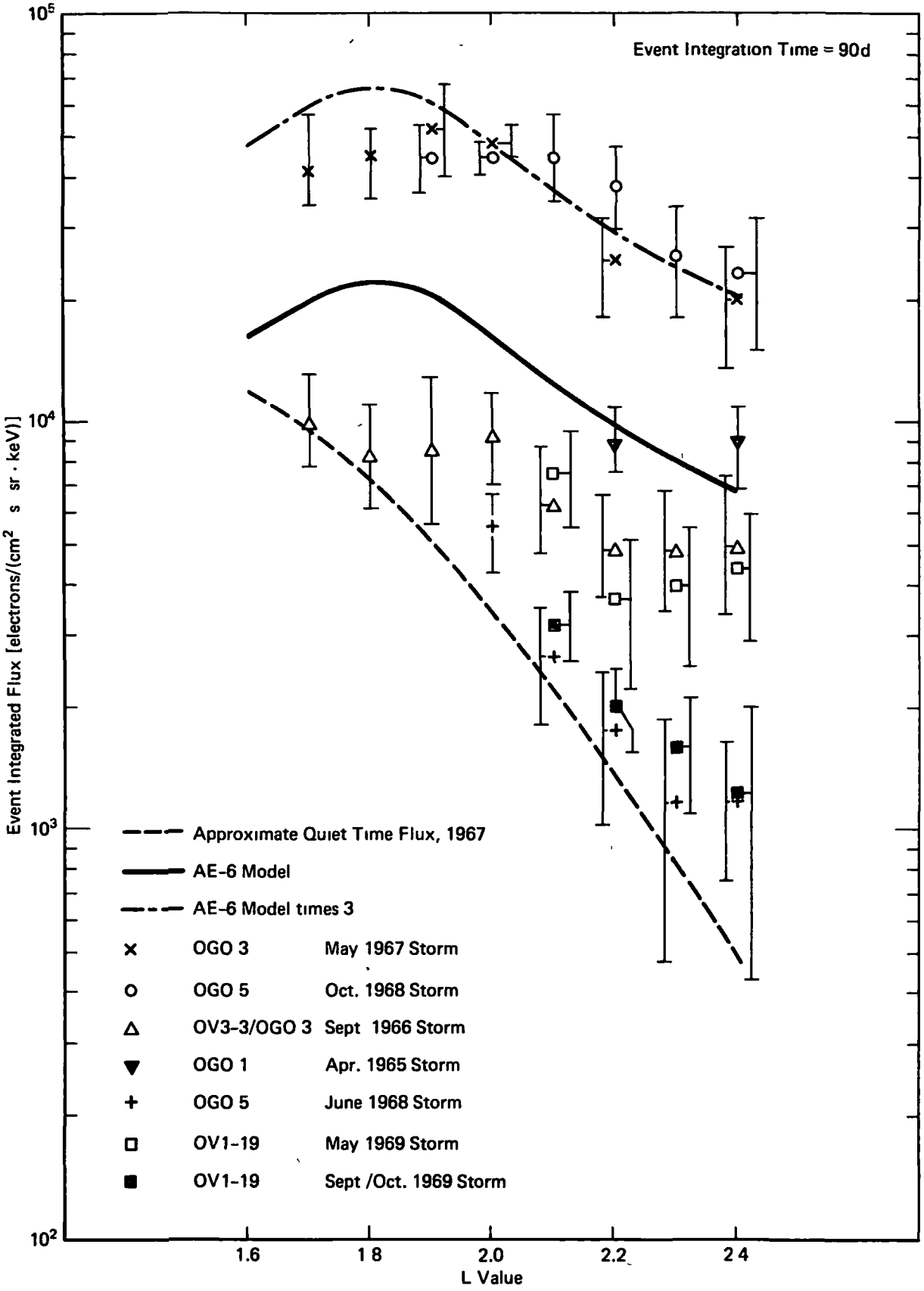

Figure 145. Event Integrated Radial Profiles E ≈ 500 keV

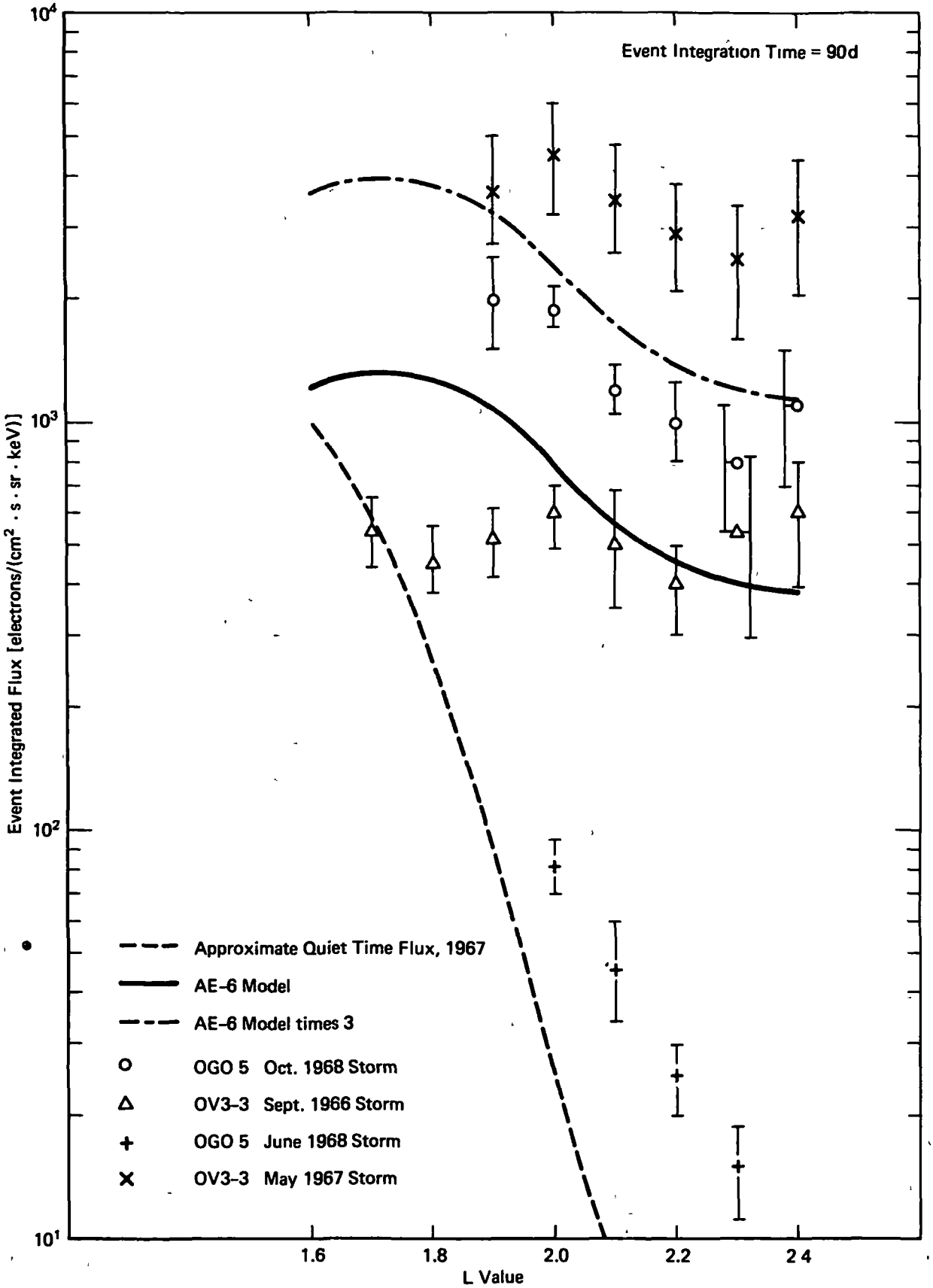

Figure 146. Event Integrated Radial Profiles E ≃ 800 keV

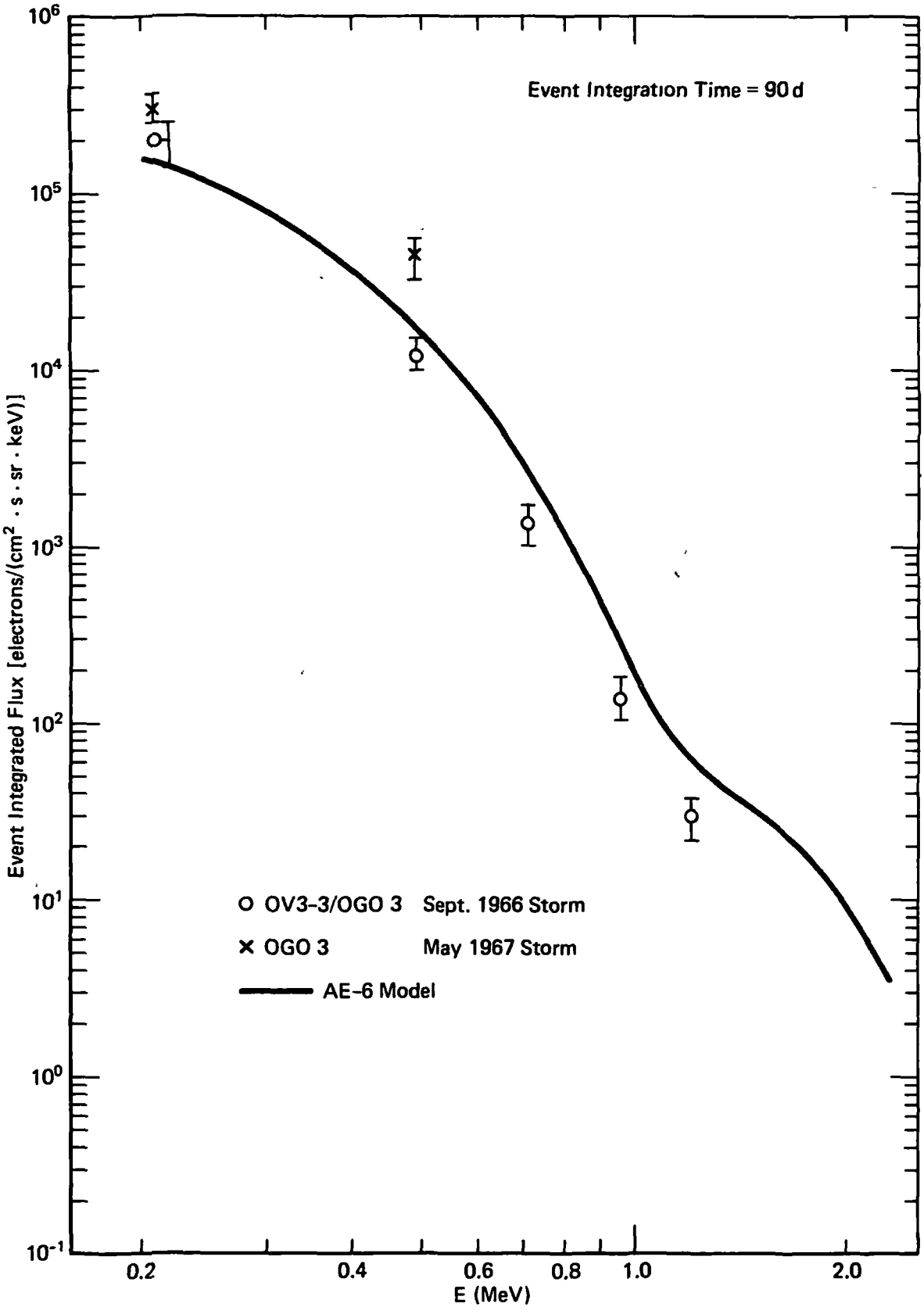

Figure 147. Event Integrated Spectra at $L = 1.8$

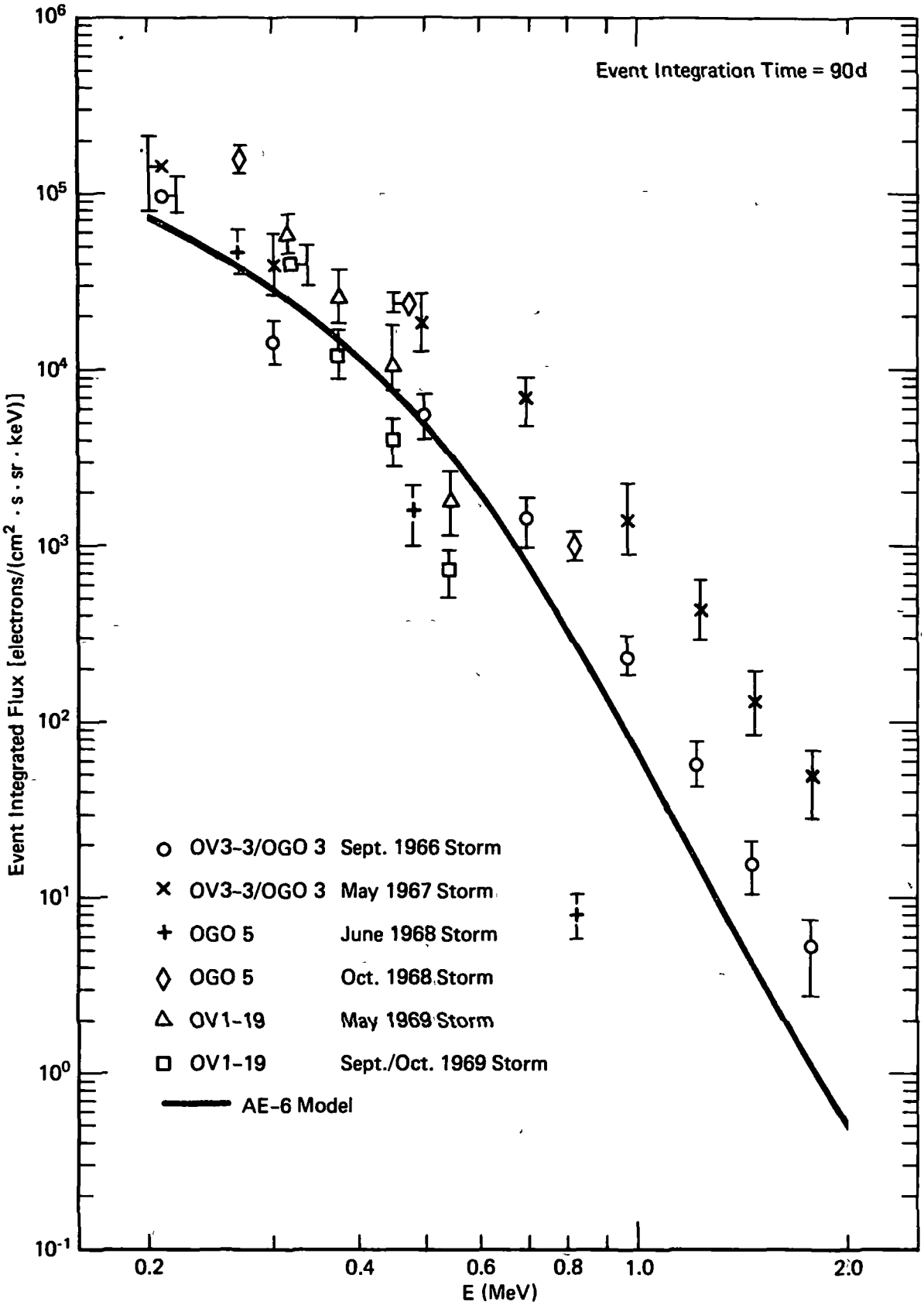

Figure 148. Event Integrated Spectra at L = 2.4

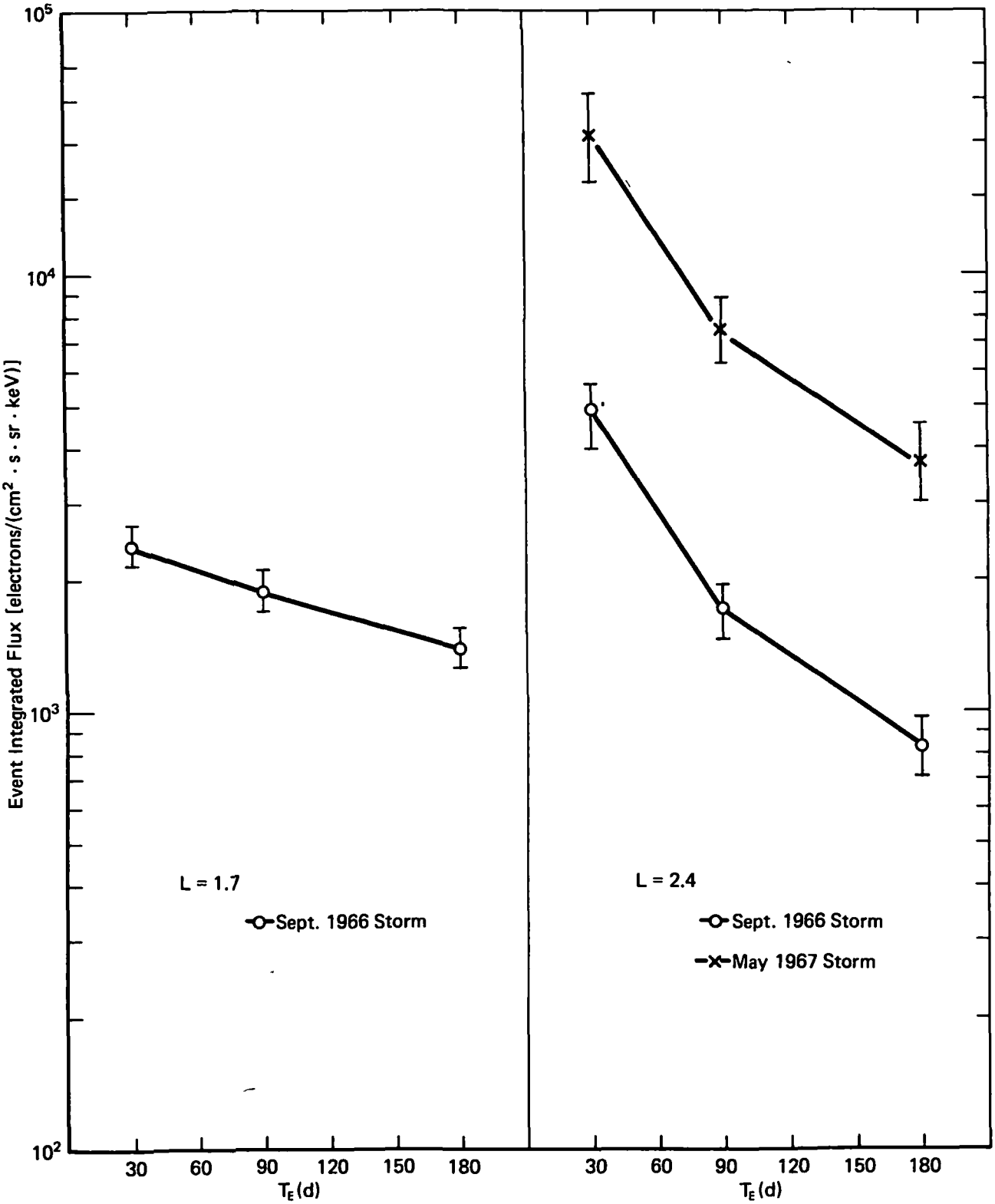

Figure 149. Comparison of Event Integrated Fluxes with Integration Time

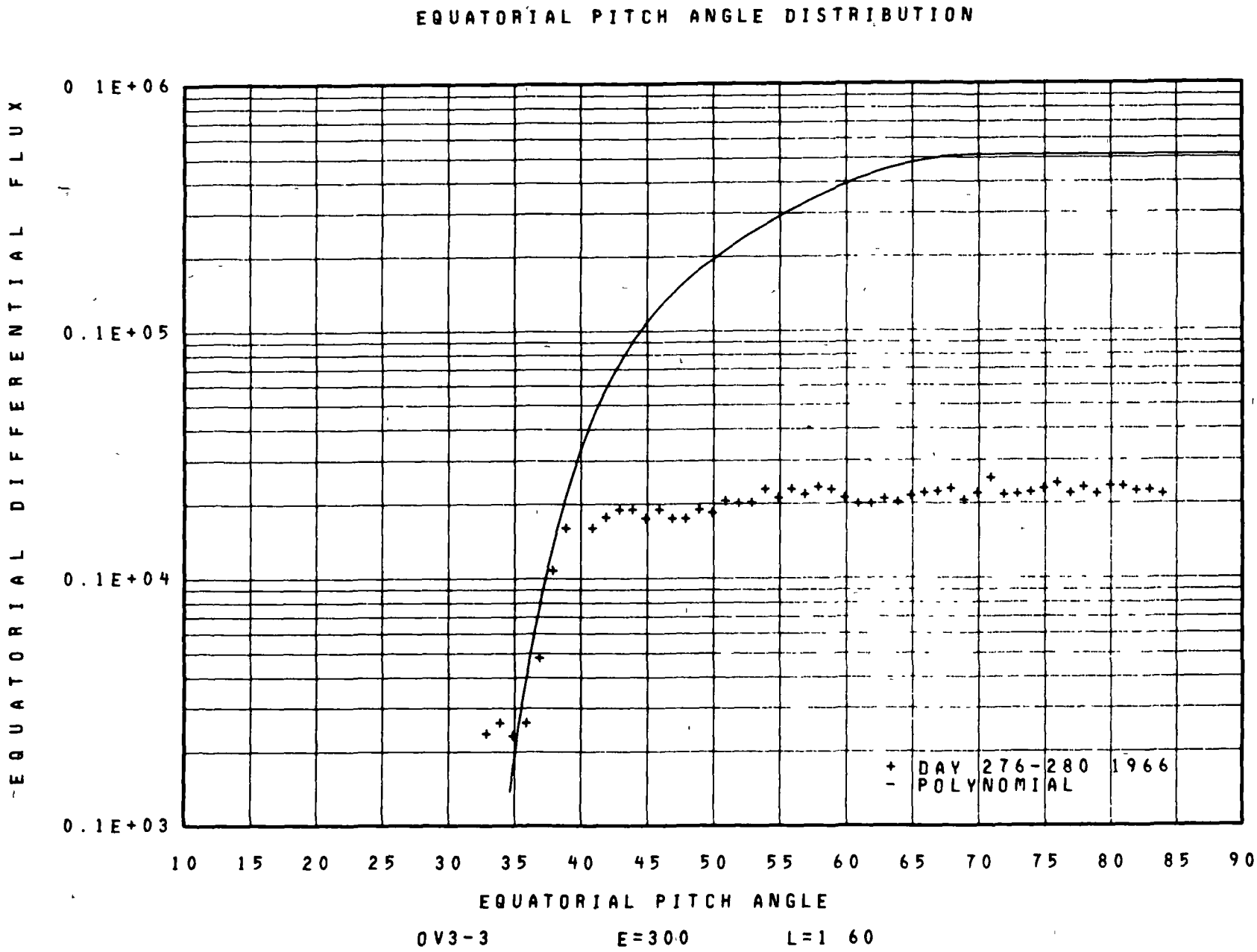
EQUATORIAL PITCH ANGLE DISTRIBUTION
EQUATORIAL DIFFERENTIAL FLUX
0 1E+06
0.1E+05
0.1E+04
0.1E+03
10 15 20 25 30 35 40 45 50 55 60 65 70 75 80 85 90
EQUATORIAL PITCH ANGLE
+ DAY 276-280 1966
- POLYNOMIAL
OV3-3 E=300 L=1 60

Figure 150

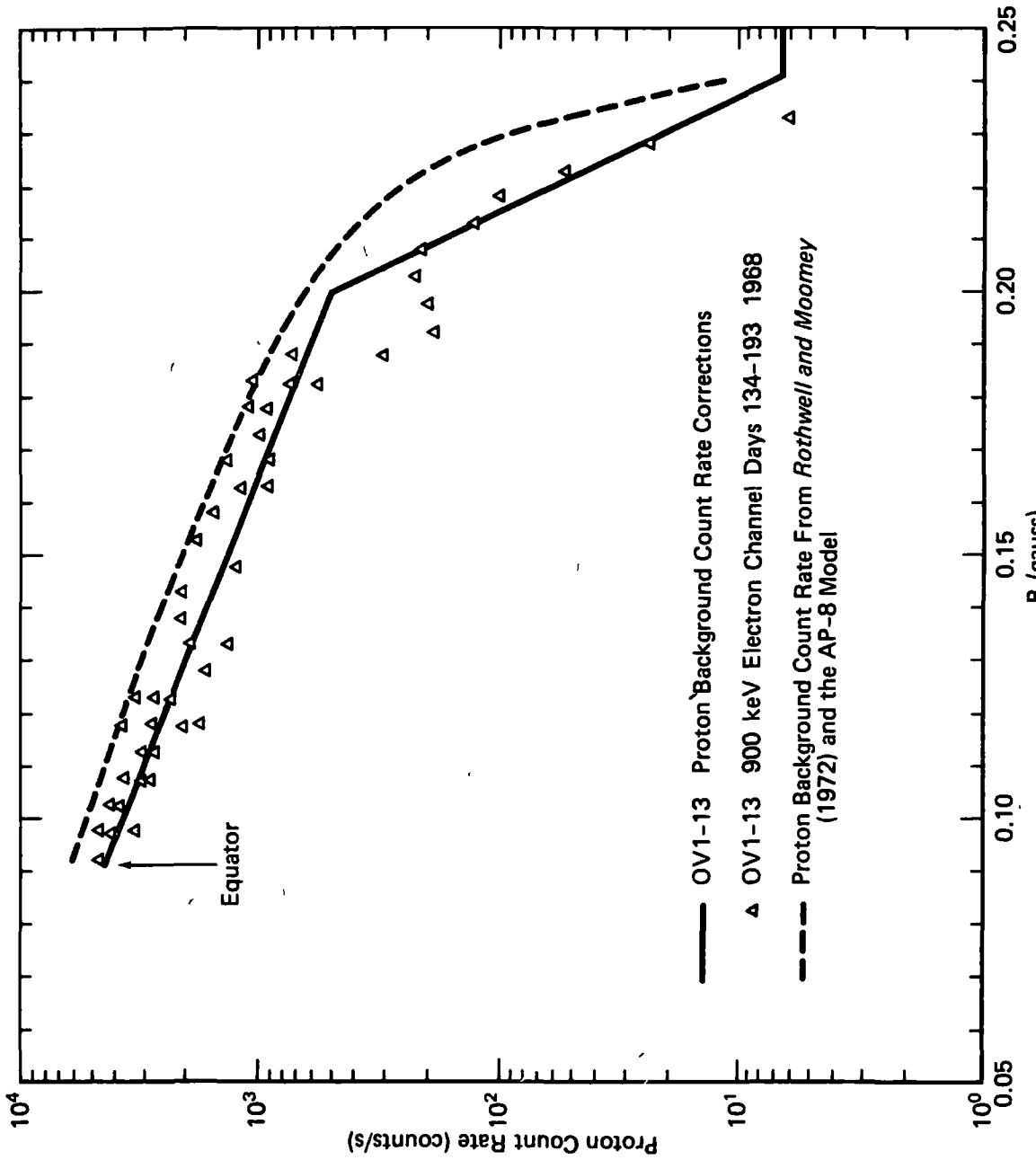

Figure 151. OV1-13 Proton B Distribution at L = 1.5

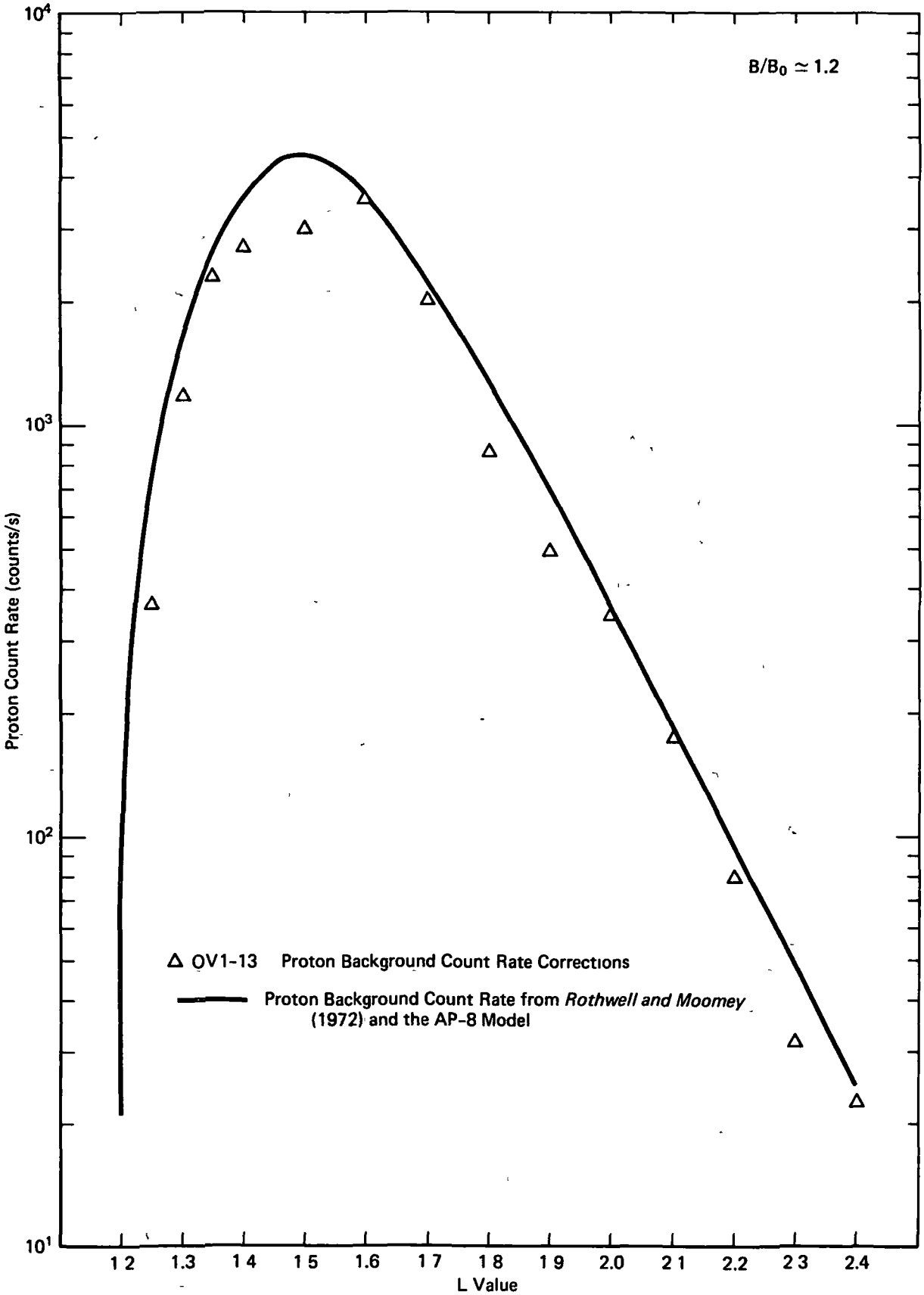

Figure 152. Radial Profile of Proton Correction for OV1-13

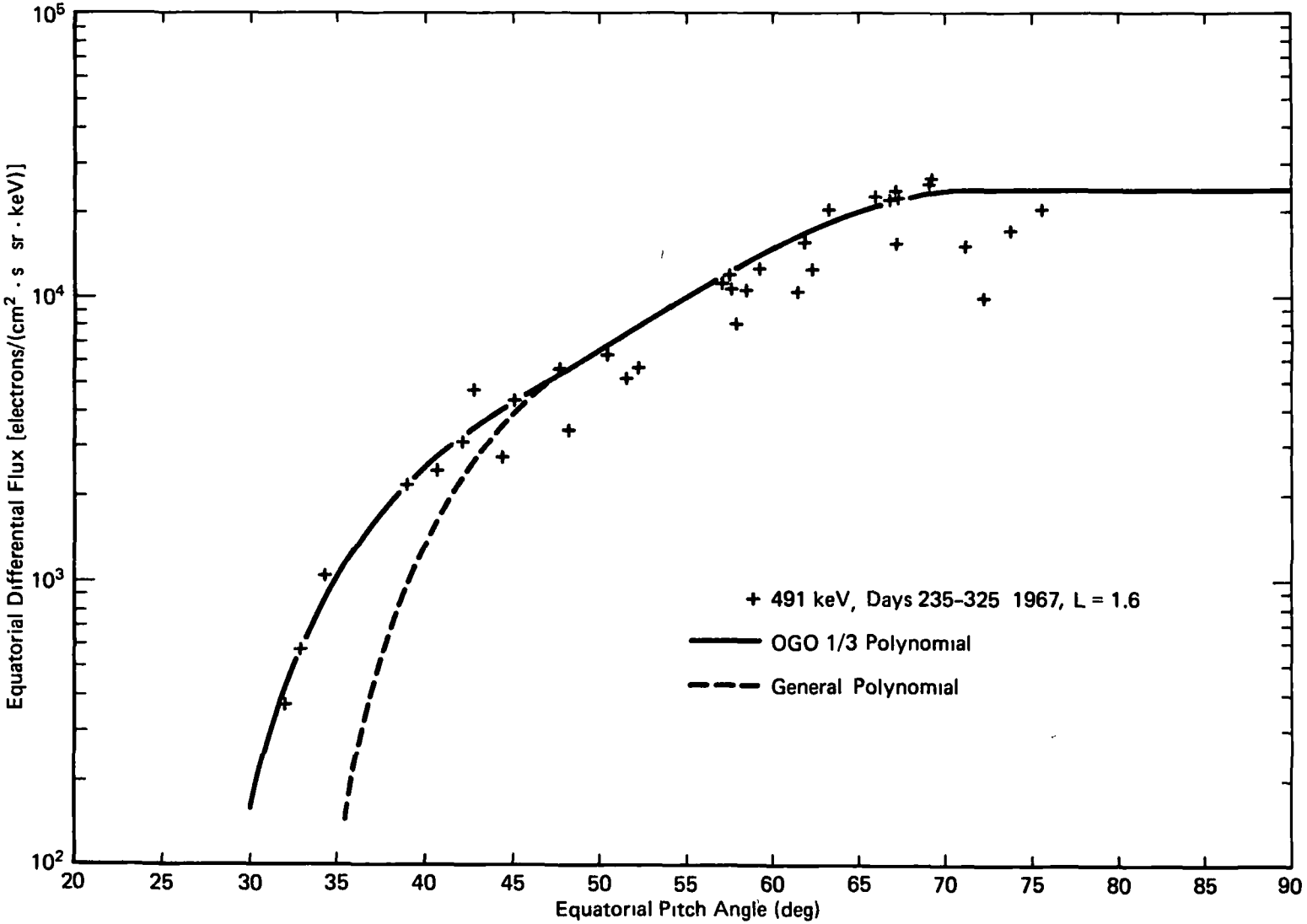

Figure 153. OGO 3 Pitch Angle Distribution

NASA
National Aeronautics and
Space Administration

Goddard Space Flight Center
Greenbelt, Maryland 20771